UNIVERSITÉ D'ORLÉANS

ÉCOLE DOCTORALE SANTE, SCIENCES BIOLOGIQUES ET CHIMIE DU VIVANT

LI2RSO - Laboratoire Interdisciplinaire pour l'Innovation et la Recherche en Santé d'Orléans

Laboratoire Immuno NEuro-Modulation (INEM) - UMR7355

THÈSE présentée par :

Thomas ADOR

soutenue le : **6 mai 2025**

pour obtenir le grade de : **Docteur de l'Université d'Orléans**

Discipline/ Spécialité : Biologie. Biochimie, biologie cellulaire et moléculaire

Gene delivery by sonoporation for Fragile X syndrome therapy

Délivrance de gènes par sonoporation pour la thérapie du syndrome de l'X fragile

THÈSE dirigée par :

Dr. MENUET Arnaud	Maître de conférences (HDR), Université d'Orléans

Encadrée par :

Dr. DELALANDE Anthony	Maître de conférences, Université d'Orléans

RAPPORTEURS :

Dr. TSAPIS Nicolas	Directeur de recherche, institut Galien
Dr. YALCIN Binnaz	Directeur de recherche, Center for Translational and Molecular Medicine Mouse NeuroGenetics

---

JURY :

Pr. PALLU Stéphane	Professeur, Université d'Orléans, Président du jury
Dr. BARBIER Emmanuel	Directeur de recherche, Grenoble Institut des Neurosciences
Dr. NOVELL Anthony	Chargé de recherche (HDR), BioMaps
Dr. MENUET Arnaud	Maître de conférences (HDR), Université d'Orléans
Dr. DELALANDE Anthony	Maître de conférences, Université d'Orléans

Remerciements :

Cette thèse a été réalisée en premier lieu au Centre de Biophysique Moléculaire (CNRS UPR 4301) durant deux ans avant le déménagement de l'équipe dans l'ART-ARNm (INSERM, US 55). Elle a été réalisée sous la direction d'Arnaud MENUET et la supervision d'Anthony DELALANDE, que je remercie pour leur aide et leur expertise.

Je souhaite tout d'abord remercier Dr. Nicolas TSAPIS et Dr. Binaz YALCIN d'avoir accepté la tâche de rapporteur de ce travail de thèse. Je remercie également tous les membres de mon jury qui me font l'honneur d'évaluer mon travail de thèse : Dr. Emmanuel BARBIER, Pr. Stéphane PALLU et tout particulièrement Dr. Anthony NOVELL pour sa patience.

Je tiens à exprimer ma gratitude la plus sincère à Mylène FOURNIE, qui m'a accompagné durant les 3 ans de ma thèse et sans qui j'aurais 2 fois moins de résultats à présenter. Elle a été présente durant la quasi-totalité des manips *in vivo*, elle s'est cassée la tête sur les protocoles de RT-qPCR, de western blot, d'immunohistochimie, et elle a traité une quantité innombrable de cerveaux pour le projet. Merci infiniment pour toute ton aide, nos discussions et tes bonnes idées.

Je remercie aussi toute l'équipe de Chantal PICHON que j'ai côtoyée au quotidien et qui a toujours été là pour m'aider. Je remercie à nouveau d'abord la partie bubble team, qui a bien évolué depuis le début de ma thèse, dont seul Mylène a fait partie du début à la fin. Je remercie donc Colleen et Hanadi, qui ont été là à mon arrivée et qui ont su démarrer des projets que j'ai repris par la suite. Mes remerciements également à Allan, stagiaire devenu collègue, puis encadrant attitré des stagiaires, partenaire de course et toujours doué pour mettre une bonne ambiance. Merci à Claire, arrivée plus tard, mais avec une expertise nouvelle et bien venue. Je remercie par ailleurs Redouan d'avoir osé faire son stage de M2 avec moi. Et enfin, merci énormément à Julie, dernière arrivée dans la bubbleteam mais qui m'aura accompagné dans la solitude de CME et qui m'a beaucoup aidé à finaliser un grand nombre de manips. Et bon courage pour ta thèse, je suis sûr que tu vas t'en sortir sans problème, de toute façon, je ne

doute pas qu'on va continuer à bosser ensemble. Je remercie ensuite chaleureusement Nabila, arrivée dans l'équipe avec moi, merci pour ta gentillesse et tous les bons moments passés ensemble. Plus généralement, merci à Cristine, Ivan, Christophe, Delphine, Milad, Magali, Natalia, Vianney, Maryvonne pour votre aide et votre bonne humeur.

J'adresse un remerciement tout particulier à Élise, pour ton soutien indéfectible au labo et en dehors, pour tous nos bons moments, merci d'avoir partagé cette période de ma vie. Tu as été là dès le début et t'avoir à mes côtés a été primordial pour moi. Merci pour tout, je n'aurais jamais pu espérer avoir avec moi une partenaire de vie telle que toi.

Je remercie ensuite mes voisins de bureau du CBM, Albert et Ayoub, toujours prompts à discuter de tout et de rien, et parfois de science (parfois). Je remercie également tous les doctorants du CBM, avec qui j'ai toujours passé de bons moments, et merci en particulier à Clémence, avec qui j'ai toujours apprécié passer du temps autour d'un jeu de société ou autre. Bon courage à tous pour la fin de vos thèses. Pour la plupart, c'est bientôt la fin, j'ai hâte d'enchainer les pots de thèse avec vous.

Je remercie également l'équipe du GIN de Grenoble, qui m'a royalement accueillie pendant mon passage à Grenoble. Merci à tous, j'ai adoré ce moment de ma thèse en grande partie grâce à vous. Je remercie tout particulièrement (Docteur !) Sébastien, merci pour ton aide précieuse et ta bonne humeur, en manip comme en réflexion, en écriture et en dehors du labo.

De plus, je remercie également chaleureusement ma famille pour leur soutien inestimable durant ces longues études. Merci de m'avoir encouragé dans cette voie et de m'avoir apporté les conditions nécessaires au bon déroulement de mes études jusqu'au bout. Je remercie tout particulièrement ma sœur, Billie, probablement la personne la plus intelligente que je connaisse, qui m'a précédé dans la recherche et m'a beaucoup inspiré.

Je remercie enfin les responsables de la plateforme MO2VING du CBM, qui m'ont apporté une aide et une expertise précieuse. Merci donc à Hervé MEUDAL pour les analyses de RMN, à Guillaume GABANT pour les analyses de spectrométries de masse et un grand merci à David

GOSSET pour ses formations et ses conseils pour la cytométrie en flux, la microscopie de fluorescence et le confocal.

Pour finir, je remercie l'Agence Nationale de la recherche d'avoir financé cette thèse.

Table des matières :

Liste des abréviations :

A.U.: Arbitrary unit

AAV: Adeno-associated virus

AAV-*Fmr1*: AAV2/9.CMV.Fmr1-eGFP

AAV-Luc: AAV2/9.CMV.Luciferase

ABC: ATP-binding cassette

AD: Alzheimer's disease

ADHD: Attention deficit and hyperactivity disorder

APP: amyloid β precursor protein

ASD: Autism spectrum disorder

ASOs: Antisense oligonucleotides

Aβ: amyloid Beta

BBB: Blood-brain barrier

BBBo: Blood-brain barrier opening

BHE: barrière hémato-encéphalique

bMB: Biotinylated microbubble

cGAS-STING: Cyclic GMP-AMP synthase–stimulator of interferon genes

cMB: Cationic microbubble

CMV: Cytomegalovirus

CNS: Central nervous system

CRISPR: Clustered Regularly Interspaced Short Palindromic Repeats

CryoTEM: Cryogenic electron microscopy

CSF: Cerebrospinal fluid

DC: Duty cycle

dCas9: Dead Cas9

DLS: Dynamic light scattering

dMB: DBCO-microbubble

DMPC: 1,2-dimyristoyl-sn-glycero-3-phosphocholine

DMPE-PEG2000: 1,2-dimyristoyl-sn-glycero-3-phosphoethanolamine-N-[methoxy(polyethylene glycol)-2000]

DOPE: 1,2-dioleoyl-sn-glycero-3-phosphoethanolamine

DSPC: 1,2-distearoyl-sn-glycero-3-phosphocholine

DSPE-NHS: 1,2-Distearoyl-sn-glycero-3-phosphoethanolamine-NHS ester

DSPE-PEG2000: 1,2-distearoyl-sn-glycero-3-phosphoethanolamine-N-[methoxy(polyethylene glycol)-2000]

DSPE-PEG2000-Biot: 1,2-distearoyl-sn-glycero-3-phosphoethanolamine-N-[biotinyl(polyethylene glycol)-2000]

DSPE-PEG2000-DBCO: 1,2-distearoyl-sn-glycero-3-phosphoethanolamine-N-[dibenzocyclooctyl(polyethylene glycol)-2000]

DTE: Differential targeted enhancement

EMA: European Medicines Agency

EPM: Elevated plus maze

EVs: Extracellular vesicles

F.I: Fluorescence intensity

FBS: Fetal bovine serum

FDA: Food and Drug Administration

Fmr1: fragile X messenger ribonucleoprotein 1

FMRP: Fragile X messenger ribonucleoprotein

FUS: Focused ultrasound

FUS-BBBo: Focused ultrasound and microbubble-mediated blood-brain-barrier opening

FXS: Fragile X syndrome

GDNF: Glial cell line-derived neurotrophic factor

H&E: Hematoxylin and Eosin

ICD: Inertial cavitation dose

ICG: Indocyanine Green

ICV: intracerebroventricular injection

ID: Intellectual deficiency

IN: Intranasal injection

IONP: Iron oxide nanoparticles

IV: Intravenous injection

KO: Knock-out

LNP: Lipid nanoparticle

MB: Microbubble

MB-MAG: Magnetic microbubble

mGlur: Metabolic glutamate receptor

MI: Mechanical index

Micro-CT: Micro-computed tomography

MRI: Magnetic resonance imaging

mRNA: Messenger RNA

NB: Nanobubble

NHEJ: Non-homologous end joining

NMR: Nuclear magnetic resonance

NOR: Novel object recognition test

NP100: 100 nm Iron oxide nanoparticles

NP50: 50 nm Iron oxide nanoparticles

NTA: Nanoparticle tracking analysis

PCD: Passive cavitation detector

PD: Parkinson's disease

pDNA: Plasmid DNA

PEI: Polyethyleneimine

PET: Positron emission tomography

pMB: polymeric cationic microbubble

PND: Post-natal day

PNP: peak-negative acoustic pressure

PRF: Pulse repetition frequency

PRP: Pulse repetition period

RMM: Resonant mass measurement

ROI: Region of interest

SCD: Stable cavitation dose

SEM: Standard error of the mean

sgRNA: Single-guide RNA

shRNA: Short hairpin RNA

siRNA: Small interfering RNA

$T_{1/2}$: Half-time

TALENs: Transcription activator-like effector nucleases

TRPS: Tunable Resistive Pulse Sensing

uMB: Unfunctionalized microbubble

US: Ultrasound

Vg: Viral genomes

WT: Wild-type

ZFNs: Zinc finger nucleases

Liste des figures :

1. Ultrasound and its applications with microbubbles

1.1 Ultrasound and its medical use

Ultrasounds (US) are high-frequency (over 20 kHz) sound waves capable of propagating through soft materials like skin and organs. They are typically generated with piezoelectric elements, converting an oscillating electric signal to ultrasound waves that can be curved in order to focus ultrasound in a focal spot. Ultrasound can be generated continuously or pulsed and is characterized by its acoustic pressure and frequency. In medicine, the intensity of ultrasound is often referred to as its mechanical index (MI), calculated as the ratio of the peak negative pressure and the square root of the frequency. When pulsed ultrasounds are used, they are also characterized by the pulse repetition frequency (PRF) and pulse duration, also referred to as duty cycle (DC) given by the product of the pulse duration and the PRF (Figure 1.A). When focused ultrasound (FUS) is used, the shape and size of the focal spot, where the acoustic pressure is at its maximum, depends on the size and curvature of the FUS probe, and the ultrasound's frequency [1]. In the medical field, it has first been used for therapeutic purposes, generally using focused ultrasound, as it allows a targeted application, limiting off-target treatment [2]. In tissues, the acoustic energy can be absorbed, leading to a heating effect on the tissue. It also leads to the propagation of acoustic radiation forces that can create microstreaming in blood vessels. These principles have been used in therapeutic applications and proved to be effective for neurostimulation or thermal ablation showing therapeutic effects in neurodegenerative disorders [3]. It has also been widely used for histotripsy, where high-energy FUS is used, leading to thermal ablation and immunological recruitment from heating and mechanical activation [4]. This application showed efficient therapeutic effect, especially in the treatment of glioblastoma. Ultrasound was later used in imaging using the

different reflection properties and propagation speed to differentiate tissues, making of it an efficient non-invasive imaging modality.

1.2 Ultrasound coupled to MB

In ultrasound imaging, a difference of echogenicity between tissues is necessary to differentiate them. However, blood vessels show little difference in echogenicity from surrounding tissue, making them difficult to observe. As gas has the property of reflecting almost all ultrasound waves, microbubbles, gas-containing contrast agents, were developed in the 1990s to increase contrast in blood flow, allowing new applications such as tissue perfusion analysis. Microbubbles (MB) are micron-sized gaseous particles stabilized by a shell composed of lipids, proteins, or polymers [5]. Their gas core is mostly composed of heavy molecular weight gases such as perfluorocarbons (C_3F_8, C_4F_{10}) or sulfur hexafluoride (SF_6), allowing better stability in the biological environment as these gases have a low solubility in blood compared to other gases like oxygen, avoiding their dissolution. In an ultrasound field, MB can also oscillate following the compression and rarefaction phases of US (Figure 1.B). This oscillation is called cavitation and is dependent on frequency and acoustic pressure [6]. It is typically divided into two subclasses, the stable and inertial cavitation [7]. Stable cavitation is associated with symmetrical oscillation of MB expansion and contraction correlated to the acoustic pressure used. On the opposite, inertial cavitation, which occurs at higher pressure, is associated with chaotic oscillation that can result in jetting or MB collapsing events. MB cavitation creates microstreaming and shear stress in the surrounding medium, allowing sonoporation of surrounding cells *in vitro* and *in vivo* [8]. In brain capillaries, this effect is combined with a push-pull effect, allowing transient blood-brain barrier (BBB) opening (BBBo) and passage of drug into the brain [9]. MB cavitation is related to MB properties and to the US parameters used and can be described using the resonance frequency of the MB, referring to the frequency at which the maximum cavitation occurs [10]. This resonance frequency is dependent on the MB size, shell surface tension and elasticity, gas core nature, and surrounding medium [10,11]. Initially, most therapeutic applications were performed using commercially available MB, FDA-approved at first for echographic contrast imaging, like Sonovue (Bracco, Milan, Italy), Definity (Lantheus Medical Imaging, North Billerica, MA, USA), Optison (GE Healthcare, Milwaukee, WI, USA), or Sonazoid (GE Healthcare,

Milwaukee, WI, USA) [12]. Many commercial MBs are currently available, mostly lipidic but with different sizes, concentrations, stability, or acoustic properties [13]. These MBs have the advantage of being well tolerated with no adverse effects, acoustically effective within circulation, and therefore easier to use in clinical trials [14].

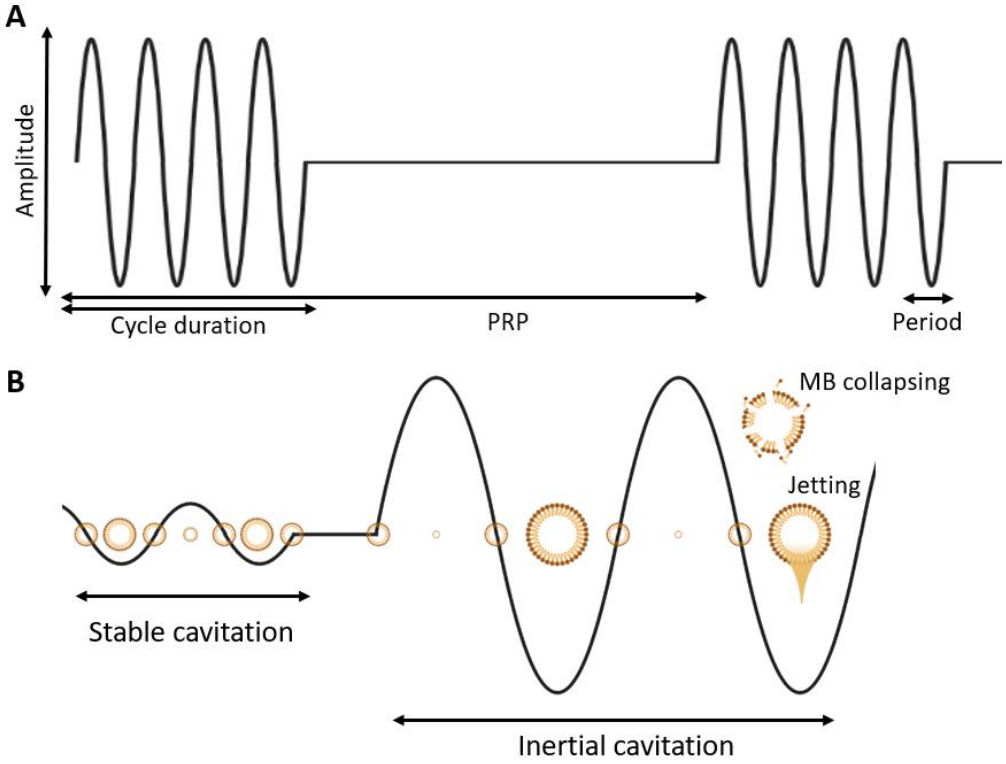

Figure 1: Ultrasound and cavitation principle. (**A**) Schematic representation of pulsed ultrasound. (**B**) Schematic representation of ultrasound-mediated MB stable and inertial cavitation

2. Microbubble formulation

2.1 Lipidic MB

Custom MBs have been developed in order to improve cavitation properties, stability, or to give specific functionalization. The most common MB formulations are lipidic, similarly to most commercially available ones, with the formation of liposomes followed by mechanical

activation with a perfluorocarbon gas. Changing the lipidic composition of MB or core gas leads to changes in MB concentration and size distribution, viscoelastic shell properties, and acoustic properties, but also immunogenicity [15,16]. Phospholipids are generally used for MB formation, with lipidic chains from 14 to 22 carbons and generally saturated. A phospholipid linked to a polyethylene glycol is generally used to enhance MB formation and stability both on the shelf and *in vivo* [17]. Although generally used at around 10% of total composition, using a lower proportion of pegylated phospholipid leads to increased *in vivo* stability and lower immunogenicity but lower MB concentration [18,19]. They can be functionalized either with the incorporation of molecules inside the lipidic layer or by interaction with a reactive group on the MB surface, creating either covalent bonds or electrostatic interactions. Lipidic MBs also have the advantage of having a wide range of commercially available lipids with different carbon chains and hydrophilic heads. This allows thorough optimization of custom MB and facilitates functionalization by changing a lipid with a different hydrophilic head to introduce a function.

2.2 Protein-based MB

Protein-shelled MB have also been developed, mostly using serum albumin, such as commercially available Optison, and have the advantage of being well tolerated, with low immunogenicity and high biocompatibility. Other proteins, like lysozyme or hemoglobin, have been used, modifying MB properties, biocompatibility, and possible functionalization [20,21]. Several protein properties play a role in MB formation, like protein structure or molecular weight [22,23]. It has been shown that disulfide bonds play an important role in MB formation through their destruction and formation induced during MB formation, stabilizing the MB [24,25]. MB with a protein shell can also be enhanced in terms of stability by the addition of active molecules during MB formulation, like crosslinking molecules or molecules inducing the formation of thiol groups for subsequent disulfide bond formation [24,26–28]. MB stability can also be enhanced with post-formation addition of carbohydrates, glycerol, or ethylene glycols, enhancing stability by electrostatic interaction between proteins [29–31]. They can also be functionalized through several processes, with the advantage of having multiple sites that can be used for functionalization. It can be done by covalent binding to the NH_2 or COOH groups [32,33], by encapsulation in the hydrophobic layer [34], or by electrostatic interactions with the positively and negatively charged groups in the proteins

[35]. By using some specific proteins, MB can also retain the protein's initial function, like with lysozyme MB that can retain antibiotic activity [21,36].

2.3 Polymer-based MB

MB with a polymeric shell has also been synthesized, generally using FDA-approved polymers to ensure its biosafety. But a wide variety of polymers have been used for MB formulation, with very different physiochemical properties, leading to different shell thickness, stiffness, and subsequent acoustic response [37]. These specific properties of polymers can be taken advantage of to enhance MB formation and stability. Dasgupta *et al.* did it by taking advantage of the low glass transition temperature of poly(butyl cyanoacrylate) to synthesize non-spherical MB to enhance circulation time *in vivo* and BBB opening when associated with FUS [38]. Polymeric MB can also be functionalized, with the possibility to load drugs such as doxorubicin inside the shell [39,40] or by taking advantage of the polymer's function for surface binding. Though surface binding strongly depends on the type of polymer used.

2.4 MB formulation

The most common method for MB formation is mechanical agitation. Prior to mechanical activation, liposomes made of the shell core materials are generally formed by the thin film hydration method. It consists of first drying the shell materials in organic solution to form a lipid film, then rehydrating in aqueous solution and sonicating. The liposome solution is then sealed in a vial with the desired gas core, and the solution is agitated using a Vialmix® or equivalent [41]. This technique is efficient, low-cost, and requires minimal training but lacks control over the microbubble size and concentration obtained [42]. Even though size and concentration can be adjusted with the MB components, or the speed and the duration of agitation, it will always result in a polydisperse MB solution. The same limitation is present with most other MB formation methods, like the sonication method, where mechanical agitation is replaced by a low-frequency and high-power sonication [43]. Moreover, it is possible to form MB using the droplet vaporization phenomenon. With this method, microdroplets need to be formed with the desired shell materials and with a volatile liquid at their core, like perfluorocarbon. Microdroplets can be formed very similarly to MB, with the

same shell materials and with the same possibility to be functionalized, but with much higher loading capabilities in its core. Microdroplets will then be turned into MB by localized heating inducing the vaporization of the liquid core [44]. This can be performed either with a laser or with ultrasound, the latter has the advantage of being possible to be performed *in vivo* and therefore takes advantage of microdroplets assets in terms of loading capacity and stability, while also having the therapeutic and imaging properties of MB at the localized point of interest.

2.5 Functionalized MB

As previously mentioned, MB can be functionalized to incorporate additional applications (Figure 2). This can be performed through either incorporation of lipophilic molecules or nanoparticles within the MB shell or by binding to the MB surface [5]. Incorporating drugs or nanoparticles into the shell is generally performed during MB formation by simply adding the molecule into the buffer prior to MB formation. The use of such method for loading of drugs like doxorubicin allows increased targeted drug delivery following FUS application and enhance treatment efficiency [45]. This method has also been used to load magnetic nanoparticles, incorporating magnetic properties. However, it has been demonstrated to be less efficient than surface binding of magnetic nanoparticles, as it destabilizes the MB shell, leading to lower stability and lower magnetic properties [46]. Surface binding is generally realized with the addition of biotin moieties or click chemistry reactive groups to the MB surface [32,46,47]. Thus, it allows specific binding of either hydrophilic drugs, magnetic nanoparticles [46], antibodies, or ligands [48,49] through streptavidin-biotin interaction or formation of a covalent bond after click chemistry. Magnetic MB provides the possibility to accumulate them at a precise location using a magnetic field, enhancing both contrast ultrasound imaging and specific drug delivery [46,50,51]. MB functionalized with an antibody provides similar targeting properties, but using specific molecular targeting to accumulate MB also enhances contrast ultrasound imaging and drug delivery [52–54]. In addition, antibody-conjugated MBs have been demonstrated to increase cell and MB proximity, enhancing MB internalization into cells and drug delivery [55]. MB have also been functionalized to incorporate tracer agents such as fluorescent molecules or radio-labeled molecules for multimodal imaging [56–58].

2.6 Cationic MB

An additional method to functionalize MB is the use of electrostatic forces to charge molecules at its surface. This is generally performed with the formulation of cationic MB, using either a protein [59], polymer [27], or more frequently a lipid with cationic properties[60,61]. This cationic property allows loading of anionic molecules, such as nucleic acid in most cases. This complexation of nucleic acids onto the MB surface allows its protection from enzymes, which can degrade nucleic acids, especially RNA, within minutes [62,63]. This loading also increases gene delivery following FUS treatment compared to the use of neutral MB both *in vitro* and *in vivo* [64–66]. Fan *et al.* used cationic MB for gene therapy to the CNS, showing important gene expression and behavioral rescue from transgene expression [61]. However, this complexation can also destabilize the MB shell, affecting MB cavitation and potentially leading to MB collapse [67,68]. A possible solution to this would be to delocalize cationic properties, and therefore nucleic acids, from the MB surface. This can be performed by anchoring a cationic polymer linked to a lipid into the MB shell [69]. Such a strategy would potentially limit the nucleic acid loading effect on the shell properties and therefore on cavitation. Finally, cationic MB described here can also be further functionalized with either magnetic particles or antibodies as previously described. This additional functionalization further increases gene delivery into cells, both *in vitro* and *in vivo* [70–72]. In addition, such a strategy limits elimination from the liver after intravenous injection due to its targeted accumulation, further increasing gene delivery.

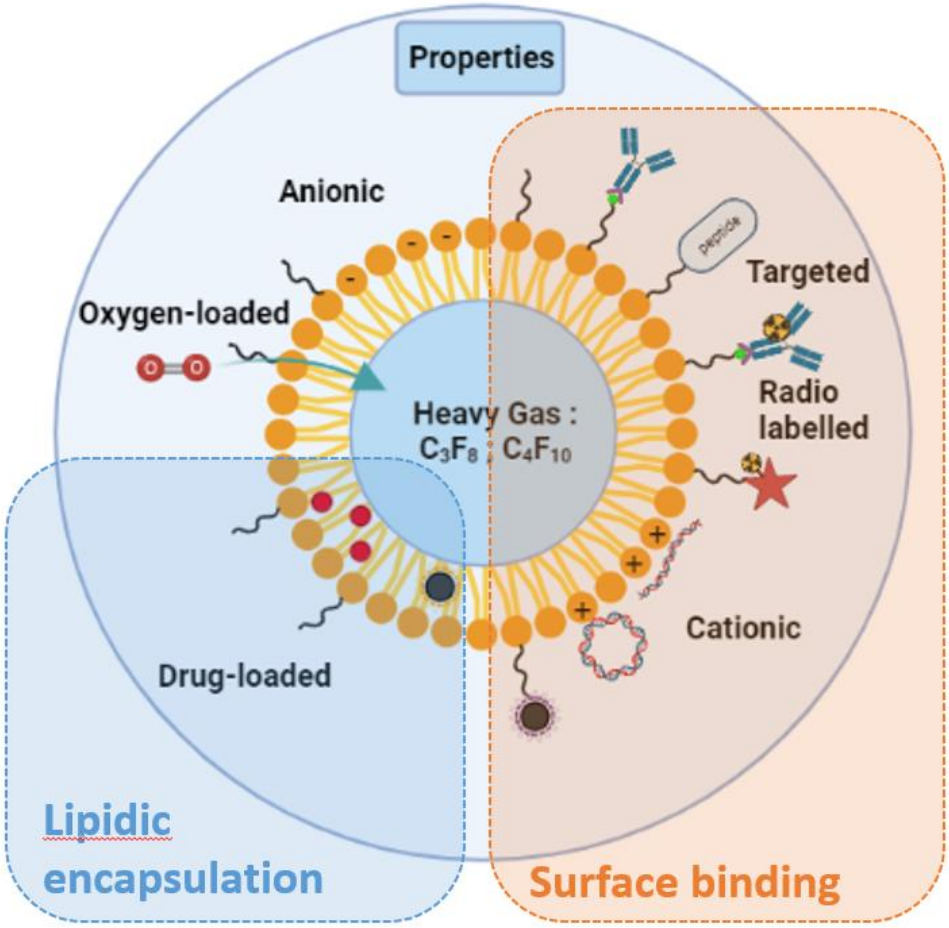

Figure 2: Overview of possible MB functionalization, with either encapsulation in a lipidic shell or at the MB surface.

2.7 Microbubble size modulation

Microbubble size has an important effect on its cavitation and the resulting BBB opening (BBBo). It has also been identified that it has an effect on inflammation caused by MB injection. While most MB formulations, both commercial and homemade, have a relatively high size polydispersity, formulation methods have been put in place to narrow the size dispersion and improve cavitation. The most used method for monodisperse MB formulation is the microfluidic method, where a microfluidic chip is used, focusing a gaseous stream with one or two continuous liquid channels with shell components [73]. The most important aspect of this method to control MB size is the flow speed and the pore size of the gaseous and liquid phases junction. The main drawback of this method is the size of the MB generated, generally relatively high at over several micrometers due to technical limitations in manufacturing a

microfluidic chip with the desired pore size [74,75]. Another similar technique is the membrane-based method, where the flow of shell materials solution and gaseous phase are separated by a porous membrane. A pressure is applied to the gaseous phase to force its passage through the pores, forming MB [76]. This method has similarities with the microfluidic system, such as the importance of optimizing pore size and flow speed and the limitation in MB size [77]. Such formation methods also have the advantage of being easy to scale up the production. But MB size modulation can also be achieved post-formation of MB. It can be achieved by using a filter, but such a method generally induces MB collapse due to the pressure applied when passing the pores [78]. The most widely used methods rather take advantage of the buoyancy differences between MB of different sizes. MB can be sorted regarding their gas volume by simply decanting the solution or by centrifugation, then monodisperse MB can be extracted at a specific height within the solution [79,80]. These methods are highly impacted by the MB concentration, as a high MB concentration will induce interference between MB and require the use of a stronger centrifugation force to separate small MB. Also, the separation is generally less efficient at producing monodisperse MB than microfluidic production since larger and smaller MB remain in the extracted phase. A last method to separate MB, the acoustophoresis, relies on their acoustic properties to separate them. To achieve that, the polydisperse MB solution is injected and focused on a microfluidic channel coupled to an ultrasound probe with at least 2 outputs. The US waves are applied at a specific frequency in a sonication chamber allowing the formation of a standing wave with one or several nodes (depending on the frequency used). Objects in flow will be moved towards the nodes depending on their acoustic properties. The MB with the specific size that has the best resonant behavior at this frequency will therefore be displaced in the channel to be extracted in the second output [81,82]. This will result in an extracted monodisperse MB solution with the best resonant properties to the frequency used.

2.8 Nanobubbles

MB sizes aimed for therapeutic applications are generally in the order of 1 to 10 μm, as such a size has the best oscillating properties for the frequency used in therapy (0.25 to 1.5 MHz). Although, smaller MB has the advantage of having a better biodistribution in smaller vessels and have therefore a better penetration in tissues. Nano-sized bubbles get an increasing

interest in research due to this aspect. Nanobubbles (NB) have similar properties to MB, with a gas core and a shell composed of lipids, polymers, or proteins [83]. They can be manufactured with the same process as MB and are generally produced as a fraction of the polydispersed MB solution. They can be separated with the same methods as MB, but more generally with centrifugation. NB typically has a diameter ranging from about 50 to 500 nm, leading to an efficient perfusion within tissue and small blood vessels. But the main drawback of NB is their resonance frequency, ranging from 30 to 250 MHz for NB of diameters ranging from 200 to 800 nm according to Helfield *et al.* [84]. Such a frequency range is much higher than the frequencies used for ultrasound imaging or therapeutic application, forcing the use of NB at off-resonant frequencies. Despite that limitation, NB has been shown to be more efficient than MB for contrast ultrasound imaging, with higher penetration in small capillaries. Furthermore, NBs have the advantage of having a much higher surface area to volume ratio, allowing higher loading capacity.

Gas vesicles, another type of acoustically active object, are also gaining interest. They are spindle- or cylindrical-shaped vesicles with a protein shell and a gas core with a size ranging from 100 to 2000 nm in length and 45 to 200 nm in width [85]. They are naturally bioproduced by some species of bacteria and can be extracted to be used as ultrasound imaging contrast agents similarly to NB. Although they have similar advantages to NB in terms of biodistribution in smaller vessels thanks to their size, they can have a very diverse acoustic behavior due to their membrane and shape. Interestingly, as they can be produced by a plasmid encoding for it after transfection in cells, they have been used as an acoustic reporter gene for gene delivery [86].

3. Microbubble characterization

3.1 Optical microscopy

As previously stated, microbubble solutions are generally polydisperse solutions with a size range from 1 to 10 μm. In addition to MB, nanosized objects can also be present in solution, either liposomes or micelles with size ranging from 20 to 300 nm, or nanobubbles, with size

lower than 1 μm and as low as about 50 nm. It is therefore necessary to measure both size ranges to fully characterize the MB solution. Currently, there is no technique allowing to characterize objects with size ranging from 20 nm to 10 μm in a single analysis, and several techniques must be used to fully assess MB and nanobubble suspension. First, optical microscopy is the most common technique to characterize the size and concentration of micron-sized MB, as it is a technique that is cheap and easy to perform with relatively good reliability [87]. The precision of such techniques relies mainly on the resolution of the microscope and camera used and the quality of the informatic treatment, generally performed with the particle analysis software Fiji [88]. Although optical microscopy resolution remains exclusively limited to 0.4 μm, a physical limit determined by the wavelength of visible light used in this technique [89]. Optical microscopy can also be used to characterize MB functionalization if coupled to lasers or fluorescent light and filters. This way, a fluorescent probe can be attached to MB functionalization, which will be excited by lasers, and the fluorescent light emitted will be measured. This will allow one to confirm that the functionalization occurred and in which proportion of MB. When using a precise enough microscope like a confocal microscope, it can provide information on the localization of the functionalization onto the MB shell or inside and co-localize different functionalizations.

3.2 Electrical impedance-based particle counting

Another technique largely used for MB size and concentration determination relies on electrical impedance like the Coulter counter (Figure 3.D) or Tunable Resistive Pulse Sensing (TRPS), where an electric field is measured and is perturbed by the passage of objects through a pore [90,91]. The measured electric modification with the passage of each object can be associated with a volume, and with the known flow a concentration can be estimated [92]. These techniques have the advantage of being able to measure both micro-sized objects and nano-sized objects, but not in the same measurement. Indeed, the apparatus pore allows to detect objects ranging from 20 to 80 % of the pore diameter without risking it to clog, thus forcing a change of the pore between the analysis of each population. Although it is generally required when using a small pore diameter to avoid having objects with bigger diameters in solution at the risk of clogging the apparatus. This is relatively difficult when analyzing a MB solution as both size range co-exist and purifying one part with centrifugation might provokes

MB and NB coalescence or collapse, changing the measured population. But clogging of the apparatus rarely happens with MB solution measures as the nano-sized objects are generally about 10-fold more concentrated, therefore limiting the amount of MB crossing the pore during analysis of smaller objects. Furthermore, as MB can easily shrink in a constricted environment, the risk of clogging is actually limited. Counter coulter and TRPS are still limited in their range of analysis, with a respective range of 0.2 to 1600 μm for Multisizer (Beckman) or 40 nm to 11 μm for Exoid (IZON), showing that although TRPS seems able to fully characterize MB solution, counter coulter does not yet allow measurement of the smallest population. Although these applications require the use of several pore sizes to cover the whole size distribution. TRPS technique also has the advantage of being able to measure zeta potential, allowing for the characterization of cationic functionalization.

3.3 Brownian movement-based particle analysis

The measure of Brownian movement, which can be associated with the particle's volume, is an alternative method to characterize MB solution. As the Brownian movement of MB is perturbed by their buoyancy, such analysis of micron-sized bubbles would not be precise [93]. Although the buoyancy effect on NB's Brownian movement can be considered negligible. Therefore, techniques relying on it should exclusively be used for the calculation of nano-sized objects and can be a good complement to optical microscopy to measure the nanobubbles and liposomes in a MB solution. The most used technique for it would be the dynamic light scattering (DLS) (Figure 3.A), allowing measurement of size distribution, and with recent version of the Zetasizer Pro Red (Malvern) it also allows to estimate the concentration of tracked particles, but with low precision [94]. Like TRPS, it also has the advantage of being able to measure zeta potentials, providing information on cationic functionalization of the MB. It offers the advantage of being capable of measuring a wide range of objects, from 0.3 nm to 10 μm, although as said before, the measure of MB is probably perturbed by their buoyancy. Furthermore, as MBs are about 10-fold less concentrated than nano-sized objects, they might not be detected during DLS measurements. Another limitation to this measure is the impossibility of separating liposomes from nanobubbles, which only gives us an overall measure of nano-sized objects. Techniques using Brownian movement measure based on interferometric light microscopy can also be used, like the nanoparticle tracking analysis

(NTA) [95]. In this system, the sample is placed under a microscope, and light is emitted at a certain angle of the sample, and the diffracted light is recorded over time [96]. The interferometric signal of particles is calculated, and the images are processed to measure the Brownian movement of the particles, leading to a measure of their size and concentration. The NTA system NanoSight Pro (Malvern) can measure objects ranging from 10 to 1000 nm and has been used for nanobubble measures in other studies.

3.4 Resonant mass measurement

The resonant mass measurement (RMM) technique uses a resonating cantilever with a microfluidic channel embedded inside and has been shown to be able to separate NB or MB from non-buoyant particles (Figure 3.C). When a particle flows in the cantilever, its resonant frequency will shift, positively for particles with lower density than the liquid (buoyant particles) and negatively for particles with higher density than the liquid (non-buoyant particles) [97]. This frequency shift is correlated with the mass of the particle which can be then be used to calculate the particle size, and by recording it over time with a known flow rate it can calculates its concentration. RMM also has the advantage of being able to measure particles in a size range of 50 nm to 5 μm, but like TRPS, it requires different sensors to measure the whole range.

3.5 Flow cytometry

Previously stated measurement methods lack the possibility to measure the entirety of a MB polydisperse solution, from NB to MB, in one measure [98,99]. However, flow cytometry does not have this limitation, with the possibility to characterize a wide range of particle sizes, ranging from about 40 nm to 10 μm for cytometers with high sensitivity like Cytoflex nano (Beckman). This technique relies on the flow focusing of particles in an analyzing chamber where the particle is illuminated by lasers and the scattered light is analyzed, providing information on particle size (Figure 3.E). With a known flow rate, it can also provide information on particle concentration. Yet, this technique does not allow precise measurement of size but only an estimation, and prior to analyses, the cytometer needs to be calibrated with monodispersed beads. Also, this method does not differentiate NB from non-buoyant particles and is difficult to operate when assessing very small objects, as impurities in the microfluidic

system will interfere in the measurement of nano-sized particles. Like fluorescent microscopy, flow cytometry has the advantage of giving information on MB functionalization if a fluorescent probe is attached to it, as the lasers are also used to excite fluorescent molecules and the emitted fluorescence is measured [100].

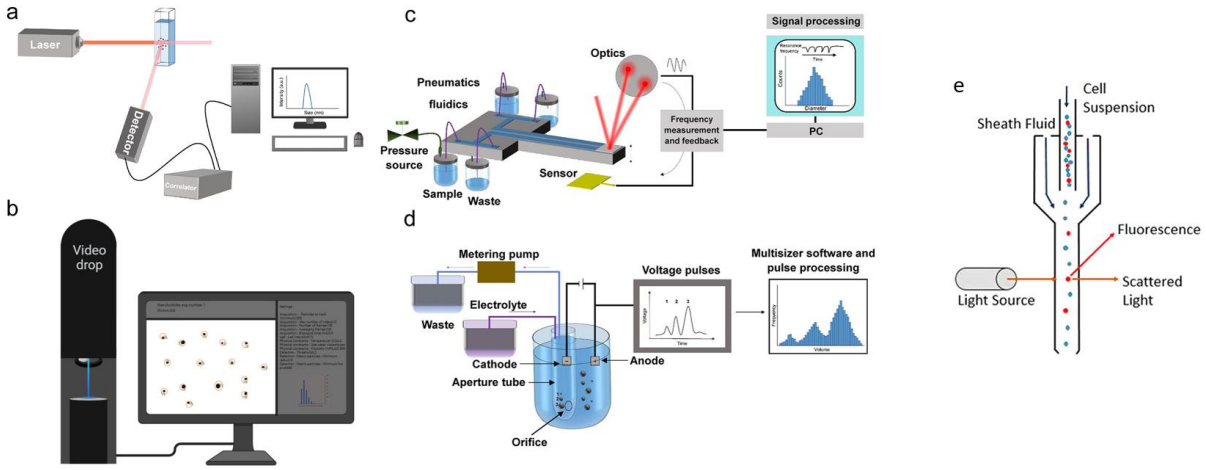

Figure 3: Microbubble characterization methods. (A) Dynamic light scattering (B) VideoDrop (C) Resonant mass measurement (D) Electrical impedance particle counting (E) Flow cytometry. Modified from D. Fernandes [42].

3.6 Nanometric-scale techniques

To better characterize MB shape and shell, the previously stated measurement methods will lack sensitivity. Electron microscopy provides very high-resolution images of MB, giving precise measurements of MB size and unique insight into MB shape, shell thickness, and functionalization distribution [101]. Although this technique is challenging to use with MB, as vacuum conditions are required and a very high-energy beam is used, which can lead to MB collapse or production of MB through heating. Several sample preparations are possible to overcome this difficulty, the most recurrent being the cryogenic electron microscopy (CryoTEM) where MB are trapped in solid water after rapid freezing of the sample. Atomic force microscopy is another technique providing highly sensitive information on MB, where a small cantilever is used to scan the particles by touching them. It provides three-dimensional images with a resolution of a fraction of a nanometer. It has been successfully used to characterize MB shape and shell thickness and composition [102–104].

3.7 Ultrasound imaging

Characterizing the size and concentration of MB is essential before using them in imaging or therapeutic applications, but it is not sufficient to fully describe MB. Acoustic characterization of MB, especially homemade, is necessary to confirm their potential for imaging and therapeutic application. Contrast enhancement properties for ultrasound imaging are the first aspect to consider as this is the primary application of MB and NB. Contrast enhancement can be measured first *in vitro* in an agarose phantom or simply in a solution to validate acoustic properties of MB and assess their stability over time in an acoustic field. But *in vitro* measurement remains limited, and *in vivo* contrast ultrasound imaging provides more relevant information. In addition to the contrast enhancement measure and the stability of MB in relevant condition it can provide information on a specific tissue perfusion with additional parameters like the time to peak, the homogeneity of contrast enhancement. This provides insight on the potential of MB for imaging but also for therapeutic applications, as the more stable MB are in the targeted tissue and the better its perfusion is, the better its therapeutic effect will be. Additionally, targeting properties of MB can also be assessed with ultrasound imaging using the differential targeted enhancement (DTE), calculated as the contrast enhancement difference after accumulation of MB in the tissue and after reperfusion following acoustic bursting of MB.

3.8 Oscillation analysis

As previously established, under an ultrasound field, MB will enter into an oscillating regime called cavitation, either stable or inertial. In BBB opening applications, stable cavitation is generally associated with safe and reproducible BBBo, whereas inertial cavitation is generally associated with severe BBBo and can induce damage like edema or hemorrhages. The characterization of the cavitation is therefore paramount to predict MB effect and efficiency in BBBo and drug delivery. This can be done both *in vivo* and *in vitro*, preferably streaming through a phantom to mimic tissue, and a skull can also be used to mimic the attenuation and scattering on ultrasound observed *in vivo*. Although *in vitro* measures can provide various information on MB oscillation it will never totally mimic the response that can

be observed *in vivo* as the size of the channel used in vitro will always be much larger than blood vessels and the cavitation will be different depending on this and the concentration of MB, that can interact with each other and coalesces. MB cavitation is generally measured using a passive cavitation detector (PCD), allowing the recording of reflected ultrasound, including MB cavitation. A Fourier transform is applied to the signal allowing the visualization of MB cavitation spectrum. This spectrum allows us to quantify separately the stable cavitation dose (SCD) and the inertial cavitation dose (ICD). SCD is generally calculated using the harmonics f_1 and f_2, and ICD is generally calculated using the broadband between these harmonics and ultra-harmonics. The sub-harmonic $½ \times f_0$ and ultra-harmonics $f_{1.5}$ and $f_{2.5}$ can also be used for ICD determination but are generally associated with a moderate inertial cavitation regime.

1. Gene therapy strategies

The European Medicines Agency (EMA) defines that gene therapy medicinal product follows two characteristics: "a) it contains an active substance which contains or consists of a recombinant nucleic acid used in or administered to human beings with a view to regulating, repairing, replacing, adding or deleting a genetic sequence; b) its therapeutic, prophylactic or diagnostic effect relates directly to the recombinant nucleic acid sequence it contains, or to the product of genetic expression of this sequence." (Commission Directive 2009/120/EC, Annex Part IV, section 2.1, amending directive 2001/83/EC). This definition encompasses a wide range of treatments, and the recombinant nucleic acid mentioned can be divided into two main categories: viral and non-viral.

1.1 Viral gene therapy

The viral strategy relies on the use of a recombinant virus encoding the desired gene sequence. In this application, the recombinant virus is composed of a viral genome encoding exclusively the therapeutic sequence. It is protected by a capsid composed of viral proteins produced by separated plasmid DNA (pDNA) during viral vector production [105]. This separation of capsid proteins and viral genome avoids self-replication of the virus after transduction to the target organism, preventing infection. Recombinant virus efficiently bypasses cellular barriers, allowing high gene expression lasting for several months [106]. This makes of viral approach the privileged method for gene therapy, as confirmed by Shchaslyvyi *et al*. that showed that 85 % of FDA- or EMA-approved gene therapy products use a viral strategy [107]. However, viral vectors display pathogen-associated molecular patterns that are recognized by pattern-recognition receptors as non-self [108]. This initiates pro-inflammatory cytokine production and activation of the innate immunity response [109]. In clinical trials this reaction is the main adverse effect and can lead to severe complications [110]. The first method to mitigate this innate immune response relies on the variation of the viral vector used, and a

large range of recombinant viruses have been assessed, as reviewed by Lundstrom [111]. Adenoviruses were the first to be used for gene therapy and have the advantage of having a large packaging capacity of up to 37 kb [112,113]. But adenovirus is frequently found to be immunogenic in clinical trials, as shown by Sterman et al. in a clinical trial where 39 patients out of 40 encountered a mild immune response following adenovirus injection, detected with cytokine release [114]. This high immunogenicity led to a decrease in adenovirus use. Lentivirus and retrovirus are largely used recombinant virus with single-stranded RNA genetic material with a lower packaging capacity of 8 kb compared to adenovirus. Their main particularity is the reverse transcriptase encoded within their genome, allowing them to transcribe viral RNA into double-stranded DNA, subsequently randomly integrated into the genome [115]. Thus, it allows stable expression of the therapeutic gene, making it an efficient gene therapy vector. In addition, it induces less immunogenic reaction compared to adenovirus [116]. However, this integration can lead to serious adverse effects depending on the integration locus. It resulted in the development of leukemia in 4 patients out of 10 in a clinical trial for X-linked SCID using a retrovirus [117]. This integration does not typically happen with adenovirus nor adeno-associated virus, where transduction is transitory [118]. Adeno-associated viruses (AAV) are predominantly used in gene therapy for the CNS since they are the only ones that demonstrated the ability to transduce neurons after systemic injection [119]. It has the lowest packaging capacity of 4 to 6 kb [120] but also displays lower immunogenicity [121]. However, it still remains a limitation to its use, since Hinderer *et al*. demonstrated that it can still induce high toxicity at high doses [122]. Another limit to the use of viral vectors is the prevalence of immunity to it within the population [123–127]. The use of some specific serotypes, such as AAV10 or AAV8, has the advantage of having a lower prevalence of immunity in the population while remaining efficient for gene delivery [128]. However, following viral vector injection, adaptive immunity will take place, importantly reducing the efficiency of any additional treatment with increased immune response [129]. Another limitation to gene therapy with viral vectors is the cost of production, leading to therapeutic application with challenging cost-effectiveness [130]. Due to all these challenges, non-viral gene therapy remains a strategy with increasing interest.

1.2 Non-viral gene therapy

Non-viral gene therapy regroups all genetic sequences that are not encapsulated in a viral capsid. It regroups a wide range of drugs that can be composed of single- or double-stranded DNA or RNA. Compared to viral gene therapy, this method has the advantage of being safer due to limited immune response and is also not limited in its packaging capacity, allowing expression of large genes [131]. However, non-viral gene therapy generally exhibits lower transfection efficiency and less stability, although it can last for several months [132]. The efficiency of non-viral gene delivery mostly relies on the delivery vector and delivery method used. These vectors encapsulate nucleic acid, protecting them from enzyme degradation and from macrophages, and allow them to overcome extracellular and intracellular barriers [133].

The most frequent vehicles used in gene therapy are cationic polymers and lipids that can complex with anionic nucleic acid through electrostatic forces, leading to nanoparticle formation of a polyplex or lipoplex, respectively, or a lipopolyplex with both polymer and lipids [134,135]. The most frequently used polymer for gene delivery is the polyethyleneimine (PEI), poly-L-lisine or chitosan [63]. A large variety of modifications have been attempted, mostly to reduce cytotoxicity [136,137] or to improve endosomal escape [138,139], nucleic acid release [140] and cell targeting [141,142]. Liposomes are generally composed of cationic lipids for nucleic acid complexation, helper lipids for sustained stability, and pegylated lipids to escape the immune system [143]. The use of ionizable lipids in liposomes has been demonstrated to initiate a proton sponge effect in late endosomes, increasing nucleic acid release in the cytoplasm [144,145]. This effect is initiated by the ionization of ionizable lipids at low pH, a condition found in late endosomes, leading to endosomal osmotic swelling and provoking endosomal membrane rupture [146]. Lipid nanoparticle (LNP) is an emerging alternative to these vectors with similar composition to liposomes, the main difference being that nucleic acid is complexed during nanoparticle formation, forming ready-to-use stable particles. In contrast to liposomes, cationic lipids are not systematically used in LNPs, and ionizable lipids are used to complex nucleic acids with a low-pH buffer during particle formation, typically allowing over 90 % nucleic acid encapsulation [147]. LNPs are also constituted of cholesterol, increasing membrane rigidity, LNP stability in blood flow, and facilitating adhesion to cell membranes [148–150]. LNP has demonstrated efficient gene delivery to muscle, liver, lungs, or lymph nodes [151,152] and, more recently, to the brain using specific delivery routes [153–155]. In addition, several LNP products are FDA- and EMA-

approved for COVID-19 vaccines with intramuscular injection, thus demonstrating the efficiency and safety of such a method [156–158].

1.3 Gene incrementation

The delivered nucleic acid can have various functions, as summarized in figure 4. The most widely used in gene therapy is the gene incrementation, where the transgene is used to restore a protein expression silenced due to a disease. In non-viral strategies, this expression can be performed using either pDNA or messenger RNA (mRNA). The use of mRNA has the advantage of allowing higher transfection efficiency than pDNA since it does not need to reach the cell's nucleus to be expressed [159]. However, mRNA has short expression kinetics, with a peak of expression from 7 to 24 hours after injection, depending on the expressing cell, as shown by Di *et al*. [151]. This kinetic expression is a safety advantage for vaccine application where prolonged expression is not required but is a disadvantage for genetic disorders where stable expression is frequently required. Plasmid DNA, on the other hand, allows longer expression that can last for months [160]. Compared to mRNA, and like viral vectors, it also has the advantage of expressing the transgene under the control of a promoter. Promoter optimization allows control of transgene expression, from its intensity to cell specificity. Strong and ubiquitous promoters are generally used, like the cytomegalovirus (CMV) promoter, which is the most frequently used [161]. An inducible promoter can also be employed, allowing stronger control over transgene expression [162]. Cell-specific promoters are also frequently used in gene therapy applications, since they allow deeper understanding of the transgene expression effect and generally induce stronger expression in the targeted cells [163–165].

1.4 Genome editing

Gene incrementation generally relies on transitory transgene expression, and when stable expression is attempted with transgene integration into the genome it generally occurs at a random locus leading to potential severe side effects as previously mentioned. In order to induce life a lifelong therapeutic effect, genome editing can be performed. Initially, this would be achieved with nucleases like zinc finger nucleases (ZFNs) or transcription activator-like effector nucleases (TALENs) that are capable of generating double-strand breaks at a specific

locus of genomic DNA. However, this method relies on complex interactions between protein and DNA, limiting its efficiency [166]. In 2012, Jinek *et al*. uncovered the function of CRISPR/Cas9 in bacteria and its potential for gene therapy [167]. Initially a defense mechanism against viruses, the Cas9 is an endonuclease protein capable of binding to a specific single-guide RNA (sgRNA). This sgRNA recognizes a specific sequence, allowing double-stranded genomic DNA cleavage at a specific locus. Following this, the cell will use its DNA repair mechanisms, mostly with non-homologous end joining (NHEJ) to bind each end together, and if co-injected, will insert the desired genetic material. This method can also be used to delete a sequence by using two sgRNAs surrounding the desired sequence [168]. Often used *ex vivo* or on gamete cells, it can also be used *in vivo* with viral or non-viral gene delivery with a specific promoter to modify the desired cells [169].

1.5 Expression regulation

Finally, nucleic acid delivered can also be used to regulate the expression of a specific gene. This can be performed with various molecules, such as small interfering RNA (siRNA), short hairpin RNA (shRNA), or antisense oligonucleotides (ASOs) to silence a specific gene. siRNA and shRNA are both short RNA molecules of about 20 base pairs that are specific to an mRNA sequence [170–172]. These molecules are first processed by a dicer and then associate with proteins to form the RNA-Induced Silencing Complex. The complex then binds the specific mRNA and induces its cleavage. Unlike siRNA and ASOs that are generally directly delivered using a non-viral vector, shRNAs are expressed in an expression cassette, allowing to use them with viral vectors [172]. ASOs also bind specific RNA sequences, leading to their silencing, but generally through the blocking of their translation [173]. They have gained increasing interest recently, with FDA and EMA approval for spinal muscular atrophy (Spinraza, Nusinersen) [174]. Aptamers are another type of short DNA or RNA molecules that can bind to specific molecules or proteins with a high affinity due to their structural conformation [175]. They are capable of regulating protein function or molecule availability, making them a versatile tool in therapeutic application [176]. Finally, dead Cas9 (dCas9) can also be used to regulate gene expression. This protein is called “dead” due to the inactivation of its endonuclease function previously described. Therefore, its sole function becomes to target specific genes with its association with the sgRNA. The dCas9 is therefore further

modified to fuse it with transcription factors that will induce DNA demethylation [177] or histone demethylation [178], inducing increased gene expression. Similarly, it can be fused with inhibitors to silence a specific gene expression [179].

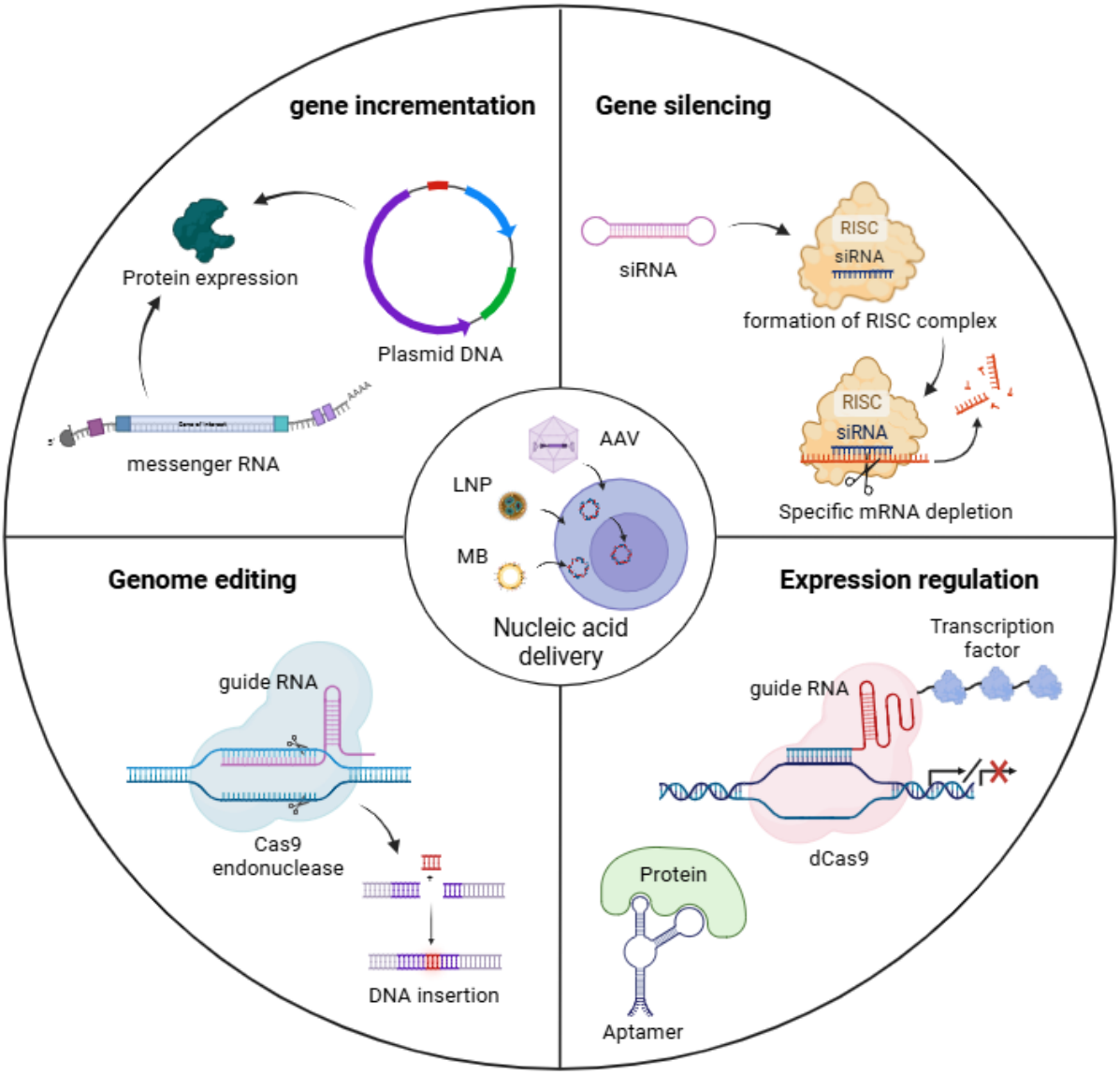

Figure 4: Overview of nucleic acid functions for gene therapy.

2. Physiological barriers to CNS gene therapy

Nucleic acids need to reach the targeted cell cytoplasm or nucleus in order to achieve their therapeutic effect. The first barrier to this is the immune system, with endocytosis from macrophages leading to a reduced amount of nucleic acid reaching the desired cell. Viral vector has means to avoid the immune system through the inhibition of pro-inflammatory pathways [180,181], although it remains the main limitation to the use of viral vector due to its recognition by pattern-recognition receptors as previously mentioned. Non-viral vectors on the other hand, typically use PEG moieties to escape the immune system [182]. Another barrier is the degradation from enzymes like DNase or RNase that degrade free nucleic acids rapidly, especially RNA, which can be degraded within minutes [63]. This is a strong limitation to nucleic acids effect, but that is easily overcome by protecting nucleic acids either in a viral capsid or with encapsulation in a non-viral vector previously described.

2.1 Cellular barriers

Once nucleic acids reach the targeted cell, they then need to reach their site of action, either the cytoplasm for RNA-based strategies or the nucleus for DNA-based strategies (Figure 5) [183]. The first barrier is the cell membrane, a lipidic bilayer negatively charged that nucleic acid does not cross on its own partially due to electrostatic forces. In most cases, the vector encapsulating the nucleic acid is endocytosed by the cell, enclosing it into an intracellular vesicle. In non-viral gene therapy, this endocytosis can occur through several pathways, the most frequent being the clathrin-dependent pathway [184,185]. The endocytosis is enhanced in viral vector with capsid proteins allowing specific cell entry, while with non-viral vectors it can be enhanced with the vector nature, size, cationic properties or with specific antibody binding [186,187]. Following this internalization, the intracellular vesicle, called an endosome, will progressively mature into a lysosome [188]. During this maturation, pH will decrease and nucleic acid will be progressively degraded. Several mechanisms can then be taken advantage of to induce endosomal escape and release nucleic acid. Membrane fusion can occur with lipid-based vector, membrane disruption with polymers due to polymers-membrane interaction, and a proton sponge effect can also take place as previously described [144,189,190]. Following

release in the cytoplasm, nucleic acids can still be degraded by intracellular mechanisms like cyclic GMP-AMP synthase–stimulator of interferon genes (cGAS-STING) [191]. The last barrier to gene expression for DNA-based strategies is the passage of the nuclear membrane, regulated by nucleopores [192]. Upon passage of each barrier, an important amount of nucleic acid is lost, highlighting the importance of efficient carriers to improve gene delivery.

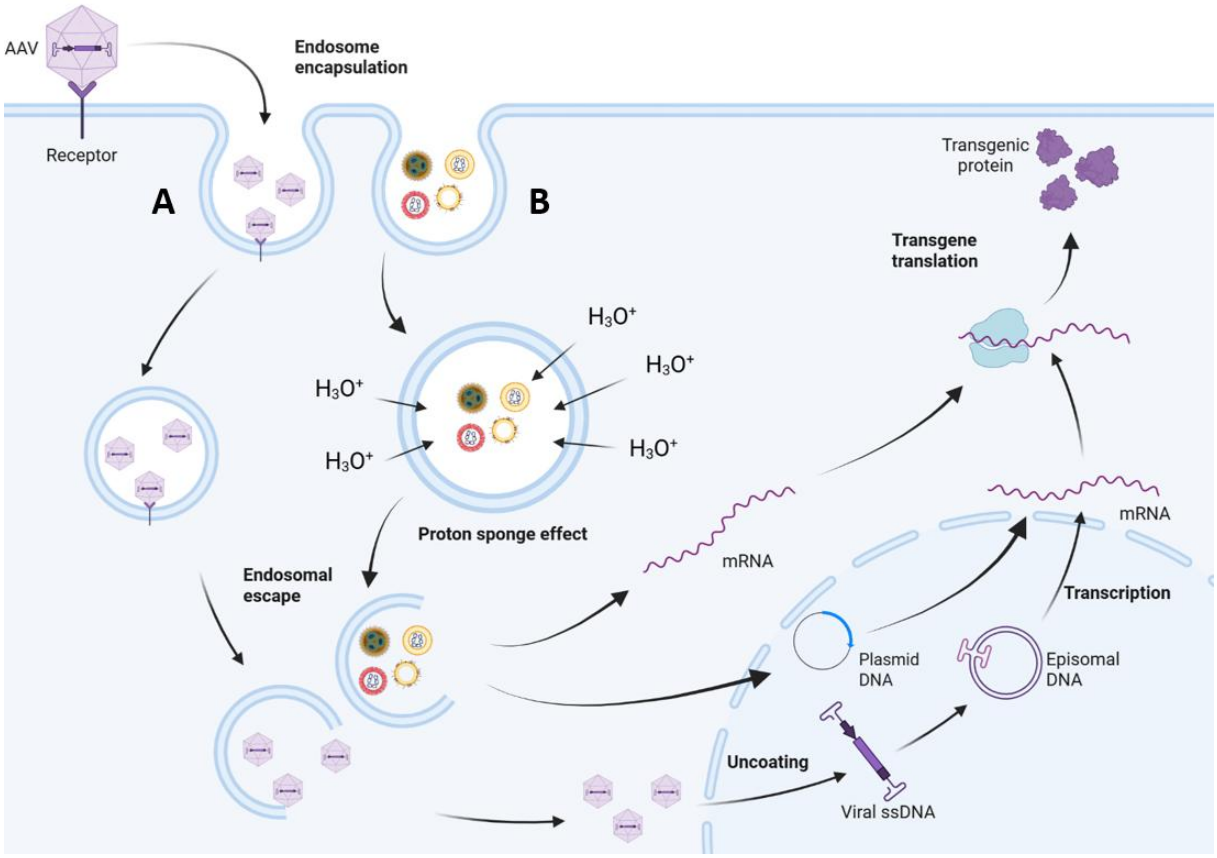

Figure 5: Schematic representation of viral (A) and non-viral (B) gene delivery to cells and their passage of cellular barriers.

2.2 *Blood-brain-barrier (BBB)*

The BBB is a barrier specific to the central nervous system (CNS) composed of several cell types assuring the homeostasis of the brain and its protection from harmful components or infections. Despite the development of innovative techniques to bypass the blood-brain barrier, this barrier remains the main obstacle for drug delivery to the brain. Several properties

give the BBB its impermeability, as resumed in figure 6, that can be dissociated into two main categories: the physical barrier and the biochemical barrier [193].

2.2.1 Physical Barrier

The physical barrier is composed of endothelial cells, tightened together by several transmembrane junction proteins. This includes first tight junctions, composed of claudin, occludin, or JAM proteins, localized at the apical membrane [194–196]. Then adherent junctions, composed of VE-cadherin and PECAM-1, are localized at the basolateral membrane [197]. These proteins are tightly locked together, reducing paracellular space between endothelial cells and preventing the passage of any lipophilic molecules larger than 400 Da [198,199]. The integrity and stability of tight junctions are maintained and regulated by ZO proteins in endothelial cells, linking these junctions to the cytoskeleton [200]. Within tight and adherent junctions, gap junctions, composed of connexin proteins, form hemi-channels allowing bidirectional flow of ions and hydrophilic signaling molecules [201]. Behind endothelial cells, pericytes play a role in the regulation of endothelial function, angiogenesis, vasoconstriction, and maintenance of barrier properties.

2.2.2 Biochemical Barrier

The biochemical barrier is mainly composed of ATP-binding cassette (ABC) proteins, a family of transporters associated with endothelial cell membranes. They are mostly expressed on the luminal membrane, facing systemic circulation. ABC transporters have a critical role in maintaining homeostasis and exobiotic clearance by ATP-driven active efflux from endothelial cells to the brain [202]. Among their many substrates, they are typically responsible for the evacuation of phospholipids, aldosterone, and amyloid beta [203,204]. Various subtypes of ABC transporters are expressed in endothelial cells, the most frequently studied being the P-glycoprotein, the multidrug resistance-associated protein, and the breast cancer resistance protein. These subtypes are particularly known due to their abundance and their role in various therapeutic drug resistance [205,206]. Typically, they have been identified as transporters of antibiotics, opioids, and chemotherapeutics [207]. ABC transporters work in consort with drug-metabolizing enzymes, such as cytochrome p-450, to help maintain brain homeostasis [208–210]. Inhibitors to this barrier have been developed in order to enhance drug

delivery to the brain. Thus, the use of ABC transporter inhibitors or cytochrome p-450 inhibitors allowed increased specific drug penetration into the brain [211,212].

2.2.3 BBB crossing

Most BBB crossing occurs through solute carriers for glucose, ions, or other small polar molecules, and through specific receptor-mediated transcytolic transport, especially for large molecules like peptides or proteins [213]. Some small molecules can cross passively the BBB, such as lipophilic molecules under 400 Da through transcellular diffusion or small hydrophilic substances through paracellular transport, limited to the transient relaxation of TJ [214]. This can be used to deliver therapeutic compounds by increasing TJ relaxation using highly osmotic solutions. Cell-derived extracellular vesicles (EVs) are another way for molecules to cross the BBB, primarily used in normal conditions for brain cell crosstalk [215]. EVs can also be loaded with therapeutic molecules and are a promising delivery vector for the CNS [216].

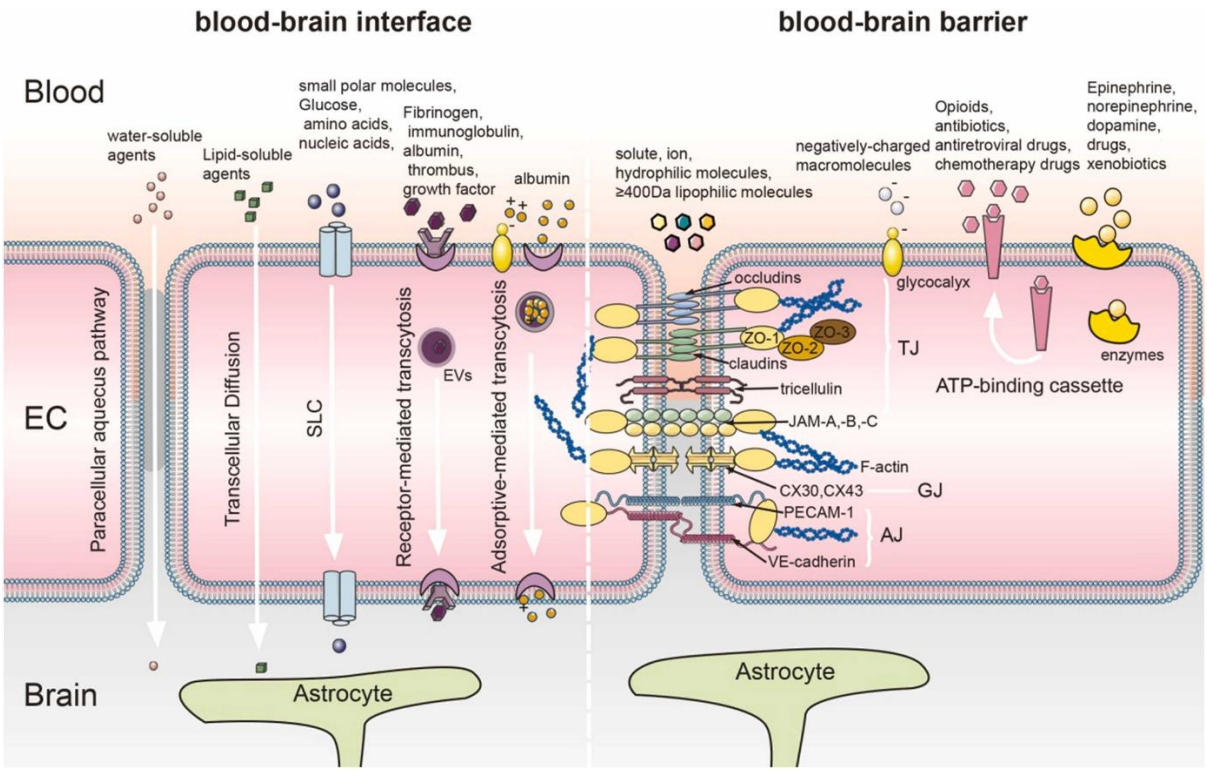

Figure 6: Schematic representation of the BBB adapted from Zhang *et al*. [193] with from left to right the molecules capable of natural crossing of the BBB at the blood-brain interface, the

physical barrier composed of tight junctions and adherent junctions, and the biochemical barrier composed of ABC transporters.

3. Injection routes for gene delivery to the CNS

In order to reach CNS cells, the most widely used technique for it is the use of injection routes allowing to bypass the BBB [217].

3.1 *Intracerebral injection*

Stereotaxic injection in the brain using a stereotaxic device and coordinates is the most widely used AAV injection route [217,218]. This technique provides an efficient transduction in a relatively precise brain region, although there is still some expression in surrounding tissues [219]. This technique has been used to deliver AAV specifically to the hippocampus, the striatum, the cortex, or the thalamus [219–221]. Such a technique requires the puncture of the skull and the insertion of a needle through brain tissue. Therefore, it will very often cause microhemorrhages and transduction in the needle path [222,223]. But it has the advantage of being less immunogenic than other injection routes [224–227]. Intracerebral injection with AAV has been used in clinical trials for several neurodegenerative diseases and for glioblastoma. Recent intertumoral combined AAV injection for cytotoxicity and immune stimulation showed to be efficient and well-tolerated, associated with a promising survival, higher than known overall survival [228]. In neurodegenerative disorders, intracerebral injection has shown its efficiency to restore patients function in several clinical trials [225,229–233]. The procedure was generally well-tolerated, with little immunogenicity induced from AAV delivery and very few severe adverse effects [224,225,231]. Although most clinical trials show hemorrhages on the needle path and recurrent mild adverse effects. As intracerebral injection allows reaching only a limited brain area, several injections are generally needed to transduce a sufficient brain region, increasing the risk of hemorrhages and adverse effects. This limits the use of intracerebral injection to gene therapy aimed at a single brain region.

3.2 *Intrathecal injection*

Intrathecal injection is an injection route that uses the cerebrospinal fluid (CSF) to reach the brain, allowing a broader transduction through the CNS, reaching both the spinal cord and the brain. Although, the transduction efficiency generally gets lower in deeper region of the brain such as the striatum or the hippocampus, where an intracerebral injection would get a higher efficiency [219]. This technique also has the advantage of being less invasive than intracerebral injection, as an injection in the lumbar or cisternal area doesn't require a skull perforation or penetration of brain tissue. Intrathecal injection requires a higher AAV dose than intracerebral injection but a lower dose than intravenous injection, lowering the risk of adverse effects. Despite these advantages, intrathecal injection still provokes minimal adverse effects, mostly with hepatotoxicity induced by AAV injection, with higher adverse effect when a higher dose is used [234,235]. Intrathecal injection has recently been used in a clinical trial for giant axonal neuropathy, showing improved sensory-nerve action potential amplitude [236]. It has also recently been used for spinal muscular atrophy, using onasemnogene abeparvovec on children from 6 to 60 months, which is FDA-approved for intravenous injection on children under 6 months [237]. It showed improvement in the Hammersmith Functional Motor Scale expanded compared to historic controls in all children. This shows that intrathecal injection allows a better transduction to the CNS than intravenous injection in older children. Although both studies show mild adverse effects in all patients and few serious adverse effects related to the treatment.

3.3 *Intranasal injection*

Intranasal injection (IN) is the least invasive way to inject molecules. Currently, it has been widely used for molecule delivery, with many successful clinical trials showing the advantages of this injection method in terms of safety and efficiency [238]. There are still few studies using IN for gene therapy to the CNS, but they also show the safety of this method, with no toxicity or serious adverse effects observed with AAV, RNA, or mesenchymal stem cell injection [239–241]. In terms of efficacy IN seems to transduce in majority the olfactory bulbs and the cortex regions of the brain, but also to the entire brain with enough efficiency to induced behavioral improvement in a mucopolysaccharidosis mice model [241,242]. Non-viral

methods using RNA and IN have been mostly used for antigen expression for vaccines, with some ongoing clinical trials [243,244]. But non-viral IN gene delivery has also been used for the CNS, showing still gene expression mostly in the olfactory bulbs and cortex [245]. It has also been used in association with FUS and MB-mediated BBB opening, showing highly improved gene delivery in the FUS-treated region. The study of Jung *et al.* also showed that IN was more efficient than intravenous injection for BBB opening gene delivery in the cortex [246,247].

3.4 *Intravenous Injection*

Unlike previously mentioned injection routes, intravenous injection does not allow bypassing the BBB. Thus, its efficiency relies on the ability of the vector used to cross the BBB. AAV9 was naturally discovered in human liver and has been shown to be able to cross the BBB to transduce the brain's neurons when injected intravenously [248]. But its transduction through the BBB is still sparse and doesn't allow a homogeneous transduction of the brain but only of a few isolated cells [249]. AAV9 is also not specific to the CNS and robustly transduces most organs such as the liver, the heart, or the lung. AAV intravenous injection has been used in several clinical trials, with some FDA-approved treatments, such as onasemnogene abeparvovec (Zolgensma), which successfully transduces the CNS to restore motor neuron function in children affected by spinal muscular atrophy [250–252]. About half of patients treated with it underwent adverse effects related to the treatment, with some serious adverse effects and a case of fatal thrombotic microangiopathy [253,254]. Despite these adverse events, the risk-benefit ratio is still positive since over 95% of treated children survived over 12 months without ventilatory support, but it shows the need to reduce AAV dose for wider use in other pathologies [254]. In addition, due to its wide biodistribution following IV injection, this injection route is the modality requiring the highest AAV amount for gene therapy, while intracerebral injection requires the lowest amount due to its located delivery [218].

Novel serotypes have been generated by Cre-recombination-based AAV targeted evolution, called AAV-PHP.B and AAV-PHP.eB [255,256]. Both shows highly increased transduction efficiency and lower expression in other organs. But the main drawback from these serotypes is their restriction to the animal model used for their development, C57BL/6

mice [257–259]. However, AAV-PHP.eB still showed its efficiency in rat brain over AAV-PHP.B, although it was not more efficient than an AAV9 in B6C3 mice [259,260].

4. FUS and MB-associated BBB opening for gene delivery

4.1 Blood-brain barrier opening

Previously mentioned methods to reach CNS cells with gene therapy products are challenging to use in clinical trials either due to their high invasiveness or due to species-specific vectors. The use of BBB opening (BBBo) however is an efficient alternative since it allows low-invasive IV injection of therapeutic products. As previously mentioned, intravenously injected MB associated with FUS is capable of oscillating, generating microstreaming and shear stress around MB, associated with a push-pull effect on capillary walls [8,261]. These forces generate a rupture of tight junctions, allowing transitory opening of the BBB and passage of molecules (Figure 7). This was first described in 2001 by Hynynen *et al*. in rabbits [9] and was later used for gene delivery in rodents with either viral [12] or non-viral methods [262]. However, BBBo only affects the physical barrier of the BBB, while the biochemical barrier still functions and can prevent accumulation of specific molecules into the brain [263].

If FUS is generally used to induce local BBBo for precise and controlled therapeutic protocols, protocols have been developed to induce wide BBBo. This has been performed either by using probe displacement in a raster scan [249] or by performing several treatments in different areas [264]. Both methods allow gene expression in the whole brain, with expression in neurons. The efficiency of this gene delivery and subsequent transgene expression is correlated with BBBo intensity, as well as BBB closure kinetics [265,266]. The main parameters influencing BBBo are first the mechanical index, which needs to surpass a threshold to induce BBBo, and the frequency, but that is generally selected regarding the model used due to differences in FUS transmission through the skull [267]. Then the PRF and DC also play an important role in BBBo, and while PRFs of 1 to 10 Hz are generally used, much faster pulses have been demonstrated as also inducing efficient BBBo [268–270]. Longer sonication duration also allows improved BBBo, though the low half-life of some MB can limit

the use of long sonication [271]. Finally, MB nature and doses strongly influence BBBo due to differences in cavitation properties regarding gas and shell composition and MB size [10,272]. In addition, for gene therapy purposes, the size of gene delivery vectors also strongly influences gene delivery, since extravasation efficiency is reduced with increased size [273].

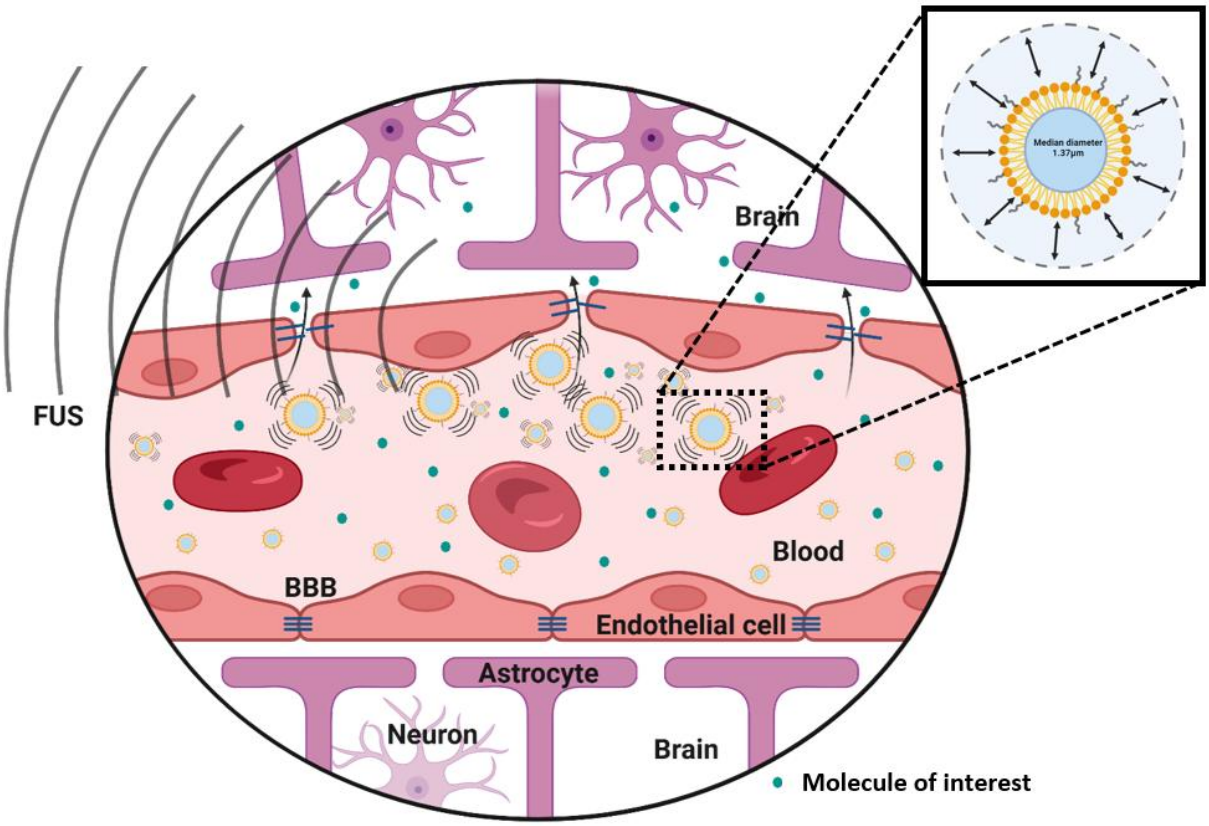

Figure 7: Schematic representation of BBBo with MBs associated with FUS.

4.2 Physiological effect of blood-brain barrier opening

As previously mentioned, severe BBBo with inertial cavitation can produce damage in the brain, like edema or hemorrhages. However, BBBo still induces physiological effects in non-harmful conditions. The first effect is pro-inflammatory, with activation of several pro-inflammatory pathways and cytokine expression [274]. This inflammatory response is mostly described as microglia and astrocyte activation, inducing cytokine expression and increased phagocytosis [275,276], but also with limited infiltration of immune cells like macrophages and T cells [277,278]. Inflammation induced by BBBo has been demonstrated to be correlated with

BBBo intensity and MB cavitation dose, increasing with more severe procedures [247,279]. However, it always remains transitory, with inflammation returning to baseline in a matter of days. In addition to this inflammatory response, BBBo induced by FUS and MB has also been demonstrated to have an effect on the glymphatic system. It typically induces enhanced glymphatic transportation in the brain and promotes protein drainage [280,281]. Finally, BBBo has also been described as able to promote neurogenesis in the brain, with upregulation of neurotrophic factors such as GDNF and early growth response protein-1 [282,283]. Furthermore, unlike the inflammatory response and the effect on the glymphatic system that can be induced by FUS alone, this neurogenesis is triggered only with BBBo associated with FUS and MB (FUS-BBBo) [284]. These effects can be limitations to the use of FUS-BBBo, as they can be considered potentially harmful adverse effects, especially for the inflammatory response. However, it can also have therapeutic effects with the clearance of harmful proteins. In addition, clinical trials demonstrated that these effects are sufficiently moderate and transitory to demonstrate that FUS-BBBo is a safe procedure in controlled conditions [285,286].

4.3 Monitoring of BBBo

In order to ensure efficient BBBo occurred and to quantify its intensity, several techniques have been used that all rely on the extravasation into the brain of a tracer molecule injected after BBBo (Figure 8). The most widely used method for BBBo monitoring is the use of magnetic resonance imaging (MRI) with injection of gadolinium and its detection through T1-weighted sequence [287]. This modality has the advantage of allowing *in vivo* and non-invasive 3D measurement of BBBo, with potential quantitative measurement of extravasated gadolinium. In addition, this imaging technique also allows visualization of edema or hemorrhages induced by BBBo with T2-weighted sequences. Apart from BBBo monitoring, this modality can also be used to measure physiological changes following FUS-BBBo, such as cerebral hemodynamics or functional connectivity [288,289]. Furthermore, MRI has also been used to guide FUS, using an MRI-compatible FUS probe and an ARFI sequence to localize the FUS focal spot on MRI images [290,291]. However, the main drawback of this modality is its high cost and need for highly trained operators.

Due to this limitation, the second most widely used method to monitor BBBo is the use of Evans blue as its extravasation can be visually assessed without the need for an imaging device [287,292]. However, this also means that this modality can only be used *ex vivo*, as it requires extracting the brain, and the resulting information is exclusively qualitative. Another frequently used imaging modality is the fluorescence imaging. This modality has the advantage of allowing *in vivo* and non-invasive monitoring of BBBo when near-infrared fluorescent molecules are used [56]. It can also be used *ex vivo* for enhanced precision, with the possibility to measure BBBo microscopically. A wide range of fluorophores can be used, the most frequent being Evans blue or fluorescently labeled dextran. In addition, as fluorescent labeling of molecules is generally available, it can be used to validate the passage of a specific molecule or to study the size of molecules that can cross the opened BBB [293]. Finally, positron emission tomography (PET) imaging is also an efficient modality for BBBo monitoring as it can quantitatively measure the extravasated molecule in 3D. In addition, molecules or vectors of interest, such as AAV, can be radiolabeled to assess specifically the extravasation of the molecule of interest [265,294]. However, similarly to MRI, its main drawbacks are its cost and the need for highly trained operators, but also its low resolution and the need to use an additional imaging modality such as micro-computed tomography (micro-CT) to visualize tissue and locate the opened region.

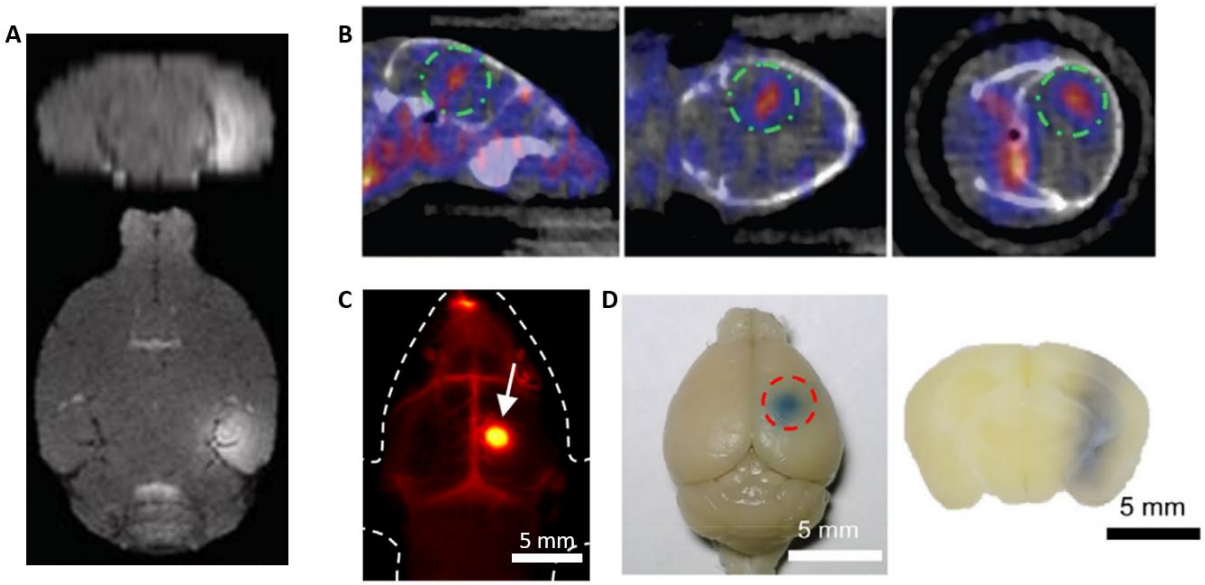

Figure 8: Imaging modalities for BBBo monitoring. (**A**) Reconstructed coronal (top) and transverse (bottom) T1 images, 1.5 h after 0.49 MI sonication using 1-2 μm MB; adapted from Vlachos *et al*. [295] (**B**) Representative sagittal, axial, and coronal plane (from left to right) PET/CT images of an example mouse at 21 h post injection of 64Cu-AAV9 after brain lateral FUS treatment (MI = 0.49), dotted green circle: radio-tagged AAV capsid accumulation; adapted from Ajenjo *et al*. [265]. (**C**) *In vivo* NIR-II fluorescence imaging at 10 minutes after i.v. injection of MBs-ICG under FUS irradiation (White arrow: BBB-opening region). Imaging conditions: Ex, 808 nm laser; long-pass filter, 1300 nm; exposure time, 200 ms; power density, 60 mW/cm²; adapted from Liang *et al*. [56]. (**D**) Representative Evans blue images (red circle: BBB opened region). Left: whole brain; right: 1-mm-thick section; adapted from Liang *et al*.

4.4 Cavitation monitoring of BBBo

As previously mentioned, FUS-BBBo is mediated by MB cavitation that can enter two modes of cavitation: the stable cavitation and the inertial cavitation. With stable cavitation being associated with safe and reproducible BBBo, while inertial cavitation is associated with chaotic and harmful BBBo. But this cavitation is not only influenced by controllable parameters; some parameters can change between animals or depending on the target region, like vascularization or skull thickness. Skull thickness can have a high influence on the ultrasound transmission and therefore on the acoustic pressure *in situ*, changing the cavitation and the BBB opening [249,296]. To overcome this difficulty, the analysis of cavitation rapidly became a major parameter for BBB opening that needed to be monitored. In order to achieve that, a passive cavitation detector (PCD) is generally used, allowing the recording of reflected ultrasound and the non-linear response of MB cavitation. A Fourier transform is applied to the signal allowing us to quantify separately the stable cavitation dose (SCD) and the inertial cavitation dose (ICD). SCD is generally calculated using the harmonics f_1 and f_2, and ICD is generally calculated using the broadband between these harmonics and ultra-harmonics. The sub-harmonic $½ \times f_0$ and ultra-harmonics $f_{1.5}$ and $f_{2.5}$ can also be used for ICD determination but are generally associated with a moderate inertial cavitation regime.

In order to ensure that no damage is generated during BBBo, acoustic monitoring in real-time has been developed, allowing feedback control of the acoustic pressure used. The

main difficulty of this technique is to calculate the Fourier transform fast enough to be able to adapt the pressure before any damage appears. In most cases it calculated between pulses during the time without FUS. There are several possibilities to monitor the BBB opening in this way. The first possibility is to use the cavitation to stop the sonication before the procedure gets too severe. A stable pressure would be applied, and the sonication is stopped whenever the amount of ICD gets over the threshold, as conceived by Huang *et al.* [297]. A second possibility relies on the use of cavitation to set the acoustic pressure. The sonication would start with a low pressure and be increased at each pulse until it reaches the desired cavitation regime. It can be used with either ICD, as described by O'Reilly *et al.* [298], or using SCD, as described by Bing *et al.* [299]. Such monitoring also showed its efficiency in monitoring BBB opening in treated patients with Alzheimer's disease [300]. The main drawback from these techniques is that if an inertial event is recorded the feedback response only occurs after the pulse, possibly after the damage is done. To overcome this, cavitation monitoring intra-pulses have been developed, which showed that MB destabilization occurs suddenly within the pulse, at a random time within it, but stays at a high ICD for the rest of the pulse [301]. This led to another feedback control, where cavitation dose is calculated in a desired temporal window within the entirety of each pulse. The acoustic pressure can then be modified after each temporal window, avoiding an entire pulse of inertial cavitation, further reducing the risk of damage [302]. Although very promising this feedback control requires a very fast calculation of the Fourier transform; such a technical issue makes it difficult to access.

5. Applications of FUS-BBBo and gene therapy to CNS disorders

5.1 Alzheimer's disease

Alzheimer's disease (AD) is a neurodegenerative disease and the leading cause of dementia, mainly characterized by memory loss and impaired cognitive functions [303,304]. The leading causes of AD are the extracellular accumulation of amyloid beta (Aβ) plaques and intracellular accumulation of hyperphosphorylated tau protein [305–307]. Several treatments are currently available for AD, and many more are currently in clinical trials, although current therapy is still limited to symptomatic measures [308–310]. In this context, gene therapy is a

promising strategy, and a first clinical trial with stereotaxic injection of an AAV2 coding for the nerve growth factor showed that it was well tolerated, with specific long-term expression for years [311]. Though the expression showed to be too restricted spatially to have a beneficial effect on cognition [312]. A more recent clinical trial delivered the granulin gene via cisterna magna AAV9 injection. It also showed gene expression and generally good tolerance though 30% moderate and one serious adverse event related to treatment were observed, and no clear effect on cognition [313]. Several other targets are being studied for gene therapy of AD with good efficiency in preclinical studies [314,315]. Although FUS-induced BBB opening has been used in very few studies, they show the possibility of using this technique for AD gene therapy [316,317]. Also, it has been demonstrated that FUS-induced BBB opening is capable of reducing amyloid plaques and phosphorylated tau concentration in AD models, with the activation of microglia and removal through lymphatic routes [280,318–323]. Several clinical trials using FUS-induced BBB opening are ongoing, showing its feasibility and efficiency for Aβ plaque reduction while promoting no adverse effect, though they also show the need to treat larger brain areas to improve therapeutic effect [285,324–326]. A study by Leinenga *et al.* showed the efficiency of combining BBB opening and an anti-Aβ antibody, suggesting that using FUS-induced BBB opening for AD gene therapy would also allow to improve the effect of gene expression with those of FUS [327]. Making FUS-induced BBB opening a particularly promising technique for AD gene therapy.

5.2 Parkinson's disease

Parkinson's disease (PD) is a neurodegenerative disorder characterized by loss of motor functions, tremor, and cognitive disorders. This disorder is primarily characterized by aggregated α-synuclein accumulation in the brain, leading to neuronal dysfunction and degeneration. In PD, FUS-BBBo gene therapy has been attempted in preclinical studies, successfully expressing GNDF or SIRT-3 transgenes, with therapeutic rescue on behavioral phenotypes [61,328]. It has also been used for gene silencing of α-synuclein using an shRNA, which significantly reduced α-synuclein expression [329]. These studies demonstrate the potential of this method for PD treatment and are supported by gene therapy studies using intracranial or intrathecal injections that demonstrate efficient rescue. Furthermore, ongoing clinical trials for gene therapy using intracranial injection of AAV2 demonstrate improvement

for up to 36 months after treatment [330]. In addition, clinical trials for FUS-BBBo alone or with tracer drug injection are ongoing and showing positive results, allowing facilitated translation of FUS-BBBo gene therapy to clinical trials [331,332].

These positive results indicate that FUS-BBBo-mediated gene therapy is a promising method for treatments of CNS disorders, with relatively easy translation to clinical trials due to its safety. It also raises interest in the treatment of other CNS disorders where gene therapy showed promising results. This could be attempted, for example, for Canavan disease [333], Leigh syndrome [334,335], Rett syndrome [336], or Fragile X syndrome [337,338].

6. Fragile X syndrome

6.1 Disease profile

Fragile X syndrome (FXS) is a neurodevelopmental monogenic disorder caused by a repetition of the CGG codons (>200) in the promoter region of the *Fmr1* gene resulting in its hypermethylation and silencing of its expression [339]. FXS was described for the first time in 1943 by Martin and Bell *[340].* It is the leading hereditary cause of intellectual deficiency with a prevalence of 1 in 7 000 males and 1 in 11 000 females, according to Hunter *et al.* meta-analysis. The prevalence of the premutation, with a limited CGG codon repetition (50 to 200) is found to be much higher, at 1 in 850 males and 1 in 300 females [341]. The asymmetry between male and female is due to the location of the *Fmr1* gene on the X chromosome, allowing females to compensate with their second X chromosome (location Xq27.3). Thus, this leads to a lower prevalence of the full mutation but a higher prevalence of the premutation in females compared to males. This also leads to asymmetry in symptoms, and unfortunately, because of these differences, most research focuses on males, leaving gaps in the understanding of female specificities in FXS [342]. The diagnosis method for FXS is performed with a PCR-based analysis of the promoter area of *Fmr1* when developmental delay or typical FXS symptoms are observed. Since this approach is not systematic due to the time and cost needed, the diagnosis is relatively late, at about 3 years old on average [343]. Intellectual deficiency (ID) is the most common symptom in children with FXS. This symptom is generally

associated with attention deficit and hyperactivity disorder (ADHD) and anxiety [344]. It can also be associated with physical features, such as an elongated face, prominent ears, and macroorchidism [345]. Furthermore, FXS is a significant genetic contributor to autism spectrum disorder (ASD) in approximately 30% of cases, characterized by symptoms such as difficulty with eye contact and social interactions.

It is also worth mentioning that FXS patients exhibit a broad and extremely variable spectrum of symptoms. Less frequent but also disturbing symptoms include ophthalmic problems such as strabismus, risk of seizures, obesity, and sleep disorders like sleep apnea. FXS also increases the risk of occurrence of several diseases, like cardiac problems, diseases of the ear, nose, and throat area, and neurodegenerative disorders like Alzheimer's or Parkinson's disease [346].

People affected by the premutation of *Fmr1* are often asymptomatic and are therefore not diagnosed and often pass on the mutation without knowing it. Similarly to the full mutation, children affected by the *Fmr1* premutation may display a wide range of symptoms, like ID and ADHD. It also frequently induces neurodegeneration at later stages of adulthood, around 50 years old, and is frequently called fragile X tremor/ataxia syndrome [347].

6.2 Molecular aspect

Under healthy conditions, the number of CGG repetitions in the promoter area of the *Fmr1* gene remains under 50. In the premutation of FXS, with 50 to 200 codon repetitions, promoter methylation is mild, and *Fmr1* gene expression is not silenced but actually upregulated. *Fmr1* mRNA overexpressed in the premutation has been shown to have toxic effects leading to neurodegeneration [348,349]. Also, symptoms associated with premutation are dependent on both the number of CGG repetitions and the amount of methylation, making it important to characterize these aspects following FXS diagnosis. CGG repeats are normally interrupted by AGG codons, stabilizing the sequence. Although, in premutated alleles, these AGG interruptions are reduced, leading to instability and enhancing the risk of expansion of the CGG repetition during transmission. This effect leads to increased CGG repetition from generation to generation and leads to full mutation. Full FXS mutation is reached with more

than 200 CGG repetitions in the promoting area of the *Fmr1* gene leading to a severe hypermethylation and the total silencing of the gene, with total absence of *Fmr1* mRNA and of its coded protein, fragile X messenger ribonucleoprotein (FMRP, formerly fragile X mental retardation protein). FMRP is an RNA-binding protein constituted of three RNA-binding units arranged as two hnRNP-K-homology domains and an arginine–glycine–glycine box, allowing FMRP to bind to several specific RNA motifs [350–353]. While ubiquitously expressed, it is primarily found in the CNS and reproductive organs [354]. FMRP's main role relies on the regulation of RNA in terms of stability, translational control, and transport through the cell (Figure 9) [355]. FMRP plays a major role in maintaining the proteome in distant axons with the transport of mRNA and localized regulation of mRNA translation [355,356]. A growing body of research has identified a number of FMRP mRNA targets, with some shown to play a significant role in the FXS phenotype. This includes the regulation of glutamatergic signaling through the regulation of several protein expressions, such as mGluR1 or mGluR5, which are involved in various FXS features, including seizures and hyperactivity [357]. GABA receptors are another target largely studied in FXS, with a major role in electrophysiological abnormalities, and have also been linked to behavioral features including hyperactivity and seizures [358]. FMRP can also bind several proteins, like ion channels (monitoring their opening) or transcription factors, further regulating gene expression [359]. While primarily studied in neurons, FMRP function extends beyond neuronal cells. In oligodendrocytes, FMRP deficiency leads to delayed axonal myelination. Furthermore, in astrocytes and microglia, FMRP absence disrupts their interactions with neurons and compromises the maintenance of metabolic homeostasis (including glutamate metabolism), ultimately impairing neuronal function [360].

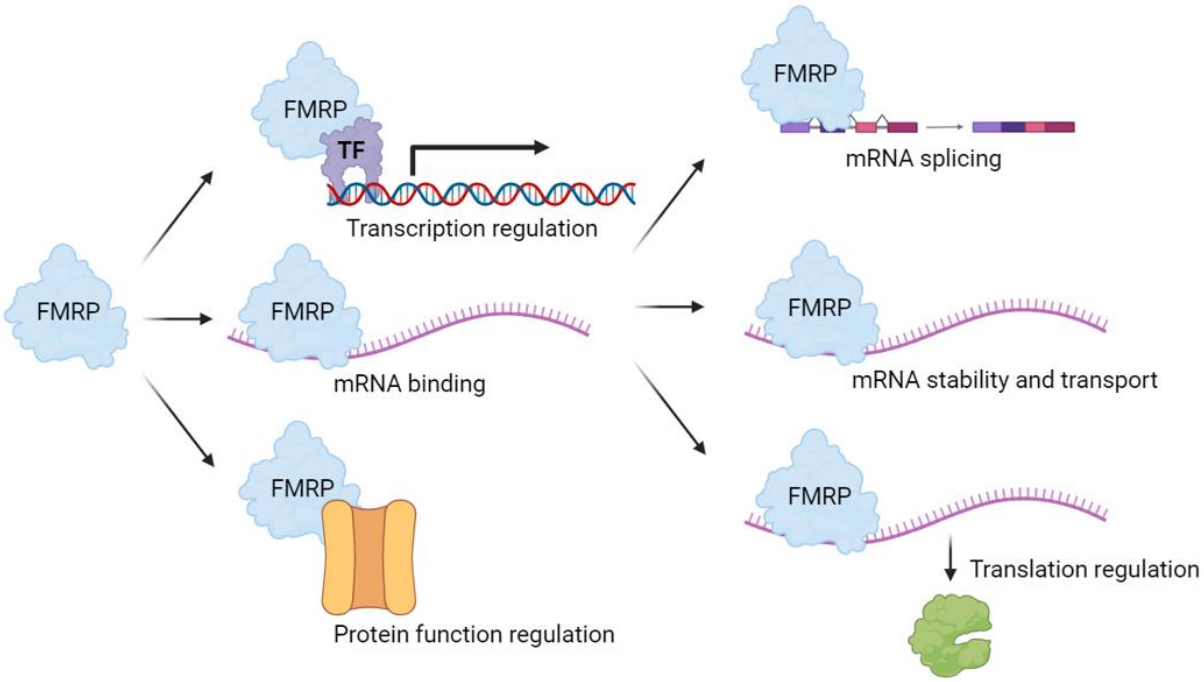

Figure 9: Overview of FMRP functions.

6.3 Treatments and clinical trials

Currently, treatments of FXS are exclusively symptomatic, and no effective therapy is available. A large part of FXS treatments focuses on educational intervention like speech and language therapy or behavior analysis [361,362]. Some drugs are currently available for FXS, allowing treatment of a part of the symptoms [363]. To treat ADHD symptoms, stimulants are generally used, either amphetamine derivatives or methylphenidate like Ritalin [364,365]. However, their use is often overlooked by parents as they are classified as a narcotic and need to be dosed with precaution to avoid language suppression. Antipsychotics like risperidone or aripiprazole can be used to treat aggressive behaviors, but their use needs to be monitored as it can induce weight gain in patients already susceptible to obesity [366,367]. Selective serotonin reuptake inhibitors are prescribed for the treatment of anxiety symptoms, like sertraline [368]. Several clinical trials have been initiated in human patients that followed successful preclinical studies, but few turned out to be efficient in patients once compared to placebo. Metabolic glutamate receptor (mGlur) modulators have been tested in clinical trials, like Mavoglurant or Basimglurant, an mGlur5 antagonist that first showed promising results in phase 1 but whose efficiency was disproved when compared to the placebo group.

Similarly, clinical trials using folic and folinic acids to restore metabolic activity showed no effect compared to placebo, and the same result was obtained with Donepezil, targeting cholinergic channels; minocycline, a neuroprotective agent; or sertraline, a selective serotonin re-uptake inhibitor. Despite these setbacks, some clinical trials managed to show their treatment efficiency in treating some aspects of FXS symptoms. Two treatments showed some efficiency in improving language and communication skills: a transdermal cannabidiol gel (ZYN002) and a phosphodiesterase-4D allosteric inhibitor (BPN14770). Two other treatments showed efficiency in reducing irritability in FXS children, though they showed no improvement in adolescents and adults: an analog of insulin-like growth factor 1 (Trofinetide) and a GABA-B agonist (Abraclofen). These findings collectively indicate that while the pharmacological approaches explored thus far have shown some promise in alleviating certain symptoms, they have not yet demonstrated complete efficacy. Consequently, there is a compelling need to pursue novel therapeutic strategies that directly target the underlying pathophysiology.

6.4 Preclinical studies

Several models have been developed to study fragile X syndrome; first *in vitro* models have been developed where primary cell culture will be used, derived most of the time from newborn rodent brains, but occasionally they can come from human biopsies [369,370]. This model offers important insight into the molecular mechanisms implied in FXS, allowing studies on the FMRP absence effect on ionic canals or cell morphology. *In vitro* models using human cells also have the advantage of providing the opportunity to assess the efficiency of specific therapies that rely on the human genetic mutation in FXS. This includes CRISPR-Cas9 therapy to remove the excess CGG repetition or epigenetic therapies to remove hypermethylation from the promoter area [371].

Rodents, particularly mice and rats, serve as the most commonly utilized animal models in this context. Mouse models attempting to mimic FXS genetic mutation with excess CGG repetitions have been developed but show genetic instability and poorly silence FMRP expression [372]. *Fmr1* knockout models on the other hand, proved to be more efficient at reproducing behavioral phenotypes. In mice, two models have been generated; in the first generation, the *Fmr1* gene is truncated by a neomycin cassette, while in the second generation,

the start codon of the *Fmr1* gene is deleted [373,374]. Second-generation mutation is generally preferred as a model of Fragile X Syndrome (FXS) because *Fmr1* expression is completely abolished. In contrast, first-generation mutation often retains traces of truncated *Fmr1* mRNA, which can retain some function and potentially influence the expression of the FXS phenotype. *Fmr1* KO mice have been thoroughly studied, and their behavior compared to WT mice clearly shows their efficiency to reproduce several FXS phenotypes. The most frequently observed is the hyperactivity phenotype, thoroughly reproduced in most studies [337,375,376]. Social impairment associated with ASD-like behavior [377,378], emotional difficulties, and cognitive deficiencies such as memory defects and seizures were also described [337,338,377,378].

These models have demonstrated their significance in recent years for advancing and developing both pharmacological and genetic therapeutic strategies. The modulation of metabotropic glutamate receptors was extensively studied with promising results, like with the modulation of mGlur4 and mGlur7 via the injection of its allosteric agonist [377,379].

In addition, a large panel of drugs are also being studied for FXS treatment, like diazepam, translational modulator ISRIB, or GABA modulators, that show partial rescue of FXS phenotype [380–382]. Currently, most of these drugs have failed to meet their primary endpoints in clinical trials.

Gene therapy aimed at restoring FMRP expression within the CNS was explored, with promising preclinical results demonstrating its potential to ameliorate certain FXS phenotypes. Lee *et al*. performed non-viral gene delivery on 1- to 2 months-old *Fmr1*-KO mice using intracerebral injection of gold nanoparticles encapsulating CRISPR/Cas9 coding sequence targeting mGlur5 [383]. It demonstrated significant behavioral rescue of anxiety-driven marbles burying and repetitive behavior, but with no effect on hyperactivity. Despite partial rescue, they still demonstrated the feasibility in vivo of the CRISPR/Cas9 strategy, a promising method for removal of excessive CGG repeats as previously mentioned [371]. Apart from this study, most gene therapy studies were performed at early development stages, using ICV [378,384], intra-cisterna magna [384], or intrathecal [338] AAV injections at PND 0 to 3. In all studies, significant rescue was observed, with effects on hyperactivity, social impairment, anxiety, repetitive behaviors, seizures, fear conditioning, and sleep impairment. Behavioral rescue varied between studies, but total rescue was never observed, suggesting the importance of FMRP during gestation. Performing this treatment at an early development stage should be

more efficient, as it would allow brain development in the presence of FMRP. However, it has also been performed by Chadman *et al.* in adult mice and also showed partial rescue of fear conditioning and learning phenotype, though it seems to show less efficient rescue compared to other studies [337]. As they all rely on an intracranial AAV injection or intravenous mice-specific AAV.PhP.eB injection, their strategies are therefore difficult to translate to clinical trials since intracranial injections impose safety issues [385,386]. The use of a microbubble-mediated BBB opening gene therapy protocol could be a way to translate these gene therapy studies to clinical trials but has not been attempted yet.

The overall objective of this PhD is to develop a gene therapy protocol, based on microbubble-associated BBB opening, for CNS monogenic disorders such as FXS. To achieve this objective, the project is constructed on 4 main axes:

At first, the development of innovative microbubbles to enhance gene delivery was explored. For this part we developed homemade microbubbles with various functionalizations. This includes first biotinylated or DBCO-MB capable of binding either an antibody or magnetic nanoparticles to incorporate targeting properties and two types of cationic MB capable of complexing with DNA. In addition, the cavitation properties of our different cationic MB were assessed in order to anticipate their response during BBBo treatments.

The second objective was to establish protocols to open the BBB and to monitor it. This was performed with our unfunctionalized MB, and BBBo monitoring was mediated with Indocyanine Green (ICG) extravasation. We used fluorescence imaging both *in vivo* and *ex vivo* and photoacoustic imaging *in vivo*. These imaging modalities were compared with the gold standard, MRI, and with Evans blue to validate the use of our monitoring modalities as an alternative method.

Thirdly, the optimization of a non-viral gene delivery protocol to the CNS was performed. We used it for our first generation of cationic MB and optimized the complexation conditions, mechanical index, and sonication duration. This was optimized in both wild-type mice and in the model of FXS, *Fmr1*-KO mice. The proof-of-concept of gene therapy for FXS with restored expression of *Fmr1* was then performed. Finally, this method was compared with another non-viral method using lipid nanoparticles.

Finally, in a final part, we performed a viral gene therapy strategy with FUS-BBBo in the FXS mouse model, *Frm1*-KO mice. Gene expression was analyzed in both bioluminescence and *Fmr1* expression to be able to compare it with our non-viral strategy. In the end, the ability of our gene therapy protocol to induce behavioral rescue was assessed and compared with the effect of FUS-BBBo alone.

Bibliography:

1. Krishna, V.; Sammartino, F.; Rezai, A. A Review of the Current Therapies, Challenges, and Future Directions of Transcranial Focused Ultrasound Technology. JAMA Neurol 2018, 75, 246, doi:10.1001/jamaneurol.2017.3129.

2. Bouakaz, A.; Michel Escoffre, J. From Concept to Early Clinical Trials: 30 Years of Microbubble-Based Ultrasound-Mediated Drug Delivery Research. Adv Drug Deliv Rev 2024, 206.

3. Zhong, Y.X.; Liao, J.C.; Liu, X.; Tian, H.; Deng, L.R.; Long, L. Low Intensity Focused Ultrasound: A New Prospect for the Treatment of Parkinson's Disease. Ann Med 2023, 55, doi:10.1080/07853890.2023.2251145.

4. Xu, Z.; Khokhlova, T.D.; Cho, C.S.; Khokhlova, V.A. Histotripsy: A Method for Mechanical Tissue Ablation with Ultrasound. Annu Rev Biomed Eng 2024, 26, 141–167, doi:10.1146/annurev-bioeng-073123-022334.

5. Dauba, A.; Delalande, A.; Kamimura, H.A.S.; Conti, A.; Larrat, B.; Tsapis, N.; Novell, A. Recent Advances on Ultrasound Contrast Agents for Blood-Brain Barrier Opening with Focused Ultrasound. Pharmaceutics 2020, 12, 1125, doi:10.3390/pharmaceutics12111125.

6. Tung, Y.-S.; Vlachos, F.; Feshitan, J.A.; Borden, M.A.; Konofagou, E.E. The Mechanism of Interaction between Focused Ultrasound and Microbubbles in Blood-Brain Barrier Opening in Mice. J Acoust Soc Am 2011, 130, 3059–3067, doi:10.1121/1.3646905.

7. Tung, Y.S.; Choi, J.J.; Baseri, B.; Konofagou, E.E. Identifying the Inertial Cavitation Threshold and Skull Effects in a Vessel Phantom Using Focused Ultrasound and Microbubbles. Ultrasound Med Biol 2010, 36, 840–852, doi:10.1016/j.ultrasmedbio.2010.02.009.

8. Collis, J.; Manasseh, R.; Liovic, P.; Tho, P.; Ooi, A.; Petkovic-Duran, K.; Zhu, Y. Cavitation Microstreaming and Stress Fields Created by Microbubbles. Ultrasonics 2010, 50, 273–279, doi:10.1016/j.ultras.2009.10.002.

9. Hynynen, K.; McDannold, N.; Vykhodtseva, N.; Jolesz, F.A. Noninvasive MR Imaging-Guided Focal Opening of the Blood-Brain Barrier in Rabbits. Radiology 2001, 220, 640–646, doi:10.1148/radiol.2202001804.

10. Marmottant, P.; van der Meer, S.; Emmer, M.; Versluis, M.; de Jong, N.; Hilgenfeldt, S.; Lohse, D. A Model for Large Amplitude Oscillations of Coated Bubbles Accounting for Buckling and Rupture. J Acoust Soc Am 2005, 118, 3499–3505, doi:10.1121/1.2109427.

11. van der Meer, S.M.; Dollet, B.; Voormolen, M.M.; Chin, C.T.; Bouakaz, A.; de Jong, N.; Versluis, M.; Lohse, D. Microbubble Spectroscopy of Ultrasound Contrast Agents. J Acoust Soc Am 2007, 121, 648–656, doi:10.1121/1.2390673.

12. Thévenot, E.; Jordão, J.F.; O'Reilly, M.A.; Markham, K.; Weng, Y.Q.; Foust, K.D.; Kaspar, B.K.; Hynynen, K.; Aubert, I. Targeted Delivery of Self-Complementary Adeno-Associated Virus Serotype 9 to the Brain, Using Magnetic Resonance Imaging-Guided Focused Ultrasound. Hum Gene Ther 2012, 23, 1144–1155, doi:10.1089/hum.2012.013.

13. Kotopoulis, S.; Popa, M.; Safont, M.M.; Murvold, E.; Haugse, R.; Langer, A.; Dimcevski, G.; Lam, C.; Bjånes, T.; Gilja, H.; et al. SonoVue ® vs. SonazoidTM vs. OptisonTM: Which Bubble Is Best for Low-Intensity Sonoporation of Pancreatic Ductal Adenocarcinoma? 2022, doi:10.3390/pharmaceutics.

14. Rezai, A.R.; Ranjan, M.; Haut, M.W.; Carpenter, J.; D'Haese, P.F.; Mehta, R.I.; Najib, U.; Wang, P.; Claassen, D.O.; Chazen, J.L.; et al. Focused Ultrasound-Mediated Blood-Brain Barrier Opening in Alzheimer's Disease: Long-Term Safety, Imaging, and Cognitive Outcomes. J Neurosurg 2023, 139, 275–283, doi:10.3171/2022.9.JNS221565.

15. Polydorou, A.E.; May, J.P.; Makris, K.; Ferri, S.; Wu, Q.; Stride, E.; Carugo, D.; Evans, N.D. An Investigation into the Cytotoxic Effects of Microbubbles and Their Constituents on Osteosarcoma and Bone Marrow Stromal Cells. Biochim Biophys Acta Gen Subj 2023, 1867, doi:10.1016/j.bbagen.2023.130481.

16. McMahon, D.; Lassus, A.; Gaud, E.; Jeannot, V.; Hynynen, K. Microbubble Formulation Influences Inflammatory Response to Focused Ultrasound Exposure in the Brain. Sci Rep 2020, 10, doi:10.1038/s41598-020-78657-9.

17. Owen, J.; Kamila, S.; Shrivastava, S.; Carugo, D.; Bernardino De La Serna, J.; Mannaris, C.; Pereno, V.; Browning, R.; Beguin, E.; McHale, A.P.; et al. The Role of PEG-40-Stearate in the Production, Morphology, and Stability of Microbubbles. Langmuir 2019, 35, 10014–10024, doi:10.1021/acs.langmuir.8b02516.

18. Navarro-Becerra, J.A.; Castillo, J.I.; Borden, M.A. Effect of Poly(Ethylene Glycol) Configuration on Microbubble Pharmacokinetics. ACS Biomater Sci Eng 2024, 10, 3331–3342, doi:10.1021/acsbiomaterials.3c01764.

19. Fix, S.M.; Nyankima, A.G.; McSweeney, M.D.; Tsuruta, J.K.; Lai, S.K.; Dayton, P.A. Accelerated Clearance of Ultrasound Contrast Agents Containing Polyethylene Glycol Is Associated with

the Generation of Anti-Polyethylene Glycol Antibodies. Ultrasound Med Biol 2018, 44, 1266–1280, doi:10.1016/j.ultrasmedbio.2018.02.006.

20. Rudakovskaya, P.G.; Barmin, R.A.; Kuzmin, P.S.; Fedotkina, E.P.; Sencha, A.N.; Gorin, D.A. Microbubbles Stabilized by Protein Shell: From Pioneering Ultrasound Contrast Agents to Advanced Theranostic Systems. Pharmaceutics 2022, 14.

21. Liao, A.H.; Hung, C.R.; Lin, C.F.; Lin, Y.C.; Chen, H.K. Treatment Effects of Lysozyme-Shelled Microbubbles and Ultrasound in Inflammatory Skin Disease. Sci Rep 2017, 7, doi:10.1038/srep41325.

22. Chen, Z.; Pulsipher, K.W.; Chattaraj, R.; Hammer, D.A.; Sehgal, C.M.; Lee, D. Engineering the Echogenic Properties of Microfluidic Microbubbles Using Mixtures of Recombinant Protein and Amphiphilic Copolymers. Langmuir 2019, 35, 10079–10086, doi:10.1021/acs.langmuir.8b03882.

23. Sigalit AVIVI and Aharon GEDANKEN S–S Bonds Are Not Required for the Sonochemical Formation of Proteinaceous Microspheres : The Case of Streptavidin. Biochem. J. 2002, 366, 705–707.

24. Vong, F.; Son, Y.; Bhuiyan, S.; Zhou, M.; Cavalieri, F.; Ashokkumar, M. A Comparison of the Physical Properties of Ultrasonically Synthesized Lysozyme- and BSA-Shelled Microbubbles. Ultrason Sonochem 2014, 21, 23–28, doi:10.1016/j.ultsonch.2013.05.004.

25. Suslick, K.S.; Grinstaff, M.W.; Kolbeck, K.J.; Wong, M. Characterization of Sonochemically Prepared Proteinaceous Microspheres. Ultrason Sonochem 1994, 1, 65–68, doi:10.1016/1350-4177(94)90030-2.

26. Ji, J.; Ji, J.; He Xia Preparation of Ultrasound Microbubbles Crosslinked to Albumin Nanoparticles Packaged with Tissue-Type Plasminogen Activator Gene Plasmid and Method of in Vivo Transfection. J Exp Pharmacol 2011, 35, doi:10.2147/jep.s17178.

27. Lentacker, I.; De Geest, B.G.; Vandenbroucke, R.E.; Peeters, L.; Demeester, J.; De Smedt, S.C.; Sanders, N.N. Ultrasound-Responsive Polymer-Coated Microbubbles That Bind and Protect DNA. Langmuir 2006, 22, 7273–7278, doi:10.1021/la0603828.

28. Estifeeva, T.M.; Nechaeva, A.M.; Le-Deygen, I.M.; Adelyanov, A.M.; Grigoryan, I. V.; Petrovskii, V.S.; Potemkin, I.I.; Abramov, A.A.; Prosvirnin, A. V.; Sencha, E.A.; et al. Ultrasound Protein-Copolymer Microbubble Library Engineering through

Poly(Vinylpyrrolidone-Co-Acrylic Acid) Structure. Biomaterials Advances 2025, 166, doi:10.1016/j.bioadv.2024.214074.

29. Chen, J.L.; Dhanaliwala, A.H.; Dixon, A.J.; Klibanov, A.L.; Hossack, J.A. Synthesis and Characterization of Transiently Stable Albumin-Coated Microbubbles via a Flow-Focusing Microfluidic Device. Ultrasound Med Biol 2014, 40, 400–409, doi:10.1016/j.ultrasmedbio.2013.09.024.

30. Shchukin, D.G.; Möhwald, H. Sonochemical Nanosynthesis at the Engineered Interface of a Cavitation Microbubble. Physical Chemistry Chemical Physics 2006, 8, 3496–3506, doi:10.1039/b606104d.

31. Upadhyay, A.; Dalvi, S. V. Synthesis, Characterization and Stability of BSA-Encapsulated Microbubbles. RSC Adv 2016, 6, 15016–15026, doi:10.1039/c5ra24304a.

32. Liu, X.; Gong, P.; Song, P.; Xie, F.; Miller, A.L.; Chen, S.; Lu, L. Fast Functionalization of Ultrasound Microbubbles Using Strain Promoted Click Chemistry. Biomater Sci 2018, 6, 623–632, doi:10.1039/c8bm00004b.

33. Liu, X.; Gong, P.; Song, P.; Xie, F.; Miller, A.L.; Chen, S.; Lu, L. Rapid Conjugation of Nanoparticles, Proteins and SiRNAs to Microbubbles by Strain-Promoted Click Chemistry for Ultrasound Imaging and Drug Delivery. Polym Chem 2019, 10, 705–717, doi:10.1039/c8py01721b.

34. Lee, S.; Kim, J.H.; Moon, H.; Lee, H.J.; Han, J.K. Combined Treatment of Sorafenib and Doxorubicin-Loaded Microbubble-Albumin Nanoparticle Complex for Hepatocellular Carcinoma: A Feasibility Study. PLoS One 2020, 15, doi:10.1371/journal.pone.0243815.

35. Chen, Z.; Chattaraj, R.; Pulsipher, K.W.; Karmacharya, M.B.; Hammer, D.A.; Lee, D.; Sehgal, C.M. Photoacoustic and Ultrasound Dual-Mode Imaging via Functionalization of Recombinant Protein-Stabilized Microbubbles with Methylene Blue. ACS Appl Bio Mater 2019, 2, 4020–4026, doi:10.1021/acsabm.9b00545.

36. Mahalingam, S.; Xu, Z.; Edirisinghe, M. Antibacterial Activity and Biosensing of PVA-Lysozyme Microbubbles Formed by Pressurized Gyration. Langmuir 2015, 31, 9771–9780, doi:10.1021/acs.langmuir.5b02005.

37. Barmin, R.A.; Moosavifar, M.; Dasgupta, A.; Herrmann, A.; Kiessling, F.; Pallares, R.M.; Lammers, T. Polymeric Materials for Ultrasound Imaging and Therapy. Chem Sci 2023, 14, 11941–11954, doi:10.1039/D3SC04339H.

38. Dasgupta, A.; Sun, T.; Palomba, R.; Rama, E.; Zhang, Y.; Power, C.; Moeckel, D.; Liu, M.; Sarode, A.; Weiler, M.; et al. Nonspherical Ultrasound Microbubbles. Proc Natl Acad Sci U S A 2023, 120, doi:10.1073/pnas.2218847120.

39. Rastegar, G.; Salman, M.M.; Sirsi, S.R. Remote Loading: The Missing Piece for Achieving High Drug Payload and Rapid Release in Polymeric Microbubbles. Pharmaceutics 2023, 15, doi:10.3390/pharmaceutics15112550.

40. Jablonowski, L.J.; Teraphongphom, N.T.; Wheatley, M.A. Drug Delivery from a Multi-Faceted Ultrasound Contrast Agent: Influence of Shell Composition. Mol Pharm 2017, 14, 3448–3456, doi:10.1021/acs.molpharmaceut.7b00451.

41. Yu, Z.; Hu, M.; Li, Z.; Dan Xu; Zhu, L.; Guo, Y.; Liu, Q.; Lan, W.; Jiang, J.; Wang, L. Anti-G250 Nanobody-Functionalized Nanobubbles Targeting Renal Cell Carcinoma Cells for Ultrasound Molecular Imaging. Nanotechnology 2020, 31, 205101, doi:10.1088/1361-6528/ab7040.

42. Fernandes, D.A. Comprehensive Review on Bubbles: Synthesis, Modification, Characterization and Biomedical Applications. Bioconjug Chem 2024, 35, 1639–1686, doi:10.1021/acs.bioconjchem.4c00137.

43. Wang, Y.; Li, X.; Zhou, Y.; Huang, P.; Xu, Y. Preparation of Nanobubbles for Ultrasound Imaging and Intracelluar Drug Delivery. Int J Pharm 2010, 384, 148–153, doi:10.1016/j.ijpharm.2009.09.027.

44. Zhang, Q.; Yang, Y.; Xue, H.; Zhang, H.; Yuan, Z.; Shen, Y.; Guo, X.; Fan, Z.; Wu, X.; Zhang, D.; et al. Intensified and Controllable Vaporization of Phase-Changeable Nanodroplets Induced by Simultaneous Exposure of Laser and Ultrasound. Ultrason Sonochem 2023, 94, doi:10.1016/j.ultsonch.2023.106312.

45. Li, H.; Wang, J.; Huang, G.; Wang, P.; Zheng, R.; Zhang, C.; Jiang, Q. Multifunctionalized Microbubbles for Cancer Diagnosis and Therapy. Anticancer Agents Med Chem 2013, 13, 403–413, doi:10.2174/1871520611313030004.

46. Beguin, E.; Bau, L.; Shrivastava, S.; Stride, E. Comparing Strategies for Magnetic Functionalization of Microbubbles. ACS Appl Mater Interfaces 2019, 11, 1829–1840, doi:10.1021/acsami.8b18418.

47. Liou, Y.R.; Wang, Y.H.; Lee, C.Y.; Li, P.C. Buoyancy-Activated Cell Sorting Using Targeted Biotinylated Albumin Microbubbles. PLoS One 2015, 10, doi:10.1371/journal.pone.0125036.

48. Goncin, U.; Curiel, L.; Geyer, C.R.; Machtaler, S. Aptamer-Functionalized Microbubbles Targeted to P-Selectin for Ultrasound Molecular Imaging of Murine Bowel Inflammation. Mol Imaging Biol 2023, 25, 283–293, doi:10.1007/s11307-022-01755-9.

49. Berezin, V.; Walmod, P.S.; Filippov, M.; Dityatev, A. Targeting of ECM Molecules and Their Metabolizing Enzymes and Receptors for the Treatment of CNS Diseases. In Progress in Brain Research; Elsevier B.V., 2014; Vol. 214, pp. 353–388.

50. Owen, J.; Crake, C.; Lee, J.Y.; Carugo, D.; Beguin, E.; Khrapitchev, A.A.; Browning, R.J.; Sibson, N.; Stride, E. A Versatile Method for the Preparation of Particle-Loaded Microbubbles for Multimodality Imaging and Targeted Drug Delivery. 2017, doi:10.5287/bodleian:Aer44Drnj.

51. Stride, E.; Porter, C.; Prieto, A.G.; Pankhurst, Q. Enhancement of Microbubble Mediated Gene Delivery by Simultaneous Exposure to Ultrasonic and Magnetic Fields. Ultrasound Med Biol 2009, 35, 861–868, doi:10.1016/j.ultrasmedbio.2008.11.010.

52. Langeveld, S.A.G.; Meijlink, B.; Beekers, I.; Olthof, M.; Van Der Steen, A.F.W.; Jong, N. de; Kooiman, K. Theranostic Microbubbles with Homogeneous Ligand Distribution for Higher Binding Efficacy. Pharmaceutics 2022, 14, doi:10.3390/pharmaceutics14020311.

53. Chen, L.; Sutharsan, R.; Lee, J.L.F.; Cruz, E.; Asnicar, B.; Palliyaguru, T.; Wasielewska, J.M.; Gaudin, A.; Song, J.; Leinenga, G.; et al. Claudin-5 Binder Enhances Focused Ultrasoundmediated Opening in an in Vitro Blood-Brain Barrier Model. Theranostics 2022, 12, 1952–1970, doi:10.7150/thno.65539.

54. Li, B.; Lin, Y.; Chen, G.; Cai, M.; Zhong, H.; Xiao, Z.; Lin, M.; Li, T.; Cai, Y.; Shuai, X.; et al. Anchoring Microbubbles on Cerebrovascular Endothelium as a New Strategy Enabling Low-Energy Ultrasound-Assisted Delivery of Varisized Agents Across Blood-Brain Barrier. Advanced Science 2023, 10, doi:10.1002/advs.202302134.

55. Beekers, I.; Langeveld, S.A.G.; Meijlink, B.; van der Steen, A.F.W.; de Jong, N.; Verweij, M.D.; Kooiman, K. Internalization of Targeted Microbubbles by Endothelial Cells and Drug Delivery by Pores and Tunnels. Journal of Controlled Release 2022, 347, 460–475, doi:10.1016/j.jconrel.2022.05.008.

56. Liang, S.; Hu, D.; Li, G.; Gao, D.; Li, F.; Zheng, H.; Pan, M.; Sheng, Z. NIR-II Fluorescence Visualization of Ultrasound-Induced Blood–Brain Barrier Opening for Enhanced Photothermal Therapy against Glioblastoma Using Indocyanine Green Microbubbles. Sci Bull (Beijing) 2022, 67, 2316–2326, doi:10.1016/j.scib.2022.10.025.

57. Barrefelt, Å.A.; Brismar, T.B.; Egri, G.; Aspelin, P.; Olsson, A.; Oddo, L.; Margheritelli, S.; Caidahl, K.; Paradossi, G.; Dähne, L.; et al. Multimodality Imaging Using SPECT/CT and MRI and Ligand Functionalized 99mTc-Labeled Magnetic Microbubbles. EJNMMI Res 2013, 3, 1–14, doi:10.1186/2191-219X-3-12.

58. Tartis, M.S.; Kruse, D.E.; Zheng, H.; Zhang, H.; Kheirolomoom, A.; Marik, J.; Ferrara, K.W. Dynamic MicroPET Imaging of Ultrasound Contrast Agents and Lipid Delivery. Journal of Controlled Release 2008, 131, 160–166, doi:10.1016/j.jconrel.2008.07.030.

59. Liao, A.H.; Hung, C.R.; Chen, H.K.; Chiang, C.P. Ultrasound-Mediated EGF-Coated-Microbubble Cavitation in Dressings for Wound-Healing Applications. Sci Rep 2018, 8, doi:10.1038/s41598-018-26702-z.

60. Lindner, J.R.; Coggins, M.P.; Kaul, S.; Klibanov, A.L.; Brandenburger, G.H.; Ley, K. Microbubble Persistence in the Microcirculation During Ischemia/Reperfusion and Inflammation Is Caused by Integrin-and Complement-Mediated Adherence to Activated Leukocytes; 2000;

61. Fan, C.H.; Ting, C.Y.; Lin, C.Y.; Chan, H.L.; Chang, Y.C.; Chen, Y.Y.; Liu, H.L.; Yeh, C.K. Noninvasive, Targeted, and Non-Viral Ultrasound-Mediated GDNF-Plasmid Delivery for Treatment of Parkinson's Disease. Sci Rep 2016, 6, doi:10.1038/srep19579.

62. Nomikou, N.; Feichtinger, G.A.; Redl, H.; McHale, A.P. Ultrasound-Mediated Gene Transfer (Sonoporation) in Fibrin-Based Matrices: Potential for Use in Tissue Regeneration. J Tissue Eng Regen Med 2016, 10, 29–39, doi:10.1002/term.1730.

63. Kumar, R.; Santa Chalarca, C.F.; Bockman, M.R.; Bruggen, C. Van; Grimme, C.J.; Dalal, R.J.; Hanson, M.G.; Hexum, J.K.; Reineke, T.M. Polymeric Delivery of Therapeutic Nucleic Acids. Chem Rev 2021, 121, 11527–11652, doi:10.1021/acs.chemrev.0c00997.

64. Panje, C.M.; Wang, D.S.; Pysz, M.A.; Paulmurugan, R.; Ren, Y.; Tranquart, F.; Tian, L.; Willmann, J.K. Ultrasound-Mediated Gene Delivery with Cationic versus Neutral Microbubbles: Effect of DNA and Microbubble Dose on In Vivo Transfection Efficiency. Theranostics 2012, 2, 1078–1091, doi:10.7150/thno.4240.

65. Xie, A.; Wu, M.D.; Cigarroa, G.; Belcik, J.T.; Ammi, A.; Moccetti, F.; Lindner, J.R. Influence of DNA-Microbubble Coupling on Contrast Ultrasound–Mediated Gene Transfection in Muscle and Liver. Journal of the American Society of Echocardiography 2016, 29, 812–818, doi:10.1016/j.echo.2016.04.011.

66. Tan, J.K.Y.; Pham, B.; Zong, Y.; Perez, C.; Maris, D.O.; Hemphill, A.; Miao, C.H.; Matula, T.J.; Mourad, P.D.; Wei, H.; et al. Microbubbles and Ultrasound Increase Intraventricular Polyplex Gene Transfer to the Brain. Journal of Controlled Release 2016, 231, 86–93, doi:10.1016/j.jconrel.2016.02.003.

67. Ho, Y.J.; Chang, H.C.; Lin, C.W.; Fan, C.H.; Lin, Y.C.; Wei, K.C.; Yeh, C.K. Oscillatory Behavior of Microbubbles Impacts Efficacy of Cellular Drug Delivery. Journal of Controlled Release 2021, 333, 316–327, doi:10.1016/j.jconrel.2021.03.044.

68. Lin, C.W.; Fan, C.H.; Yeh, C.K. The Impact of Surface Drug Distribution on the Acoustic Behavior of DOX-Loaded Microbubbles. Pharmaceutics 2021, 13, doi:10.3390/pharmaceutics13122080.

69. Jin, Q.; Wang, Z.; Yan, F.; Deng, Z.; Ni, F.; Wu, J.; Shandas, R.; Liu, X.; Zheng, H. A Novel Cationic Microbubble Coated with Stearic Acid-Modified Polyethylenimine to Enhance DNA Loading and Gene Delivery by Ultrasound. PLoS One 2013, 8, doi:10.1371/journal.pone.0076544.

70. Zhou, Y.; Gu, H.; Xu, Y.; Li, F.; Kuang, S.; Wang, Z.; Zhou, X.; Ma, H.; Li, P.; Zheng, Y.; et al. Targeted Antiangiogenesis Gene Therapy Using Targeted Cationic Microbubbles Conjugated with CD105 Antibody Compared with Untargeted Cationic and Neutral Microbubbles. Theranostics 2015, 5, 399–417, doi:10.7150/thno.10351.

71. Yan, P.; Chen, K.J.; Wu, J.; Sun, L.; Sung, H.W.; Weisel, R.D.; Xie, J.; Li, R.K. The Use of MMP2 Antibody-Conjugated Cationic Microbubble to Target the Ischemic Myocardium, Enhance Timp3 Gene Transfection and Improve Cardiac Function. Biomaterials 2014, 35, 1063–1073, doi:10.1016/j.biomaterials.2013.10.043.

72. Liu, Y.; Lai, X.; Zhu, Y.; Guo, F.; Su, L.; Arkin, G.; He, T.; Xu, J.; Ran, H. Contrast-Enhanced Ultrasound Imaging Using Long-Circulating Cationic Magnetic Microbubbles in Vitro and in Vivo Validations. Int J Pharm 2022, 616, 121299, doi:10.1016/J.IJPHARM.2021.121299.

73. Ning, R.; Acree, B.; Wu, M.; Gao, Y. Microfluidic Monodispersed Microbubble Generation for Production of Cavitation Nuclei. Micromachines (Basel) 2024, 15, doi:10.3390/mi15121531.

74. Liu, K.; Wang, M.-W.; Lin, W.-Y.; Phung, D.L.; D. Girgis, M.; M. Wu, A.; S. Tomlinson, J.; K.-F. Shen, C. Molecular Imaging Probe Development Using Microfluidics. Curr Org Synth 2011, 8, 473–487, doi:10.2174/157017911796117205.

75. Pulsipher, K.W.; Hammer, D.A.; Lee, D.; Sehgal, C.M. Engineering Theranostic Microbubbles Using Microfluidics for Ultrasound Imaging and Therapy: A Review. Ultrasound Med Biol 2018, 44, 2441–2460.

76. Melich, R.; Valour, J.P.; Urbaniak, S.; Padilla, F.; Charcosset, C. Preparation and Characterization of Perfluorocarbon Microbubbles Using Shirasu Porous Glass (SPG) Membranes. Colloids Surf A Physicochem Eng Asp 2019, 560, 233–243, doi:10.1016/j.colsurfa.2018.09.058.

77. Kukizaki, M.; Wada, T. Effect of the Membrane Wettability on the Size and Size Distribution of Microbubbles Formed from Shirasu-Porous-Glass (SPG) Membranes. Colloids Surf A Physicochem Eng Asp 2008, 317, 146–154, doi:10.1016/j.colsurfa.2007.10.005.

78. Emmer, M.; Vos, H.J.; Goertz, D.E.; van Wamel, A.; Versluis, M.; de Jong, N. Pressure-Dependent Attenuation and Scattering of Phospholipid-Coated Microbubbles at Low Acoustic Pressures. Ultrasound Med Biol 2009, 35, 102–111, doi:10.1016/j.ultrasmedbio.2008.07.005.

79. Goertz, D.E.; de Jong, N.; van der Steen, A.F.W. Attenuation and Size Distribution Measurements of DefinityTM and Manipulated DefinityTM Populations. Ultrasound Med Biol 2007, 33, 1376–1388, doi:10.1016/j.ultrasmedbio.2007.03.009.

80. Feshitan, J.A.; Chen, C.C.; Kwan, J.J.; Borden, M.A. Microbubble Size Isolation by Differential Centrifugation. J Colloid Interface Sci 2009, 329, 316–324, doi:10.1016/j.jcis.2008.09.066.

81. Segers, T.; Versluis, M. Acoustic Bubble Sorting for Ultrasound Contrast Agent Enrichment. Lab Chip 2014, 14, 1705–1714, doi:10.1039/c3lc51296g.

82. Segers, T.; de Jong, N.; Versluis, M. Uniform Scattering and Attenuation of Acoustically Sorted Ultrasound Contrast Agents: Modeling and Experiments. J Acoust Soc Am 2016, 140, 2506–2517, doi:10.1121/1.4964270.

83. Wegierak, D.; Nittayacharn, P.; Cooley, M.B.; Berg, F.M.; Kosmides, T.; Durig, D.; Kolios, M.C.; Exner, A.A. Nanobubble Contrast Enhanced Ultrasound Imaging: A Review. Wiley Interdiscip Rev Nanomed Nanobiotechnol 2024, 16, doi:10.1002/wnan.2007.

84. Helfield, B.; Zou, Y.; Matsuura, N. Acoustically-Stimulated Nanobubbles: Opportunities in Medical Ultrasound Imaging and Therapy. Front Phys 2021, 9, doi:10.3389/fphy.2021.654374.

85. Pfeifer, F. Distribution, Formation and Regulation of Gas Vesicles. Nat Rev Microbiol 2012, 10, 705–715, doi:10.1038/nrmicro2834.

86. Howells, A.R.; Welch, P.J.; Kim, J.; Forest, C.R.; Shi, C.; Lian, X.L. A Drug-Selectable Acoustic Reporter Gene System for Human Cell Ultrasound Imaging. Bioeng Transl Med 2024, 9, doi:10.1002/btm2.10584.

87. Sennoga, C.A.; Mahue, V.; Loughran, J.; Casey, J.; Seddon, J.M.; Tang, M.; Eckersley, R.J. On Sizing and Counting of Microbubbles Using Optical Microscopy. Ultrasound Med Biol 2010, 36, 2093–2096, doi:10.1016/j.ultrasmedbio.2010.09.004.

88. Schindelin, J.; Arganda-Carreras, I.; Frise, E.; Kaynig, V.; Longair, M.; Pietzsch, T.; Preibisch, S.; Rueden, C.; Saalfeld, S.; Schmid, B.; et al. Fiji: An Open-Source Platform for Biological-Image Analysis. Nat Methods 2012, 9, 676–682.

89. Burch, C.R.; Stock, J.P.P. Phase-Contrast Microscopy. J Sci Instrum 1942, 19, 71–75, doi:10.1088/0950-7671/19/5/302.

90. Manta, S.; Delalande, A.; Bessodes, M.; Bureau, M.F.; Scherman, D.; Pichon, C.; Mignet, N. Characterization of Positively Charged Lipid Shell Microbubbles with Tunable Resistive Pulse Sensing (TRPS) Method: A Technical Note. Ultrasound Med Biol 2016, 42, 624–630, doi:10.1016/j.ultrasmedbio.2015.10.010.

91. Rhyner, M.N. The Coulter Principle for Analysis of Subvisible Particles in Protein Formulations. AAPS J 2011, 13, 54–58, doi:10.1208/s12248-010-9245-6.

92. Bryan, A.K.; Engler, A.; Gulati, A.; Manalis, S.R. Continuous and Long-Term Volume Measurements with a Commercial Coulter Counter. PLoS One 2012, 7, doi:10.1371/journal.pone.0029866.

93. Hassan, P.A.; Rana, S.; Verma, G. Making Sense of Brownian Motion: Colloid Characterization by Dynamic Light Scattering. Langmuir 2015, 31, 3–12, doi:10.1021/la501789z.

94. Minton, A.P. Recent Applications of Light Scattering Measurement in the Biological and Biopharmaceutical Sciences. Anal Biochem 2016, 501, 4–22, doi:10.1016/j.ab.2016.02.007.

95. Abenojar, E.C.; Bederman, I.; de Leon, A.C.; Zhu, J.; Hadley, J.; Kolios, M.C.; Exner, A.A. Theoretical and Experimental Gas Volume Quantification of Micro-and Nanobubble Ultrasound Contrast Agents. Pharmaceutics 2020, 12, doi:10.3390/pharmaceutics12030208.

96. Filipe, V.; Hawe, A.; Jiskoot, W. Critical Evaluation of Nanoparticle Tracking Analysis (NTA) by NanoSight for the Measurement of Nanoparticles and Protein Aggregates. Pharm Res 2010, 27, 796–810, doi:10.1007/s11095-010-0073-2.

97. Hernandez, C.; Abenojar, E.C.; Hadley, J.; De Leon, A.C.; Coyne, R.; Perera, R.; Gopalakrishnan, R.; Basilion, J.P.; Kolios, M.C.; Exner, A.A. Sink or Float? Characterization of Shell-Stabilized Bulk Nanobubbles Using a Resonant Mass Measurement Technique. Nanoscale 2019, 11, 851–855, doi:10.1039/c8nr08763f.

98. Tu, J.; Swalwell, J.E.; Giraud, D.; Cui, W.; Chen, W.; Matula, T.J. Microbubble Sizing and Shell Characterization Using Flow Cytometry. IEEE Trans Ultrason Ferroelectr Freq Control 2011, 58, 955–963, doi:10.1109/TUFFC.2011.1896.

99. Hall, R.L.; Juan-Sing, Z.D.; Hoyt, K.; Sirsi, S.R. Formulation and Characterization of Chemically Cross-Linked Microbubble Clusters. Langmuir 2019, 35, 10977–10986, doi:10.1021/acs.langmuir.9b00475.

100. Manta, S.; Renault, G.; Delalande, A.; Couture, O.; Lagoutte, I.; Seguin, J.; Lager, F.; Houzé, P.; Midoux, P.; Bessodes, M.; et al. Cationic Microbubbles and Antibiotic-Free Miniplasmid for Sustained Ultrasound–Mediated Transgene Expression in Liver. Journal of Controlled Release 2017, 262, 170–181, doi:10.1016/j.jconrel.2017.07.015.

101. Owen, J.; Stride, E. Technique for the Characterization of Phospholipid Microbubbles Coatings by Transmission Electron Microscopy. Ultrasound Med Biol 2015, 41, 3253–3258, doi:10.1016/j.ultrasmedbio.2015.07.024.

102. Lytra, A.; Sboros, V.; Giannakopoulos, A.; Pelekasis, N. Modeling Atomic Force Microscopy and Shell Mechanical Properties Estimation of Coated Microbubbles. Soft Matter 2020, 16, 4661–4681, doi:10.1039/d0sm00300j.

103. Uddin, M.H.; Tan, S.Y.; Dagastine, R.R. Novel Characterization of Microdrops and Microbubbles in Emulsions and Foams Using Atomic Force Microscopy. Langmuir 2011, 27, 2536–2544, doi:10.1021/la104458z.

104. Shafi, A.S.; McClements, J.; Albaijan, I.; Abou-Saleh, R.H.; Moran, C.; Koutsos, V. Probing Phospholipid Microbubbles by Atomic Force Microscopy to Quantify Bubble Mechanics and Nanostructural Shell Properties. Colloids Surf B Biointerfaces 2019, 181, 506–515, doi:10.1016/j.colsurfb.2019.04.062.

105. Fernandez-Sendin, M.; Tenesaca, S.; Vasquez, M.; Aranda, F.; Berraondo, P. Production and Use of Adeno-Associated Virus Vectors as Tools for Cancer Immunotherapy. In Methods in Enzymology; Academic Press Inc., 2020; Vol. 635, pp. 185–203 ISBN 9780128186770.

106. Stavarache, M.A.; Petersen, N.; Jurgens, E.M.; Milstein, E.R.; Rosenfeld, Z.B.; Ballon, D.J.; Kaplitt, M.G. Safe and Stable Noninvasive Focal Gene Delivery to the Mammalian Brain Following Focused Ultrasound. J Neurosurg 2019, 130, 989–998, doi:10.3171/2017.8.JNS17790.

107. Shchaslyvyi, A.Y.; Antonenko, S. V.; Tesliuk, M.G.; Telegeev, G.D. Current State of Human Gene Therapy: Approved Products and Vectors. Pharmaceuticals 2023, 16, doi:10.3390/ph16101416.

108. Faure, M.; Rabourdin-Combe, C. Innate Immunity Modulation in Virus Entry. Curr Opin Virol 2011, 1, 6–12, doi:10.1016/j.coviro.2011.05.013.

109. Rogers, G.L.; Martino, A.T.; Aslanidi, G. V.; Jayandharan, G.R.; Srivastava, A.; Herzog, R.W. Innate Immune Responses to AAV Vectors. Front Microbiol 2011, 2, doi:10.3389/fmicb.2011.00194.

110. Duan, D. Lethal Immunotoxicity in High-Dose Systemic AAV Therapy. Molecular Therapy 2023, 31, 3123–3126, doi:10.1016/j.ymthe.2023.10.015.

111. Lundstrom, K. Viral Vectors in Gene Therapy: Where Do We Stand in 2023? Viruses 2023, 15, doi:10.3390/v15030698.

112. Ricobaraza, A.; Gonzalez-Aparicio, M.; Mora-Jimenez, L.; Lumbreras, S.; Hernandez-Alcoceba, R. High-Capacity Adenoviral Vectors: Expanding the Scope of Gene Therapy. Int J Mol Sci 2020, 21.

113. Crystal, R.G. Adenovirus: The First Effective in Vivo Gene Delivery Vector. Hum Gene Ther 2014, 25, 3–11, doi:10.1089/hum.2013.2527.

114. Sterman, D.H.; Alley, E.; Stevenson, J.P.; Friedberg, J.; Metzger, S.; Recio, A.; Moon, E.K.; Haas, A.R.; Vachani, A.; Katz, S.I.; et al. Pilot and Feasibility Trial Evaluating Immuno-Gene Therapy of Malignant Mesothelioma Using Intrapleural Delivery of Adenovirus-IFNa Combined with Chemotherapy. Clinical Cancer Research 2016, 22, 3791–3800, doi:10.1158/1078-0432.CCR-15-2133.

115. Lesbats, P.; Engelman, A.N.; Cherepanov, P. Retroviral DNA Integration. Chem Rev 2016, 116, 12730–12757, doi:10.1021/acs.chemrev.6b00125.

116. Wang, Y.; Shao, W. Innate Immune Response to Viral Vectors in Gene Therapy. Viruses 2023, 15, 1801, doi:10.3390/v15091801.

117. Howe, S.J.; Mansour, M.R.; Schwarzwaelder, K.; Bartholomae, C.; Hubank, M.; Kempski, H.; Brugman, M.H.; Pike-Overzet, K.; Chatters, S.J.; De Ridder, D.; et al. Insertional Mutagenesis Combined with Acquired Somatic Mutations Causes Leukemogenesis Following Gene Therapy of SCID-X1 Patients. Journal of Clinical Investigation 2008, 118, 3143–3150, doi:10.1172/JCI35798.

118. Deyle, D.R.; Russell, D.W. Adeno-Associated Virus Vector Integration. Curr Opin Mol Ther. 2009, 11, 442–447.

119. Zhang, H.; Yang, B.; Mu, X.; Ahmed, S.S.; Su, Q.; He, R.; Wang, H.; Mueller, C.; Sena-Esteves, M.; Brown, R.; et al. Several RAAV Vectors Efficiently Cross the Blood-Brain Barrier and Transduce Neurons and Astrocytes in the Neonatal Mouse Central Nervous System. Molecular Therapy 2011, 19, 1440–1448, doi:10.1038/mt.2011.98.

120. Grieger, J.C.; Samulski, R.J. Packaging Capacity of Adeno-Associated Virus Serotypes: Impact of Larger Genomes on Infectivity and Postentry Steps. J Virol 2005, 79, 9933–9944, doi:10.1128/jvi.79.15.9933-9944.2005.

121. Hareendran, S.; Balakrishnan, B.; Sen, D.; Kumar, S.; Srivastava, A.; Jayandharan, G.R. Adeno-Associated Virus (AAV) Vectors in Gene Therapy: Immune Challenges and Strategies to Circumvent Them. Rev Med Virol 2013, 23, 399–413.

122. Hinderer, C.; Katz, N.; Buza, E.L.; Dyer, C.; Goode, T.; Bell, P.; Richman, L.K.; Wilson, J.M. Severe Toxicity in Nonhuman Primates and Piglets Following High-Dose Intravenous Administration of an Adeno-Associated Virus Vector Expressing Human SMN. Hum Gene Ther 2018, 29, 285–298, doi:10.1089/hum.2018.015.

123. Calcedo, R.; Vandenberghe, L.H.; Gao, G.; Lin, J.; Wilson, J.M. Worldwide Epidemiology of Neutralizing Antibodies to Adeno-Associated Viruses. Journal of Infectious Diseases 2009, 199, 381–390, doi:10.1086/595830.

124. Halbert, C.L.; Miller, A.D.; McNamara, S.; Emerson, J.; Gibson, R.L.; Ramsey, B.; Aitken, M.L. Prevalence of Neutralizing Antibodies against Adeno-Associated Virus (AAV) Types 2, 5, and 6 in Cystic Fibrosis and Normal Populations: Implications for Gene Therapy Using AAV Vectors. Hum Gene Ther 2006, 17, 440–447, doi:10.1089/hum.2006.17.440.

125. Chirmule, N.; Propert, K.J.; Magosin, S.A.; Qian, Y.; Qian, R.; Wilson, J.M. Immune Responses to Adenovirus and Adeno-Associated Virus in Humans; 1999; Vol. 6;.

126. Xicluna, R.; Avenel, A.; Vandamme, C.; Devaux, M.; Jaulin, N.; Couzinie, C.; Duff, J. LE; Charrier, A.; Guilbaud, M.; Adjali, O.; et al. Prevalence Study of Cellular Capsid-Specific Immune Responses to AAV1, 2, 4, 5, 8, 9 and Rh10 Reveals Particular Features for AAV9. Hum Gene Ther 2024, 35, 355–364, doi:10.1101/2023.12.20.570598.

127. Tatsis, N.; Ertl, H.C.J. Adenoviruses as Vaccine Vectors. Molecular Therapy 2004, 10, 616–629.

128. Zhang, H.; Yang, B.; Mu, X.; Ahmed, S.S.; Su, Q.; He, R.; Wang, H.; Mueller, C.; Sena-Esteves, M.; Brown, R.; et al. Several RAAV Vectors Efficiently Cross the Blood-Brain Barrier and Transduce Neurons and Astrocytes in the Neonatal Mouse Central Nervous System. Molecular Therapy 2011, 19, 1440–1448, doi:10.1038/mt.2011.98.

129. Park, K.; Kim, W.-J.; Cho, Y.-H.; Lee, Y.-I.; Lee, H.; Jeong, S.; Cho, E.-S.; Chang, S.-I.; Moon, S.-K.; Kang, B.-S.; et al. Cancer Gene Therapy Using Adeno-Associated Virus Vectors; 2008; Vol. 13;.

130. Kieu, T.C.; Look, K. Cost-Effectiveness of a Hypothetical Gene Therapy for Alzheimer's Disease: A Markov Simulation Analysis. Innov Pharm 2023, 14, 3, doi:10.24926/iip.v14i3.5500.

131. Taghdiri, M.; Mussolino, C. Viral and Non-Viral Systems to Deliver Gene Therapeutics to Clinical Targets. Int J Mol Sci 2024, 25, doi:10.3390/ijms25137333.

132. Touchard, E.; Heiduschka, P.; Berdugo, M.; Kowalczuk, L.; Bigey, P.; Chahory, S.; Gandolphe, C.; Jeanny, J.C.; Behar-Cohen, F. Non-Viral Gene Therapy for GDNF Production in RCS Rat: The Crucial Role of the Plasmid Dose. Gene Ther 2012, 19, 886–898, doi:10.1038/gt.2011.154.

133. Zhang, H.; Vandesompele, J.; Braeckmans, K.; De Smedt, S.C.; Remaut, K. Nucleic Acid Degradation as Barrier to Gene Delivery: A Guide to Understand and Overcome Nuclease Activity. Chem Soc Rev 2023, 53, 317–360, doi:10.1039/d3cs00194f.

134. Tros de Ilarduya, C.; Sun, Y.; Düzgüneş, N. Gene Delivery by Lipoplexes and Polyplexes. European Journal of Pharmaceutical Sciences 2010, 40, 159–170, doi:10.1016/j.ejps.2010.03.019.

135. Rezaee, M.; Oskuee, R.K.; Nassirli, H.; Malaekeh-Nikouei, B. Progress in the Development of Lipopolyplexes as Efficient Non-Viral Gene Delivery Systems. Journal of Controlled Release 2016, 236, 1–14, doi:10.1016/j.jconrel.2016.06.023.

136. Liu, J.; Jiang, X.; Xu, L.; Wang, X.; Hennink, W.E.; Zhuo, R. Novel Reduction-Responsive Cross-Linked Polyethylenimine Derivatives by Click Chemistry for Nonviral Gene Delivery. Bioconjug Chem 2010, 21, 1827–1835, doi:10.1021/bc100191r.

137. Wang, H.; Wang, S.; Su, H.; Chen, K.J.; Armijo, A.L.; Lin, W.Y.; Wang, Y.; Sun, J.; Kamei, K.I.; Czernin, J.; et al. A Supramolecular Approach for Preparation of Size-Controlled Nanoparticles. Angewandte Chemie - International Edition 2009, 48, 4344–4348, doi:10.1002/anie.200900063.

138. Shim, M.S.; Kwon, Y.J. Controlled Delivery of Plasmid DNA and SiRNA to Intracellular Targets Using Ketalized Polyethylenimine. Biomacromolecules 2008, 9, 444–455, doi:10.1021/bm7007313.

139. Gonçalves, C.; Gross, F.; Guégan, P.; Cheradame, H.; Midou, P. A Robust Transfection Reagent for the Transfection of CHO and HEK293 Cells and Production of Recombinant Proteins and Lentiviral Particles - PTG1. Biotechnol J 2014, 9, 1380–1388, doi:10.1002/biot.201400324.

140. Zhou, J.; Ma, S.; Zhang, Y.; He, Y.; Yang, J.; Zhang, H.; Luo, K.; Gu, Z. Virus-Inspired Mimics: Dual-PH-Responsive Modular Nanoplatforms for Programmable Gene Delivery without DNA Damage with the Assistance of Light. ACS Appl Mater Interfaces 2020, 12, 22519–22533, doi:10.1021/acsami.0c03486.

141. Bus, T.; Englert, C.; Reifarth, M.; Borchers, P.; Hartlieb, M.; Vollrath, A.; Hoeppener, S.; Traeger, A.; Schubert, U.S. 3rd Generation Poly(Ethylene Imine)s for Gene Delivery. J Mater Chem B 2017, 5, 1258–1274, doi:10.1039/c6tb02592g.

142. Germershaus, O.; Merdan, T.; Bakowsky, U.; Behe, M.; Kissel, T. Trastuzumab-Polyethylenimine-Polyethylene Glycol Conjugates for Targeting Her2-Expressing Tumors. Bioconjug Chem 2006, 17, 1190–1199, doi:10.1021/bc0601119.

143. Hald Albertsen, C.; Kulkarni, J.A.; Witzigmann, D.; Lind, M.; Petersson, K.; Simonsen, J.B. The Role of Lipid Components in Lipid Nanoparticles for Vaccines and Gene Therapy. Adv Drug Deliv Rev 2022, 188, doi:10.1016/j.addr.2022.114416.

144. Gonçalves, C.; Akhter, S.; Pichon, C.; Midoux, P. Intracellular Availability of PDNA and MRNA after Transfection: A Comparative Study among Polyplexes, Lipoplexes, and Lipopolyplexes. Mol Pharm 2016, 13, 3153–3163, doi:10.1021/acs.molpharmaceut.6b00376.

145. Van De Wetering, P.; Moret, E.E.; Schuurmans-Nieuwenbroek, N.M.E.; Van Steenbergen, M.J.; Hennink, W.E. Structure-Activity Relationships of Water-Soluble Cationic Methacrylate/Methacrylamide Polymers for Nonviral Gene Delivery. Bioconjug Chem 1999, 10, 589–597, doi:10.1021/bc980148w.

146. Yang, S.; May, S. Release of Cationic Polymer-DNA Complexes from the Endosome: A Theoretical Investigation of the Proton Sponge Hypothesis. Journal of Chemical Physics 2008, 129, doi:10.1063/1.3009263.

147. Leung, A.K.K.; Tam, Y.Y.C.; Chen, S.; Hafez, I.M.; Cullis, P.R. Microfluidic Mixing: A General Method for Encapsulating Macromolecules in Lipid Nanoparticle Systems. Journal of Physical Chemistry B 2015, 119, 8698–8706, doi:10.1021/acs.jpcb.5b02891.

148. Rodrigueza, W. V; Pritchard, H.; Hope, M.J. The Influence of Size and Composition on the Cholesterol Mobilizing Properties of Liposomes in Vivo; 1993;

149. Semple, S.C.; Chonn, A.; Cullis, P.R. Influence of Cholesterol on the Association of Plasma Proteins with Liposomes †; 1996;

150. Krause, M.R.; Regen, S.L. The Structural Role of Cholesterol in Cell Membranes: From Condensed Bilayers to Lipid Rafts. Acc Chem Res 2014, 47, 3512–3521, doi:10.1021/ar500260t.

151. Di, J.; Du, Z.; Wu, K.; Jin, S.; Wang, X.; Li, T.; Xu, Y. Biodistribution and Non-Linear Gene Expression of MRNA LNPs Affected by Delivery Route and Particle Size. Pharm Res 2021, doi:10.1007/s11095-022-03166-5/Published.

152. Liu, B.; Sajiki, Y.; Sridharan, A.; Stuart, W.; Cui, X.; Siefert, M.; Araki, K.; Ziady, A.; Shi, D.; Whitsett, J.A.; et al. PBAE-PEG Based Lipid Nanoparticles for Lung Cell-Specific Gene Delivery 2024.

153. Tuma, J.; Chen, Y.J.; Collins, M.G.; Paul, A.; Li, J.; Han, H.; Sharma, R.; Murthy, N.; Lee, H.Y. Lipid Nanoparticles Deliver MRNA to the Brain after an Intracerebral Injection. Biochemistry 2023, 62, 3533–3547, doi:10.1021/acs.biochem.3c00371.

154. Ogawa, K.; Kato, N.; Yoshida, M.; Hiu, T.; Matsuo, T.; Mizukami, S.; Omata, D.; Suzuki, R.; Maruyama, K.; Mukai, H.; et al. Focused Ultrasound/Microbubbles-Assisted BBB Opening Enhances LNP-Mediated MRNA Delivery to Brain. Journal of Controlled Release 2022, 348, 34–41, doi:10.1016/J.JCONREL.2022.05.042.

155. Khare, P.; Edgecomb, S.X.; Hamadani, C.M.; Tanner, E.E.L.; S Manickam, D. Lipid Nanoparticle-Mediated Drug Delivery to the Brain. Adv Drug Deliv Rev 2023, 197.

156. Oda, Y.; Kumagai, Y.; Kanai, M.; Iwama, Y.; Okura, I.; Minamida, T.; Yagi, Y.; Kurosawa, T.; Greener, B.; Zhang, Y.; et al. Immunogenicity and Safety of a Booster Dose of a Self-Amplifying RNA COVID-19 Vaccine (ARCT-154) versus BNT162b2 MRNA COVID-19 Vaccine: A Double-

Blind, Multicentre, Randomised, Controlled, Phase 3, Non-Inferiority Trial. Lancet Infect Dis 2024, 24, 351–360, doi:10.1016/S1473-3099(23)00650-3.

157. Baden, L.R.; El Sahly, H.M.; Essink, B.; Kotloff, K.; Frey, S.; Novak, R.; Diemert, D.; Spector, S.A.; Rouphael, N.; Creech, C.B.; et al. Efficacy and Safety of the MRNA-1273 SARS-CoV-2 Vaccine. New England Journal of Medicine 2021, 384, 403–416, doi:10.1056/nejmoa2035389.

158. Polack, F.P.; Thomas, S.J.; Kitchin, N.; Absalon, J.; Gurtman, A.; Lockhart, S.; Perez, J.L.; Pérez Marc, G.; Moreira, E.D.; Zerbini, C.; et al. Safety and Efficacy of the BNT162b2 MRNA Covid-19 Vaccine. New England Journal of Medicine 2020, 383, 2603–2615, doi:10.1056/nejmoa2034577.

159. Bailey-Hytholt, C.M.; Ulinski, G.; Dugas, J.; Haines, M.; Lazebnik, M.; Piepenhagen, P.; Zarraga, I.E.; Bandekar, A. Intracellular Trafficking Kinetics of Nucleic Acid Escape from Lipid Nanoparticles via Fluorescence Imaging. Curr Pharm Biotechnol 2024, 25, 102–112, doi:10.2174/1389201024666230403094238.

160. Hughes, T.S.; Langer, S.J.; Johnson, K.W.; Chavez, R.A.; Watkins, L.R.; Milligan, E.D.; Leinwand, L.A. Intrathecal Injection of Naked Plasmid DNA Provides Long-Term Expression of Secreted Proteins. Molecular Therapy 2009, 17, 88–94, doi:10.1038/mt.2008.230.

161. Gray, S.J.; Foti, S.B.; Schwartz, J.W.; Bachaboina, L.; Taylor-Blake, B.; Coleman, J.; Ehlers, M.D.; Zylka, M.J.; McCown, T.J.; Samulski, R.J. Optimizing Promoters for Recombinant Adeno-Associated Virus-Mediated Gene Expression in the Peripheral and Central Nervous System Using Self-Complementary Vectors. Hum Gene Ther 2011, 22, 1143–1153, doi:10.1089/hum.2010.245.

162. Marro, B.S.; Grist, J.J.; Lane, T.E. Inducible Expression of CXCL1 within the Central Nervous System Amplifies Viral-Induced Demyelination. The Journal of Immunology 2016, 196, 1855–1864, doi:10.4049/jimmunol.1501802.

163. Hollidge, B.S.; Carroll, H.B.; Qian, R.; Fuller, M.L.; Giles, A.R.; Mercer, A.C.; Danos, O.; Liu, Y.; Bruder, J.T.; Smith, J.B. Kinetics and Durability of Transgene Expression after Intrastriatal Injection of AAV9 Vectors. Front Neurol 2022, 13, doi:10.3389/fneur.2022.1051559.

164. Nieuwenhuis, B.; Haenzi, B.; Hilton, S.; Carnicer-Lombarte, A.; Hobo, B.; Verhaagen, J.; Fawcett, J.W. Optimization of Adeno-Associated Viral Vector-Mediated Transduction of the Corticospinal Tract: Comparison of Four Promoters. Gene Ther 2021, 28, 56–74, doi:10.1038/s41434-020-0169-1.

165. Koh, W.; Park, Y.M.; Lee, S.E.; Lee, C.J. AAV-Mediated Astrocyte-Specific Gene Expression under Human ALDH1L1 Promoter in Mouse Thalamus. Exp Neurobiol 2017, 26, 350–361, doi:10.5607/en.2017.26.6.350.

166. Urnov, F.D. Genome Editing B.C. (Before CRISPR): Lasting Lessons from the "Old Testament." CRISPR J 2018, 1, 34–46, doi:10.1089/crispr.2018.29007.fyu.

167. Jinek, M.; Chylinski, K.; Fonfara, I.; Hauer, M.; Doudna, J.A.; Charpentier, E. A Programmable Dual-RNA–Guided DNA Endonuclease in Adaptive Bacterial Immunity. Science (1979) 2012, 337, 816–821, doi:10.1126/science.1225829.

168. Neldeborg, S.; Lin, L.; Stougaard, M.; Luo, Y. Rapid and Efficient Gene Deletion by CRISPR/Cas9. Methods in Molecular Biology 2019, 1961, 233–247, doi:10.1007/978-1-4939-9170-9_14.

169. Gillmore, J.D.; Gane, E.; Taubel, J.; Kao, J.; Fontana, M.; Maitland, M.L.; Seitzer, J.; O'Connell, D.; Walsh, K.R.; Wood, K.; et al. CRISPR-Cas9 In Vivo Gene Editing for Transthyretin Amyloidosis. New England Journal of Medicine 2021, 385, 493–502, doi:10.1056/nejmoa2107454.

170. Xu, W.; Jiang, X.; Huang, L. RNA Interference Technology. In Comprehensive Biotechnology; Elsevier, 2019; pp. 560–575.

171. Lam, J.K.W.; Chow, M.Y.T.; Zhang, Y.; Leung, S.W.S. SiRNA Versus MiRNA as Therapeutics for Gene Silencing. Mol Ther Nucleic Acids 2015, 4, e252, doi:10.1038/mtna.2015.23.

172. Moore, C.B.; Guthrie, E.H.; Huang, M.T.H.; Taxman, D.J. Short Hairpin RNA (ShRNA): Design, Delivery, and Assessment of Gene Knockdown. Methods Mol Biol 2010, 629, 141–158, doi:10.1007/978-1-60761-657-3_10.

173. Dhuri, K.; Bechtold, C.; Quijano, E.; Pham, H.; Gupta, A.; Vikram, A.; Bahal, R. Antisense Oligonucleotides: An Emerging Area in Drug Discovery and Development. J Clin Med 2020, 9, 2004, doi:10.3390/jcm9062004.

174. Erdos, J.; Wild, C. Mid- and Long-Term (at Least 12 Months) Follow-up of Patients with Spinal Muscular Atrophy (SMA) Treated with Nusinersen, Onasemnogene Abeparvovec, Risdiplam or Combination Therapies: A Systematic Review of Real-World Study Data. European Journal of Paediatric Neurology 2022, 39, 1–10, doi:10.1016/j.ejpn.2022.04.006.

175. Crivianu-Gaita, V.; Thompson, M. Aptamers, Antibody ScFv, and Antibody Fab' Fragments: An Overview and Comparison of Three of the Most Versatile Biosensor Biorecognition Elements. Biosens Bioelectron 2016, 85, 32–45, doi:10.1016/j.bios.2016.04.091.

176. Adachi, T.; Nakamura, Y. Aptamers: A Review of Their Chemical Properties and Modifications for Therapeutic Application. Molecules 2019, 24, 4229, doi:10.3390/molecules24234229.

177. Xu, X.; Tao, Y.; Gao, X.; Zhang, L.; Li, X.; Zou, W.; Ruan, K.; Wang, F.; Xu, G.L.; Hu, R. A CRISPR-Based Approach for Targeted DNA Demethylation. Cell Discov 2016, 2, doi:10.1038/celldisc.2016.9.

178. Kearns, N.A.; Pham, H.; Tabak, B.; Genga, R.M.; Silverstein, N.J.; Garber, M.; Maehr, R. Functional Annotation of Native Enhancers with a Cas9-Histone Demethylase Fusion. Nat Methods 2015, 12, 401–403, doi:10.1038/nmeth.3325.

179. Cano-Rodriguez, D.; Gjaltema, R.A.F.; Jilderda, L.J.; Jellema, P.; Dokter-Fokkens, J.; Ruiters, M.H.J.; Rots, M.G. Writing of H3K4Me3 Overcomes Epigenetic Silencing in a Sustained but Context-Dependent Manner. Nat Commun 2016, 7, doi:10.1038/ncomms12284.

180. Tian, M.; Liu, W.; Zhang, Q.; Huang, Y.; Li, W.; Wang, W.; Zhao, P.; Huang, S.; Song, Y.; Shereen, M.A.; et al. MYSM1 Represses Innate Immunity and Autoimmunity through Suppressing the CGAS-STING Pathway. Cell Rep 2020, 33, 108297, doi:10.1016/j.celrep.2020.108297.

181. Xiao, Q.; Guo, D.; Chen, S. Application of CRISPR/Cas9-Based Gene Editing in HIV-1/AIDS Therapy. Front Cell Infect Microbiol 2019, 9, doi:10.3389/fcimb.2019.00069.

182. Li, S.-D.; Huang, L. Stealth Nanoparticles: High Density but Sheddable PEG Is a Key for Tumor Targeting. Journal of Controlled Release 2010, 145, 178–181, doi:10.1016/j.jconrel.2010.03.016.

183. Mollé, L.M.; Smyth, C.H.; Yuen, D.; Johnston, A.P.R. Nanoparticles for Vaccine and Gene Therapy: Overcoming the Barriers to Nucleic Acid Delivery. WIREs Nanomedicine and Nanobiotechnology 2022, 14, doi:10.1002/wnan.1809.

184. Xiang, S.; Tong, H.; Shi, Q.; Fernandes, J.C.; Jin, T.; Dai, K.; Zhang, X. Uptake Mechanisms of Non-Viral Gene Delivery. Journal of Controlled Release 2012, 158, 371–378, doi:10.1016/j.jconrel.2011.09.093.

185. El-Sayed, A.; Harashima, H. Endocytosis of Gene Delivery Vectors: From Clathrin-Dependent to Lipid Raft-Mediated Endocytosis. Molecular Therapy 2013, 21, 1118–1130, doi:10.1038/mt.2013.54.

186. Akinc, A.; Querbes, W.; De, S.; Qin, J.; Frank-Kamenetsky, M.; Jayaprakash, K.N.; Jayaraman, M.; Rajeev, K.G.; Cantley, W.L.; Dorkin, J.R.; et al. Targeted Delivery of RNAi Therapeutics With Endogenous and Exogenous Ligand-Based Mechanisms. Molecular Therapy 2010, 18, 1357–1364, doi:10.1038/mt.2010.85.

187. Hoffmann, M.; Hersch, N.; Gerlach, S.; Dreissen, G.; Springer, R.; Merkel, R.; Csiszár, A.; Hoffmann, B. Complex Size and Surface Charge Determine Nucleic Acid Transfer by Fusogenic Liposomes. Int J Mol Sci 2020, 21, doi:10.3390/ijms21062244.

188. Rennick, J.J.; Johnston, A.P.R.; Parton, R.G. Key Principles and Methods for Studying the Endocytosis of Biological and Nanoparticle Therapeutics. Nat Nanotechnol 2021, 16, 266–276, doi:10.1038/s41565-021-00858-8.

189. Won, Y.-Y.; Sharma, R.; Konieczny, S.F. Missing Pieces in Understanding the Intracellular Trafficking of Polycation/DNA Complexes. Journal of Controlled Release 2009, 139, 88–93, doi:10.1016/j.jconrel.2009.06.031.

190. Selby, L.I.; Cortez-Jugo, C.M.; Such, G.K.; Johnston, A.P.R. Nanoescapology: Progress toward Understanding the Endosomal Escape of Polymeric Nanoparticles. WIREs Nanomedicine and Nanobiotechnology 2017, 9, doi:10.1002/wnan.1452.

191. Kessler, N.; Viehmann, S.F.; Krollmann, C.; Mai, K.; Kirschner, K.M.; Luksch, H.; Kotagiri, P.; Böhner, A.M.C.; Huugen, D.; de Oliveira Mann, C.C.; et al. Monocyte-Derived Macrophages Aggravate Pulmonary Vasculitis via CGAS/STING/IFN-Mediated Nucleic Acid Sensing. Journal of Experimental Medicine 2022, 219, doi:10.1084/jem.20220759.

192. Medina-Kauwe, L.K.; Xie, J.; Hamm-Alvarez, S. Intracellular Trafficking of Nonviral Vectors. Gene Ther 2005, 12, 1734–1751, doi:10.1038/sj.gt.3302592.

193. Zhang, S.; Gan, L.; Cao, F.; Wang, H.; Gong, P.; Ma, C.; Ren, L.; Lin, Y.; Lin, X. The Barrier and Interface Mechanisms of the Brain Barrier, and Brain Drug Delivery. Brain Res Bull 2022, 190, 69–83, doi:10.1016/j.brainresbull.2022.09.017.

194. Farquhar, M.G.; Palade, G.E. Junctional Complexes in Various Epithelia. J Cell Biol 1963, 375–412.

195. Heinemann, U.; Schuetz, A. Structural Features of Tight-Junction Proteins. Int J Mol Sci 2019, 20.

196. Sugiyama, S.; Sasaki, T.; Tanaka, H.; Yan, H.; Ikegami, T.; Kanki, H.; Nishiyama, K.; Beck, G.; Gon, Y.; Okazaki, S.; et al. The Tight Junction Protein Occludin Modulates Blood–Brain Barrier Integrity and Neurological Function after Ischemic Stroke in Mice. Sci Rep 2023, 13, doi:10.1038/s41598-023-29894-1.

197. Haseloff, R.F.; Dithmer, S.; Winkler, L.; Wolburg, H.; Blasig, I.E. Transmembrane Proteins of the Tight Junctions at the Blood–Brain Barrier: Structural and Functional Aspects. Semin Cell Dev Biol 2015, 38, 16–25, doi:10.1016/j.semcdb.2014.11.004.

198. Pardridge, W.M. The Blood-Brain Barrier: Bottleneck in Brain Drug Development. The American Society for Experimental NeuroTherapeutics 2005, 2, 3–14.

199. Fischer, H.; Gottschlich, R.; Seelig, A. Blood-Brain Barrier Permeation: Molecular Parameters Governing Passive Diffusion. J. Membrane Biol. 1998, 165, 201–211.

200. Citi, S. The Mechanobiology of Tight Junctions. Biophys Rev 2019, 11, 783–793, doi:10.1007/s12551-019-00582-7.

201. Hansson, E. Astroglia and Glutamate in Physiology and Pathology: Aspects on Glutamate Transport, Glutamate-Induced Cell Swelling and Gap-Junction Communication. Neurochem Int 2000, 37, 317–329, doi:10.1016/S0197-0186(00)00033-4.

202. Eng, M.E.; Imperio, G.E.; Bloise, E.; Matthews, S.G. ATP-Binding Cassette (ABC) Drug Transporters in the Developing Blood–Brain Barrier: Role in Fetal Brain Protection. Cellular and Molecular Life Sciences 2022, 79.

203. Masuda, M.; Nakai, E.; Mizutani, T. Study of Oxidized Lipids as Endogenous Substrates of P-Gp (ABCB1). Drug Metab Lett 2008, 2, 238–244, doi:10.2174/187231208786734139.

204. Shubbar, M.H.; Penny, J.I. Therapeutic Drugs Modulate ATP-Binding Cassette Transporter-Mediated Transport of Amyloid Beta(1–42) in Brain Microvascular Endothelial Cells. Eur J Pharmacol 2020, 874, 173009, doi:10.1016/j.ejphar.2020.173009.

205. Taskar, K.S.; Yang, X.; Neuhoff, S.; Patel, M.; Yoshida, K.; Paine, M.F.; Brouwer, K.L.R.; Chu, X.; Sugiyama, Y.; Cook, J.; et al. Clinical Relevance of Hepatic and Renal P-gp/BCRP Inhibition of Drugs: An International Transporter Consortium Perspective. Clin Pharmacol Ther 2022, 112, 573–592, doi:10.1002/cpt.2670.

206. Zheng, Y.; Chen, X.; Benet, L.Z. Reliability of In Vitro and In Vivo Methods for Predicting the Effect of P-Glycoprotein on the Delivery of Antidepressants to the Brain. Clin Pharmacokinet 2016, 55, 143–167.

207. Wu, J.-Q.; Shao, K.; Wang, X.; Wang, R.-Y.; Cao, Y.-H.; Yu, Y.-Q.; Lou, J.-N.; Chen, Y.-Q.; Zhao, H.-Z.; Zhang, Q.-Q.; et al. In Vitro and In Vivo Evidence for Amphotericin B as a P-Glycoprotein Substrate on the Blood-Brain Barrier. Antimicrob Agents Chemother 2014, 58, 4464–4469, doi:10.1128/AAC.02535-14.

208. Declèves, X.; Jacob, A.; Yousif, S.; Shawahna, R.; Potin, S.; Scherrmann, J.-M. Interplay of Drug Metabolizing CYP450 Enzymes and ABC Transporters in the Blood-Brain Barrier; 2011; Vol. 12;.

209. Sakakibara, Y.; Katoh, M.; Imai, K.; Kondo, Y.; Asai, Y.; Ikushiro, S.I.; Nadai, M. Expression of UGT1A Subfamily in Rat Brain. Biopharm Drug Dispos 2016, 314–319, doi:10.1002/bdd.2012.

210. Kliewer, S.A.; Goodwin, B.; Willson, T.M. The Nuclear Pregnane X Receptor: A Key Regulator of Xenobiotic Metabolism. Endocr Rev 2002, 23, 687–702, doi:10.1210/er.2001-0038.

211. Kort, A.; Van Hoppe, S.; Sparidans, R.W.; Wagenaar, E.; Beijnen, J.H.; Schinkel, A.H. Brain Accumulation of Ponatinib and Its Active Metabolite, N-Desmethyl Ponatinib, Is Limited by P-Glycoprotein (P-GP/ABCB1) and Breast Cancer Resistance Protein (BCRP/ABCG2). Mol Pharm 2017, 14, 3258–3268, doi:10.1021/acs.molpharmaceut.7b00257.

212. Bauer, M.; Zeitlinger, M.; Karch, R.; Matzneller, P.; Stanek, J.; Jäger, W.; Böhmdorfer, M.; Wadsak, W.; Mitterhauser, M.; Bankstahl, J.P.; et al. Pgp-Mediated Interaction between (R)-11CVerapamil and Tariquidar at the Human Blood-Brain Barrier: A Comparison with Rat Data. Clin Pharmacol Ther 2012, 91, 227–233, doi:10.1038/clpt.2011.217.

213. Sweeney, M.D.; Zhao, Z.; Montagne, A.; Nelson, A.R.; Zlokovic, B. V From Physiology to Disease and Back. Physiol Rev 2019, 99, 21–78, doi:10.1152/physrev.00050.2017.-The.

214. Barar, J.; Rafi, M.A.; Pourseif, M.M.; Omidi, Y. Blood-Brain Barrier Transport Machineries and Targeted Therapy of Brain Diseases. BioImpacts 2016, 6, 225–248, doi:10.15171/bi.2016.30.

215. Ramirez, S.H.; Andrews, A.M.; Paul, D.; Pachter, J.S. Extracellular Vesicles: Mediators and Biomarkers of Pathology along CNS Barriers. Fluids Barriers CNS 2018, 15, 19, doi:10.1186/s12987-018-0104-7.

216. Rufino-Ramos, D.; Albuquerque, P.R.; Carmona, V.; Perfeito, R.; Nobre, R.J.; Pereira de Almeida, L. Extracellular Vesicles: Novel Promising Delivery Systems for Therapy of Brain Diseases. Journal of Controlled Release 2017, 262, 247–258, doi:10.1016/j.jconrel.2017.07.001.

217. Zhou, K.; Han, J.; Wang, Y.; Zhang, Y.; Zhu, C. Routes of Administration for Adeno-Associated Viruses Carrying Gene Therapies for Brain Diseases. Front Mol Neurosci 2022, 15.

218. Daci, R.; Flotte, T.R. Delivery of Adeno-Associated Virus Vectors to the Central Nervous System for Correction of Single Gene Disorders. Int J Mol Sci 2024, 25, doi:10.3390/ijms25021050.

219. Pietersz, K.L.; Martier, R.M.; Baatje, M.S.; Liefhebber, J.M.; Brouwers, C.C.; Pouw, S.M.; Fokkert, L.; Lubelski, J.; Petry, H.; Martens, G.J.M.; et al. Transduction Patterns in the CNS Following Various Routes of AAV-5-Mediated Gene Delivery. Gene Ther 2021, 28, 435–446, doi:10.1038/s41434-020-0178-0.

220. Kaspar, B.K.; Erickson, D.; Schaffer, D.; Hinh, L.; Gage, F.H.; Peterson, D.A. Targeted Retrograde Gene Delivery for Neuronal Protection. Molecular Therapy 2002, 5, 50–56, doi:10.1006/mthe.2001.0520.

221. Boussicault, L.; Alves, S.; Lamazière, A.; Planques, A.; Heck, N.; Moumné, L.; Despres, G.; Bolte, S.; Hu, A.; Pagès, C.; et al. CYP46A1, the Rate-Limiting Enzyme for Cholesterol Degradation, Is Neuroprotective in Huntington's Disease. Brain 2016, 139, 953–970, doi:10.1093/brain/awv384.

222. Terse, P.S.; Kells, A.P.; Noker, P.; Wright, J.F.; Bankiewicz, K.S. Safety Assessment of AAV2-HGDNF Administered Via Intracerebral Injection in Rats for Treatment of Parkinson's Disease. Int J Toxicol 2021, 40, 4–14, doi:10.1177/1091581820966315.

223. Neuman, S.S.; Metzger, J.M.; Bondarenko, V.; Wang, Y.; Felton, J.; Levine, J.E.; Saha, K.; Gong, S.; Emborg, M.E. Striatonigral Distribution of a Fluorescent Reporter Following Intracerebral Delivery of Genome Editors. Front Bioeng Biotechnol 2023, 11, doi:10.3389/fbioe.2023.1237613.

224. Michel Zerah; Françoise Piguet; Marie-Anne Colle; Sylvie Raoul; Jack-Yves Deschamps; Johan Deniaud; Patrick Aubourg Intracerebral Gene Therapy Using AAVrh.10-HARSA Recombinant Vector to Treat Patients with early-Onset Forms of Metachromatic Leukodystrophy: Preclinical Feasibility and Safety in Non-Human Primates. Hum Gene Ther Clin Dev 2015.

225. McPhee, S.W.J.; Janson, C.G.; Li, C.; Samulski, R.J.; Camp, A.S.; Francis, J.; Shera, D.; Lioutermann, L.; Feely, M.; Freese, A.; et al. Immune Responses to AAV in a Phase I Study for Canavan Disease. Journal of Gene Medicine 2006, 8, 577–588, doi:10.1002/jgm.885.

226. Kumar, S.R.P.; Duan, D.; Herzog, R.W. Immune Responses to Muscle-Directed Adeno-Associated Viral Gene Transfer in Clinical Studies. Hum Gene Ther 2023, 34, 365–371, doi:10.1089/hum.2023.056.

227. Muhuri, M.; Zhan, W.; Maeda, Y.; Li, J.; Lotun, A.; Chen, J.; Sylvia, K.; Dasgupta, I.; Arjomandnejad, M.; Nixon, T.; et al. Novel Combinatorial MicroRNA-Binding Sites in AAV Vectors Synergistically Diminish Antigen Presentation and Transgene Immunity for Efficient and Stable Transduction. Front Immunol 2021, 12, doi:10.3389/fimmu.2021.674242.

228. Umemura, Y.; Junck, L.; Leung, D.; Orringer, (D; Varela, M.L.; West, M.E.J.; Faisal, S.M.; Comba, A.; Heth, J.; Hervey-Jumper, S.; et al. Combined Cytotoxic and Immune-Stimulatory Gene Therapy for Primary Adult High-Grade Glioma: A Phase 1, First-in-Human Trial; 2023; Vol. 24;.

229. Corti, M.; Byrne, B.J.; Gessler, D.J.; Thompson, G.; Norman, S.; Lammers, J.; Coleman, K.E.; Liberati, C.; Elder, M.E.; Escolar, M.L.; et al. Adeno-Associated Virus-Mediated Gene Therapy in a Patient with Canavan Disease Using Dual Routes of Administration and Immune Modulation. Mol Ther Methods Clin Dev 2023, 30, 303–314, doi:10.1016/j.omtm.2023.06.001.

230. Leone, P.; Shera, D.; McPhee, S.W.J.; Francis, J.S.; Kolodny, E.H.; Bilaniuk, L.T.; Wang, D.J.; Assadi, M.; Goldfarb, O.; Goldman, H.W.; et al. Long-Term Follow-up after Gene Therapy for Canavan Disease. Sci Transl Med 2012, 4, doi:10.1126/scitranslmed.3003454.

231. Christine, C.W.; Richardson, R.M.; van Laar, A.D.; Thompson, M.E.; Fine, E.M.; Khwaja, O.S.; Li, C.; Liang, G.S.; Meier, A.; Roberts, E.W.; et al. Safety of AADC Gene Therapy for Moderately Advanced Parkinson Disease: Three-Year Outcomes from the PD-1101 Trial. Neurology 2022, 98, E40–E50, doi:10.1212/WNL.0000000000012952.

232. Christine, C.W.; Starr, P.A.; Larson, P.S.; Eberling, J.L.; Jagust, W.J.; Hawkins, R.A.; Vanbrocklin, H.F.; Wright, J.F.; Bankiewicz, K.S.; Aminoff, M.J. Safety and Tolerability of Putaminal AADC Gene Therapy for Parkinson Disease; 2009;

233. Bugiani, M.; Abbink, T.E.M.; Edridge, A.W.D.; van der Hoek, L.; Hillen, A.E.J.; van Til, N.P.; Hu-A-Ng, G. V.; Breur, M.; Aiach, K.; Drevot, P.; et al. Focal Lesions Following Intracerebral

Gene Therapy for Mucopolysaccharidosis IIIA. Ann Clin Transl Neurol 2023, 10, 904–917, doi:10.1002/acn3.51772.

234. Xin Chen; Thomas Dong; Yuhui Hu; J. Gray Intrathecal AAV9/AP4M1 Gene Therapy for Hereditary Paraplegia 50 Shows Safety and efficacy in Preclinical Studies. Journal of Clinical Investigation 2023, 133, doi:10.1172/JCI170226.

235. Hudry, E.; Aihara, F.; Meseck, E.; Mansfield, K.; McElroy, C.; Chand, D.; Tukov, F.F.; Penraat, K. Liver Injury in Cynomolgus Monkeys Following Intravenous and Intrathecal ScAAV9 Gene Therapy Delivery. Molecular Therapy 2023, 31, 2999–3014, doi:10.1016/j.ymthe.2023.07.020.

236. Bharucha-Goebel, D.X.; Todd, J.J.; Saade, D.; Norato, G.; Jain, M.; Lehky, T.; Bailey, R.M.; Chichester, J.A.; Calcedo, R.; Armao, D.; et al. Intrathecal Gene Therapy for Giant Axonal Neuropathy. New England Journal of Medicine 2024, 390, 1092–1104, doi:10.1056/nejmoa2307952.

237. Finkel, R.S.; Darras, B.T.; Mendell, J.R.; Day, J.W.; Kuntz, N.L.; Connolly, A.M.; Zaidman, C.M.; Crawford, T.O.; Butterfield, R.J.; Shieh, P.B.; et al. Intrathecal Onasemnogene Abeparvovec for Sitting, Nonambulatory Patients with Spinal Muscular Atrophy: Phase I Ascending-Dose Study (STRONG). J Neuromuscul Dis 2023, 10, 389–404, doi:10.3233/JND-221560.

238. Cárdenas, G.; Chávez-Canales, M.; Espinosa, A.M.; Jordán-Ríos, A.; Malagon, D.A.; Murillo, M.F.M.; Araujo, L.V.T.; Campos, R.L.B.; Wong-Chew, R.M.; González, L.E.R.; et al. Intranasal Versus Intravenous Dexamethasone to Treat Hospitalized COVID-19 Patients: A Randomized Multicenter Clinical Trial. Arch Med Res 2024, 55, doi:10.1016/j.arcmed.2024.102960.

239. Aguilera, Y.; Mellado-Damas, N.; Olmedo-Moreno, L.; López, V.; Panadero-Morón, C.; Benito, M.; Guerrero-Cázares, H.; Márquez-Vega, C.; Martín-Montalvo, A.; Capilla-González, V. Preclinical Safety Evaluation of Intranasally Delivered Human Mesenchymal Stem Cells in Juvenile Mice. Cancers (Basel) 2021, 13, 1–18, doi:10.3390/cancers13051169.

240. Fatani, A.S.; Schätzlein, A.G.; Uchegbu, I.F. Targeting Intracranial Tumours with a Combination of RNA and Chemotherapy. Pharmaceutics 2024, 16, 829, doi:10.3390/pharmaceutics16060829.

241. Belur, L.R.; Temme, A.; Podetz-Pedersen, K.M.; Riedl, M.; Vulchanova, L.; Robinson, N.; Hanson, L.R.; Kozarsky, K.F.; Orchard, P.J.; Frey, W.H.; et al. Intranasal Adeno-Associated Virus Mediated Gene Delivery and Expression of Human Iduronidase in the Central Nervous

System: A Noninvasive and Effective Approach for Prevention of Neurologic Disease in Mucopolysaccharidosis Type i. Hum Gene Ther 2017, 28, 576–587, doi:10.1089/hum.2017.187.

242. Belur, L.R.; Romero, M.; Lee, J.; Podetz-Pedersen, K.M.; Nan, Z.; Riedl, M.S.; Vulchanova, L.; Kitto, K.F.; Fairbanks, C.A.; Kozarsky, K.F.; et al. Comparative Effectiveness of Intracerebroventricular, Intrathecal, and Intranasal Routes of AAV9 Vector Administration for Genetic Therapy of Neurologic Disease in Murine Mucopolysaccharidosis Type I. Front Mol Neurosci 2021, 14, doi:10.3389/fnmol.2021.618360.

243. Suberi, A.; Grun, M.K.; Mao, T.; Israelow, B.; Reschke, M.; Grundler, J.; Akhtar, L.; Lee, T.; Shin, K.; Piotrowski-Daspit, A.S.; et al. Polymer Nanoparticles Deliver MRNA to the Lung for Mucosal Vaccination. Sci Transl Med 2023, 15, doi:10.1126/scitranslmed.abq0603.

244. Kehagia, E.; Papakyriakopoulou, P.; Valsami, G. Advances in Intranasal Vaccine Delivery: A Promising Non-Invasive Route of Immunization. Vaccine 2023, 41, 3589–3603.

245. Fatani, A.S.; Petkova, A.; Schatzlein, A.G.; Uchegbu, I.F. Dose-Dependent Delivery of Genes to the Cerebral Cortex via the Nasal Route. Int J Pharm 2023, 644, doi:10.1016/j.ijpharm.2023.123343.

246. Mascotte-Cruz, J.U.; Vera, A.; Leija, L.; Lopez-Salas, F.E.; Gradzielski, M.; Koetz, J.; Gatica-García, B.; Rodríguez-Oviedo, C.P.; Valenzuela-Arzeta, I.E.; Escobedo, L.; et al. Focused Ultrasound on the Substantia Nigra Enables Safe Neurotensin-Polyplex Nanoparticle-Mediated Gene Delivery to Dopaminergic Neurons Intranasally and by Blood Circulation. Discover Nano 2024, 19, doi:10.1186/s11671-024-04005-9.

247. Jung, O.; Thomas, A.; Burks, S.R.; Dustin, M.L.; Frank, J.A.; Ferrer, M.; Stride, E. Neuroinflammation Associated with Ultrasound-Mediated Permeabilization of the Blood–Brain Barrier. Trends Neurosci 2022, 45, 459–470.

248. Serguera, C.; Bemelmans, A.P. Gene Therapy of the Central Nervous System: General Considerations on Viral Vectors for Gene Transfer into the Brain. Rev Neurol (Paris) 2014, 170, 727–738, doi:10.1016/j.neurol.2014.09.004.

249. Felix, M.S.; Borloz, E.; Metwally, K.; Dauba, A.; Larrat, B.; Matagne, V.; Ehinger, Y.; Villard, L.; Novell, A.; Mensah, S.; et al. Ultrasound-Mediated Blood-Brain Barrier Opening Improves Whole Brain Gene Delivery in Mice. Pharmaceutics 2021, 13, doi:10.3390/pharmaceutics13081245.

250. Day, J.W.; Finkel, R.S.; Chiriboga, C.A.; Connolly, A.M.; Crawford, T.O.; Darras, B.T.; Iannaccone, S.T.; Kuntz, N.L.; Peña, L.D.M.; Shieh, P.B.; et al. Onasemnogene Abeparvovec Gene Therapy for Symptomatic Infantile-Onset Spinal Muscular Atrophy in Patients with Two Copies of SMN2 (STR1VE): An Open-Label, Single-Arm, Multicentre, Phase 3 Trial; 2021; Vol. 20;.

251. Mercuri, E.; Muntoni, F.; Baranello, G.; Masson, R.; Boespflug-Tanguy, O.; Bruno, C.; Corti, S.; Daron, A.; Deconinck, N.; Servais, L.; et al. Onasemnogene Abeparvovec Gene Therapy for Symptomatic Infantile-Onset Spinal Muscular Atrophy Type 1 (STR1VE-EU): An Open-Label, Single-Arm, Multicentre, Phase 3 Trial; 2021;

252. Thomsen, G.; Burghes, A.H.M.; Hsieh, C.; Do, J.; Chu, B.T.T.; Perry, S.; Barkho, B.; Kaufmann, P.; Sproule, D.M.; Feltner, D.E.; et al. Biodistribution of Onasemnogene Abeparvovec DNA, MRNA and SMN Protein in Human Tissue. Nat Med 2021, 27, 1701–1711, doi:10.1038/s41591-021-01483-7.

253. Guillou, J.; de Pellegars, A.; Porcheret, F.; Frémeaux-Bacchi, V.; Allain-Launay, E.; Debord, C.; Denis, M.; Péréon, Y.; Barnérias, C.; Desguerre, I.; et al. Fatal Thrombotic Microangiopathy Case Following Adeno-Associated Viral SMN Gene Therapy. Blood Adv 2022, 6, 4266–4270, doi:10.1182/bloodadvances.2021006419.

254. Fernandes, B.D.; Krug, B.C.; Rodrigues, F.D.A.; Cirilo, H.N.C.; Borges, S.S.; Schwartz, I.V.D.; Probst, L.F.; Zimmermann, I. Efficacy and Safety of Onasemnogene Abeparvovec for the Treatment of Patients with Spinal Muscular Atrophy Type 1: A Systematic Review with Meta-Analysis. PLoS One 2024, 19, doi:10.1371/journal.pone.0302860.

255. Deverman, B.E.; Pravdo, P.L.; Simpson, B.P.; Kumar, S.R.; Chan, K.Y.; Banerjee, A.; Wu, W.L.; Yang, B.; Huber, N.; Pasca, S.P.; et al. Cre-Dependent Selection Yields AAV Variants for Widespread Gene Transfer to the Adult Brain. Nat Biotechnol 2016, 34, 204–209, doi:10.1038/nbt.3440.

256. Chan, K.Y.; Jang, M.J.; Yoo, B.B.; Greenbaum, A.; Ravi, N.; Wu, W.L.; Sánchez-Guardado, L.; Lois, C.; Mazmanian, S.K.; Deverman, B.E.; et al. Engineered AAVs for Efficient Noninvasive Gene Delivery to the Central and Peripheral Nervous Systems. Nat Neurosci 2017, 20, 1172–1179, doi:10.1038/nn.4593.

257. Matsuzaki, Y.; Konno, A.; Mochizuki, R.; Shinohara, Y.; Nitta, K.; Okada, Y.; Hirai, H. Intravenous Administration of the Adeno-Associated Virus-PHP.B Capsid Fails to Upregulate

Transduction Efficiency in the Marmoset Brain. Neurosci Lett 2018, 665, 182–188, doi:10.1016/j.neulet.2017.11.049.

258. Hordeaux, J.; Wang, Q.; Katz, N.; Buza, E.L.; Bell, P.; Wilson, J.M. The Neurotropic Properties of AAV-PHP.B Are Limited to C57BL/6J Mice. Molecular Therapy 2018, 26, 664–668.

259. Mathiesen, S.N.; Lock, J.L.; Schoderboeck, L.; Abraham, W.C.; Hughes, S.M. CNS Transduction Benefits of AAV-PHP.EB over AAV9 Are Dependent on Administration Route and Mouse Strain. Mol Ther Methods Clin Dev 2020, 19, 447–458, doi:10.1016/j.omtm.2020.10.011.

260. Dayton, R.D.; Grames, M.S.; Klein, R.L. More Expansive Gene Transfer to the Rat CNS: AAV PHP.EB Vector Dose–Response and Comparison to AAV PHP.B. Gene Ther 2018, 25, 392–400, doi:10.1038/s41434-018-0028-5.

261. Khodabakhshi, Z.; Hosseinkhah, N.; Ghadiri, H. Pulsating Microbubble in a Micro-Vessel and Mechanical Effect on Vessel Wall: A Simulation Study. J Biomed Phys Eng 2021, 11, 629–640, doi:10.31661/jbpe.v0i0.1131.

262. Burgess, A.; Huang, Y.; Querbes, W.; Sah, D.W.; Hynynen, K. Focused Ultrasound for Targeted Delivery of SiRNA and Efficient Knockdown of Htt Expression. Journal of Controlled Release 2012, 163, 125–129, doi:10.1016/j.jconrel.2012.08.012.

263. Goutal, S.; Gerstenmayer, M.; Auvity, S.; Caillé, F.; Mériaux, S.; Buvat, I.; Larrat, B.; Tournier, N.; Buvat, I. Physical Blood-Brain Barrier Disruption Induced by Focused Ultrasound Does Not Overcome the Transporter-Mediated Efflux of Erlotinib. Journal of Controlled Release 2018, 292, 210–220, doi:10.1016/j.jconrel.2018.11.009ï.

264. Nouraein, S.; Lee, S.; Saenz, V.A.; Del Mundo, H.C.; Yiu, J.; Szablowski, J.O. Acoustically Targeted Noninvasive Gene Therapy in Large Brain Volumes. Gene Ther 2024, 31, 85–94, doi:10.1038/s41434-023-00421-1.

265. Ajenjo, J.; Seo, J.W.; Foiret, J.; Wu, B.; Raie, M.N.; Wang, J.; Fite, B.Z.; Zhang, N.; Malek, R.; Beinat, C.; et al. PET Imaging of Focused-Ultrasound Enhanced Delivery of AAVs into the Murine Brain. Theranostics 2023, 13, 5151–5169, doi:10.7150/thno.85549.

266. Samiotaki, G.; Vlachos, F.; Tung, Y.S.; Konofagou, E.E. A Quantitative Pressure and Microbubble-Size Dependence Study of Focused Ultrasound-Induced Blood-Brain Barrier Opening Reversibility in Vivo Using MRI. Magn Reson Med 2012, 67, 769–777, doi:10.1002/mrm.23063.

267. Baseri, B.; Choi, J.J.; Tung, Y.-S.; Konofagou, E.E. Multi-Modality Safety Assessment of Blood-Brain Barrier Opening Using Focused Ultrasound and Definity Microbubbles: A Short-Term Study. Ultrasound Med Biol 2010, 36, 1445–1459, doi:10.1016/j.ultrasmedbio.2010.06.005.

268. Choi, J.J.; Selert, K.; Gao, Z.; Samiotaki, G.; Baseri, B.; Konofagou, E.E. Noninvasive and Localized Blood—Brain Barrier Disruption Using Focused Ultrasound Can Be Achieved at Short Pulse Lengths and Low Pulse Repetition Frequencies. Journal of Cerebral Blood Flow & Metabolism 2011, 31, 725–737, doi:10.1038/jcbfm.2010.155.

269. Choi, J.J.; Selert, K.; Vlachos, F.; Wong, A.; Konofagou, E.E. Noninvasive and Localized Neuronal Delivery Using Short Ultrasonic Pulses and Microbubbles. Proceedings of the National Academy of Sciences 2011, 108, 16539–16544, doi:10.1073/pnas.1105116108.

270. Morse, S. V.; Pouliopoulos, A.N.; Chan, T.G.; Copping, M.J.; Lin, J.; Long, N.J.; Choi, J.J. Rapid Short-Pulse Ultrasound Delivers Drugs Uniformly across the Murine Blood-Brain Barrier with Negligible Disruption. Radiology 2019, 291, 459–466, doi:10.1148/radiol.2019181625.

271. Chopra, R.; Vykhodtseva, N.; Hynynen, K. Influence of Exposure Time and Pressure Amplitude on Blood−Brain-Barrier Opening Using Transcranial Ultrasound Exposures. ACS Chem Neurosci 2010, 1, 391–398, doi:10.1021/cn9000445.

272. Hsu, Y.H.; Lee, W.C.; Chu, S.S.; Chao, M.E.; Wu, K.S.; Liu, R.S.; Wong, T.T. Influence of Acoustic Parameters and Sonication Schemes on Transcranial Blood–Brain Barrier Disruption Induced by Pulsed Weakly Focused Ultrasound. Pharmaceutics 2022, 14, doi:10.3390/pharmaceutics14061207.

273. Marty, B.; Larrat, B.; Van Landeghem, M.; Robic, C.; Robert, P.; Port, M.; Le Bihan, D.; Pernot, M.; Tanter, M.; Lethimonnier, F.; et al. Dynamic Study of Blood-Brain Barrier Closure after Its Disruption Using Ultrasound: A Quantitative Analysis. Journal of Cerebral Blood Flow and Metabolism 2012, 32, 1948–1958, doi:10.1038/jcbfm.2012.100.

274. Presset, A.; Bodard, S.; Lefèvre, A.; Millet, A.; Oujagir, E.; Dupuy, C.; Iazourène, T.; Bouakaz, A.; Emond, P.; Escoffre, J.M.; et al. First Metabolomic Signature of Blood-Brain Barrier Opening Induced by Microbubble-Assisted Ultrasound. Front Mol Neurosci 2022, 15, doi:10.3389/fnmol.2022.888318.

275. Kong, C.; Yang, E.-J.; Shin, J.; Park, J.; Kim, S.-H.; Park, S.-W.; Chang, W.S.; Lee, C.-H.; Kim, H.; Kim, H.-S.; et al. Enhanced Delivery of a Low Dose of Aducanumab via FUS in 5×FAD Mice, an AD Model. Transl Neurodegener 2022, 11, 57, doi:10.1186/s40035-022-00333-x.

276. Kovacs, Z.I.; Burks, S.R.; Frank, J.A. Focused Ultrasound with Microbubbles Induces Sterile Inflammatory Response Proportional to the Blood Brain Barrier Opening: Attention to Experimental Conditions. Theranostics 2018, 8, 2245–2248, doi:10.7150/thno.24181.

277. Bathini, P.; Sun, T.; Schenk, M.; Schilling, S.; McDannold, N.J.; Lemere, C.A. Acute Effects of Focused Ultrasound-Induced Blood-Brain Barrier Opening on Anti-Pyroglu3 Abeta Antibody Delivery and Immune Responses. Biomolecules 2022, 12, 951, doi:10.3390/biom12070951.

278. Poon, C.; Pellow, C.; Hynynen, K. Neutrophil Recruitment and Leukocyte Response Following Focused Ultrasound and Microbubble Mediated Blood-Brain Barrier Treatments. Theranostics 2021, 11, 1655–1671, doi:10.7150/thno.52710.

279. Angolano, C.; Hansen, E.; Ajjawi, H.; Nowlin, P.; Zhang, Y.; Thunemann, N.; Ferran, C.; Todd, N.; contributions, equal Characterization of Focused Ultrasound Blood-Brain Barrier Disruption Effect on Inflammation as a Function of Treatment Parameters. bioRxiv 2024, doi:10.1101/2024.07.10.602776.

280. Lee, Y.; Choi, Y.; Park, E.J.; Kwon, S.; Kim, H.; Lee, J.Y.; Lee, D.S. Improvement of Glymphatic–Lymphatic Drainage of Beta-Amyloid by Focused Ultrasound in Alzheimer's Disease Model. Sci Rep 2020, 10, doi:10.1038/s41598-020-73151-8.

281. Ye, D.; Chen, S.; Liu, Y.; Weixel, C.; Hu, Z.; Chen, H. Mechanically Manipulate Glymphatic Transportation by Ultrasound Combined with Microbubbles. 2022, doi:10.1101/2022.10.28.514316.

282. Scarcelli, T.; Jordão, J.F.; O'Reilly, M.A.; Ellens, N.; Hynynen, K.; Aubert, I. Stimulation of Hippocampal Neurogenesis by Transcranial Focused Ultrasound and Microbubbles in Adult Mice. Brain Stimul 2014, 7, 304–307, doi:10.1016/j.brs.2013.12.012.

283. Shin, J.; Kong, C.; Lee, J.; Choi, B.Y.; Sim, J.; Koh, C.S.; Park, M.; Na, Y.C.; Suh, S.W.; Chang, W.S.; et al. Focused Ultrasound-Induced Blood-Brain Barrier Opening Improves Adult Hippocampal Neurogenesis and Cognitive Function in a Cholinergic Degeneration Dementia Rat Model. Alzheimers Res Ther 2019, 11, 110, doi:10.1186/s13195-019-0569-x.

284. Mooney, S.J.; Shah, K.; Yeung, S.; Burgess, A.; Aubert, I.; Hynynen, K. Focused Ultrasound-Induced Neurogenesis Requires an Increase in Blood-Brain Barrier Permeability. PLoS One 2016, 11, e0159892, doi:10.1371/journal.pone.0159892.

285. Rezai, A.R.; Ranjan, M.; Haut, M.W.; Carpenter, J.; D'Haese, P.F.; Mehta, R.I.; Najib, U.; Wang, P.; Claassen, D.O.; Chazen, J.L.; et al. Focused Ultrasound–Mediated Blood-Brain Barrier

Opening in Alzheimer's Disease: Long-Term Safety, Imaging, and Cognitive Outcomes. J Neurosurg 2023, 139, 275–283, doi:10.3171/2022.9.JNS221565.

286. Gasca-Salas, C.; Fernández-Rodríguez, B.; Pineda-Pardo, J.A.; Rodríguez-Rojas, R.; Obeso, I.; Hernández-Fernández, F.; del Álamo, M.; Mata, D.; Guida, P.; Ordás-Bandera, C.; et al. Blood-Brain Barrier Opening with Focused Ultrasound in Parkinson's Disease Dementia. Nat Commun 2021, 12, doi:10.1038/s41467-021-21022-9.

287. Gandhi, K.; Barzegar-Fallah, A.; Banstola, A.; Rizwan, S.B.; Reynolds, J.N.J. Ultrasound-Mediated Blood–Brain Barrier Disruption for Drug Delivery: A Systematic Review of Protocols, Efficacy, and Safety Outcomes from Preclinical and Clinical Studies. Pharmaceutics 2022, 14, doi:10.3390/pharmaceutics14040833.

288. Todd, N.; Zhang, Y.; Arcaro, M.; Becerra, L.; Borsook, D.; Livingstone, M.; McDannold, N. Focused Ultrasound Induced Opening of the Blood-Brain Barrier Disrupts Inter-Hemispheric Resting State Functional Connectivity in the Rat Brain. Neuroimage 2018, 178, 414–422, doi:10.1016/j.neuroimage.2018.05.063.

289. Rigollet, S.; Rome, C.; Ador, T.; Dumont, E.; Pichon, C.; Delalande, A.; Barbier, E.L.; Stupar, V. FUS-Mediated BBB Opening Leads to Transient Perfusion Decrease and Inflammation without Acute or Chronic Brain Lesion. Theranostics 2024, 14, 4147–4160, doi:10.7150/thno.96721.

290. Chopra, R.; Curiel, L.; Staruch, R.; Morrison, L.; Hynynen, K. An MRI-Compatible System for Focused Ultrasound Experiments in Small Animal Models. Med Phys 2009, 36, 1867–1874, doi:10.1118/1.3115680.

291. Magnin, R.; Rabusseau, F.; Salabartan, F.; Mériaux, S.; Aubry, J.F.; Le Bihan, D.; Dumont, E.; Larrat, B. Magnetic Resonance-Guided Motorized Transcranial Ultrasound System for Blood-Brain Barrier Permeabilization along Arbitrary Trajectories in Rodents. J Ther Ultrasound 2015, 3, doi:10.1186/s40349-015-0044-5.

292. Xu, L.; Gong, Y.; Chen, H. Transcranial Focused Ultrasound-Induced Blood-Brain Barrier Opening in Mice without Shaving Hairs. 2023, doi:10.21203/rs.3.rs-2562134/v1.

293. Chen, H.; Konofagou, E.E. The Size of Blood-Brain Barrier Opening Induced by Focused Ultrasound Is Dictated by the Acoustic Pressure. Journal of Cerebral Blood Flow and Metabolism 2014, 34, 1197–1204, doi:10.1038/jcbfm.2014.71.

294. Blesa, J.; Pineda-Pardo, J.A.; Inoue, K.-I.; Gasca-Salas, C.; Balzano, T.; López-González, N.; Rey, D.; Reinares-Sebastián, A.; Esteban-García, N.; Rodríguez-Rojas, R.; et al. BBB Opening with

Focused Ultrasound in Nonhuman Primates and Parkinson's Disease Patients: Targeted AAV Vector Delivery and PET Imaging. Neuroscience 2023.

295. Vlachos, F.; Tung, Y.; Konofagou, E. Permeability Dependence Study of the Focused Ultrasound-induced Blood–Brain Barrier Opening at Distinct Pressures and Microbubble Diameters Using DCE-MRI. Magn Reson Med 2011, 66, 821–830, doi:10.1002/mrm.22848.

296. Gerstenmayer, M.; Fellah, B.; Magnin, R.; Selingue, E.; Larrat, B.; Acoustic, B.L. Acoustic Transmission Factor through the Rat Skull as a Function of Body Mass, Frequency and Position. Ultrasound Med Biol 2018, 44, doi:10.1016/j.ultrasmedbio.2018.06.005ï.

297. Huang, Y.; Alkins, R.; Schwartz, M.L.; Hynynen, K. Opening the Blood-Brain Barrier with MR Imaging-Guided Focused Ultrasound: Preclinical Testing on a Trans-Human Skull Porcine Model. Radiology 2017, 282, 123–130, doi:10.1148/radiol.2016152154.

298. O'Reilly, M.A.; Hynynen, K. Blood-Brain Barrier: Real-Time Feedback-Controlled Focused Ultrasound Disruption by Using an Acoustic Emissions-Based Controller. Radiology 2012, 263, 96–106, doi:10.1148/radiol.11111417.

299. Bing, C.; Hong, Y.; Hernandez, C.; Rich, M.; Cheng, B.; Munaweera, I.; Szczepanski, D.; Xi, Y.; Bolding, M.; Exner, A.; et al. Characterization of Different Bubble Formulations for Blood-Brain Barrier Opening Using a Focused Ultrasound System with Acoustic Feedback Control. Sci Rep 2018, 8, doi:10.1038/s41598-018-26330-7.

300. Huang, Y.; Meng, Y.; Pople, C.B.; Bethune, A.; Jones, R.M.; Abrahao, A.; Hamani, C.; Kalia, S.K.; Kalia, L. V.; Lipsman, N.; et al. Cavitation Feedback Control of Focused Ultrasound Blood-Brain Barrier Opening for Drug Delivery in Patients with Parkinson's Disease. Pharmaceutics 2022, 14, doi:10.3390/pharmaceutics14122607.

301. Novell, A.; Kamimura, H.A.S.; Cafarelli, A.; Gerstenmayer, M.; Flament, J.; Valette, J.; Agou, P.; Conti, A.; Selingue, E.; Aron Badin, R.; et al. A New Safety Index Based on Intrapulse Monitoring of Ultra-Harmonic Cavitation during Ultrasound-Induced Blood-Brain Barrier Opening Procedures. Sci Rep 2020, 10, doi:10.1038/s41598-020-66994-8.

302. Cornu, C.; Guédra, M.; Béra, J.C.; Liu, H.L.; Chen, W.S.; Inserra, C. Ultrafast Monitoring and Control of Subharmonic Emissions of an Unseeded Bubble Cloud during Pulsed Sonication. Ultrason Sonochem 2018, 42, 697–703, doi:10.1016/j.ultsonch.2017.12.026.

303. Zvěřová, M. Clinical Aspects of Alzheimer's Disease. Clin Biochem 2019, 72, 3–6.

304. 2023 Alzheimer's Disease Facts and Figures; John Wiley and Sons Inc, 2023; Vol. 19;.

305. Huang, S.Y.; Zhang, Y.R.; Guo, Y.; Du, J.; Ren, P.; Wu, B.S.; Feng, J.F.; Cheng, W.; Yu, J.T. Glymphatic System Dysfunction Predicts Amyloid Deposition, Neurodegeneration, and Clinical Progression in Alzheimer's Disease. Alzheimer's and Dementia 2024, 20, 3251–3269, doi:10.1002/alz.13789.

306. Price, J.L.; Morris, J.C. Tangles and Plaques in Nondemented Aging and "preclinical" Alzheimer's Disease. Ann Neurol 1999, 45, 358–368, doi:10.1002/1531-8249(199903)45:3<358::AID-ANA12>3.0.CO;2-X.

307. Nasb, M.; Tao, W.; Chen, N. Alzheimer's Disease Puzzle: Delving into Pathogenesis Hypotheses. Aging Dis 2024, 15, 43–73.

308. Bhole, R.P.; Chikhale, R. V.; Rathi, K.M. Current Biomarkers and Treatment Strategies in Alzheimer Disease: An Overview and Future Perspectives. IBRO Neurosci Rep 2024, 16, 8–42.

309. By, S.; Kahl, A.; Cogswell, P.M. Alzheimer's Disease Clinical Trials: What Have We Learned From Magnetic Resonance Imaging. Journal of Magnetic Resonance Imaging 2024.

310. Asher, S.; Priefer, R. Alzheimer's Disease Failed Clinical Trials. Life Sci 2022, 306.

311. Rafii, M.S.; Baumann, T.L.; Bakay, R.A.E.; Ostrove, J.M.; Siffert, J.; Fleisher, A.S.; Herzog, C.D.; Barba, D.; Pay, M.; Salmon, D.P.; et al. A Phase1 Study of Stereotactic Gene Delivery of AAV2-NGF for Alzheimer's Disease. Alzheimers Dement 2014, 10, 571–581, doi:10.1016/j.jalz.2013.09.004.

312. Castle, M.J.; Baltanás, F.C.; Kovacs, I.; Nagahara, A.H.; Barba, D.; Tuszynski, M.H. Postmortem Analysis in a Clinical Trial of AAV2-NGF Gene Therapy for Alzheimer's Disease Identifies a Need for Improved Vector Delivery. Hum Gene Ther 2020, 31, 415–422, doi:10.1089/hum.2019.367.

313. Sevigny, J.; Uspenskaya, O.; Heckman, L.D.; Wong, L.C.; Hatch, D.A.; Tewari, A.; Vandenberghe, R.; Irwin, D.J.; Saracino, D.; Le Ber, I.; et al. Progranulin AAV Gene Therapy for Frontotemporal Dementia: Translational Studies and Phase 1/2 Trial Interim Results. Nat Med 2024, 30, 1406–1415, doi:10.1038/s41591-024-02973-0.

314. Jackson, R.J.; Keiser, M.S.; Meltzer, J.C.; Fykstra, D.P.; Dierksmeier, S.E.; Hajizadeh, S.; Kreuzer, J.; Morris, R.; Melloni, A.; Nakajima, T.; et al. APOE2 Gene Therapy Reduces Amyloid Deposition and Improves Markers of Neuroinflammation and Neurodegeneration in a Mouse

Model of Alzheimer Disease. Molecular Therapy 2024, 32, 1373–1386, doi:10.1016/j.ymthe.2024.03.024.

315. Zhang, W. bin; Huang, Y.; Guo, X. rou; Zhang, M. qi; Yuan, X. shan; Zu, H. bing DHCR24 Reverses Alzheimer's Disease-Related Pathology and Cognitive Impairment via Increasing Hippocampal Cholesterol Levels in 5xFAD Mice. Acta Neuropathol Commun 2023, 11, doi:10.1186/s40478-023-01593-y.

316. Kofoed, R.H.; Heinen, S.; Silburt, J.; Dubey, S.; Dibia, C.L.; Maes, M.; Simpson, E.M.; Hynynen, K.; Aubert, I. Transgene Distribution and Immune Response after Ultrasound Delivery of RAAV9 and PHP.B to the Brain in a Mouse Model of Amyloidosis. Mol Ther Methods Clin Dev 2021, 23, 390–405, doi:10.1016/j.omtm.2021.10.001.

317. Weber-Adrian, D.; Kofoed, R.H.; Chan, J.W.Y.; Silburt, J.; Noroozian, Z.; Kügler, S.; Hynynen, K.; Aubert, I. Strategy to Enhance Transgene Expression in Proximity of Amyloid Plaques in a Mouse Model of Alzheimer's Disease. Theranostics 2019, 9, 8127–8137, doi:10.7150/thno.36718.

318. Jordão, J.F.; Thévenot, E.; Markham-Coultes, K.; Scarcelli, T.; Weng, Y.Q.; Xhima, K.; O'Reilly, M.; Huang, Y.; McLaurin, J.A.; Hynynen, K.; et al. Amyloid-β Plaque Reduction, Endogenous Antibody Delivery and Glial Activation by Brain-Targeted, Transcranial Focused Ultrasound. Exp Neurol 2013, 248, 16–29, doi:10.1016/j.expneurol.2013.05.008.

319. Poon, C.; Pellow, C.; Hynynen, K. Neutrophil Recruitment and Leukocyte Response Following Focused Ultrasound and Microbubble Mediated Blood-Brain Barrier Treatments. Theranostics 2021, 11, 1655–1671, doi:10.7150/thno.52710.

320. Shen, Y.; Hua, L.; Yeh, C.K.; Shen, L.; Ying, M.; Zhang, Z.; Liu, G.; Li, S.; Chen, S.; Chen, X.; et al. Ultrasound with Microbubbles Improves Memory, Ameliorates Pathology and Modulates Hippocampal Proteomic Changes in a Triple Transgenic Mouse Model of Alzheimer's Disease. Theranostics 2020, 10, 11794–11819, doi:10.7150/thno.44152.

321. Pandit, R.; Leinenga, G.; Götz, J. Repeated Ultrasound Treatment of Tau Transgenic Mice Clears Neuronal Tau by Autophagy and Improves Behavioral Functions. Theranostics 2019, 9, 3754–3767, doi:10.7150/thno.34388.

322. Karakatsani, M.E.; Kugelman, T.; Ji, R.; Murillo, M.; Wang, S.; Niimi, Y.; Small, S.A.; Duff, K.E.; Konofagou, E.E. Unilateral Focused Ultrasound-Induced Blood-Brain Barrier Opening Reduces Phosphorylated Tau from the RTg4510 Mouse Model. Theranostics 2019, 9, 5396–5411, doi:10.7150/thno.28717.

323. Poon, C.T.; Shah, K.; Lin, C.; Tse, R.; Kim, K.K.; Mooney, S.; Aubert, I.; Stefanovic, B.; Hynynen, K. Time Course of Focused Ultrasound Effects on β-Amyloid Plaque Pathology in the TgCRND8 Mouse Model of Alzheimer's Disease. Sci Rep 2018, 8, doi:10.1038/s41598-018-32250-3.

324. Mehta, R.I.; Carpenter, J.S.; Mehta, R.I.; Haut, M.W.; Wang, P.; Ranjan, M.; Najib, U.; D'Haese, P.F.; Rezai, A.R. Ultrasound-Mediated Blood–Brain Barrier Opening Uncovers an Intracerebral Perivenous Fluid Network in Persons with Alzheimer's Disease. Fluids Barriers CNS 2023, 20, doi:10.1186/s12987-023-00447-y.

325. Epelbaum, S.; Burgos, N.; Canney, M.; Matthews, D.; Houot, M.; Santin, M.D.; Desseaux, C.; Bouchoux, G.; Stroer, S.; Martin, C.; et al. Pilot Study of Repeated Blood-Brain Barrier Disruption in Patients with Mild Alzheimer's Disease with an Implantable Ultrasound Device. Alzheimers Res Ther 2022, 14, doi:10.1186/s13195-022-00981-1.

326. Mehta, R.I.; Carpenter, J.S.; Mehta, R.I.; Haut, M.W.; Ranjan, M.; Najib, U.; Lockman, P.; Wang, P.; D'Haese, P.F.; Rezai, A.R. Blood-Brain Barrier Opening with MRI-Guided Focused Ultrasound Elicits Meningeal Venous Permeability in Humans with Early Alzheimer Disease. Radiology 2021, 298, 654–662, doi:10.1148/radiol.2021200643.

327. Leinenga, G.; Koh, W.K.; Götz, J. A Comparative Study of the Effects of Aducanumab and Scanning Ultrasound on Amyloid Plaques and Behavior in the APP23 Mouse Model of Alzheimer Disease. Alzheimers Res Ther 2021, 13, doi:10.1186/s13195-021-00809-4.

328. Trinh, D.; Nash, J.; Goertz, D.; Hynynen, K.; Bulner, S.; Iqbal, U.; Keenan, J. Microbubble Drug Conjugate and Focused Ultrasound Blood Brain Barrier Delivery of AAV-2 SIRT-3. Drug Deliv 2022, 29, 1176–1183, doi:10.1080/10717544.2022.2035855.

329. Xhima, K.; Nabbouh, F.; Hynynen, K.; Aubert, I.; Tandon, A. Noninvasive Delivery of an α-Synuclein Gene Silencing Vector with Magnetic Resonance–Guided Focused Ultrasound. Movement Disorders 2018, 33, 1567–1579, doi:10.1002/mds.101.

330. Christine, C.W.; Richardson, R.M.; van Laar, A.D.; Thompson, M.E.; Fine, E.M.; Khwaja, O.S.; Li, C.; Liang, G.S.; Meier, A.; Roberts, E.W.; et al. Safety of AADC Gene Therapy for Moderately Advanced Parkinson Disease: Three-Year Outcomes from the PD-1101 Trial. Neurology 2022, 98, E40–E50, doi:10.1212/WNL.0000000000012952.

331. Gasca-Salas, C.; Fernández-Rodríguez, B.; Pineda-Pardo, J.A.; Rodríguez-Rojas, R.; Obeso, I.; Hernández-Fernández, F.; del Álamo, M.; Mata, D.; Guida, P.; Ordás-Bandera, C.; et al. Blood-

Brain Barrier Opening with Focused Ultrasound in Parkinson's Disease Dementia. Nat Commun 2021, 12, doi:10.1038/s41467-021-21022-9.

332. Gasca-Salas, C.; Pineda-Pardo, J.A.; Del Álamo, M.; Jiménez, T.; Trompeta, C.; Toltsis, G.; Garcia-Cañamaque, L.; Fernández-Rodríguez, B.; Matarazzo, M.; Plaza de las Heras, I.; et al. Nigrostriatal Blood-Brain Barrier Opening in Parkinson's Disease. J Neurol Neurosurg Psychiatry 2024, 95, 1089–1092, doi:10.1136/jnnp-2023-332967.

333. Corti, M.; Byrne, B.J.; Gessler, D.J.; Thompson, G.; Norman, S.; Lammers, J.; Coleman, K.E.; Liberati, C.; Elder, M.E.; Escolar, M.L.; et al. Adeno-Associated Virus-Mediated Gene Therapy in a Patient with Canavan Disease Using Dual Routes of Administration and Immune Modulation. Mol Ther Methods Clin Dev 2023, 30, 303–314, doi:10.1016/j.omtm.2023.06.001.

334. Ling, Q.; Rioux, M.; Hu, Y.; Lee, M.J.; Gray, S.J. Adeno-Associated Viral Vector Serotype 9-Based Gene Replacement Therapy for SURF1-Related Leigh Syndrome. Mol Ther Methods Clin Dev 2021, 23, 158–168, doi:10.1016/j.omtm.2021.09.001.

335. Silva-Pinheiro, P.; Cerutti, R.; Luna-Sanchez, M.; Zeviani, M.; Viscomi, C. A Single Intravenous Injection of AAV-PHP.B-HNDUFS4 Ameliorates the Phenotype of Ndufs4−/− Mice. Mol Ther Methods Clin Dev 2020, 17, 1071–1078, doi:10.1016/j.omtm.2020.04.026.

336. Sadhu, C.; Lyons, C.; Oh, J.; Jagadeeswaran, I.; Gray, S.J.; Sinnett, S.E. The Efficacy of a Human-Ready MiniMECP2 Gene Therapy in a Pre-Clinical Model of Rett Syndrome. Genes (Basel) 2024, 15, doi:10.3390/genes15010031.

337. Chadman, K.K.; Adayev, T.; Udayan, A.; Ahmed, R.; Dai, C.L.; Goodman, J.H.; Meeker, H.; Dolzhanskaya, N.; Velinov, M. Efficient Delivery of FMR1 across the Blood Brain Barrier Using AAVphp Construct in Adult FMR1 KO Mice Suggests the Feasibility of Gene Therapy for Fragile X Syndrome. Genes (Basel) 2023, 14, doi:10.3390/genes14020505.

338. Wong, H.; Hooper, A.W.M.; Kang, H.R.; Lee, S.J.; Zhao, J.; Sadhu, C.; Rawat, S.; Gray, S.J.; Hampson, D.R. CNS-Dominant Human FMRP Isoform Rescues Seizures, Fear, and Sleep Abnormalities in Fmr1-KO Mice. 2023, doi:10.1172/jci.

339. Hagerman, R.J.; Berry-Kravis, E.; Hazlett, H.C.; Bailey, D.B.; Moine, H.; Kooy, R.F.; Tassone, F.; Gantois, I.; Sonenberg, N.; Mandel, J.L.; et al. Fragile X Syndrome. Nat Rev Dis Primers 2017, 3, doi:10.1038/NRDP.2017.65.

340. Purdon Martin, J.; Bell, J. A PEDIGREE OF MENTAL DEFECT SHOWING SEX-LINKAGE. 1943.

341. Hunter, J.; Rivero-Arias, O.; Angelov, A.; Kim, E.; Fotheringham, I.; Leal, J. Epidemiology of Fragile X Syndrome: A Systematic Review and Meta-Analysis. Am J Med Genet A 2014, 164, 1648–1658, doi:10.1002/ajmg.a.36511.

342. Miller, J.G.; Bartholomay, K.L.; Lee, C.H.; Bruno, J.L.; Lightbody, A.A.; Reiss, A.L. Empathy and Anxiety in Young Girls with Fragile X Syndrome. J Autism Dev Disord 2022, 52, 2213–2223, doi:10.1007/s10803-021-05105-6.

343. Bailey, D.B.; Raspa, M.; Bishop, E.; Holiday, D. No Change in the Age of Diagnosis for Fragile X Syndrome: Findings from a National Parent Survey. Pediatrics 2009, 124, 527–533, doi:10.1542/peds.2008-2992.

344. Thurman, A.J.; McDuffie, A.; Hagerman, R.; Abbeduto, L. Psychiatric Symptoms in Boys with Fragile X Syndrome: A Comparison with Nonsyndromic Autism Spectrum Disorder. Res Dev Disabil 2014, 35, 1072–1086, doi:10.1016/j.ridd.2014.01.032.

345. Heulens, I.; Suttie, M.; Postnov, A.; De Clerck, N.; Perrotta, C.S.; Mattina, T.; Faravelli, F.; Forzano, F.; Frank Kooy, R.; Hammond, P. Craniofacial Characteristics of Fragile X Syndrome in Mouse and Man. European Journal of Human Genetics 2013, 21, 816–823, doi:10.1038/ejhg.2012.265.

346. Kidd, S.A.; Lachiewicz, A.; Barbouth, D.; Blitz, R.K.; Delahunty, C.; McBrien, D.; Visootsak, J.; Berry-Kravis, E. Fragile X Syndrome: A Review of Associated Medical Problems. Pediatrics 2014, 134, 995–1005.

347. Tassone, F.; Protic, D.; Allen, E.G.; Archibald, A.D.; Baud, A.; Brown, T.W.; Budimirovic, D.B.; Cohen, J.; Dufour, B.; Eiges, R.; et al. Insight and Recommendations for Fragile X-Premutation-Associated Conditions from the Fifth International Conference on FMR1 Premutation. Cells 2023, 12.

348. Loomis, E.W.; Sanz, L.A.; Chédin, F.; Hagerman, P.J. Transcription-Associated R-Loop Formation across the Human FMR1 CGG-Repeat Region. PLoS Genet 2014, 10, doi:10.1371/journal.pgen.1004294.

349. Jin, P.; Duan, R.; Qurashi, A.; Qin, Y.; Tian, D.; Rosser, T.C.; Liu, H.; Feng, Y.; Warren, S.T. Pur α Binds to RCGG Repeats and Modulates Repeat-Mediated Neurodegeneration in a Drosophila Model of Fragile X Tremor/ Ataxia Syndrome. Neurons 2007, 55, 556–564.

350. Bassell, G.J.; Warren, S.T. Fragile X Syndrome: Loss of Local MRNA Regulation Alters Synaptic Development and Function. Neuron 2008, 60, 201–214, doi:10.1016/j.neuron.2008.10.004.

351. Darnell, J.C.; Jensen, K.B.; Jin, P.; Brown, V.; Warren, S.T.; Darnell, R.B. Fragile X Mental Retardation Protein Targets G Quartet MRNAs Important for Neuronal Function in Proteins Involved in Many Aspects of RNA Metabolism Including Splicing Factors and HnRNP Proteins and Are Commonly Found in Conjunction with Other RNA Binding. Cell 2001, 107, 489–499.

352. Bechara, E.G.; Didiot, M.C.; Melko, M.; Davidovic, L.; Bensaid, M.; Martin, P.; Castets, M.; Pognonec, P.; Khandjian, E.W.; Moine, H.; et al. A Novel Function for Fragile X Mental Retardation Protein in Translational Activation. PLoS Biol 2009, 7, doi:10.1371/journal.pbio.1000016.

353. Darnell, J.C.; Fraser, C.E.; Mostovetsky, O.; Stefani, G.; Jones, T.A.; Eddy, S.R.; Darnell, R.B. Kissing Complex RNAs Mediate Interaction between the Fragile-X Mental Retardation Protein KH2 Domain and Brain Polyribosomes. Genes Dev 2005, 19, 903–918, doi:10.1101/gad.1276805.

354. Ferder, I.; Parborell, F.; Sundblad, V.; Chiauzzi, V.; Gómez, K.; Charreau, E.H.; Tesone, M.; Dain, L. Expression of Fragile X Mental Retardation Protein and Fmr1 MRNA during Folliculogenesis in the Rat. Reproduction 2013, 145, 335–343, doi:10.1530/REP-12-0305.

355. Jung, J.; Ohk, J.; Kim, H.; Holt, C.E.; Park, H.J.; Jung, H. MRNA Transport, Translation, and Decay in Adult Mammalian Central Nervous System Axons. Neuron 2023, 111, 650-668.e4, doi:10.1016/j.neuron.2022.12.015.

356. De Diego Otero, Y.; Severijnen, L.-A.; van Cappellen, G.; Schrier, M.; Oostra, B.; Willemsen, R. Transport of Fragile X Mental Retardation Protein via Granules in Neurites of PC12 Cells. Mol Cell Biol 2002, 22, 8332–8341, doi:10.1128/mcb.22.23.8332-8341.2002.

357. Pop, A.S.; Gomez-Mancilla, B.; Neri, G.; Willemsen, R.; Gasparini, F. Fragile X Syndrome: A Preclinical Review on Metabotropic Glutamate Receptor 5 (MGluR5) Antagonists and Drug Development. Psychopharmacology (Berl) 2014, 231, 1217–1226, doi:10.1007/s00213-013-3330-3.

358. Olmos-Serrano, J.L.; Corbin, J.G.; Burns, M.P. The GABA A Receptor Agonist THIP Ameliorates Specific Behavioral Deficits in the Mouse Model of Fragile X Syndrome. Dev Neurosci 2011, 33, 395–403.

359. Shah, S.; Molinaro, G.; Liu, B.; Wang, R.; Huber, K.M.; Richter, J.D. FMRP Control of Ribosome Translocation Promotes Chromatin Modifications and Alternative Splicing of Neuronal Genes Linked to Autism. Cell Rep 2020, 30, 4459-4472.e6, doi:10.1016/j.celrep.2020.02.076.

360. Lucas, A.; Poleg, S.; Klug, A.; McCullagh, E.A. Myelination Deficits in the Auditory Brainstem of a Mouse Model of Fragile X Syndrome. Front Neurosci 2021, 15, doi:10.3389/fnins.2021.772943.

361. Mirrett, P.L.; Roberts, J.E.; Price, J. Early Intervention Practices and Communication Intervention Strategies for Young Males With Fragile X Syndrome. Lang Speech Hear Serv Sch 2003, 34, 320–331, doi:10.1044/0161-1461(2003/026).

362. Martin, G.E.; Ausderau, K.K.; Raspa, M.; Bishop, E.; Mallya, U.; Bailey, D.B. Therapy Service Use among Individuals with Fragile X Syndrome: Findings from a US Parent Survey. Journal of Intellectual Disability Research 2013, 57, 837–849, doi:10.1111/j.1365-2788.2012.01608.x.

363. Protic, D.; Hagerman, R. State-of-the-Art Therapies for Fragile X Syndrome. Dev Med Child Neurol 2024, 66, 863–871, doi:10.1111/dmcn.15885.

364. Roberts, J.E.; Miranda, M.; Boccia, M.; Janes, H.; Tonnsen, B.L.; Hatton, D.D. Treatment Effects of Stimulant Medication in Young Boys with Fragile X Syndrome. J Neurodev Disord 2011, 3, 175–184, doi:10.1007/s11689-011-9085-4.

365. Hagerman, R.J.; Murphy, M.A.; Wittenberger, M.D. A Controlled Trial of Stimulant Medication in Children with the Fragile X Syndrome. Am J Med Genet 1988, 30, 377–392, doi:10.1002/ajmg.1320300138.

366. Burris, K.D.; Molski, T.F.; Xu, C.; Ryan, E.; Tottori, K.; Kikuchi, T.; Yocca, F.D.; Molinoff, P.B. Aripiprazole, a Novel Antipsychotic, Is a High-Affinity Partial Agonist at Human Dopamine D2 Receptors. J Pharmacol Exp Ther 2002, 302, 381–389, doi:10.1124/jpet.102.033175.

367. Jordan, S.; Koprivica, V.; Chen, R.; Tottori, K.; Kikuchi, T.; Altar, C.A. The Antipsychotic Aripiprazole Is a Potent, Partial Agonist at the Human 5-HT1A Receptor. Eur J Pharmacol 2002, 441, 137–140, doi:10.1016/S0014-2999(02)01532-7.

368. Rynn, M.A.; Walkup, J.T.; Compton, S.N.; Sakolsky, D.J.; Sherrill, J.T.; Shen, S.; Kendall, P.C.; McCracken, J.; Albano, A.M.; Piacentini, J.; et al. Child/Adolescent Anxiety Multimodal Study: Evaluating Safety. J Am Acad Child Adolesc Psychiatry 2015, 54, 180–190, doi:10.1016/j.jaac.2014.12.015.

369. Peteri, U.K.; Castrén, M.L. Modeling FXS with Mouse Neural Progenitors. In Methods in Molecular Biology; Humana Press Inc., 2019; Vol. 1942, pp. 71–78.

370. Diab, M.A.; Eiges, R. The Contribution of Pluripotent Stem Cell (PSC)-Based Models to the Study of Fragile X Syndrome (Fxs). Brain Sci 2019, 9, doi:10.3390/brainsci9020042.

371. Park, C.Y.; Halevy, T.; Lee, D.R.; Sung, J.J.; Lee, J.S.; Yanuka, O.; Benvenisty, N.; Kim, D.W. Reversion of FMR1 Methylation and Silencing by Editing the Triplet Repeats in Fragile X IPSC-Derived Neurons. Cell Rep 2015, 13, 234–241, doi:10.1016/j.celrep.2015.08.084.

372. Bontekoe, C.J.M.; Bakker, C.E.; Nieuwenhuizen, I.M.; Van Der Linde, H.; Lans, H.; De Lange, D.; Hirst, M.C.; Oostra, B.A. Instability of a (CGG) 98 Repeat in the Fmr1 Promoter; 2001; Vol. 10;.

373. Cathy E. Bakker; Coleta Verheij; Rob Willemsen; Robert van der Heim; Frank Oerlemans; Marcel Vermey; Anne Bygrave; André T. Hoogeveen; Ben A. Oostra Fmrl Knockout Mice: A Model to Study Fragile X Mental Retardation. Cell 1994, 78, 23–33.

374. Mientjes, E.J.; Nieuwenhuizen, I.; Kirkpatrick, L.; Zu, T.; Hoogeveen-Westerveld, M.; Severijnen, L.; Rifé, M.; Willemsen, R.; Nelson, D.L.; Oostra, B.A. The Generation of a Conditional Fmr1 Knock out Mouse Model to Study Fmrp Function in Vivo. Neurobiol Dis 2006, 21, 549–555, doi:10.1016/j.nbd.2005.08.019.

375. Spencer, C.M.; Graham, D.F.; Yuva-Paylor, L.A.; Nelson, D.L.; Paylor, R. Social Behavior in Fmr1 Knockout Mice Carrying a Human FMR1 Transgene. Behavioral Neuroscience 2008, 122, 710–715, doi:10.1037/0735-7044.122.3.710.

376. Qin, M.; Kang, J.; Smith, C.B. A Null Mutation for Fmr1 in Female Mice: Effects on Regional Cerebral Metabolic Rate for Glucose and Relationship to Behavior. Neuroscience 2005, 135, 999–1009, doi:10.1016/j.neuroscience.2005.06.081.

377. Martín, R.; Suárez-Pinilla, A.S.; García-Font, N.; Laguna-Luque, M.L.; López-Ramos, J.C.; Oset-Gasque, M.J.; Gruart, A.; Delgado-García, J.M.; Torres, M.; Sánchez-Prieto, J. The Activation of MGluR4 Rescues Parallel Fiber Synaptic Transmission and LTP, Motor Learning and Social Behavior in a Mouse Model of Fragile X Syndrome. Mol Autism 2023, 14, doi:10.1186/s13229-023-00547-4.

378. Jiang, Y.; Han, L.; Meng, J.; Wang, Z.; Zhou, Y.; Yuan, H.; Xu, H.; Zhang, X.; Zhao, Y.; Lu, J.; et al. Gene Therapy Using Human FMRP Isoforms Driven by the Human FMR1 Promoter Rescues Fragile X Syndrome Mouse Deficits. Mol Ther Methods Clin Dev 2022, 27, 246–258, doi:10.1016/j.omtm.2022.10.002.

379. Kumar, V.; Lee, K.Y.; Acharya, A.; Babik, M.S.; Christian-Hinman, C.A.; Rhodes, J.S.; Tsai, N.P. MGluR7 Allosteric Modulator AMN082 Corrects Protein Synthesis and Pathological Phenotypes in FXS. EMBO Mol Med 2024, 16, 506–522, doi:10.1038/s44321-024-00038-w.

380. Shakhawat, A.M.; Foltz, J.G.; Nance, A.B.; Bhateja, J.; Raymond, J.L. Systemic Pharmacological Suppression of Neural Activity Reverses Learning Impairment in a Mouse Model of Fragile X Syndrome. 2023, doi:10.7554/eLife.92543.1.

381. Coulson, R.L.; Frattini, V.; Moyer, C.E.; Hodges, J.; Walter, P.; Mourrain, P.; Zuo, Y.; Wang, G.X. Translational Modulator ISRIB Alleviates Synaptic and Behavioral Phenotypes in Fragile X Syndrome. iScience 2024, 27, doi:10.1016/j.isci.2024.109259.

382. Chadwick, W.; Angulo-Herrera, I.; Cogram, P.; Deacon, R.J.M.; Mason, D.J.; Brown, D.; Roberts, I.; O'Donovan, D.J.; Tranfaglia, M.R.; Guilliams, T.; et al. A Novel Combination Treatment for Fragile X Syndrome Predicted Using Computational Methods. Brain Commun 2024, 6, doi:10.1093/braincomms/fcad353.

383. Lee, B.; Lee, K.; Panda, S.; Gonzales-Rojas, R.; Chong, A.; Bugay, V.; Park, H.M.; Brenner, R.; Murthy, N.; Lee, H.Y. Nanoparticle Delivery of CRISPR into the Brain Rescues a Mouse Model of Fragile X Syndrome from Exaggerated Repetitive Behaviours. Nat Biomed Eng 2018, 2, 497–507, doi:10.1038/s41551-018-0252-8.

384. Hooper, A.W.M.; Wong, H.; Niibori, Y.; Abdoli, R.; Karumuthil-Melethil, S.; Qiao, C.; Danos, O.; Bruder, J.T.; Hampson, D.R. Gene Therapy Using an Ortholog of Human Fragile X Mental Retardation Protein Partially Rescues Behavioral Abnormalities and EEG Activity. Mol Ther Methods Clin Dev 2021, 22, 196–209, doi:10.1016/j.omtm.2021.06.013.

385. Hordeaux, J.; Wang, Q.; Katz, N.; Buza, E.L.; Bell, P.; Wilson, J.M. The Neurotropic Properties of AAV-PHP.B Are Limited to C57BL/6J Mice. Molecular Therapy 2018, 26, 664–668.

386. Terse, P.S.; Kells, A.P.; Noker, P.; Wright, J.F.; Bankiewicz, K.S. Safety Assessment of AAV2-HGDNF Administered Via Intracerebral Injection in Rats for Treatment of Parkinson's Disease. Int J Toxicol 2021, 40, 4–14, doi:10.1177/1091581820966315.

RESULTATS

Partie 1 : Formulation de microbulles fonctionnalisées pour la délivrance améliorée de gènes

Résumé en français :

Introduction :

Les microbulles de gaz sont des agents de contraste pour l'imagerie échographique, augmentant l'échogénicité du sang. Elles sont également capables d'osciller sous ultrasons, créant des forces de cisaillement et des micro-flux, capables dans un capillaire cérébral d'ouvrir la barrière hémato-encéphalique. Cette ouverture permet la délivrance de molécules thérapeutiques telles que des acides nucléiques, permettant l'utilisation dans le cerveau d'une méthode non invasive de thérapie génique. Les microbulles utilisées pour cette application peuvent être fonctionnalisées, permettant d'améliorer la délivrance de gènes. Cette fonctionnalisation peut se faire en utilisant les propriétés hydrophobes de la coque, permettant d'encapsuler des molécules ou des nanoparticules hydrophobes. Cela peut également être réalisé par liaison à la surface des microbulles de composés hydrophiles, en se servant de couplage streptavidine-biotine, de chimie clic ou d'interactions électrostatiques. La fonctionnalisation de microbulles peut permettre d'ajouter des agents de contraste pour réaliser de l'imagerie multimodale, d'ajouter des nanoparticules magnétiques ou des anticorps pour donner des propriétés de ciblage aux microbulles, ou d'utiliser des composants cationiques capables de lier des acides nucléiques, permettant d'en augmenter la délivrance.

Résultats :

Dans cette partie, plusieurs microbulles ont été formulées, incorporant diverses fonctionnalisations pour augmenter la délivrance d'acides nucléiques. Nous avons commencé par formuler des microbulles non fonctionnalisées, servant de référence pour la formulation de microbulles fonctionnalisées. Cette formulation démontre une importante concentration et une distribution de taille faiblement polydisperse et comprenant une large concentration de nanobulles. Par la suite, nous avons développé des microbulles comprenant une fonction biotine ou une fonction DBCO et avons validé leur couplage avec un anticorps. Les bulles biotines ont également été utilisées pour attacher des nanoparticules magnétiques. La capacité de ces microbulles de se déplacer avec un champ magnétique a été démontrée, ainsi que l'absence de

cytotoxicité de leur part ou de leurs composants. Nous avons ensuite développé un protocole de centrifugation permettant de sélectionner des microbulles d'une certaine taille. Puis, nous avons démontré la capacité des microbulles de taille proche d'1 μm à pénétrer plus facilement et de manière plus homogène dans une tumeur, augmentant le signal d'échographie de contraste. Un protocole de modulation de la taille et de la concentration des microbulles a également été développé, démontrant une diminution de la taille et une augmentation de la concentration corrélées avec l'augmentation du temps d'agitation mécanique lors de la formation des microbulles.

Deux types de microbulles cationiques ont ensuite été développés, utilisant soit des lipides cationiques complexant l'ADN à la surface, ou utilisant un polymère cationique ancré dans la coque de la microbulle, délocalisant la complexation de l'ADN. Les deux types de microbulles cationiques ont démontré leur capacité à complexer un ADN plasmidique, ainsi qu'une stabilité suffisante pour être utilisés dans un protocole de transfert de gène assisté par ultrasons. Cependant, les microbulles avec un polymère ont démontré la capacité de complexer plus d'ADN et sont plus stables comparé à la première génération de microbulles cationiques.

Pour finir, la cavitation sous ultrasons focalisés des deux types de microbulles cationiques a été analysée et comparée aux microbulles non fonctionnalisées. Les trois types de bulles ont démontré une cavitation stable et inertielle augmentant avec la pression acoustique, validant la possibilité de les utiliser dans un protocole de transfert de gène assisté par ultrasons. En revanche, les microbulles cationiques comprenant un polymère ont démontré une cavitation stable significativement plus forte que la première génération et proche du niveau de cavitation des microbulles fonctionnalisées.

Pour conclure, nous avons développé dans cette partie un large panel de microbulles fonctionnalisées qui pourront permettre d'optimiser un protocole de transfert de gène. La caractérisation des deux types de microbulles cationiques présentés dans cette partie a fait l'objet d'une présentation de poster durant le congrès international ISTU 2023 à Lyon. La sélection de taille des microbulles par centrifugation et leur effet échogène dans une tumeur a fait l'objet d'une courte présentation orale durant le congrès SFNano 2022 à Strasbourg.

Title:

Functionalized microbubble formulation for enhanced gene delivery

Authors:

Thomas Ador[1,2,3], Julie Schlederer[1,2], Mylène Fournié[1], Redouan MOUFTAH[2], Chantal Pichon[1,2.4], Arnaud Menuet[3], Anthony Delalande[1,2,5]

Affiliation:

[1] ART mRNA INSERM US55, Orléans, France

[2] LI²RSO, Université d'Orléans, France

[3] Laboratory of Experimental and Molecular Immunology and Neuromodulation (INEM), UMR 7355 CNRS-University of Orleans, Orleans, France

[4] Institut Universitaire de France, Paris, France

[5] Lead contact.

ABSTRACT

Microbubble (MB) functionalization can be performed by incorporation of specific drugs, particles, ligands, or contrast agents in the hydrophobic shell or at the MB surface. Such functionalization can be used to improve imaging or drug delivery both *in vitro* and *in vivo*. In this study we developed several custom functionalized MBs taking advantage of biotin-streptavidin binding, click chemistry, or electrostatic forces. We demonstrate successful surface binding to different molecules or particles such as magnetic nanoparticles and antibodies, providing magnetic or targeting properties. We also successfully developed two types of cationic MB, capable of complexing a plasmid DNA directly at the surface or in a polymer anchored in the MB shell. Acoustic analyses revealed efficient cavitation of unfunctionalized MB and both cationic MB, displaying their potential for gene delivery. It also demonstrated that the polymeric cationic MB had the best stability under focused ultrasound and displayed strong stable cavitation with lower inertial cavitation occurrences.

Keywords: Ultrasound; Microbubble; Targeting; Magnetic; Cationic; Oscillation

1. INTRODUCTION

Microbubbles (MB) were initially developed as an ultrasound imaging contrast agent, composed of a gas core, generally a perfluorocarbon, stabilized by a shell made of lipids, proteins, or polymers [1]. Apart from their contrast agent properties, MB's oscillation in an ultrasound field can create a push-pull action, microstreaming, and shear forces capable of opening pores in surrounding cells and transiently opening the blood-brain barrier (BBB) when occurring in a brain capillary [2–4]. As the BBB acts as a major limitation to the delivery of therapeutic drugs to the central nervous system (CNS), preventing over 98 % of small molecules and anything larger than 400 Da from crossing it, this application is a major step forward for the treatment of several brain diseases [5–7]. It allowed the development of several innovative treatments, such as gene therapy for several monogenic brain disorders [8–11], and even showed a therapeutic effect from BBB opening alone in Alzheimer's disease [12,13]. Many of these treatments already reached clinical trials and show promising results [14,15]. The oscillations allowing BBB opening can be divided into two cavitation regimes, the stable and inertial cavitation. The stable cavitation occurs at lower pressures and is characterized by linear expansion and contraction of MB volume depending on acoustic pressure. It is typically associated with a safe and predictable BBB opening [16–18]. Inertial cavitation on the other hand, occurs at higher pressure and is characterized by chaotic expansion and contraction of MB volume, leading to jetting events and bursts of MB. This cavitation regime is associated with strong BBB opening and potential brain damage like edema or hemorrhages [19–23]. MB cavitation can be monitored *in vivo* and processed post-treatment, providing information on the quality of the procedure and allowing us to anticipate potential damage or insufficient BBB opening. Or it can be processed in real time with the appropriate equipment, allowing the adaptation of acoustic pressure to the oscillations, ensuring sufficient BBB opening, and allowing the procedure to stop when inertial cavitation is detected, therefore preventing damages from occurring [21,24–27].

Commercially available MBs like SonoVue (Bracco, Milan, Italy) or Optison (GE Healthcare, Milwaukee, WI, USA) are generally used, as they are FDA-approved for human use making them easier to use in clinical trials and ensuring good biocompatibility, thus reducing the risk of adverse effects [15,28]. These MBs are generally not functionalized and are

used as BBB opening agents, co-injected with the therapeutic agents, but it is possible to add functionalization to MB to increase its efficiency. Numerous functionalizations are possible; they are generally drugs and particles added either within the hydrophobic shell or at the MB surface. Functionalized homemade MB can be used as contrast agents in other imaging modalities, like PET scans or fluorescence imaging, with the binding of a radioactive or fluorescent agent on the MB surface [29–31]. The addition of a specific antibody or ligand provides molecular targeting properties to MB that can improve ultrasound imaging or targeted gene delivery [32–35]. Magnetic properties can also be added by loading magnetic nanoparticles on MBs, making them responsive to a magnetic field. This allows them to accumulate in a precise location, improving ultrasound contrast imaging and gene delivery [36–38]. Finally, MB can be functionalized to load the therapeutic drug, either by charging the hydrophobic drug within the MB shell or binding it to the MB surface, using the drug's affinity with an available group, like by using electrostatic forces to complex nucleic acids to a cationic MB [39–41]. In gene delivery, the use of cationic MB allows the protection of nucleic acid from enzymes and improves targeted delivery and gene expression [8,42]. In addition, these functionalizations are compatible and can be used in the same MB, further improving gene delivery [30,34]. In this study, we show the development and characterization of several custom functionalized MBs based on an efficient and well-known lipidic homemade MB, providing targeting and cationic properties for enhanced delivery of nucleic acid.

2. MATERIALS AND METHODS

2.1 Animals

Adult male and female C57BL/6 aged above 8 weeks (Charles River, France) were used. All experiments were conducted in accordance with European ethical rules; the protocol was approved by the local ethical committees (protocol registered under numbers APAFIS#13749). Mice were housed under 12/12 light conditions in a controlled atmosphere (22 °C) and fed ad libitum.

2.2 Chemicals

1,2-distearoyl-sn-glycero-3-phosphocholine (DSPC), 1,2-distearoyl-sn-glycero-3-phosphoethanolamine-N-[methoxy(polyethylene glycol)-2000] (DSPE-PEG2000), 1,2-distearoyl-sn-glycero-3-phosphoethanolamine-N-[biotinyl(polyethylene glycol)-2000] (DSPE-PEG2000-Biot), 1,2-distearoyl-sn-glycero-3-phosphoethanolamine-N-[dibenzocyclooctyl(polyethylene glycol)-2000] (DSPE-PEG2000-DBCO), 1,2-dimyristoyl-sn-glycero-3-phosphocholine (DMPC), and 1,2-dimyristoyl-sn-glycero-3-phosphoethanolamine-N-[methoxy(polyethylene glycol)-2000] (DMPE-PEG2000) were purchased from Avanti Polar Lipids (Alabaster, Alabama, USA). 1,2-Distearoyl-sn-glycero-3-phosphoethanolamine-NHS ester (DSPE-NHS) was purchased from Broadpharm (San Diego, USA). The cationic lipid KLN27 (Figure S7.A) and the ionizable lipid MM30 (Figure S7.B) were synthesized by the Synanovect platform (Brest, France) and WuXiAppTech (China). Amine iron oxide nanoparticles were purchased from Bioparticles (Shirley, New York, USA). Perfluorobutane was obtained from F2 Chemicals (Preston, United Kingdom).

2.3 MB formulations

Unfunctionalized MB (uMB): Homemade lipidic microbubbles composed of DSPC and DSPE-PEG2000 (22: 3 molar ratio) were prepared as previously described [43]. Briefly, lipids were mixed in ethanol at a final concentration of 5 mM in 1.5 mL glass vials, followed by the formation of liposomes and freeze-drying of the sample. The headspace of the vial was filled with perfluorobutane, and the liposomes were hydrated with an HEPES solution (10 mM, pH = 7.4). Microbubbles were activated by mechanical agitation at 4500 rpm for 45 s using a Vialmix (BMS, Princeton, New Jersey, USA).

Biotinylated MB (bMB): Custom biotinylated MB were prepared as described above but were composed of DSPC, DSPE-PEG2000, and DSPE-PEG2000-Biot at a molar ratio of 88: 11.5: 0.5. For subsequent functionalization, bMB was first incubated for 10 minutes with 1 μg of streptavidin for 1 μL of bMB, followed by another 10 minutes of incubation with either 0.025 to 0.5 μg of biotinylated antibody or 50 μg (ratio 1) to 250 μg (ratio 2) of biotinylated magnetic particles (50 or 100 nm). Amine iron oxide nanoparticles were modified into biotinylated

magnetic nanoparticles with an overnight incubation with an NHS-biotin (sigma) in DMSO, followed by two magnetic separation purifications, replacing DMSO with HEPES buffer (10 mM, pH = 7.4).

DBCO-MB (dMB): Custom DBCO-MB for click chemistry were prepared as described above but were composed of DSPC, DSPE-PEG2000, and DSPE-PEG2000-DBCO at a molar ratio of 88: 11.5: 0.5. Before functionalization, the desired antibody was modified using the SiteClick™ Antibody Azido Modification Kit (Invitrogen, Waltham, Massachusetts, USA). This kit modifies the antibody's carbohydrate domain to introduce the N_3 group through the action of a transferase. Two strategies were evaluated to functionalize dMB. The first strategy consisted of incubating dMB after mechanical activation for 30 minutes with 0.05 µg of N_3 antibody. The second strategy relies on the modification of the DSPE-PEG2000-DBCO prior to MB formulation. For this, DSPE-PEG2000-DBCO was incubated overnight at room temperature with an N_3 antibody (molar ratio 44: 1), MB was then formulated as described above using the modified lipid. With this strategy, 0.05 µg of N_3 antibody was used for 1 µL of dMB.

Cationic MB (cMB) 1st generation: The first generation of custom cationic MB was prepared as described above but was made of DMPC, DMPE-PEG2000, KLN27, and MM30 at a molar ratio of 44.76: 2.9: 43.67: 8.67.

Polymeric cationic MB (pMB): This second generation of cationic MB were prepared using a polyethyleneimine 25 000 Da (PEI) modified as follow: first, it would be incubated for over 6 hours with DSPE-NHS (molar ratio 1: 1) in an EtOH: chloroform mix, with the addition of DIEA base. It is followed by an incubation with Boc-His(1-Boc)-Osu (molar ratio 1: 33) for over 6 hours. Excess trifluoroacetic acid is then added to the mix to unprotect histidine from Boc protective groups, and the mix is incubated overnight. The product is then purified by ether precipitation, and the resulting final product is dried before resuspension in absolute ethanol for MB formulation and will be called DSPE-PEI-His. The polymeric cMB is then prepared as described above but is made of DSPC, DSPE-PEG2000, and DSPE-PEI-His at a molar ratio of 87: 12: 1.

Size selection protocol: In order to collect MB in the function of size, the activated MB vial was placed upside down in a custom holder and centrifuged at 100 g for 5 minutes. The vial was then gently removed, and a syringe was used to remove 150 µL of solution, with the needle

placed at the bottom limit with the sealed cap to collect the lower part of the solution. The solution was placed in a new sealed vial filled with perfluorobutane; this solution is then called fraction 1. This collection was repeated twice and placed each time in a new sealed vial; these fractions were called fraction 2 and 3 respectively. The rest of the MB solution was discarded.

2.4 MB characterization

Optical imaging: Following activation, MB concentration and size distribution were measured using an upright trinocular microscope (Leitz Laborlux D, obj ×25) connected to a camera (The Imaging Source, Germany) on a 0.2 mm Thoma slide, and images were analyzed using the particle analysis plugin of ImageJ software.

Videodrop: Activated MB were dispersed in an HEPES buffer at a 1/100 dilution, and 7 µL of the diluted solution were deposited on the Videodrop (Myriade, France) slide for the measure. Myriade company provided custom analysis software that we used in this study but is not commercially available, thought to be capable of differentiating gas-filled particles like nanobubbles from liquid-filled particles like liposomes. Briefly, the particles are illuminated by a blue light, and the diffracted light is recorded. The interferometric signal of particles is then calculated, forming a white and dark doublet, and the images are processed to measure the Brownian movement of the particles. Theoretically, the white and dark doublet is inverted when the particle is filled with gas instead of water.

2.5 Characterization of MB functionalization

Optical imaging: Magnetic properties of MB functionalized with magnetic nanoparticles (MB-MAG) were assessed in optical imaging. Briefly, following functionalization, MB-MAGs were dispersed in HEPES buffer and deposited on a 0.2 mm Thoma slide under an inverted microscope (Leitz Laborlux D, obj ×25). A 50×15×15 mm neodymium magnet was placed on the slide's side, and the displacement of MB-MAGs was recorded with a camera (The Imaging Source, Germany) and analyzed using ImageJ software.

Flow cytometry: To study pDNA complexation on cMB, pDNA was first labeled using the Label IT® Nucleic Acid Labeling Kit Cy5 (Mirus, Madison, USA) following their protocol, then 2.5 µL of cMB was diluted in 250 µL of HEPES buffer (10 mM, pH = 7.4) and were complexed with increasing Cy5-labeled pDNA, from 0.5 to 7.5 µg. cMB and Cy5-labeled pDNA were allowed to complex directly in the cytometer tube and fluorescence of cMB were assessed after 1, 2, 5, and 10 minutes of complexation. SSC was performed with the violet laser (λ = 450 nm) to improve sensibility with small objects, and fluorescence intensity was assessed with the red laser (λ = 633 nm) with a filter band-pass of 660/10 nm. Cytometer gating was calibrated using non-cationic MB, with the ratio 1 µL of MB for 1 µg of pDNA.

Fluorescence imaging: To confirm streptavidin coupling, bMB was complexed with fluorescein-labeled streptavidin for 10 minutes (1 µg for 1 µL of bMB) and was imaged with Vidéo Observer Z7 Apotome2 (Carl ZEISS, Jena, Germany). For antibody coupling, bMB was first complexed with streptavidin (1 µg for 1 µL of bMB), followed by 10 minutes of complexation with a biotinylated antibody. They were then labeled with an Alexa 594 secondary antibody for over 45 minutes before imaging using Vidéo Observer Z7 Apotome2 (Carl ZEISS, Jena, Germany).

To confirm cMB complexation DNA, confocal microscopy was performed using LSM 980 AiryScan 2 (Carl ZEISS, Jena, Germany) with 1 µL of MB complexed with 1 µg of Cy5-labeled pDNA for 1 minute before being deposited on the slide.

Dynamic light scattering (DLS): Activated MB were dispersed in a 5 mM NaCl buffer at a 1/100 dilution in a specific tank for zeta potential measures. DLS was performed with a Zetasizer Ultra Red (Malvern), and the zeta potential measures were the average of 3 successive measures.

Gel shift assay: A 0.6% agarose gel was prepared with 1/10 000th SYBRSafe and was allowed to cool down and polymerize. 1 µg of pDNA was complexed with an increasing amount of MB solution (from 0.5 to 5 µL) for 2 minutes before the addition of the loading dye and deposition in the gel. Migration was performed with a 120 mV electric current for 20 minutes. Images were recorded under a UV light.

2.6 Characterization of acoustic properties

Ultrasound imaging: For *in vitro* measure of echogenic properties of MB, and stability over time, using an ultrasound imaging system (VEVOLAZR, Visualsonics, Fujifilm, Canada), with 1×10^8 MB diluted in 50 mL of PBS with 7.5% of BSA to mimic blood homeostasis and total protein concentration. The solution was deposited in a beaker with acoustic absorbents at the bottom, and the MS250 probe (22 MHz, VisualSonics, Fujifilm, Canada) was immersed in it. Echographic contrast power was measured for 30 minutes at a 1 Hz framerate under 150 rpm magnetic steering.

For *in vivo* measurement of echogenic properties of MB, 100 µL of MB solution in 5 % sucrose was injected in the tail vein of mice under gaseous anesthesia (2 to 4 % isoflurane in air). The tissue of interest was imaged with an ultrasound imaging system (VEVOLAZR, Visualsonics, Fujifilm, Canada).

Oscillation analysis: Cavitation was assessed using a 1 MHz focused bowl transducer with a 45 mm diameter active element (DL-47 piezo material, radius of curvature 45 mm, Precision Acoustics, UK) pierced in the middle to insert a passive cavitation detector. It has an ellipsoid-shaped focal spot of 6×1.5 mm and was controlled with a custom 3-axis motorized stage (IndustryLab, Orléans, France) with a laser beam used to guide the focal spot to the targeted region. The transducer was connected to a linear amplifier (E&I, 210L) connected to a waveform generator (Agilent 33210A) to deliver the ultrasound treatment. All systems were calibrated using a hydrophone (Onda HGL200, USA) in a separate tank in degassed water. A 1.5 % agarose phantom was prepared with a linear canal formed by an 18G needle (OD: 1.27 mm), removed once the gel was fully polymerized. Ultrasound coupling between the gel and the transducer was done with water (Figure 1.A). A 1×10^8 MB/mL solution was pushed into the canal at 0.5 mL/min using a syringe pump (Harvard Apparatus, Holliston, Massachusetts, USA), and 1 MHz pulsed ultrasound (1 Hz PRF, 5 % DC) was applied. A 10 MHz PCD placed at the center of the bowl transducer was used to detect non-linear cavitation signals. The signal was amplified by a 20 dB preamplifier (Precision Acoustics) and recorded by a picoscope 5244 MSO and the picoscope 7 software (Pico Technology, UK). Stable and inertial cavitation were then calculated using Matlab software.

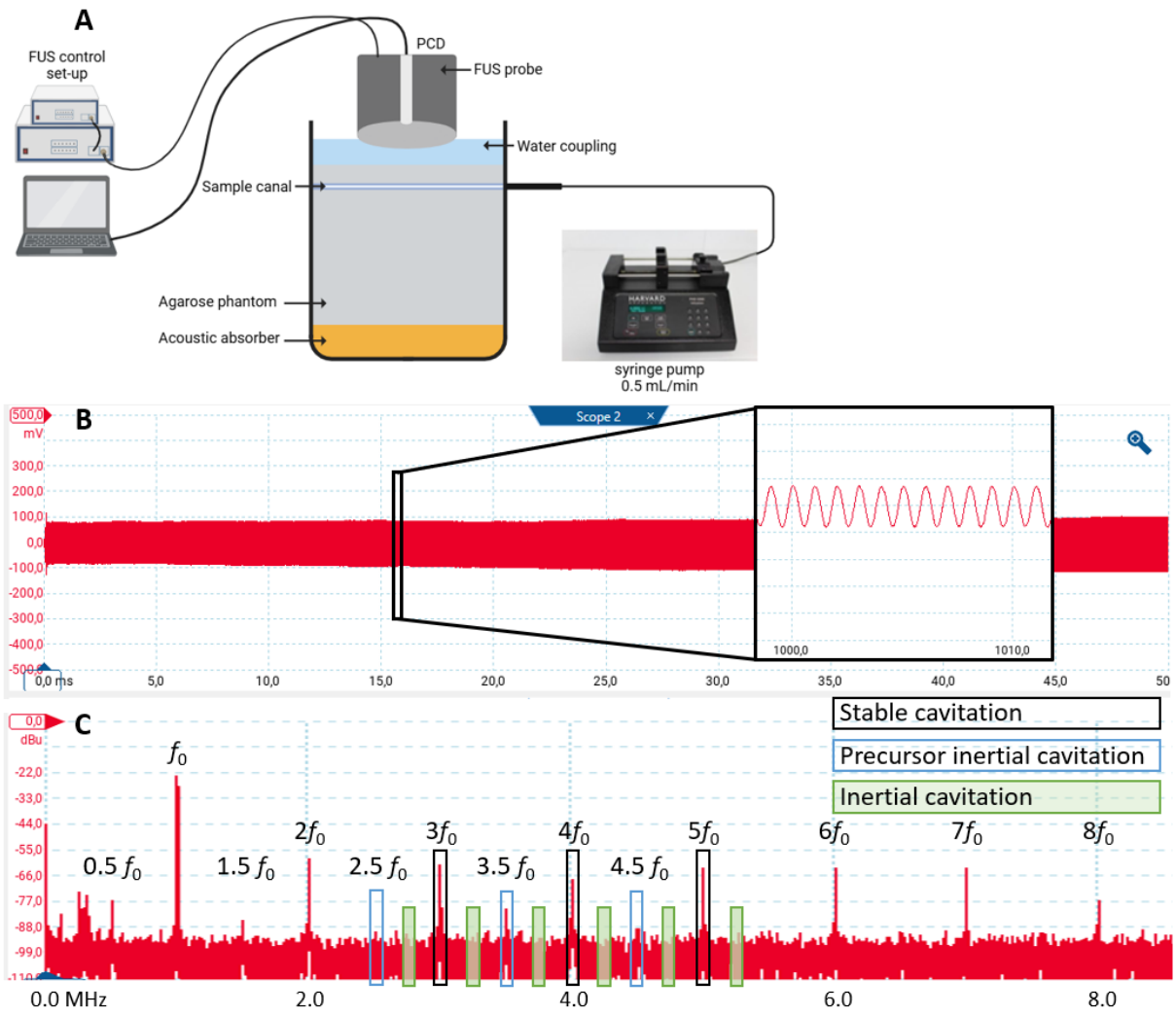

Figure 1: MB cavitation analysis set-up. (**A**) Schematic representation of the experimental set-up for cavitation analysis (**B**) Oscilloscope signal received from the passive cavitation detector (PCD) as observed in PicoScope 7 software. (**C**) Fourier transform spectrum of the signal from the PCD, with harmonics included in the analysis.

2.7 Cell culture

For subcutaneous tumor implantation, CT2A cells were first cultivated *in vitro* in DMEM supplemented with 5 % fetal bovine serum (FBS) and 1 % penicillin and streptomycin in a controlled atmosphere (37 °C, 5 % CO_2). Cells were harvested and pelleted before resuspension in PBS buffer. Prior to implantation, mice were anesthetized with gaseous anesthesia (isoflurane 1.5 to 3 % in air) and depilated at injection sites. 50 µL of CT2A

suspension containing 1×10^5 cells was injected subcutaneously in mice's flanks under gaseous anesthesia.

For cytotoxicity assessment of magnetic MB, primary cells were obtained from juvenile mice brains. The meninges, olfactory bulbs, cerebellum, brain stem, and hippocampus were removed to obtain a more homogeneous cell batch. Cells of the remaining brain parts were isolated by mechanical cell dissociation. Cells were then incubated in culture flasks in DMEM enriched with 20 mM L-alanyl-L-glutamine, 5 % fetal bovine serum (FBS), and 1 % penicillin and streptomycin in a controlled atmosphere (37 °C, 5 % CO_2). They were cultured until sufficient confluency was reached, then they were placed in a 24-wells plate. XTT assays were then performed by adding 0.1 µL of magnetic MB or its isolated components for 24 h in the cell media. For isolated IONP, 25 µg were used, corresponding to the ratio with the highest IONP amount. 50 µL of XTT reagents were added to the wells and were incubated for 3 hours at 37 °C. Absorbance was measured at 490 and 690 nm and was assessed using a CLARIOstar Plus (BMG Labtech, Ortenberg, Germany).

2.8 Statistics

Nonparametric Mann-Whitney bilateral tests were performed using the R language (version 4.4.0, used with R Studio software). Non-linear fit and F-test were performed using GraphPad Prism v10. A *p*-value below 0.05 was considered significant. All data are expressed as mean +/- standard error of the mean (SEM).

3. RESULTS AND DISCUSSION

3.1 Characterization of unfunctionalized MB

Our first homemade unfunctionalized MB is inspired by a well-known lipidic MB composition, with DSPC and DSPE-PEG, usually at a 9:1 molar ratio but optimized in our team at an 88:12 molar ratio (data not shown). We show with optical microscopy an expected

polydisperse distribution of MB size, with an average median size of 1.30 +/- 0.01 µm (Figure 1.A), similar to equivalent MB in other studies or some commercially available MB like DEFINITY® [44]. We also display an important concentration, reaching 2.41×10^{10} +/- 2.11×10^{9} MB/mL. However, optical microscopy is physically limited to objects below 400 nm, hiding potential nanoscale objects in solution. VideoDrop measurements were performed to assess lower-sized objects and indicated a concentration of nanoscale particles over 10-fold higher than MB, as calculated with optical microscopy. The modified non-commercial software provided by the Myriade company turned out to be efficient at discerning liposomes from nanobubbles, as no nanobubbles can be detected before MB activation, whereas 1.6×10^{11} +/- 1.7×10^{10} nanobubbles are detected after MB activation. In addition, we detected a significant 30-fold drop in liposome concentration after activation, from 5.1×10^{11} +/- 6.3×10^{10} to 1.5×10^{10} +/- 4.1×10^{9}, suggesting a gas incorporation to form NB and MB through mechanical activation. Although, to fully confirm the ability of the Videodrop to discern NB from liposomes, we still need to compare it with the resonant mass measurement (RMM) technique, whose ability to discern buoyant from non-buoyant particles has been demonstrated by Hernandez *et al.* [45]. It also showed a polydisperse NB size distribution with a low average median size of 229.3 +/- 9.8 nm (Figure 1.C). Remaining liposomes display a wider size distribution, with an average median diameter of 339.9 +/- 19.7 nm. 31P RMN has also been used to measure and confirm molar ratios of particle constituents (Figure S1). Separated constituents can be successfully detected with a single signal, and their relative proportion can be assessed with integral determination. Though precision of calculated integration seemed too limited to calculate molar ratio with sufficient precision to detect small manipulation errors or constituents with a small proportion, like DMPE-PEG2000 in the first generation of cationic MB.

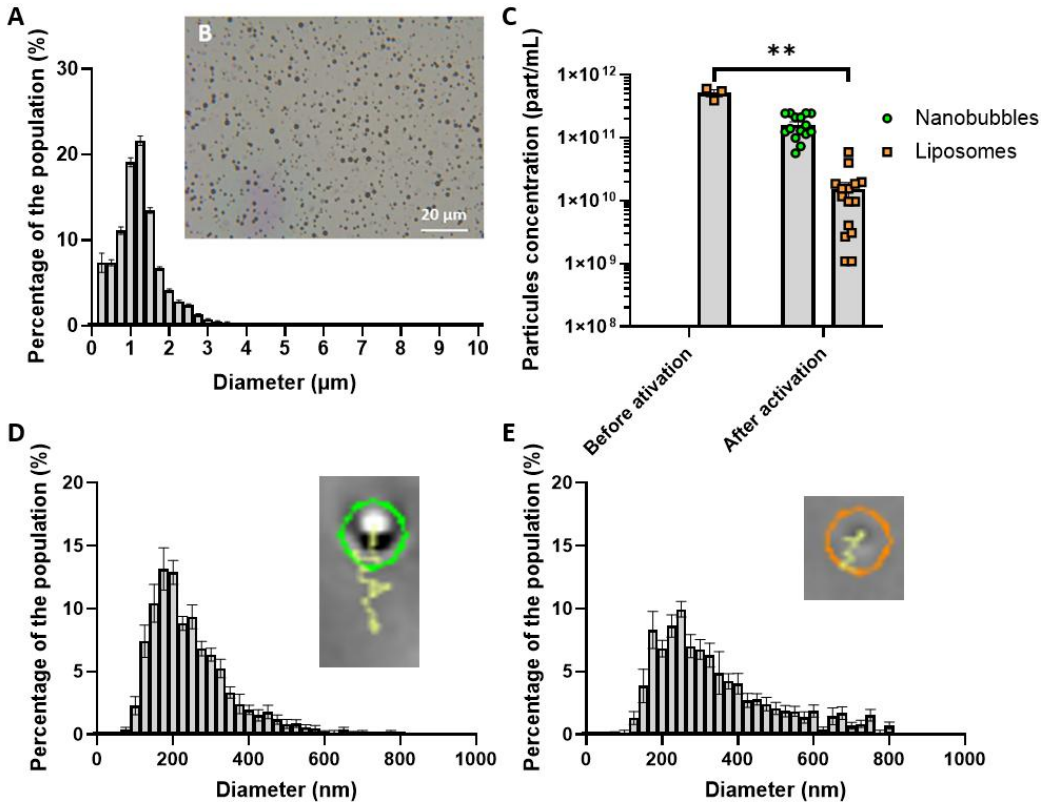

Figure 2: Unfunctionalized MB characterization. (**A**) Size distribution of unfunctionalized MB measured in optical microscopy. (**B**) Optical microscopy image of unfunctionalized MB. (**C**) Nanobubble and liposome concentration in unfunctionalized MB solution, before and after MB activation. (**D**) Size distribution diagram measured in VideoDrop® of nanobubbles in unfunctionalized MB solution and image of a typical nanobubble after image processing. (**E**) Size distribution diagram measured in VideoDrop® of liposomes in unfunctionalized MB solution and typical liposome object after image processing. Data expressed as mean +/- SEM. * = *p*-value < 0.05; ** = *p*-value < 0.01; Mann-Whitney bilateral test.

3.2 Targeted MB

In order to functionalize the MB surface, the most usual technique relies on the use of the biotin and streptavidin complex [32]. To use it, a biotinylated MB (bMB) formulation was developed prior to further functionalization and showed very similar characteristics to unfunctionalized MB, with an average concentration of 2.3×10^{10} +/- 2.3×10^{9} MB/mL, an average median diameter of 1.33 +/- 0.01 µm, and a similar size distribution (Figure S2). First, the bMB-streptavidin complex was confirmed with fluorescence microscopy using FITC-labeled

streptavidin (Figure 3.A). Almost all bMB were successfully linked to streptavidin with the ratio used. We then attempted to give our bMB targeting properties by linking a biotinylated antibody to the linked streptavidin. This was assessed first in flow cytometry, using a secondary antibody to fluorescently label bMB and to measure the minimum amount of antibody required to functionalize MB. This showed a clear correlation of labeled bMB with the amount of antibody from 0.025 to 0.375 µg ($R^2 = 0.91$), where a maximum of 17.2 +/- 1.5 % labeled bMB was reached in the conditions studied. This was confirmed in fluorescence microscopy, where we observed several fluorescent bMB (Figure 3.B). It is most likely possible to increase the amount of functionalized bMB higher, but this would probably require a largely higher amount of antibody since the linear correlation between functionalized bMB and antibody amount was lost starting from 0.5 µg. Furthermore, this amount of MB functionalization could be enough while avoiding MB destabilization from an excess of antibody on the MB surface.

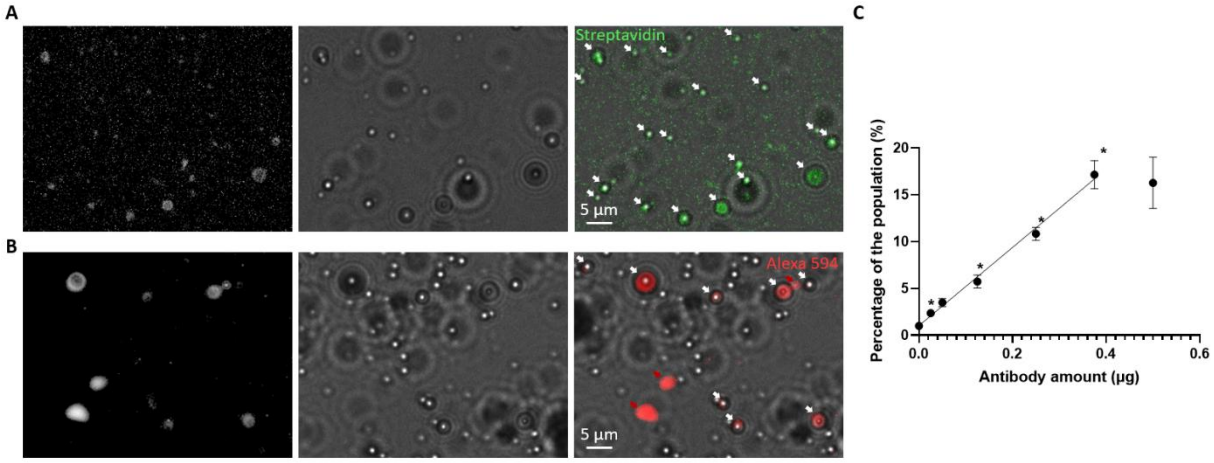

Figure 3: MB antibody functionalization with streptavidin-biotin complex. (**A**) Fluorescent microscopy of bMB after over 10 minutes of complexation with streptavidin-fluorescein; the white arrow indicates positive MB (**left**: fluorescein; **middle**: brightfield; **right**: merge) (**B**) Fluorescent microscopy of bMB after complexation with streptavidin and biotinylated antibody, followed by incubation with Alexa 594 secondary antibody; the white arrow indicates positive MB and the red arrow indicates secondary antibody aggregates (**left**: Alexa 594; **middle**: brightfield; **right**: merge) (**C**) Percentage of fluorescent MB after complexation with streptavidin and increasing amounts of antibody, followed by incubation

with Alexa 594 secondary antibody. Data expressed as mean +/- SEM. * = *p*-value < 0.05; Mann-Whitney bilateral test for each antibody amount compared to the previous tested quantity.

Another method used in this study to develop targeting functionalization relies on the use of click chemistry. Previous studies suggest that this could be an effective and reliable approach to functionalize MB since an unbreakable covalent bond is formed. DBCO-MB (dMB) was formulated for this purpose which also appeared to be very similar to unfunctionalized and biotinylated MB. It had a similar polydisperse size distribution, with an average median diameter of 1.33 +/- 0.05 μm and a concentration of 1.9×10^{10} +/- 1.9×10^{9} MB/mL. We first assessed its ability to link with an N_3 antibody in fluorescent microscopy like before, where we did not obtain any labeled dMB. However, when click chemistry was performed prior to dMB formulation and functionalization, we showed a significant population of labeled dMB with 6.2 +/- 0.6 % of positive MB. This proportion of functionalized dMB is relatively positive considering the low amount of antibody used compared to bMB and would probably get higher with increased antibody amount, similarly to bMB. dMB functionalization was further confirmed in fluorescent microscopy; we were able to detect labeled MB (Figure 4). We also confirmed the successful click chemistry with mass spectrometry, depicting an m/z weight peak shift from 147 839 +/- 114 Da to 155 346 +/- 1038 Da. This corresponds to about 2 DSPE-PEG2000-DBCO (3075.88 Da) labeling and is confirmed by the wider peak due to the PEG size heterogeneity (Figure S3). It highlights the difficulties for the DBCO group to react with the antibody N_3 group once on the dMB surface. Using HSA-DBCO MB, Liu *et al.* demonstrated that the DBCO-N_3 reaction was fast, with a noteworthy portion of MB already functionalized after 1 minute, and most functionalization was done after 5 minutes of incubation [46]. Thus, this shows that our reaction time was more than sufficient. Goncin *et al.* also performed this click chemistry reaction using PE-PEG2000-DBCO, obtaining very similar MB than in our study, and demonstrated successful linkage with an N_3-aptamer [35]. The notable difference with our study is their use of a purification step following MB formation. Thus, it is likely that in our study the remaining liposomes and free DSPE-PEG2000-DBCO reacted with the N_3 antibody before dMB, preventing their functionalization.

Altogether, we developed here two functionalized MBs capable of linking with an antibody to their surface. This will allow us in future studies to improve drug delivery both *in vitro* and *in vivo* as shown in previous studies [32,33,47,48].

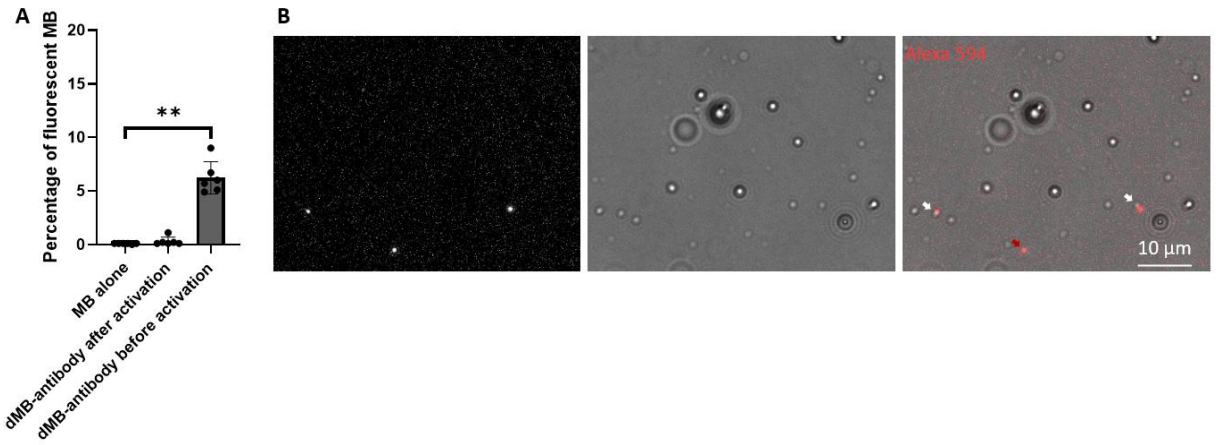

Figure 4: MB antibody functionalization with click chemistry (**A**) Fluorescent microscopy of dMB after complexation with streptavidin and biotinylated antibody, followed by incubation with Alexa 594 secondary antibody; the white arrow indicates positive MB, and the red arrow indicates secondary antibody aggregates (**left**: Alexa 594; **middle**: brightfield; **right**: merge) (**B**) Percentage of fluorescent MB after click chemistry with N_3 antibody before or after MB activation followed by incubation with Alexa 594 secondary antibody. Data expressed as mean +/- SEM. * = *p*-value < 0.05; ** = *p*-value < 0.01; Mann-Whitney bilateral test.

3.3 Magnetic MB

We formulated custom MB with magnetic functionalization inspired by the SurfMB described by Beguin *et al.*, with iron oxide nanoparticles (IONP) attached to the bMB surface by streptavidin-biotin coupling [36]. These bMB were functionalized as described for antibody linking with either 50 nm (NP50) or 100 nm (NP100) IONP at two different ratios, and their displacement under a magnetic field showed a uniform movement toward the magnet. Their movement speed was assessed by manually tracking the MB and showed a displacement at an average speed of 12 µm/s with the first ratio and reached 25 µm/s with the second ratio, independently of IONP diameter. If magnetic MB are allowed to move upward with buoyant movement prior to applying a magnetic field, the friction forces at the interface with the slide become too strong and the MB don't move with the application of a magnetic field. However,

these magnetic MBs will then get oriented according to the magnetic field, forming the typical shape of magnetic particles (Figure 5). The absence of cytotoxic effect of each component was assessed with MTT, which showed no significant difference between the control and magnetic MB or its components at any ratio used. This shows the possibility to use these MBs for drug delivery *in vitro* or *in vivo*. Moving forward, we will use these magnetic MB both *in vitro* and *in vivo* by applying a magnetic field to accumulate them in the desired area. It can be used either on cells for enhanced drug delivery or in the targeted area *in vivo* to enhance contrast imaging, BBB opening, and targeted drug delivery, as shown by previous studies [38,49–51].

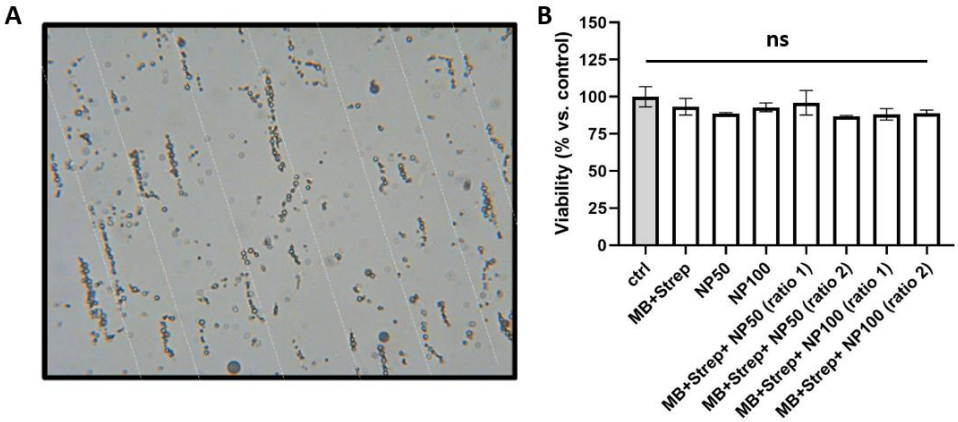

Figure 5: Magnetic MB characterization. (**A**) Microscopic image of magnetic MB oriented with the magnetic field, as represented by the white dotted lines. (**B**) Cell viability measured in XTT, 24 h after incubation with components of magnetic MB. Data expressed as mean +/- SEM. * = *p*-value < 0.05; Kruskal-Wallis test.

3.4 Size-specific MB

Size-specific MB has the advantage of having a more homogenous response to ultrasound and often shows improved BBBo and contrast ultrasound imaging. Furthermore, Perera *et al.* showed the ability of NB to penetrate in tumors to improve ultrasound contrast imaging [52]. Based on these principles, we aimed to isolate the smaller-sized MB from our polydisperse MB solution by centrifugation. We used our biotinylated MB in order to be able to later functionalize them with an antibody to target tumor-specific biomarkers beyond tumor vasculature. Our centrifugation protocol allowed us to isolate 3 different fractions with narrower size distribution and significantly lower median size compared to uncentrifuged

MB, as assessed in optical microscopy. It reached an average median size of 0.90 +/- 0.01 µm for the first phase, significantly lower than phases 2 and 3 which showed no significant difference (1.10 +/- 0.01 and 1.18 +/- 0.03 µm, respectively). Even though the first phase was largely composed of NB, it did not show significant improvement in ultrasound contrast imaging of the CT2A tumor, reaching 4158 +/- 1959 A.U. compared to 1000 +/- 461 A.U. with uncentrifuged MB. However, the use of the second phase significantly improved peak contrast enhancement, achieving 12394 +/- 2091 A.U., demonstrating the ability of small MB to better penetrate tumor vasculature (Figure 6). This enhanced vasculature penetration was confirmed by a more homogeneous signal within the tumor (Figure 6.D). The third phase showed a similar signal to the second phase, with 12482 +/- 4693 A.U., further confirming the advantage of small and homogeneous MB for contrast imaging of tumor tissues. The low efficiency of NB compared to other studies could be due to the imaging probe used (MS250 probe at 22 MHz) that might not be adapted to sub-micron bubbles. Another possible explanation is the lower total gas volume, which could be addressed by increasing NB concentration.

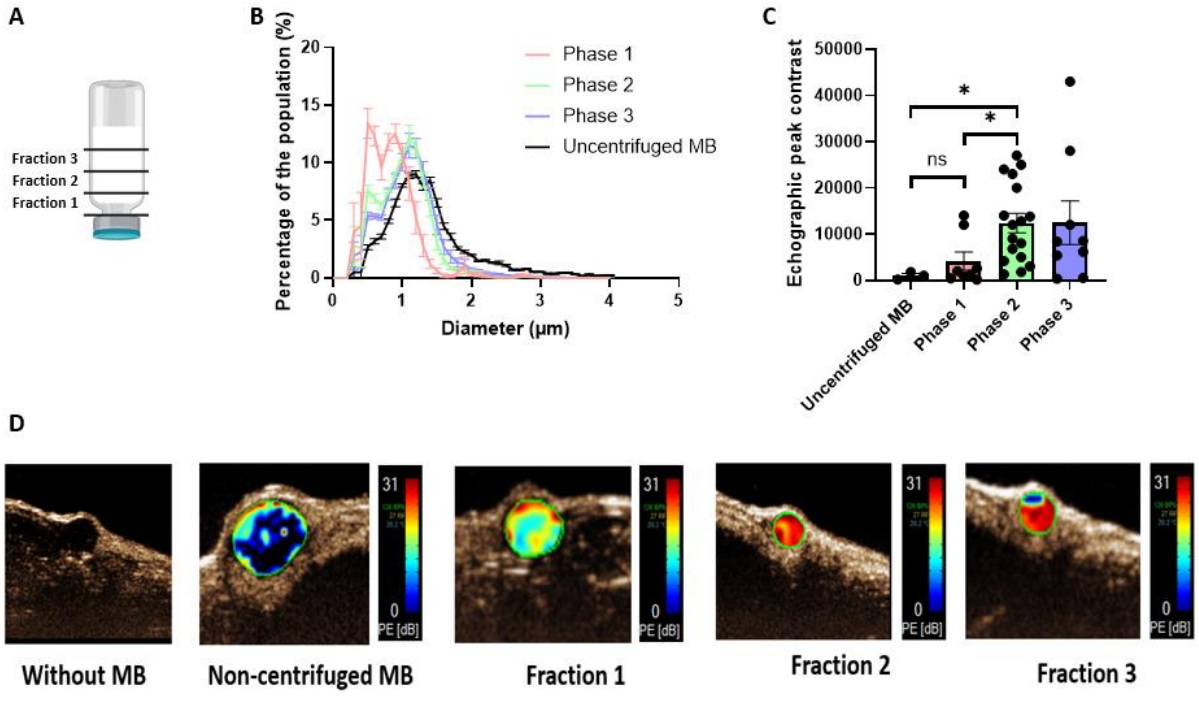

Figure 6: Size modification of microbubble and its effect on contrast enhancement. (**A**) Schematic representation of different fractions following centrifugation-based size exclusion. (**B**) Size distribution of the different fractions following size exclusion centrifugation. (**C**) Ultrasound imaging peak contrast power induced by different fractions following size exclusion centrifugation in CT2A subcutaneous

tumor. (**D**) Ultrasound imaging contrast power images induced by different fractions following size exclusion centrifugation in CT2A subcutaneous tumor. Data expressed as mean +/- SEM. * = *p*-value < 0.05; Mann-Whitney bilateral test.

We described a way to increase MB concentration with increased mechanical MB activation time with the Vialmix (Figure 7). It showed an increased concentration of MB with mechanical activation time for up to 180 seconds, where a maximum is reached, as assessed in optical microscopy. A linear regression was calculated from 45 to 180 seconds of activation, showing a clear correlation ($R^2 = 0.99$). It also indicated that the median size decreased with higher activation time, though the limit was not reached for up to 240 seconds, reaching 1.12 µm. This suggests that bubble concentration might reach a maximum later than 180 seconds due to an increasing formation of objects below the optical microscopy range. VideoDrop measures will be required moving forward to assess this NB evolution with activation time that is probably increasing and potentially even after 180 seconds as the particles will probably remain within measure range (80 to 500 nm). This could also be a promising method to generate NB and small MB with a narrow size distribution. These NBs will also be used for *in vivo* drug delivery, since NB has been shown to improve drug and gene delivery in the brain [53]. NB also has the advantage of being able to penetrate smaller capillaries, therefore improving the procedure's efficiency [54].

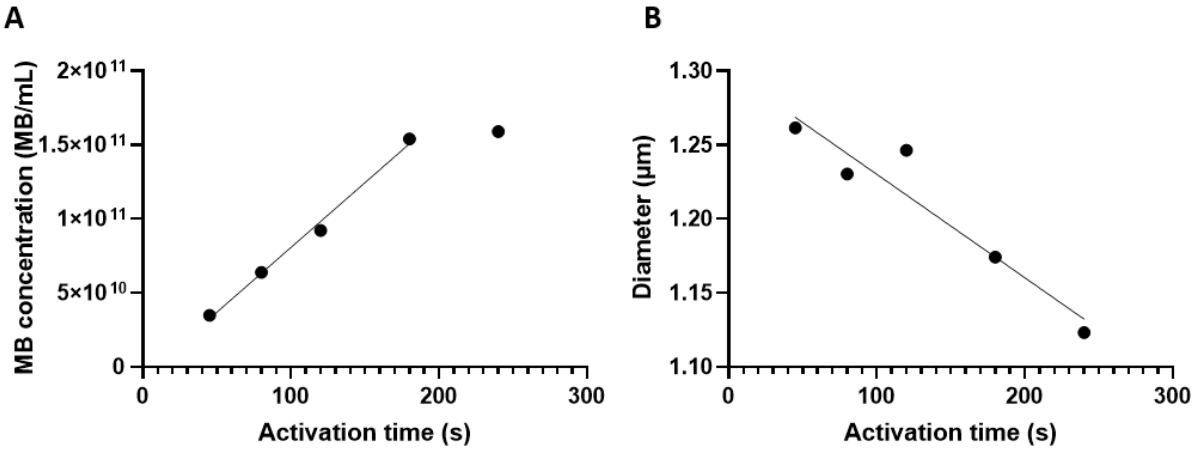

Figure 7: MB size modulation with mechanical agitation time. (n = 1) (**A**) Evolution of MB concentration as a function of mechanical activation time. (**B**) Evolution of MB median diameter as a function of mechanical activation time. Data expressed as mean +/- SEM. Linear regression calculated with GraphPad.

3.5 Cationic MB

3.5.1 Cationic MB first generation

In order to improve non-viral gene delivery, cationic microbubbles (cMB) can be used. These bubbles are capable of complexing nucleic acids, thereby protecting them and enhancing their targeted delivery [41,55,56]. We formulated a first generation of novel cMB constituted of cationic and ionizable lipids, adapted from a known liposome formulation that previously proved its efficiency to deliver nucleic acid [57,58]. First, optical microscopy characterization of cMB showed a slightly lower concentration (9.9×10^{9} +/- 5.0×10^{8} MB/mL) compared to unfunctionalized MB, but with a similar size distribution and a comparable median diameter of 1.19 +/- 0.02 μm (Figure 8.A). We then confirmed with the Zetasizer the cationic properties of these MB, with a 19.1 +/- 0.5 mV zeta potential. VideoDrop was used to measure the proportion of free liposomes and nanobubbles in our solutions. This analysis showed a significantly lower NB concentration compared to unfunctionalized MB, of respectively 8.1×10^{10} +/- 2.6×10^{10} and 1.6×10^{11} +/- 1.7×10^{10} NB/mL. Similarly, a significantly higher liposome concentration was measured in cMB compared to unfunctionalized MB, with 4.0×10^{11} +/- 7.3×10^{10} and 1.5×10^{10} +/- 4.1×10^{9} parts/mL, respectively. However, NB and liposomes show similar size distributions when compared to experiments made with unfunctionalized MB, suggesting that similar objects are formed, but with lower efficiency with this first generation of cMB (Figure 8.C, D). Their ability to complex with nucleic acids is demonstrated later in this study, alongside their application for BBBo and gene delivery.

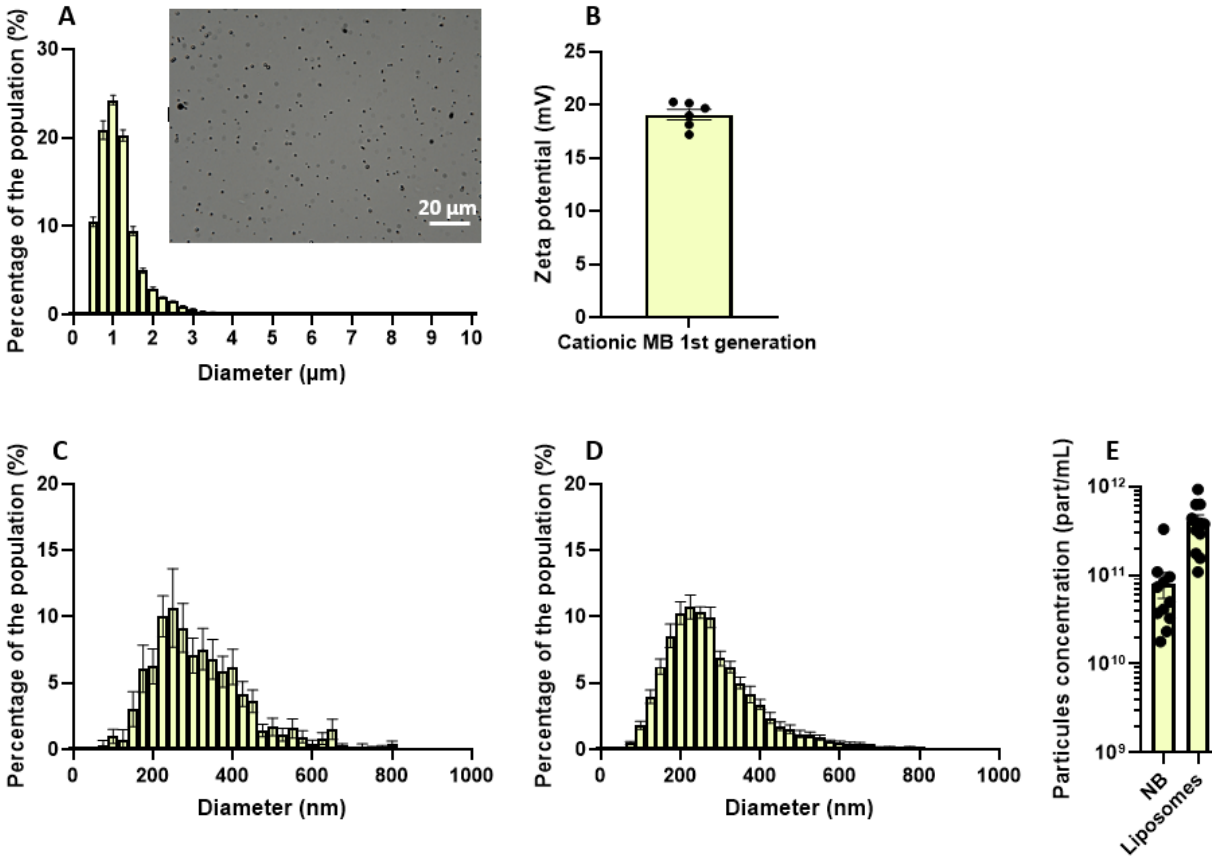

Figure 8: Cationic MB first-generation characterization. (**A**) Size distribution of the custom cationic microbubbles (mean with SEM, n = 53), with an optical image used for size and concentration determination, optical microscope, magnification ×25. (**B**) Zeta potential of cationic MB first generation (**C**) Size distribution diagram of nanobubbles measured in VideoDrop® in cationic MB solution. (**D**) Size distribution diagram of liposomes measured in VideoDrop® in cationic MB solution. (**E**) Nanobubble and liposome concentration in cationic MB solution. Data expressed as mean +/- SEM.

3.5.2 Polymeric cationic MB (pMB)

Cationic MB surface binding of nucleic acid can lead to modification of the MB acoustic properties and eventually to MB collapse due to surface tension modifications. Delocalizing the cationic charge from the MB surface, and therefore loading of pDNA, can be a way to avoid MB destabilization. This can be done either by complexing pDNA in a liposome, later bound onto the MB surface like previously presented, or by incorporation of a cationic polymer in the MB [59,60]. Based on this principle, we developed another formulation of cationic MB inspired by Jin *et al.*, with an MB shell similar to unfunctionalized MB and with a polyethyleneimine

(PEI) cationic polymer anchored in the MB shell [61]. We adapted them with DSPC anchoring to better fit in our MB formulations and modified the PEI with histidine to initiate the proton pump effect for endosomal escape as developed by Gonçalves *et al.* for polyplexes-mediated gene delivery [62]. These polymeric cationic MB (pMB) displays similar MB concentration and size distribution as the unfunctionalized MB, with 1.6×10^{10} +/- 1.6×10^{9} MB/mL and an average median diameter of 1.24 +/- 0.04 μm. With VideoDrop analyses, we also see similar NB concentration and size distribution, with 1.0×10^{11} +/- 1.9×10^{10} NB/mL and an average median diameter of 241.3 +/- 7.2 nm. Similarly, it showed equivalent liposome concentration, but with a larger proportion of large particles, reaching 2.1×10^{10} +/- 1.3×10^{9} part/mL with an average median diameter of 418 +/- 31.75 nm. Compared to uMB and the first cMB, they also display similar MB and NB size distributions (Figure 9). Furthermore, these data show significantly higher MB and NB concentrations than the first generation of cationic MB and lower liposome concentrations. They also showed significantly higher stability under ultrasound imaging *in vitro*, with a significantly higher contrast enhancement signal over time. This demonstrates the higher efficiency for MB and NB formation from this cationic pMB formulation, which might be due to the use of C18:0 phospholipids compared to the C14:0 phospholipids used in the first generation.

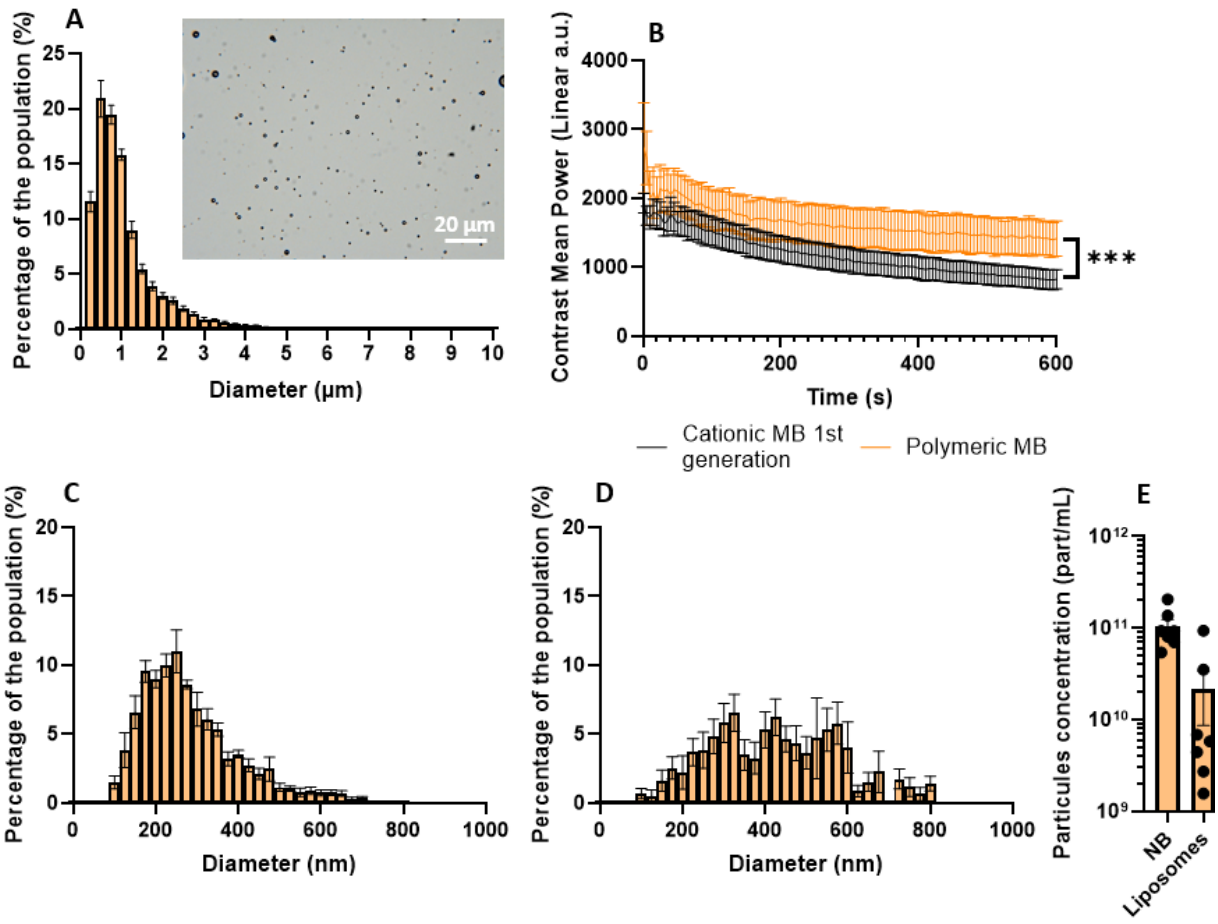

Figure 9: Polymeric cationic MB characterization. (**A**) Size distribution of the cationic microbubbles (mean with SEM), with an optical image used for size and concentration determination, optical microscope, magnification ×25. (**B**) 1st generation cationic MB and polymeric cationic MB ultrasound imaging contrast power over time in PBS with 7.5 % BSA of 1×10^8 MB, non-linear regression, and F-test performed with GraphPad Prism v10. (**C**) Size distribution diagram of nanobubbles measured in Videodrop® in polymeric cationic MB solution. (**D**) Size distribution diagram of liposomes measured in Videodrop® in polymeric cationic MB solution. (**E**) Nanobubble and liposome concentration in polymeric cationic MB solution. Data expressed as mean +/- SEM. *** = *p*-value < 0.001; F-test

3.5.3 Polymeric cationic MB can complex with pDNA

Similarly to the first generation of cMB, pMB's ability to complex with pDNA was validated first with a gel shift assay. It showed their ability to fully complex 1 µg of pDNA with only 1 µL of MB, 2-fold lower than the first cMB (Figure 10.A). This demonstrates a higher loading capacity compared to the previous cMB despite a similar zeta potential, as calculated with DLS. This was further confirmed with flow cytometry, which reached up to 93.9 +/- 1.8

% of Cy5-labeled pMB. However, unlike with the first generation of cMB, where the maximum of functionalized cMB was reached with the same amount needed to fully load cMB, with pMB only 3.9 +/- 0.6 % were labeled with 1 µg of DNA. A significant increase in labeled pMB occurs with higher pDNA amounts, reaching a plateau at 5 µg, with 86.6 +/- 7.4 % of labeled pMB. This is most likely be due to liposomes, polyplexes and free PEI complexing with pDNA before MB, and that are too small to be detected in flow cytometry. This limitation could be addressed with a purification step with centrifugation. This was performed prior to confocal microscopy of pMB complexed with Cy5-labeled pDNA. It confirmed MB loading with pDNA in most MB, despite the amount of pDNA used, showing the efficiency of this purification step to induce pDNA complexation on the pMB surface. However, like the first generation of cMB, we observe a strong MB loss due to flocculation, ranging from 45.8 +/- 9.9 % to 85.0 +/- 2.3 %, with a maximum reached using 2 µg of pDNA for 1 µL of pMB with 10 minutes of complexation. Since only one minute is also sufficient to complex with pDNA, it is likely that the flocculation can be addressed with a short complexation time with some pDNA amount. Unlike the first generation of cMB, we did not observe an overlay-labeled pMB population corresponding to MB flocculation, preventing us from assessing the flocculation at early complexation time.

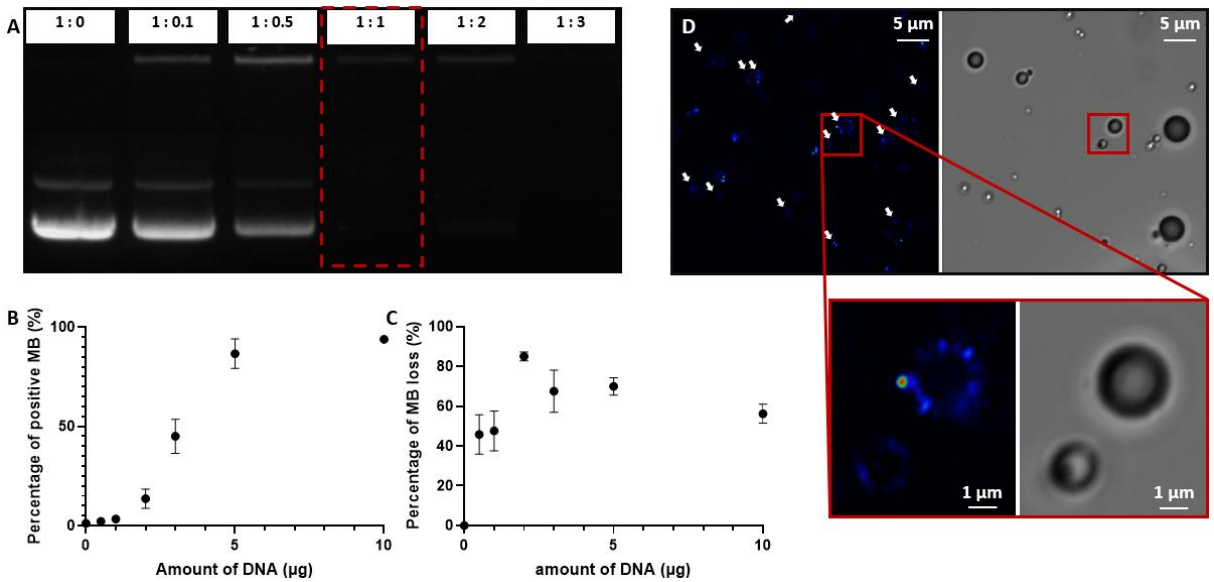

Figure 10: Cationic polymeric MB properties. (**A**) Gel shift assay of 1 µg of pDNA complexed with an increasing amount of MB solution, represented as a ratio of pDNA (µg) : MB (µL). (**B**) Flow cytometry

of 1 μL of cationic MB complexed with increasing Cy5-labeled pDNA (**C**) Percentage of loss of MB from flocculation assessed in optical microscopy after over 10 minutes of complexation with pDNA, with an increasing amount of pDNA (**D**) Confocal microscopy of cationic MB complexed with Cy5-labeled pDNA at a ratio of 1 μg for 1×10^7 MB with zoomed images below. **Left**: fluorescence image; **right**: brightfield. Data expressed as mean +/- SEM.

3.6 MB shell composition influences oscillation

As previously stated, MB can oscillate under ultrasound, inducing microstreaming and shear stress that can induce cell sonoporation and BBB opening. The model developed by Marmottant *et al.* demonstrates that this oscillation is dictated by the MB shell characteristics [63]. These characteristics depend on the MB composition, which in turn influences MB cavitation. Since BBB opening and gene delivery are closely linked to the intensity of cavitation, characterizing the cavitation behavior of each MB is essential for predicting their response in drug delivery applications [64–66]. To this end, we characterized both stable and inertial cavitation doses (SCD and ICD) *in vitro* for our formulations to better anticipate their behavior *in vivo*. Cavitation was measured using pulsed focused ultrasound (FUS) at 1 MHz with a pulse repetition frequency (PRF) of 1 Hz and a duty cycle of 5%, and the analysis was performed on either the entire 50 ms pulse or consecutive 5 ms fractions of it (Figure S4-6). Inertial cavitation events are typically considered to occur randomly, with a higher probability at higher mechanical indices. Since our analysis used the average value of several pulses, we did not directly assess the probability of these events. However, this probability is reflected in the ICD values, as more frequent occurrences result in higher ICD values. Our results show a clear pressure-dependent increase in both stable and inertial cavitation for all the custom MBs studied. At the lowest pressure of 100 kPa, we observed significant SCD but no inertial cavitation in any of the MBs (Figure 11).

Using the entire pulse, unfunctionalized MBs show a significant increase in SCD from 100 to 300 kPa, where a plateau is reached (Figure 11.A). ICD and precursor ICD are first detected starting at 150 kPa, followed by a rapid and significant increase until plateaus are reached at 300 kPa and 400 kPa for precursor ICD and ICD, respectively (Figure 11.A, B). At higher pressures, a slight decrease in stable and inertial cavitation doses is observed, which may indicate MB collapse. Both cationic MBs show significantly lower SCD at 100 kPa compared to

unfunctionalized MBs, and inertial cavitation is detected only at 200 kPa. This highlights the need for stronger acoustic pressure with our cMBs to induce cavitation similar to that seen with uMBs. Moreover, the first generation of cMBs exhibits significantly lower stable and inertial cavitation doses than uMBs at any pressure. For these cMBs, a significant increase in SCD is observed from 100 to 300 kPa, where a plateau is reached (Figure 11.A). ICD shows a slight but significant increase from 200 to 450 kPa, followed by a decrease at higher pressures, aligning with the behavior of SCD. This demonstrates the lower acoustic properties and stability of these cMBs compared to uMBs, both in terms of stable and inertial cavitation. The polymeric cationic MBs display significantly higher stable and inertial cavitation doses, starting at 150 kPa and 250 kPa, respectively, compared to the first generation of cMBs. These MBs show a rapid increase in SCD from 100 to 200 kPa, reaching similar values to uMBs, followed by a slight but significant increase until 600 kPa. Precursor ICD increases steadily and significantly from 200 to 600 kPa, remaining significantly lower than uMBs between 300 and 400 kPa but significantly higher than the first cMBs starting from 450 kPa. ICD shows different kinetics, with a low but significant increase from 200 to 400 kPa, followed by a strong and significant rise from 400 to 600 kPa. It also shows significantly higher inertial cavitation than the first cMBs starting from 250 kPa, but significantly lower than uMBs between 350 and 500 kPa. Furthermore, no significant difference is observed compared to uMBs in SCD and ICD or precursor ICD at their respective maximum values. These results highlight the more stable acoustic properties of pMBs, which exhibit stable cavitation similar to uMBs, but with inertial cavitation occurring at higher pressures and with similar intensity.

As demonstrated by Novell *et al*., the inertial cavitation regime occurs during FUS pulses and is characterized by random events between pulses, with a higher probability at higher mechanical index [21]. Since our analysis uses the average value across several pulses, we are unable to observe this cavitation regime appear within the pulse itself. However, by focusing on the first 5 μs of the pulse, we can observe MB cavitation before most of the onset of the inertial cavitation regime and MB collapse. The stable and inertial cavitation kinetics in the lower pressure range are similar across all MBs. Notably, uMBs show that SCD, as well as ICD and precursor ICD, continue to increase after reaching the previously observed plateau, confirming that uMB collapse occurs at these pressures. This also suggests that shorter pulses could be advantageous for FUS treatments at high pressures, as they would help avoid MB

collapse, as shown with RASTA sequences [67]. The first generation of cMBs exhibits the same kinetics as previously described but with significantly lower SCD and ICD at the same pressures. This suggests that cMB collapse begins relatively quickly within the pulse, occurring within the first 5 μs. The polymeric cationic MBs, on the other hand, show similar kinetics but with a smaller difference in SCD compared to uMBs and the first cMBs. SCD, as well as ICD and precursor ICD, were significantly lower than uMBs at all pressures, except at 600 kPa for SCD.

These data highlight that while the first cMBs exhibit lower cavitation and greater MB collapse at high pressures, pMBs can achieve similar stable cavitation with slightly higher acoustic pressure but with reduced MB collapse. Additionally, although all MBs show a limited pressure range where only stable cavitation is detected, pMBs demonstrate the ability to maintain stable cavitation over a wider pressure range, albeit with relatively weak ICD. This makes pMBs particularly promising for applications such as sonoporation, BBB opening, and gene delivery. However, since MB cavitation also depends on their concentration, which is much lower in brain capillaries, these results should be interpreted cautiously before being used to predict MB behavior *in vivo* during BBB opening [68].

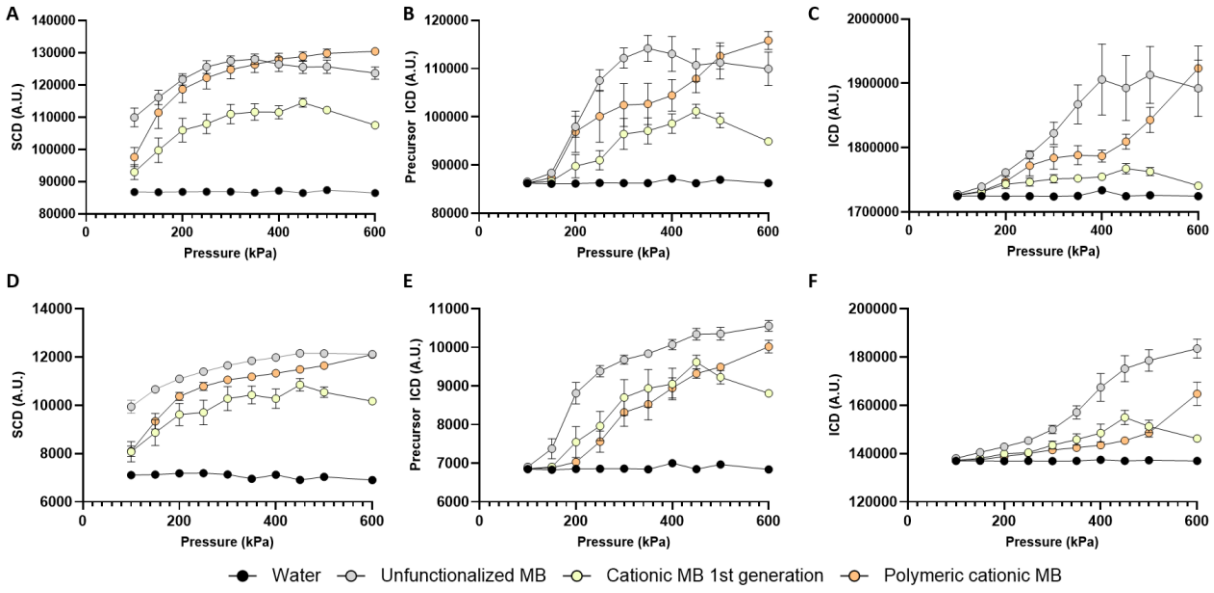

Figure 11: Cavitation analysis from unfunctionalized and cationic microbubbles. (**A**) Stable cavitation dose (SCD) (**B**) Precursor inertial cavitation dose (ICD), and (**C**) inertial cavitation dose, calculated with the 50 μs pulse signal and as a function of pressure. (**D**) Stable cavitation dose (**E**) Precursor inertial

cavitation dose, and (**F**) inertial cavitation dose, calculated with the first 5 μs signal of the FUS pulse and as a function of pressure (PNP). Data expressed as mean +/- SEM.

CONCLUSION

In this study we successfully developed and characterized homemade MB with targeted, magnetic, or cationic MB. We demonstrated for it two possible strategies for surface binding, using either streptavidin-biotin coupling or DBCO-N_3 click chemistry. In addition, we also demonstrated two protocols for MB size selection, allowing us to obtain a narrower size distribution with MB close to 1 μm. These smaller MBs demonstrated improved tumor penetration and higher ultrasound imaging contrast signal. Two cationic MBs were developed, both capable of complexing pDNA either directly on the surface or delocalized on a polymer. While both exhibited satisfying size, concentration, stability, and cavitation properties, the polymeric cationic MB demonstrated enhanced features. Indeed, compared to the first generation of cationic MB, they showed higher concentration, nucleic acid loading, stability under ultrasound imaging, and higher cavitation, reaching an SCD close to unfunctionalized MB but with lower ICD.

REFERENCES

1. Dauba, A.; Delalande, A.; Kamimura, H.A.S.; Conti, A.; Larrat, B.; Tsapis, N.; Novell, A. Recent Advances on Ultrasound Contrast Agents for Blood-Brain Barrier Opening with Focused Ultrasound. Pharmaceutics 2020, 12, 1125, doi:10.3390/pharmaceutics12111125.

2. Khodabakhshi, Z.; Hosseinkhah, N.; Ghadiri, H. Pulsating Microbubble in a Micro-Vessel and Mechanical Effect on Vessel Wall: A Simulation Study. J Biomed Phys Eng 2021, 11, 629–640, doi:10.31661/jbpe.v0i0.1131.

3. Hynynen, K.; McDannold, N.; Vykhodtseva, N.; Jolesz, F.A. Noninvasive MR Imaging-Guided Focal Opening of the Blood-Brain Barrier in Rabbits. Radiology 2001, 220, 640–646, doi:10.1148/radiol.2202001804.

4. Qiu, Y.; Zhang, C.; Tu, J.; Zhang, D. Microbubble-Induced Sonoporation Involved in Ultrasound-Mediated DNA Transfection in Vitro at Low Acoustic Pressures. J Biomech 2012, 45, 1339–1345, doi:10.1016/j.jbiomech.2012.03.011.

5. Pardridge, W.M. Drug Transport across the Blood-Brain Barrier. Journal of Cerebral Blood Flow and Metabolism 2012, 32, 1959–1972.

6. Pardridge, W.M. The Blood-Brain Barrier: Bottleneck in Brain Drug Development. The American Society for Experimental NeuroTherapeutics 2005, 2, 3–14.

7. Fischer, H.; Gottschlich, R.; Seelig, A. Blood-Brain Barrier Permeation: Molecular Parameters Governing Passive Diffusion. J. Membrane Biol. 1998, 165, 201–211.

8. Fan, C.H.; Ting, C.Y.; Lin, C.Y.; Chan, H.L.; Chang, Y.C.; Chen, Y.Y.; Liu, H.L.; Yeh, C.K. Noninvasive, Targeted, and Non-Viral Ultrasound-Mediated GDNF-Plasmid Delivery for Treatment of Parkinson's Disease. Sci Rep 2016, 6, doi:10.1038/srep19579.

9. Lin, C.Y.; Hsieh, H.Y.; Chen, C.M.; Wu, S.R.; Tsai, C.H.; Huang, C.Y.; Hua, M.Y.; Wei, K.C.; Yeh, C.K.; Liu, H.L. Non-Invasive, Neuron-Specific Gene Therapy by Focused Ultrasound-Induced Blood-Brain Barrier Opening in Parkinson's Disease Mouse Model. Journal of Controlled Release 2016, 235, 72–81, doi:10.1016/j.jconrel.2016.05.052.

10. Owusu-Yaw, B.S.; Zhang, Y.; Garrett, L.; Yao, A.; Shing, K.; Batista, A.R.; Sena-Esteves, M.; Upadhyay, J.; Kegel-Gleason, K.; Todd, N. Focused Ultrasound-Mediated Disruption of the

Blood–Brain Barrier for AAV9 Delivery in a Mouse Model of Huntington's Disease. Pharmaceutics 2024, 16, doi:10.3390/pharmaceutics16060710.

11. Weber-Adrian, D.; Kofoed, R.H.; Chan, J.W.Y.; Silburt, J.; Noroozian, Z.; Kügler, S.; Hynynen, K.; Aubert, I. Strategy to Enhance Transgene Expression in Proximity of Amyloid Plaques in a Mouse Model of Alzheimer's Disease. Theranostics 2019, 9, 8127–8137, doi:10.7150/thno.36718.

12. Shen, Y.; Hua, L.; Yeh, C.K.; Shen, L.; Ying, M.; Zhang, Z.; Liu, G.; Li, S.; Chen, S.; Chen, X.; et al. Ultrasound with Microbubbles Improves Memory, Ameliorates Pathology and Modulates Hippocampal Proteomic Changes in a Triple Transgenic Mouse Model of Alzheimer's Disease. Theranostics 2020, 10, 11794–11819, doi:10.7150/thno.44152.

13. Jordão, J.F.; Thévenot, E.; Markham-Coultes, K.; Scarcelli, T.; Weng, Y.Q.; Xhima, K.; O'Reilly, M.; Huang, Y.; McLaurin, J.A.; Hynynen, K.; et al. Amyloid-β Plaque Reduction, Endogenous Antibody Delivery and Glial Activation by Brain-Targeted, Transcranial Focused Ultrasound. Exp Neurol 2013, 248, 16–29, doi:10.1016/j.expneurol.2013.05.008.

14. Karakatsani, M.E.; Ji, R.; Murillo, M.F.; Kugelman, T.; Kwon, N.; Lao, Y.H.; Liu, K.; Pouliopoulos, A.N.; Honig, L.S.; Duff, K.E.; et al. Focused Ultrasound Mitigates Pathology and Improves Spatial Memory in Alzheimer's Mice and Patients. Theranostics 2023, 13, 4102–4120, doi:10.7150/thno.79898.

15. Rezai, A.R.; Ranjan, M.; Haut, M.W.; Carpenter, J.; D'Haese, P.F.; Mehta, R.I.; Najib, U.; Wang, P.; Claassen, D.O.; Chazen, J.L.; et al. Focused Ultrasound–Mediated Blood-Brain Barrier Opening in Alzheimer's Disease: Long-Term Safety, Imaging, and Cognitive Outcomes. J Neurosurg 2023, 139, 275–283, doi:10.3171/2022.9.JNS221565.

16. He, S.; Singh, D.; Yusefi, H.; Helfield, B. Stable Cavitation-Mediated Delivery of MiR-126 to Endothelial Cells. Pharmaceutics 2022, 14, doi:10.3390/pharmaceutics14122656.

17. Ji, R.; Karakatsani, M.E.; Burgess, M.; Smith, M.; Murillo, M.F.; Konofagou, E.E. Cavitation-Modulated Inflammatory Response Following Focused Ultrasound Blood-Brain Barrier Opening. Journal of Controlled Release 2021, 337, 458–471, doi:10.1016/j.jconrel.2021.07.042.

18. Bader, K.B.; Holland, C.K. Gauging the Likelihood of Stable Cavitation from Ultrasound Contrast Agents. Phys Med Biol 2013, 58, 127–144, doi:10.1088/0031-9155/58/1/127.

19. Mondou, P.; Mériaux, S.; Nageotte, F.; Vappou, J.; Novell, A.; Larrat, B. State of the Art on Microbubble Cavitation Monitoring and Feedback Control for Blood-Brain-Barrier Opening Using Focused Ultrasound. Phys Med Biol 2023, 68, doi:10.1088/1361-6560/ace23e.

20. Pascal, A.; Li, N.; Lechtenberg, K.J.; Rosenberg, J.; Airan, R.D.; James, M.L.; Bouley, D.M.; Pauly, K.B. Histologic Evaluation of Activation of Acute Inflammatory Response in a Mouse Model Following Ultrasound-Mediated Blood-Brain Barrier Using Different Acoustic Pressures and Microbubble Doses. Nanotheranostics 2020, 4, 210–213, doi:10.7150/ntno.49898.

21. Novell, A.; Kamimura, H.A.S.; Cafarelli, A.; Gerstenmayer, M.; Flament, J.; Valette, J.; Agou, P.; Conti, A.; Selingue, E.; Aron Badin, R.; et al. A New Safety Index Based on Intrapulse Monitoring of Ultra-Harmonic Cavitation during Ultrasound-Induced Blood-Brain Barrier Opening Procedures. Sci Rep 2020, 10, doi:10.1038/s41598-020-66994-8.

22. Chu, P.C.; Chai, W.Y.; Tsai, C.H.; Kang, S.T.; Yeh, C.K.; Liu, H.L. Focused Ultrasound-Induced Blood-Brain Barrier Opening: Association with Mechanical Index and Cavitation Index Analyzed by Dynamic Contrast-Enhanced Magnetic-Resonance Imaging. Sci Rep 2016, 6, doi:10.1038/srep33264.

23. Tung, Y.S.; Choi, J.J.; Baseri, B.; Konofagou, E.E. Identifying the Inertial Cavitation Threshold and Skull Effects in a Vessel Phantom Using Focused Ultrasound and Microbubbles. Ultrasound Med Biol 2010, 36, 840–852, doi:10.1016/j.ultrasmedbio.2010.02.009.

24. Huang, Y.; Meng, Y.; Pople, C.B.; Bethune, A.; Jones, R.M.; Abrahao, A.; Hamani, C.; Kalia, S.K.; Kalia, L. V.; Lipsman, N.; et al. Cavitation Feedback Control of Focused Ultrasound Blood-Brain Barrier Opening for Drug Delivery in Patients with Parkinson's Disease. Pharmaceutics 2022, 14, doi:10.3390/pharmaceutics14122607.

25. Çavuşoğlu, M.; Zhang, J.; Ielacqua, G.D.; Pellegrini, G.; Signorell, R.D.; Papachristodoulou, A.; Brambilla, D.; Roth, P.; Weller, M.; Rudin, M.; et al. Closed-Loop Cavitation Control for Focused Ultrasound-Mediated Blood-Brain Barrier Opening by Long-Circulating Microbubbles. Phys Med Biol 2019, 64, doi:10.1088/1361-6560/aafaa5.

26. Cornu, C.; Guédra, M.; Béra, J.C.; Liu, H.L.; Chen, W.S.; Inserra, C. Ultrafast Monitoring and Control of Subharmonic Emissions of an Unseeded Bubble Cloud during Pulsed Sonication. Ultrason Sonochem 2018, 42, 697–703, doi:10.1016/j.ultsonch.2017.12.026.

27. Marquet, F.; Teichert, T.; Wu, S.Y.; Tung, Y.S.; Downs, M.; Wang, S.; Chen, C.; Ferrera, V.; Konofagou, E.E. Real-Time, Transcranial Monitoring of Safe Blood-Brain Barrier Opening in Non-Human Primates. PLoS One 2014, 9, doi:10.1371/journal.pone.0084310.

28. Thévenot, E.; Jordão, J.F.; O'Reilly, M.A.; Markham, K.; Weng, Y.Q.; Foust, K.D.; Kaspar, B.K.; Hynynen, K.; Aubert, I. Targeted Delivery of Self-Complementary Adeno-Associated Virus

Serotype 9 to the Brain, Using Magnetic Resonance Imaging-Guided Focused Ultrasound. Hum Gene Ther 2012, 23, 1144–1155, doi:10.1089/hum.2012.013.

29. Liang, S.; Hu, D.; Li, G.; Gao, D.; Li, F.; Zheng, H.; Pan, M.; Sheng, Z. NIR-II Fluorescence Visualization of Ultrasound-Induced Blood–Brain Barrier Opening for Enhanced Photothermal Therapy against Glioblastoma Using Indocyanine Green Microbubbles. Sci Bull (Beijing) 2022, 67, 2316–2326, doi:10.1016/j.scib.2022.10.025.

30. Barrefelt, Å.A.; Brismar, T.B.; Egri, G.; Aspelin, P.; Olsson, A.; Oddo, L.; Margheritelli, S.; Caidahl, K.; Paradossi, G.; Dähne, L.; et al. Multimodality Imaging Using SPECT/CT and MRI and Ligand Functionalized 99mTc-Labeled Magnetic Microbubbles. EJNMMI Res 2013, 3, 1–14, doi:10.1186/2191-219X-3-12.

31. Tartis, M.S.; Kruse, D.E.; Zheng, H.; Zhang, H.; Kheirolomoom, A.; Marik, J.; Ferrara, K.W. Dynamic MicroPET Imaging of Ultrasound Contrast Agents and Lipid Delivery. Journal of Controlled Release 2008, 131, 160–166, doi:10.1016/j.jconrel.2008.07.030.

32. Langeveld, S.A.G.; Meijlink, B.; Beekers, I.; Olthof, M.; Van Der Steen, A.F.W.; Jong, N. de; Kooiman, K. Theranostic Microbubbles with Homogeneous Ligand Distribution for Higher Binding Efficacy. Pharmaceutics 2022, 14, doi:10.3390/pharmaceutics14020311.

33. Chen, L.; Sutharsan, R.; Lee, J.L.F.; Cruz, E.; Asnicar, B.; Palliyaguru, T.; Wasielewska, J.M.; Gaudin, A.; Song, J.; Leinenga, G.; et al. Claudin-5 Binder Enhances Focused Ultrasoundmediated Opening in an in Vitro Blood-Brain Barrier Model. Theranostics 2022, 12, 1952–1970, doi:10.7150/thno.65539.

34. Zhou, Y.; Gu, H.; Xu, Y.; Li, F.; Kuang, S.; Wang, Z.; Zhou, X.; Ma, H.; Li, P.; Zheng, Y.; et al. Targeted Antiangiogenesis Gene Therapy Using Targeted Cationic Microbubbles Conjugated with CD105 Antibody Compared with Untargeted Cationic and Neutral Microbubbles. Theranostics 2015, 5, 399–417, doi:10.7150/thno.10351.

35. Goncin, U.; Curiel, L.; Geyer, C.R.; Machtaler, S. Aptamer-Functionalized Microbubbles Targeted to P-Selectin for Ultrasound Molecular Imaging of Murine Bowel Inflammation. Mol Imaging Biol 2023, 25, 283–293, doi:10.1007/s11307-022-01755-9.

36. Beguin, E.; Bau, L.; Shrivastava, S.; Stride, E. Comparing Strategies for Magnetic Functionalization of Microbubbles. ACS Appl Mater Interfaces 2019, 11, 1829–1840, doi:10.1021/acsami.8b18418.

37. Owen, J.; Crake, C.; Lee, J.Y.; Carugo, D.; Beguin, E.; Khrapitchev, A.A.; Browning, R.J.; Sibson, N.; Stride, E. A Versatile Method for the Preparation of Particle-Loaded Microbubbles for Multimodality Imaging and Targeted Drug Delivery. 2017, doi:10.5287/bodleian:Aer44Drnj.

38. Stride, E.; Porter, C.; Prieto, A.G.; Pankhurst, Q. Enhancement of Microbubble Mediated Gene Delivery by Simultaneous Exposure to Ultrasonic and Magnetic Fields. Ultrasound Med Biol 2009, 35, 861–868, doi:10.1016/j.ultrasmedbio.2008.11.010.

39. Zhou, N.Q.; Fang, Z.X.; Huang, N.; Zuo, Y.; Qiu, Y.; Guo, L.J.; Song, P.; Xu, J.; Wan, G.R.; Tian, X.Q.; et al. AFGF Targeted Mediated by Novel Nanoparticles-Microbubble Complex Combined With Ultrasound-Targeted Microbubble Destruction Attenuates Doxorubicin-Induced Heart Failure via Anti-Apoptosis and Promoting Cardiac Angiogenesis. Front Pharmacol 2021, 12, doi:10.3389/fphar.2021.607785.

40. Dong, L.; Li, N.; Wei, X.; Wang, Y.; Chang, L.; Wu, H.; Song, L.; Guo, K.; Chang, Y.; Yin, Y.; et al. A Gambogic Acid-Loaded Delivery System Mediated by Ultrasound-Targeted Microbubble Destruction: A Promising Therapy Method for Malignant Cerebral Glioma. Int J Nanomedicine 2022, 17, 2001–2017, doi:10.2147/IJN.S344940.

41. Vannan, M.; McCreery, T.; Li, P.; Han, Z.; Unger, E.; Kuersten, B.; Nabel, E.; Rajagopalan, S. Ultrasound-Mediated Transfection of Canine Myocardium by Intravenous Administration of Cationic Microbubble-Linked Plasmid DNA. Journal of the American Society of Echocardiography 2002, 15, 214–218, doi:10.1067/mje.2002.119913.

42. Nomikou, N.; Tiwari, P.; Trehan, T.; Gulati, K.; McHale, A.P. Studies on Neutral, Cationic and Biotinylated Cationic Microbubbles in Enhancing Ultrasound-Mediated Gene Delivery in Vitro and in Vivo. Acta Biomater 2012, 8, 1273–1280, doi:10.1016/j.actbio.2011.09.010.

43. Rigollet, S.; Rome, C.; Ador, T.; Dumont, E.; Pichon, C.; Delalande, A.; Barbier, E.L.; Stupar, V. FUS-Mediated BBB Opening Leads to Transient Perfusion Decrease and Inflammation without Acute or Chronic Brain Lesion. Theranostics 2024, 14, 4147–4160, doi:10.7150/thno.96721.

44. Wang, S.; Samiotaki, G.; Olumolade, O.; Feshitan, J.A.; Konofagou, E.E. Microbubble Type and Distribution Dependence of Focused Ultrasound-Induced Blood-Brain Barrier Opening. Ultrasound Med Biol 2014, 40, 130–137, doi:10.1016/j.ultrasmedbio.2013.09.015.

45. Hernandez, C.; Abenojar, E.C.; Hadley, J.; De Leon, A.C.; Coyne, R.; Perera, R.; Gopalakrishnan, R.; Basilion, J.P.; Kolios, M.C.; Exner, A.A. Sink or Float? Characterization of

Shell-Stabilized Bulk Nanobubbles Using a Resonant Mass Measurement Technique. Nanoscale 2019, 11, 851–855, doi:10.1039/c8nr08763f.

46. Liu, X.; Gong, P.; Song, P.; Xie, F.; Miller, A.L.; Chen, S.; Lu, L. Fast Functionalization of Ultrasound Microbubbles Using Strain Promoted Click Chemistry. Biomater Sci 2018, 6, 623–632, doi:10.1039/c8bm00004b.

47. Chang, E.L.; Ting, C.Y.; Hsu, P.H.; Lin, Y.C.; Liao, E.C.; Huang, C.Y.; Chang, Y.C.; Chan, H.L.; Chiang, C.S.; Liu, H.L.; et al. Angiogenesis-Targeting Microbubbles Combined with Ultrasound-Mediated Gene Therapy in Brain Tumors. Journal of Controlled Release 2017, 255, 164–175, doi:10.1016/j.jconrel.2017.04.010.

48. Yu, C.G.; Deng, Q.; Cao, S.; Zhao, Z.Y.; Mei, D.E.; Feng, C.L.; Zhou, Q.; Chen, J.L. Ultrasound-Targeted Cationic Microbubbles Combined with the NFκB Binding Motif Increase SDF-1α Gene Transfection: A Protective Role in Hearts after Myocardial Infarction. Kaohsiung Journal of Medical Sciences 2022, 38, 594–604, doi:10.1002/kjm2.12529.

49. Liu, Y.; Lai, X.; Zhu, Y.; Guo, F.; Su, L.; Arkin, G.; He, T.; Xu, J.; Ran, H. Contrast-Enhanced Ultrasound Imaging Using Long-Circulating Cationic Magnetic Microbubbles in Vitro and in Vivo Validations. Int J Pharm 2022, 616, 121299, doi:10.1016/J.IJPHARM.2021.121299.

50. Sheng, Y.; Beguin, E.; Nesbitt, H.; Kamila, S.; Owen, J.; Barnsley, L.C.; Callan, B.; O'Kane, C.; Nomikou, N.; Hamoudi, R.; et al. Magnetically Responsive Microbubbles as Delivery Vehicles for Targeted Sonodynamic and Antimetabolite Therapy of Pancreatic Cancer. Journal of Controlled Release 2017, 262, 192–200, doi:10.1016/j.jconrel.2017.07.040.

51. Fan, C.H.; Cheng, Y.H.; Ting, C.Y.; Ho, Y.J.; Hsu, P.H.; Liu, H.L.; Yeh, C.K. Ultrasound/Magnetic Targeting with SPIO-DOX-Microbubble Complex for Image-Guided Drug Delivery in Brain Tumors. Theranostics 2016, 6, 1542–1556, doi:10.7150/thno.15297.

52. Perera, R.H.; Hernandez, C.; Zhou, H.; Kota, P.; Burke, A.; Exner, A.A. Ultrasound Imaging beyond the Vasculature with New Generation Contrast Agents. Wiley Interdiscip Rev Nanomed Nanobiotechnol 2015, 7, 593–608, doi:10.1002/wnan.1326.

53. Koga, T.; Kida, H.; Yamasaki, Y.; Feril, L.B.; Endo, H.; Itaka, K.; Abe, H.; Tachibana, K. Intracranial Gene Delivery Mediated by Albumin-Based Nanobubbles and Low-Frequency Ultrasound. Nanomaterials 2024, 14, doi:10.3390/nano14030285.

54. Katz, S.; Gattegno, R.; Peko, L.; Zarik, R.; Hagani, Y.; Ilovitsh, T. Diameter-Dependent Assessment of Microvascular Leakage Following Ultrasound-Mediated Blood-Brain Barrier Opening. iScience 2023, 26, doi:10.1016/j.isci.2023.106965.

55. Wu, M.X.; Zhou, Y.; Zhou, X.Y.; Xu, Y. Ultrasound-Targeted Cationic Microbubble-Mediated Gene Transfection and Inhibition of Retinal Neovascularization. Int J Ophthalmol 2022, 15, 876–885, doi:10.18240/ijo.2022.06.04.

56. Tlaxca, J.L.; Anderson, C.R.; Klibanov, A.L.; Lowrey, B.; Hossack, J.A.; Alexander, J.S.; Lawrence, M.B.; Rychak, J.J. Analysis of in Vitro Transfection by Sonoporation Using Cationic and Neutral Microbubbles. Ultrasound Med Biol 2010, 36, 1907–1918, doi:10.1016/j.ultrasmedbio.2010.05.014.

57. Chatin, B.; Mével, M.; Devallière, J.; Dallet, L.; Haudebourg, T.; Peuziat, P.; Colombani, T.; Berchel, M.; Lambert, O.; Edelman, A.; et al. Liposome-Based Formulation for Intracellular Delivery of Functional Proteins. Mol Ther Nucleic Acids 2015, 4, e244, doi:10.1038/mtna.2015.17.

58. Gonçalves, C.; Akhter, S.; Pichon, C.; Midoux, P. Intracellular Availability of PDNA and MRNA after Transfection: A Comparative Study among Polyplexes, Lipoplexes, and Lipopolyplexes. Mol Pharm 2016, 13, 3153–3163, doi:10.1021/acs.molpharmaceut.6b00376.

59. Lentacker, I.; De Geest, B.G.; Vandenbroucke, R.E.; Peeters, L.; Demeester, J.; De Smedt, S.C.; Sanders, N.N. Ultrasound-Responsive Polymer-Coated Microbubbles That Bind and Protect DNA. Langmuir 2006, 22, 7273–7278, doi:10.1021/la0603828.

60. Du, M.; Chen, Y.; Tu, J.; Liufu, C.; Yu, J.; Yuan, Z.; Gong, X.; Chen, Z. Ultrasound Responsive Magnetic Mesoporous Silica Nanoparticle-Loaded Microbubbles for Efficient Gene Delivery. ACS Biomater Sci Eng 2020, 6, 2904–2912, doi:10.1021/acsbiomaterials.0c00014.

61. Jin, Q.; Wang, Z.; Yan, F.; Deng, Z.; Ni, F.; Wu, J.; Shandas, R.; Liu, X.; Zheng, H. A Novel Cationic Microbubble Coated with Stearic Acid-Modified Polyethylenimine to Enhance DNA Loading and Gene Delivery by Ultrasound. PLoS One 2013, 8, doi:10.1371/journal.pone.0076544.

62. Gonçalves, C.; Gross, F.; Guégan, P.; Cheradame, H.; Midou, P. A Robust Transfection Reagent for the Transfection of CHO and HEK293 Cells and Production of Recombinant Proteins and Lentiviral Particles - PTG1. Biotechnol J 2014, 9, 1380–1388, doi:10.1002/biot.201400324.

63. Marmottant, P.; van der Meer, S.; Emmer, M.; Versluis, M.; de Jong, N.; Hilgenfeldt, S.; Lohse, D. A Model for Large Amplitude Oscillations of Coated Bubbles Accounting for Buckling and Rupture. J Acoust Soc Am 2005, 118, 3499–3505, doi:10.1121/1.2109427.

64. Ho, Y.J.; Chang, H.C.; Lin, C.W.; Fan, C.H.; Lin, Y.C.; Wei, K.C.; Yeh, C.K. Oscillatory Behavior of Microbubbles Impacts Efficacy of Cellular Drug Delivery. Journal of Controlled Release 2021, 333, 316–327, doi:10.1016/j.jconrel.2021.03.044.

65. Lin, J.; Qiao, C.; Jiang, H.; Liu, Z.; Hu, Y.; Liu, W.; Yong, Y.; Li, F. Reversible Ca2+ Signaling and Enhanced Paracellular Transport in Endothelial Monolayer Induced by Acoustic Bubbles and Targeted Microbeads. Ultrason Sonochem 2024, doi:10.1016/j.ultsonch.2024.107181.

66. Tung, Y.-S.; Vlachos, F.; Feshitan, J.A.; Borden, M.A.; Konofagou, E.E. The Mechanism of Interaction between Focused Ultrasound and Microbubbles in Blood-Brain Barrier Opening in Mice. J Acoust Soc Am 2011, 130, 3059–3067, doi:10.1121/1.3646905.

67. Batts, A.J.; Ji, R.; Noel, R.L.; Kline-Schoder, A.R.; Bae, S.; Kwon, N.; Konofagou, E.E. Using a Novel Rapid Alternating Steering Angles Pulse Sequence to Evaluate the Impact of Theranostic Ultrasound-Mediated Ultra-Short Pulse Length on Blood-Brain Barrier Opening Volume and Closure, Cavitation Mapping, Drug Delivery Feasibility, and Safety. Theranostics 2023, 13, 1180–1197, doi:10.7150/thno.76199.

68. Haghi, H.; Yaali, M.; Exner, A.A.; Kolios, M.C. Experimental Investigation on the Effect of Concentration on the Resonance Frequency of Lipid Coated Ultrasonically Excited Microbubbles. Ultrason Sonochem 2025, 112, doi:10.1016/j.ultsonch.2024.107170.

1. SUPPLEMENTARY DATA

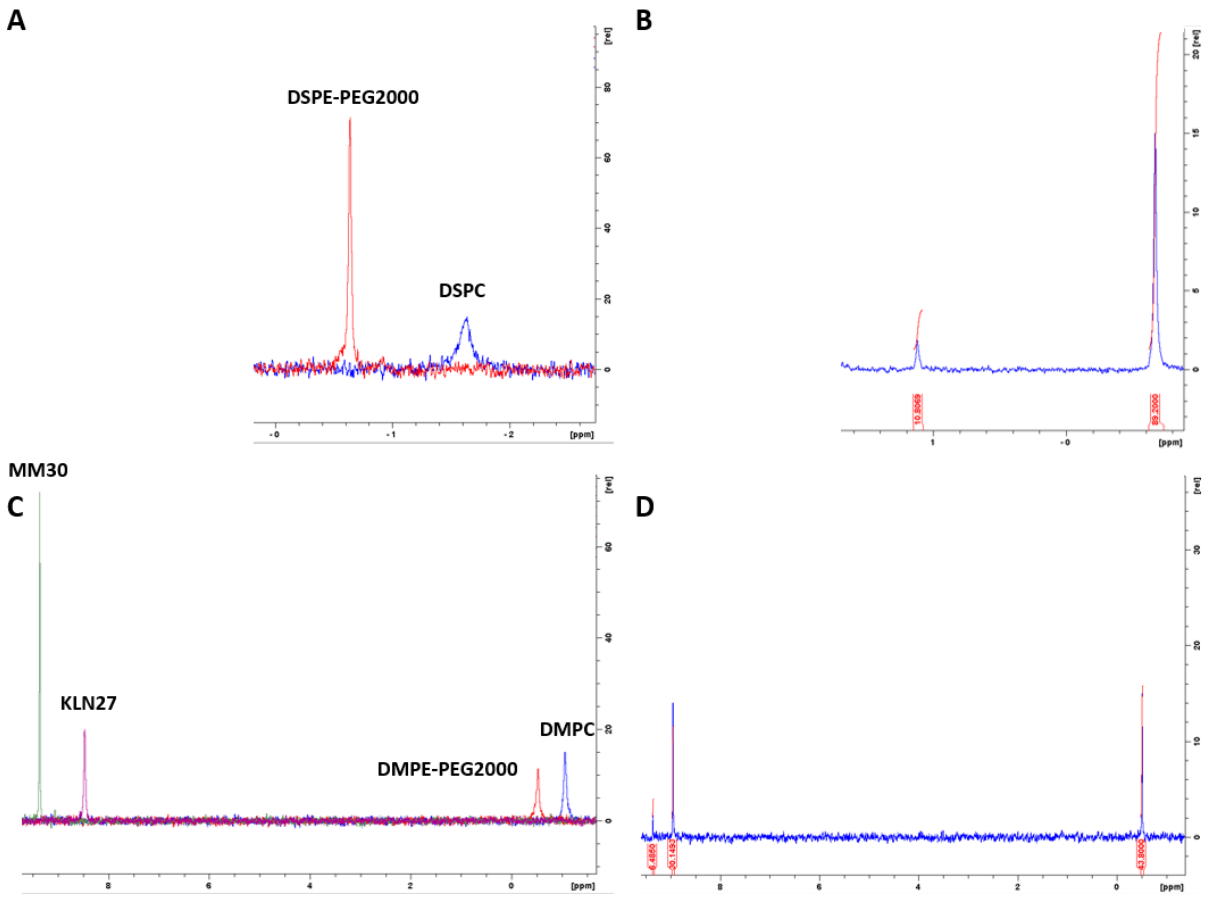

Figure S1: 31P nuclear magnetic resonance (NMR). (**A**) 31P NMR spectrum of isolated unfunctionalized MB components. (**B**) 31P NMR spectrum of unfunctionalized MB. (**C**) 31P NMR spectrum of isolated components from the first-generation cationic MB. (**D**) 31P NMR spectrum of first-generation cationic MB

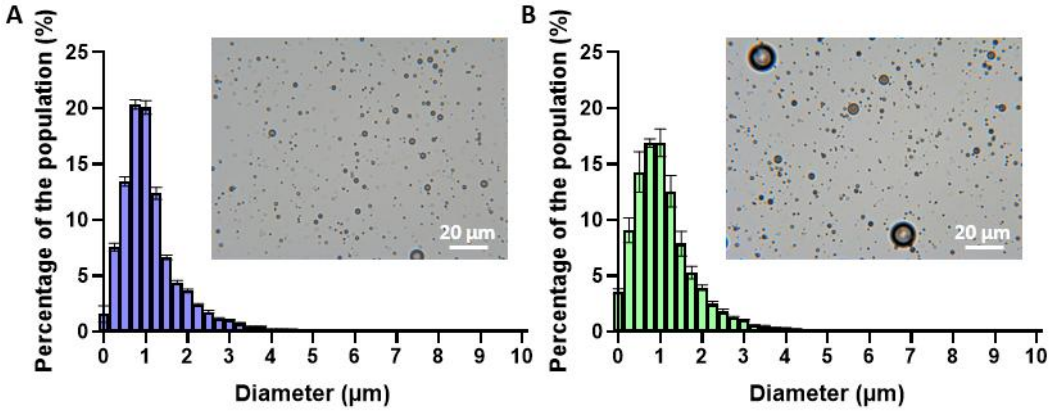

Figure S2: bMB and dMB size distribution. (**A**) Size distribution of the biotinylated microbubbles (mean with SEM), with an optical image used for size and concentration determination, optical microscope, magnification ×25. (**B**) Size distribution of the DBCO-microbubbles (mean with SEM), with an optical image used for size and concentration determination, optical microscope, magnification ×25. Data expressed as mean +/- SEM.

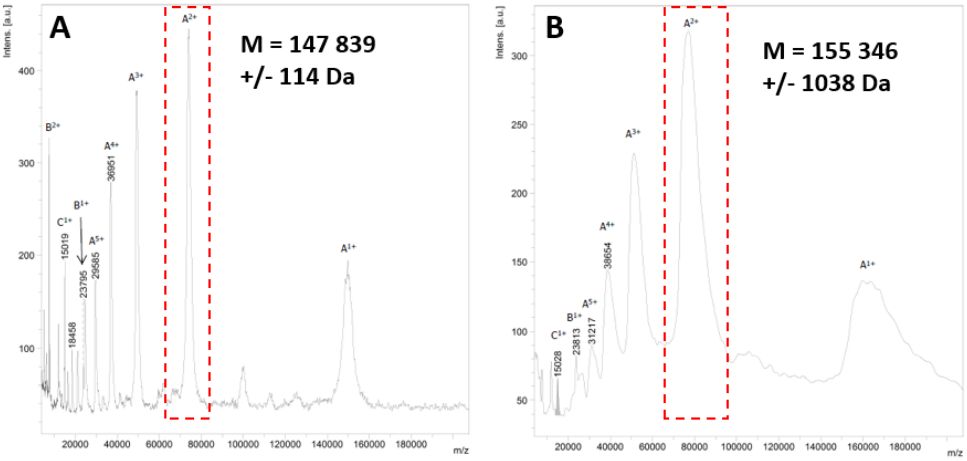

Figure S3: Mass spectrometry of antibody azide modification. (**A**) Mass spectrometry of N_3antibody. (**B**) Mass spectrometry of N_3-antibody following click chemistry with DSPE-NHS.

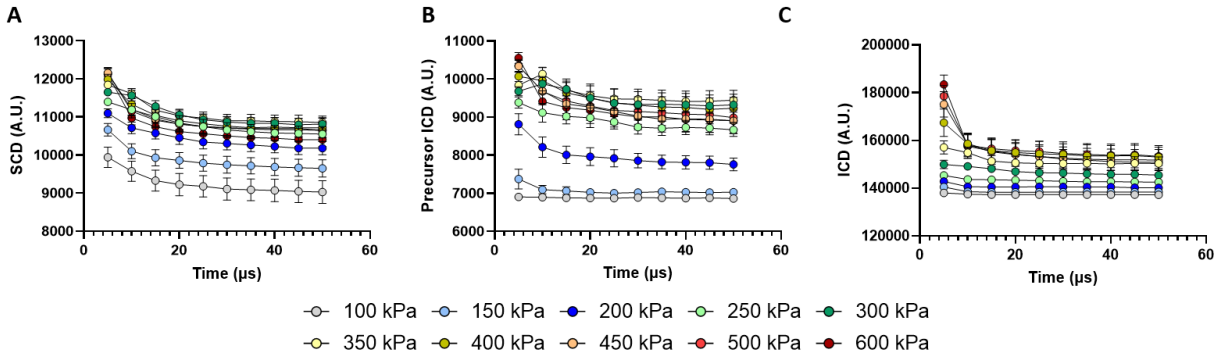

Figure S4: Cavitation evolution of unfunctionalized MB during pulse. (**A**) Stable cavitation dose (SCD) (**B**) Precursor inertial cavitation dose (ICD), and (**C**) inertial cavitation dose, calculated with each consecutive 5 µs in the pulse and at different pressures. Data expressed as mean +/- SEM.

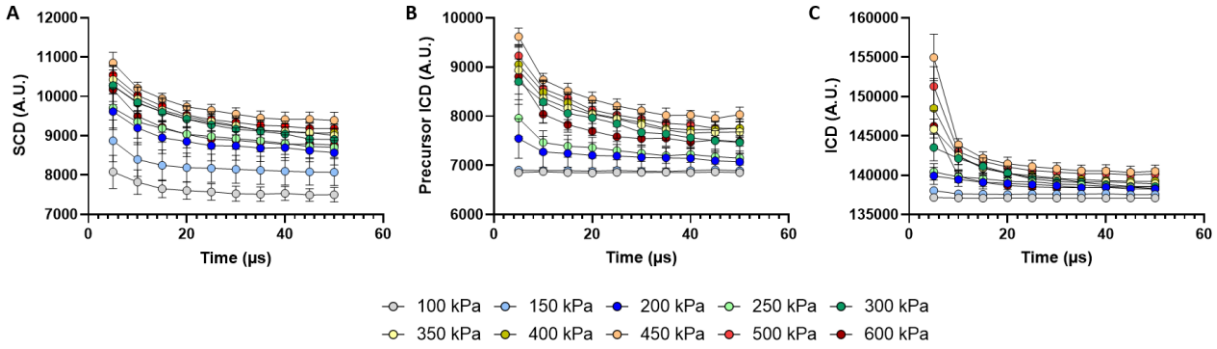

Figure S5: Cavitation evolution of the first generation of cationic MB during pulse. (**A**) Stable cavitation dose (SCD) (**B**) Precursor inertial cavitation dose (ICD), and (**C**) inertial cavitation dose, calculated with each consecutive 5 µs in the pulse and at different pressures. Data expressed as mean +/- SEM.

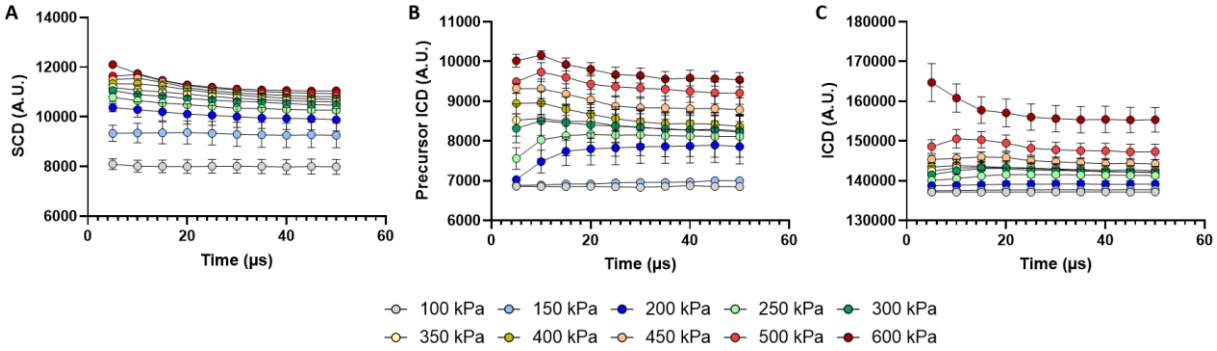

Figure S6: Cavitation evolution of polymeric cationic MB during pulse. (**A**) Stable cavitation dose (SCD) (**B**) Precursor inertial cavitation dose (ICD), and (**C**) inertial cavitation dose, calculated with each consecutive 5 µs in the pulse and at different pressures. Data expressed as mean +/- SEM.

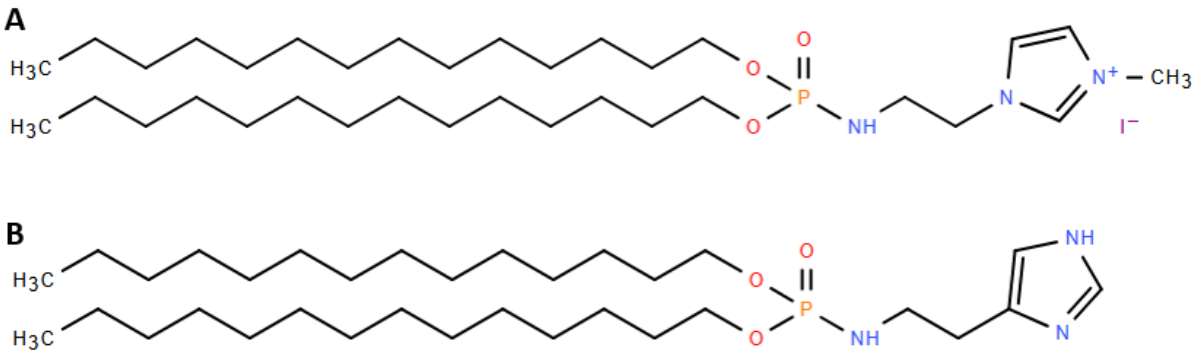

Figure S7: Lipid chemical structures (**A**) KLN27 chemical structure. (**B**) MM30 chemical structure.

Partie 2 : Suivi de l'ouverture par ultrasons de la barrière hémato-encéphalique

Résumé en français :

Introduction :

La barrière hémato-encéphalique (BHE) est une membrane sélectivement perméable assurant la protection du système nerveux central des pathogènes, mais empêchant également le passage de la majorité des molécules thérapeutiques. L'ouverture de cette barrière par ultrason focalisé associé à des microbulles est une technique non invasive permettant de délivrer des molécules thérapeutiques dans le cerveau. Afin de s'assurer que l'ouverture reste sûre, transitoire et reproductible, il est crucial de disposer d'un moyen de suivre cette ouverture. La méthode de référence pour cela est l'utilisation d'imagerie par résonance magnétique, avec injection d'un agent de contraste composé de gadolinium, extravasé dans le cerveau au niveau de l'ouverture. Cette technique permet de quantifier l'ouverture *in vivo* de manière non invasive, en 3D et avec une haute résolution, tout en permettant de mesurer des changements physiologiques, en particulier l'apparition d'œdèmes ou de saignements. Cependant, cette technique est également difficile d'accès dû à son coût et à sa nécessité d'être utilisée par des opérateurs hautement qualifiés. Par conséquent, nous nous sommes intéressés dans cette étude à l'utilisation d'imagerie de fluorescence et de photoacoustique, utilisant l'extravasation d'Indocyanine Green (ICG) comme agent de contraste bimodal pour suivre l'ouverture de la BHE.

Méthodes :

Pour cela, nous avons utilisé les microbulles non fonctionnalisées décrites dans la partie précédente. Nous avons tout d'abord testé deux doses d'ICG (0.5 et 0,25 mg) injectées directement après ultrasons et avons suivi l'ouverture *in vivo* par imagerie de fluorescence et photoacoustique à différents temps pour déterminer le meilleur protocole. Par la suite, la cinétique de fermeture de la BHE a été déterminée par imagerie de fluorescence *in vivo* et *ex vivo*, en injectant l'ICG immédiatement après ultrasons ou délayé de 30 à 120 minutes. L'effet de la dose de microbulles a ensuite été évalué avec cette modalité d'imagerie, en injectant 1×10^6 à 1×10^8 microbulles. Pour finir, nous avons comparé l'efficacité de l'imagerie de fluorescence *ex vivo* avec la méthode de référence, l'imagerie par résonance magnétique, pour mesurer la cinétique de fermeture de la BHE.

Résultats :

Nos résultats montrent que les deux doses d'ICG permettent de voir l'ouverture par imagerie de photoacoustique jusqu'à 1 h après la procédure, et également par imagerie de fluorescence 24 h après la procédure. L'imagerie de fluorescence a montré qu'une diminution de la dose de microbulles d'un facteur 10 induit une diminution significative de l'ouverture, mesurable à la fois *in vivo* et *ex vivo*. Cependant, cela a aussi montré la meilleure sensibilité de la mesure *ex vivo*, permettant de mesurer de faibles ouvertures. Cette observation s'est confirmée avec la mesure de la cinétique de la fermeture de la BHE. Nous avons montré qu'avec nos protocoles, la BHE restait majoritairement ouverte à 30 minutes, mais était en partie refermée à 120 minutes après la procédure. Si cela était mesurable autant *in vivo* qu'*ex vivo* en imagerie de fluorescence, seule la mesure *ex vivo* a permis une mesure fiable de la demi-vie de fermeture. De plus, nous démontrons une forte corrélation entre la cinétique de fermeture mesurée en imagerie par résonance magnétique et avec l'imagerie de fluorescence *ex vivo*, validant l'efficacité de cette technique pour le suivi de l'ouverture de la BHE.

Dans cette partie, nous avons donc démontré l'efficacité de notre protocole d'ouverture de la BHE de manière transitoire. Nous avons également validé l'utilisation de l'ICG comme agent de contraste bimodal de l'imagerie de fluorescence et photoacoustique ainsi que l'efficacité de ces techniques pour suivre l'ouverture de la BHE *in vivo* ou *ex vivo*, en tant qu'alternatives à l'imagerie par résonance magnétique. L'article présenté dans cette partie a été publié dans le journal Ultrasound in Medicine & Biology (DOI : 10.1016/j.ultrasmedbio.2025.02.016). Ces travaux ont également fait l'objet d'un poster présenté au congrès international ISTU 2023 à Lyon.

Title:

Ultrasound-Assisted Blood Brain Barrier Opening Monitoring by Photoacoustic and Fluorescence Imaging Using Indocyanine Green

Authors:

Thomas Ador [1,2,3], Mylène Fournié [1], Sébastien Rigollet [4, 5], Claire Counil [1,2], Vasile Stupar [4,6], Emmanuel L. Barbier [4,6], Chantal Pichon [1, 2, 7], Anthony Delalande [1, 2]*

Affiliation:

[1] ART mRNA INSERM US55, Orléans, France,

[2] Université d'Orléans, LI²RSO, France,

[3] Laboratory of Experimental and Molecular Immunology and Neuromodulation, UMR 7355 CNRS-Université d'Orléans, Orleans, France,

[4] Univ. Grenoble Alpes, Inserm, Grenoble Institut Neurosciences, U1216, Grenoble, France,

[5] Image Guided Therapy, Pessac, France,

[6] Univ. Grenoble Alpes, Inserm, CNRS, CHU Grenoble Alpes, IRMaGe, Grenoble, France,

[7] Institut Universitaire de France, Paris, France.

Contact information:

*Correspondence: anthony.delalande@inserm.fr

Abstract:

Objective

The blood-brain barrier (BBB) is a selectively permeable membrane that restricts drug delivery to the central nervous system (CNS). Focused ultrasound (FUS) combined with microbubbles (MB) is a promising technique to transiently open the BBB, enabling therapeutic delivery. However, real-time monitoring of BBB permeability changes remains challenging. This study investigates the use of indocyanine green (ICG) as a bimodal contrast agent for photoacoustic and fluorescence imaging to assess BBB opening and closure dynamics.

Methods

BALB/c mice underwent FUS-mediated BBB opening with different doses of MB and ICG administration. Photoacoustic and fluorescence imaging were performed at various time points post-FUS to evaluate ICG extravasation dynamics. MRI with gadolinium contrast was used as the gold

standard for BBB permeability assessment. The effect of MB dose and injection timing on BBB closure kinetics was analyzed.

Results

Photoacoustic imaging provided reliable BBB monitoring within the first hour post-FUS, whereas fluorescence imaging was more effective at detecting ICG extravasation at 24 hours. A strong correlation was observed between fluorescence intensity and MRI-based contrast enhancement, confirming BBB opening dynamics. BBB closure followed an exponential decay model, with a half-closure time of approximately 81 minutes. The degree of BBB opening was proportional to the MB dose administered.

Conclusion

ICG-based photoacoustic and fluorescence imaging provide a non-invasive and cost-effective alternative to MRI for monitoring FUS-induced BBB opening. These techniques offer complementary temporal windows for assessment, improving the precision of BBB permeability evaluation in preclinical and potentially clinical applications.

Keywords: blood-brain barrier; ultrasound; microbubble; live imaging; photoacoustic imaging

1. Introduction

The blood-brain barrier (BBB) is a selectively permeable membrane that protects the central nervous system (CNS) from pathogen entry. This barrier is impermeable due to several properties [1], including specific transporters [2], drug-metabolizing enzymes [3,4], or tight junction proteins, such as Claudin-5 or Occludin, expressed by endothelial cells [5–7]. Over 98% of molecules under 400 Da [8,9] and about all larger molecules are unable to cross the BBB [10,11]. Its impermeability prevents most therapeutic molecules from entering the CNS. Developing innovative strategies to overcome this barrier is essential for treating CNS diseases [1], for example, using gene therapy or immunotherapy.

However, the precise control of the BBB opening is still challenging. The use of focused ultrasound (FUS) combined with gaseous microbubbles (MB) is currently the technique offering the best potential for clinical use [12–15]. When exposed to ultrasound, MB can oscillate, either in a stable regime, provoking shear forces capable of forcing the transient rupture of endothelial tight junctions and thereby opening the BBB [16–18], or in an inertial regime, causing MB collapse and potential damage and hemorrhage [19,20]. This technique holds great potential for drug delivery in the CNS, with many therapeutic applications and several ongoing clinical trials for Parkinson's and Alzheimer's [21,22]. To ensure that this technique remains safe and reproducible, it is crucial to precisely monitor the BBB opening [23,24]. T1-weighted Magnetic Resonance Imaging (MRI) with contrast agents such as Dotarem® is the most common technique used for this purpose [12,25,26]. It allows a quantitative assessment *in vivo* of the BBB permeability with a great spatial resolution [23,27]. Moreover, it has the advantage of providing information on tissue damage and on physiological changes such as blood perfusion or oxygenation induced by the BBB opening [28]. MRI can also be used as a tool to guide the ultrasound beam to target specific brain structures [29]. Despite those advantages, the cost, availability, and time-consuming aspects of this monitoring and guiding technique are strong limitations to its widespread application, making it challenging to use when large cohorts of animals are required. Evans Blue dye extravasation is another widely used technique to assess BBB opening. This dye has fluorescence and photoacoustic properties, but this low-cost technique, mainly used *ex vivo*

[30,31], is problematic for monitoring BBB opening with *in vivo* imaging due to its long-term and static accumulation in tissues.

Near-infrared probes are widely applied for *in vivo* fluorescence imaging since these wavelengths have a better transmission through tissues and a lower autofluorescence signal [32]. Indocyanine Green (ICG), an FDA-approved drug for imaging and fluorescence-guided surgery [33–35], is a commonly used dye. Liang *et al.* reported the use of homemade ICG-loaded MBs to follow BBB opening *in vivo.* They recorded fluorescence accumulation caused by ICG extravasation following FUS treatment to detect the BBB-opened region *in vivo* [36]. The use of optical imaging techniques with such probes provides qualitative or quantitative measures of BBB opening faster and at a lower cost than MRI. Furthermore, ICG has also been described as a photoacoustic imaging contrast agent [37]. The photoacoustic effect refers to the emission of an ultrasonic wave after a laser excitation due to a thermo-elastic vibration that can be detected by echography. This modality has been used by Le Floc'h *et al.* to monitor BBB opening *in vivo* [38]; the authors successfully detected ICG extravasation through photoacoustic imaging using concentrations between 30 and 50 mg/kg. Like MRI, this technique enables *in vivo* measurements of physiologic parameters such as blood flow, blood vessel size, and blood oxygenation in real-time [39–43]. Photoacoustic imaging has been applied to various diseases including cancer [44], stroke [45], or neurodegenerative disorders [46]. This modality can achieve a spatial resolution of hundreds of micrometers in three dimensions when using a high-frequency custom ultrasound scanner, making it a cost-effective alternative to MRI (43,47–49).

MRI-based contrast agents are already largely characterized [47,48] and are the gold-standard method for BBB opening monitoring in patients. Yet, ICG extravasation dynamics was not assessed by previous studies, and a non-quantitative MRI approach was used [38]. We propose to bridge this gap with quantitative evaluation of MRI-based contrast agents along with ICG contrast agent extravasation dynamics. For the first time, we compare optical imaging modalities for monitoring BBB opening, using ICG as a bimodal agent for both photoacoustic and fluorescence imaging, offering an alternative to MRI.

We present the ability of ICG to monitor the BBB opening within the first hour post-FUS treatment using photoacoustic imaging and within the first 24 hours post-FUS treatment with

fluorescence imaging. Afterward, we measure the kinetics of BBB opening induced by FUS and MB treatments using a delayed injection of ICG. We also assess the influence of the amount of MB injected for the induction of the BBB opening. Finally, we compare our technique with MRI, which remains the gold standard for BBB opening monitoring.

2. Materials and Methods

2.1 Animals

A total of 79 adult male and female BALB/c mice aged above 6 weeks (weight ranging from 18 to 35 g) were used in this study (Charles River, France). All experiments were conducted in accordance with European ethical rules; the protocol was approved by the local ethical committees CEEA-003 and CEEA-012, protocols are registered under numbers APAFIS#13749 and APAFIS#43777. Mice were housed under a 12h/12h light/dark cycle in a controlled atmosphere (22 °C) and fed *ad libitum*.

2.2 Chemicals

1,2-distearoyl-sn-glycero-3-phosphocholine (DSPC) and 1,2-distearoyl-sn-glycero-3-phosphoethanolamine-N-[methoxy(polyethylene glycol)-2000] (ammonium salt) (DSPE-PEG2000) were purchased from Avanti Polar Lipids (Alabaster, Alabama, USA). Perfluorobutane was obtained from F2 Chemicals (Preston, United Kingdom). ICG was obtained from TCI (Portland, USA). Gadolinium contrast agent Gd-DOTA (DOTAREM®) was obtained from Guerbet (Villepinte, France). All chemicals, unless otherwise stated, were supplied by Sigma Merck.

2.3 Microbubbles

Homemade microbubbles composed of DSPC and DSPE-PEG2000 (22:3 molar ratio) were prepared by solubilizing lipids in ethanol in 1.5 mL glass vials at a concentration of lipids of 5 mg/mL, followed by formation of liposomes and freeze-drying of the sample [49]. The headspace of the vial was filled with perfluorobutane. Microbubbles were activated by mechanical agitation at 4500 rpm for 45 s using a Vialmix (BMS, Princeton, New Jersey, USA). MB concentration and size distribution were measured by optical imaging on a 0.2 mm Thoma slide using an inverted microscope (Leitz, obj ×25). The MB solution was diluted, and 20 µL

were dropped on a Thoma slide. Images were taken 5 minutes after loading allowing all the microbubbles to reach the top of the slide. A minimum of 15 images were analyzed (1000 events minimum) for microbubble size distribution and concentration analysis. Images were analyzed using the particle analysis plugin of ImageJ software. Our custom microbubble formulations were concentrated at $2.35\times10^{10} \pm 1.93\times10^{9}$ MB/mL, with a median diameter of 1.37 ± 0.2 µm. (Figure 1).

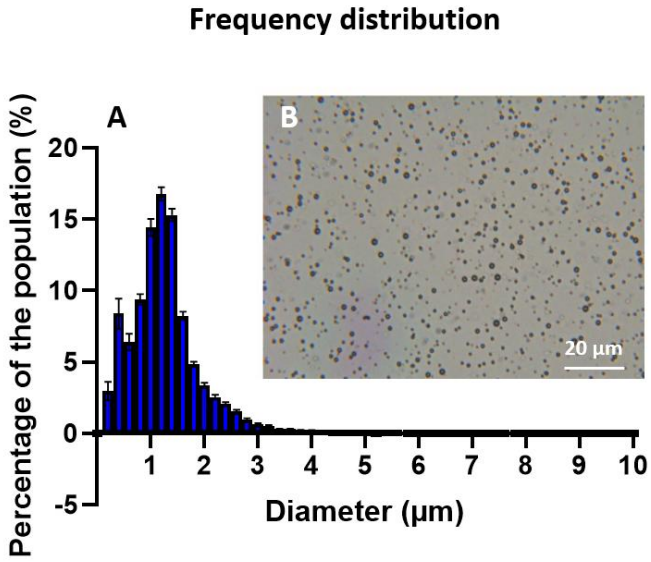

Figure 1. MB characterization: (**A**) Size distribution of microbubbles used for BBB opening, obtained with optical imaging (mean with SEM, n = 13). (**B**) Optical image of microbubbles used to determine size and concentration, obtained with an inverted microscope, magnification ×25.

2.4 Blood brain barrier opening using focused ultrasound and microbubbles

The experiment was conducted on mice with at least 4 animals per group. Mice were anesthetized with 2% isoflurane in air. A catheter (26 G) was placed in the tail vein, and the skull was shaved using depilatory cream. Then the mice were placed on a dedicated contention system (Minerve, France) equipped with an isoflurane anesthesia mask. Degassed ultrasound gel was applied on the shaved skull. The transducer was put in the probe holder containing degassed water within a silicone membrane (0.2 mm) to conduct ultrasound signals through the gel. This transducer is a 1 MHz focused bowl transducer with a 45 mm diameter active element (DL-47 piezo material, radius of curvature 45 mm, Precision Acoustics, UK) with an ellipsoid-shaped focal spot of 6×1.5 mm (height × width) (Figure S1, C) [50]. The transducer was controlled by a custom 3-axis motorized stage (IndustryLab,

Orléans, France) and the position of the focal spot was located using a laser beam guide relative to the eyes and ear bar to approximately reach the interaural position +2.5 and lateral +1.5 or -1.5 depending on hair removal quality. Ultrasound probe focal spot locations relative to the laser beam were determined in a degassed water tank using a hydrophone (Onda HGL200, USA). A 100 µL bolus of MB (10 µL MB solution, ranging between 3×10^7 and 3×10^8 MB, diluted in 90 µL of 10 mM HEPES buffer 5% sucrose) was injected in the tail vein *via* the catheter. Ultrasound was turned on 10 s after injection. Ultrasound pulses were set at 1 MHz, 315 kPa peak negative pressure pulsed at 1 Hz with 5% duty cycle (DC) during 60 s. According to Gerstenmayer *et al.*, *in situ* peak negative pressure was estimated at 305 kPa and a mechanical index of 0.305 [51]. FUS treatment was performed on a single spot located on either the left or the right hemisphere. The untreated hemisphere was considered as contralateral control. The ultrasound signal was generated using a waveform generator (Agilent 33210A or Rigol DG1032Z) and amplified with a linear amplifier (E&I, 210L or 2100, USA). All ultrasound systems were calibrated using a hydrophone (Onda HGL200, USA) in a degassed water tank. After the 60 s FUS treatment, 50 µL of freshly prepared ICG solution (0.25 or 0.5 mg of ICG) was injected through the catheter, undelayed (< 2 min) or with a delay of 30 or 120 minutes to analyze the kinetics of BBB closing. Mice were kept under anesthesia for the 5- and 30-minute timepoints, but for the 120-minute timepoint, mice were awakened in a dedicated cage before being put under anesthesia again for the injection.

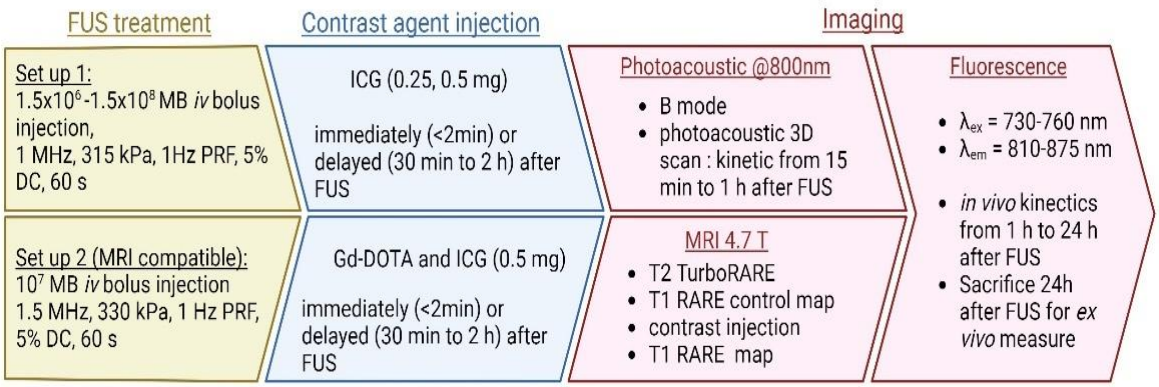

Figure 2. Schematic representation of the experimental timeline. With FUS: focused ultrasound; MB: microbubbles; PRF: pulse repetition frequency; ICG: Indocyanine Green.

2.5 In vivo imaging

The experiments were conducted following the timeline shown in figure 2.

2.5.1 Photoacoustic and ultrasound imaging

We used in this study the VEVOLAZR device (VisualSonics, Fujifilm, Canada), a photoacoustic and ultrasound imaging system with the LZ400 probe (image width 15.36 mm and 20 mm depth, axial resolution 50 μm; full details of acquisition in supplementary method). Photoacoustic emission maxima of the ICG probe were determined *in vitro.* Each solution to be analyzed was injected into a channel of a six-channel microfluidic slide (Ibidi μ-slide VI 0.4, Clinisciences, France). The slide was immersed in water for ultrasound coupling. The LZ400 ultrasound probe (Visual Sonics) was positioned at 10 mm from the microfluidic slide. The spectrum was measured from 680 to 970 nm. Each point of the spectrum was obtained at a 1 nm step and is the result of an average of 3 images.

Photoacoustic and ultrasound imaging were performed on animals under anesthesia (2% isoflurane in air). After FUS treatment, mice were placed on the 3D stage of the VEVOLAZR device (VisualSonics, Fujifilm, Canada), a photoacoustic and ultrasound imaging system. The LZ400 probe (30 MHz, VisualSonics, Fujifilm, Canada) was placed in contact with the skin coupled with degassed gel to position the mouse skin 10 mm from the probe. A 3D scan of the brain was performed by photoacoustic imaging at 800 nm every 15 min up to 1 h after FUS and undelayed ICG injection (Figure 2). The 3D scans (3D range 8.03 mm, step size 0.102 mm) were used to localize the BBB-opened region and measure its volume with a 3D region of interest calculated with VevoLab software (VisualSonics, Fujifilm, Canada). After photoacoustic imaging, mice underwent fluorescence imaging up to 24 hours after FUS. Complete photoacoustic imaging acquisition parameters are presented in supplementary methods.

2.5.2 Fluorescence imaging

Imaging was performed on anesthetized mice (2% isoflurane in air) using the IVIS Lumina LT Series III (Perkin Elmer, Massachusetts, USA). For all studies, the parameters used were λ_{ex} = 730-760 nm and λ_{em} = 810-875 nm, with an exposure time of 0.5 to 2 s, binning of 2

or 4, and f/stop of 2 or 4. Fluorescence imaging was performed *in vivo* on living animals and *ex vivo* on mice brains after euthanasia to assess the BBB opening using two ICG doses (0.25 or 0.5 mg). We expressed all fluorescence measurements in this study as the total fluorescence measured in a circular 5.76 mm^2 region of interest (ROI), and its unit $(p/s/cm^2)/(\mu W/cm^2)$ will be referred to as fluorescence intensity (F.I) for the rest of the paper. The circular ROI size was chosen to be slightly larger than the ultrasound probe focal spot, as we know that the BBB can be opened in a larger area than the focal spot (Figure S1). The signal of ICG injected directly after the FUS treatment was measured 1, 4, and 24 hours after FUS treatment (Figure 2). Mice were sacrificed following the 24h *in vivo* imaging to be imaged *ex vivo*. Fluorescence imaging was also used to determine BBB closure after FUS treatment with a delayed ICG injection, either 30 minutes or 2 h after FUS. For this purpose, fluorescence was measured *in vivo* and *ex vivo* 24 h after FUS.

2.5.3 BBB opening monitoring by MRI

To confirm the use of ICG for BBB opening monitoring, we compared our data to MRI, the gold standard of BBB permeabilization evaluation with a gadolinium T1 contrast agent. Due to limited access to an MRI scanner in our laboratory, we performed this experiment in the IRMaGe facility (Grenoble, France). In this section we detail the steps and devices used to make this comparative experiment. MRI was performed at 4.7T (BioSpec 47/40, Avance III, Bruker, Ettlingen, Germany); the scanner was equipped with a volume transmit coil and a single-element surface receive coil. The MRI protocol performed after the FUS treatment was: T2-weighted TurboRARE sequence (TR/TE = 2200/36 ms; 13 axial slices; FOV = 20×20 mm^2; matrix 256×256; voxel size, 78×78×1000 μm^3, RARE-factor, 8; Tacq = 3 min 31 s), T1 map RARE VTR sequence (TR, 3000 to 18 ms; TE =6.6 ms; FOV = 20×20 mm^2; matrix 128×128; voxel size, 156×156×1000 μm^3, RARE-factor, 4; 2 slices, Tacq = 12 min 39 s) performed before and after the intravascular co-injection of a gadolinium chelate (Gd-DOTA; DOTAREM®, Guerbet, Villepinte, France) and 0.5 mg of ICG, T1-weighted RARE sequence (TR/TE = 800/7 ms; 13 slices; FOV = 20×20 mm^2; matrix 256×256; voxel size, 78×78×1000 μm^3, RARE-factor, 4; axial and coronal orientations; Tacq = 1 min 16 s) to evaluate the BBB opening. To evaluate the dynamics of BBB permeabilization, the co-injection of ICG and Gd-DOTA was carried out at three time points after the FUS-induced BBB opening: 0 minutes, 30 minutes, and 120 minutes.

Mice were euthanized 24 h after FUS treatment, their brains were collected, and they were directly freeze-dried in liquid nitrogen. ICG fluorescence was then assessed *ex vivo* as described before. BBB was permeabilized with an MR-guided FUS device (Image Guided Therapy, Pessac, France) (Figure 2). Briefly, a 7-concentric-element transducer (Imasonic, Voray-sur-l'Ognon, France) is embedded on a 2-axis motorized system enabling planar displacement, all controlled by the Thermoguide® software (Image Guided Therapy, Pessac, France). For BBB permeabilization, 2.5 µL of activated MB were diluted in 97.5 µL of HEPES buffer supplemented with sucrose (5% final concentration). This dilution corresponds to an injection of about 10^8 MB. A bolus injection of the 100 µL diluted microbubbles was administered through the tail vein *via* a 26 G catheter 10 seconds before delivering sixty 1.5 MHz pulses of 50 ms for a total FUS sequence duration of 1 minute. FUS was delivered in the left hemisphere with a peak negative pressure calculated in water at 330 kPa negative peak (considering a 90% transmission factor, corresponding to 300 kPa *in situ* according to Gerstenmayer *et al*. [51] and a mechanical index of 0.245).

For MRI image processing, T1 maps were reconstructed using ParaVision software. Then, MRI data were processed and analyzed using MP3 software [52]. Gd-DOTA concentration C was derived from the T1 maps acquired before (T1, 0) and after (T1, t) the injection of Gd-DOTA using the following equation [53]: considering the longitudinal relaxivity $\boldsymbol{r_1 = 3.4\, mM^{-1} \times s^{-1}}$ [54]:

$$\boldsymbol{C = \frac{1}{r_1}\left(\frac{1}{T_{1,t}} - \frac{1}{T_{1,0}}\right)} \quad (\mathbf{1})$$

Then, according to Marty *et al.*, we normalized the concentration of Gd-DOTA extravasation by drawing regions of interest in the contralateral region and in the muscle as depicted in Figure 9. Apparent concentration $\boldsymbol{C^{\Delta}}$ was obtained considering the acoustic pressure (IPac) equal to 1, the concentration in the ipsilateral region $\boldsymbol{C_{ROI,ipsi}}$, the concentration in the contralateral region $\boldsymbol{C_{ROI,contra}}$ and the concentration in the muscle $\boldsymbol{C_{ROI,muscle}}$ all calculated with equation (1) and using the following equation [55]:

$$\boldsymbol{C^{\Delta} = \frac{C_{ROI,ipsi} - C_{ROI,contra}}{C_{ROI,muscle} \times IP_{ac}}} \quad (\mathbf{2})$$

IPac was not evaluated in our study and was set to 1. MRI and fluorescence kinetic data were normalized with the average signal obtained at 0 minutes to observe and compare the signal decay.

2.6 Statistics

Non-parametric Wilcoxon and Mann-Whitney bilateral tests were conducted using the R language (version 4.4.0, used with RStudio software). Nonlinear fit and F-test were performed using GraphPad Prism v10.4. The derived parameters were used to calculate the half closure time ($T_{1/2}$) using the following equations:

$$\mathbf{Y} = (\boldsymbol{Y0} - \boldsymbol{Plateau}) \times \boldsymbol{e^{-Kt}} + \boldsymbol{Plateau} \quad (\mathbf{3})$$

$$\boldsymbol{T_{1/2}} = \frac{\boldsymbol{ln(2)}}{\boldsymbol{K}} \quad (\mathbf{4})$$

With Y0 being the Y value when X (time) is zero, Plateau being the Y value at infinite times, and K being the rate constant, expressed in reciprocal of the X axis time units. A *p*-value below 0.05 was considered significant; all data are represented as mean +/- standard error of the mean (SEM).

3. Results

3.1 ICG dose response by photoacoustic imaging

ICG photoacoustic spectra were analyzed *in vitro* to determine the maximum emission wavelength and concentration range suitable for *in vivo* imaging (Figure 3). A peak photoacoustic effect of 21.07 arbitrary units (A.U.) was obtained at 800 nm. A significant drop in photoacoustic signal was measured from 21.07 to 4.00 A.U. using ICG at 1 mg/mL and 0.1 mg/mL, respectively, corresponding to a 6-fold decrease.

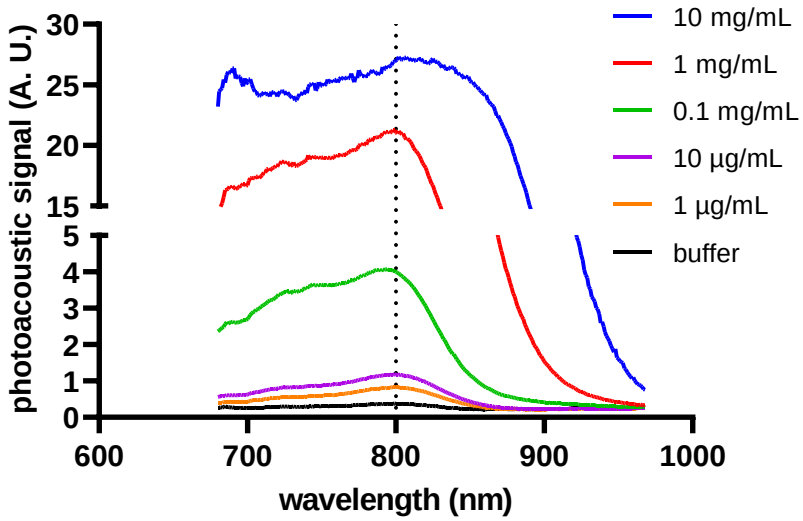

Figure 3. *In vitro* ICG photoacoustic spectrum at concentrations ranging from 1 µg/mL to 10 mg/mL in 5% sucrose 10 mM HEPES buffer.

Photoacoustic response of ICG at 800 nm was then evaluated *in vivo* (Figure 4). The photoacoustic signal was measured after FUS treatment in the ipsilateral treated hemisphere using the contralateral hemisphere as a control. The maximum signal was observed at 800 nm *in vivo*, as obtained *in vitro*. This signal was 1.5-fold stronger in the treated region (0.509 A.U., purple curve) compared to the contralateral (0.332 A.U., blue curve). However, an even stronger photoacoustic signal was measured in the skin with 3.2 A.U. (green curve). These signals in the skin and the contralateral region could be attributed to circulating ICG after the intravenous injection, with the signal decreasing after the skull and with tissue depth.

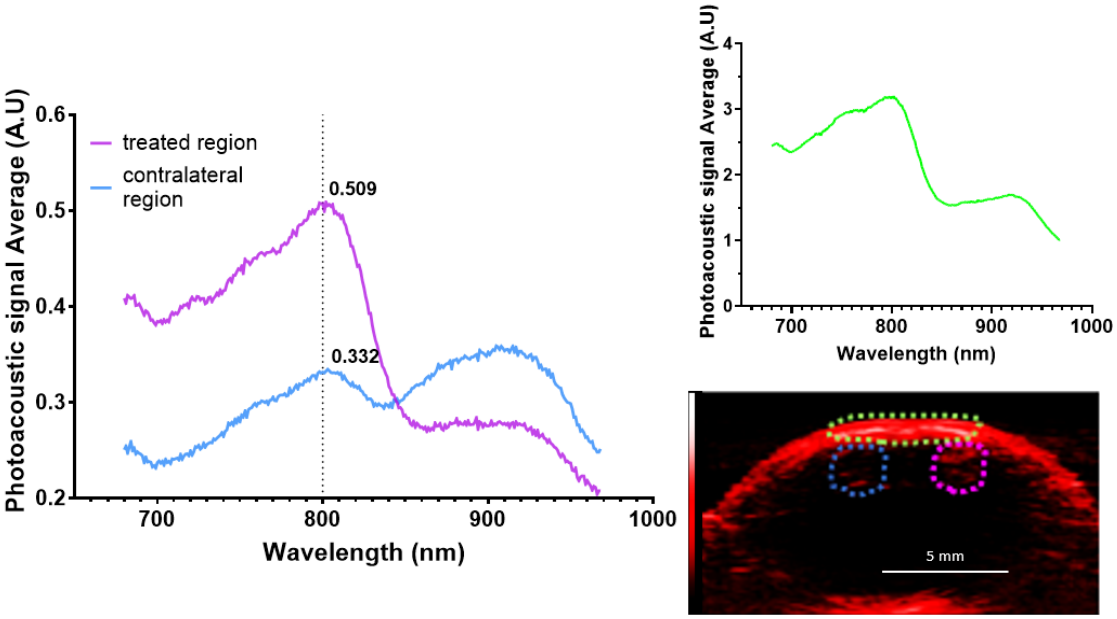

Figure 4. *In vivo* ICG photoacoustic spectrum after FUS treatment. Pink: signal in the ipsilateral BBB-opened region. Blue: signal in the contralateral region. Green: signal in the skin.

3.2 ICG extravasation allows detection of the BBB opening using photoacoustic imaging

The signal-to-noise ratio was calculated for the treated (T) and contralateral untreated (C) ROIs for both doses (0.5 mg and 0.25 mg) every 15 min after FUS and during one hour (Figure 5). Noise was measured in a region outside the skull (ROI called N on the figure). The photoacoustic signal-to-noise ratio in T was significantly higher than in region C from 30 to 60 min after FUS when using 0.5 mg of ICG, whereas at a lower dose (0.25 mg) the signal-to-noise ratio in region T was found to be significantly increased regarding region C from 15 to 30 minutes. From 30 to 45 minutes, we observed a significant drop with the 0.25 mg dose, with a signal-to-noise ratio decreasing from 3.42 to 2.32 A.U. (Figure 5B). However, we were still able to distinguish the BBB-opened region for up to 60 min (Figure 5A) for the two doses of ICG. A signal-to-noise ratio decay is observed after 30 min, and the values tend to go back to the baseline (reaching 1.85 and 2.10 A.U. at 1 h for 0.5 mg and 0.25 mg respectively), probably due to the low half-life of ICG [56]. No significant difference in either signal-to-noise ratio or BBB-opened volume was observed between the two chosen doses (Figure S2). Regarding the control region, the signal-to-noise ratio measured was significantly higher 15 min after FUS (1.68 A.U. for 0.5 mg and 1.52 A.U. for 0.25 mg) compared to the one measured 30 to 60 min

after FUS (about 1.2 A.U. for both doses). This higher signal-to-noise ratio at 15 min for the control region could be attributed to the presence of ICG in the blood pool.

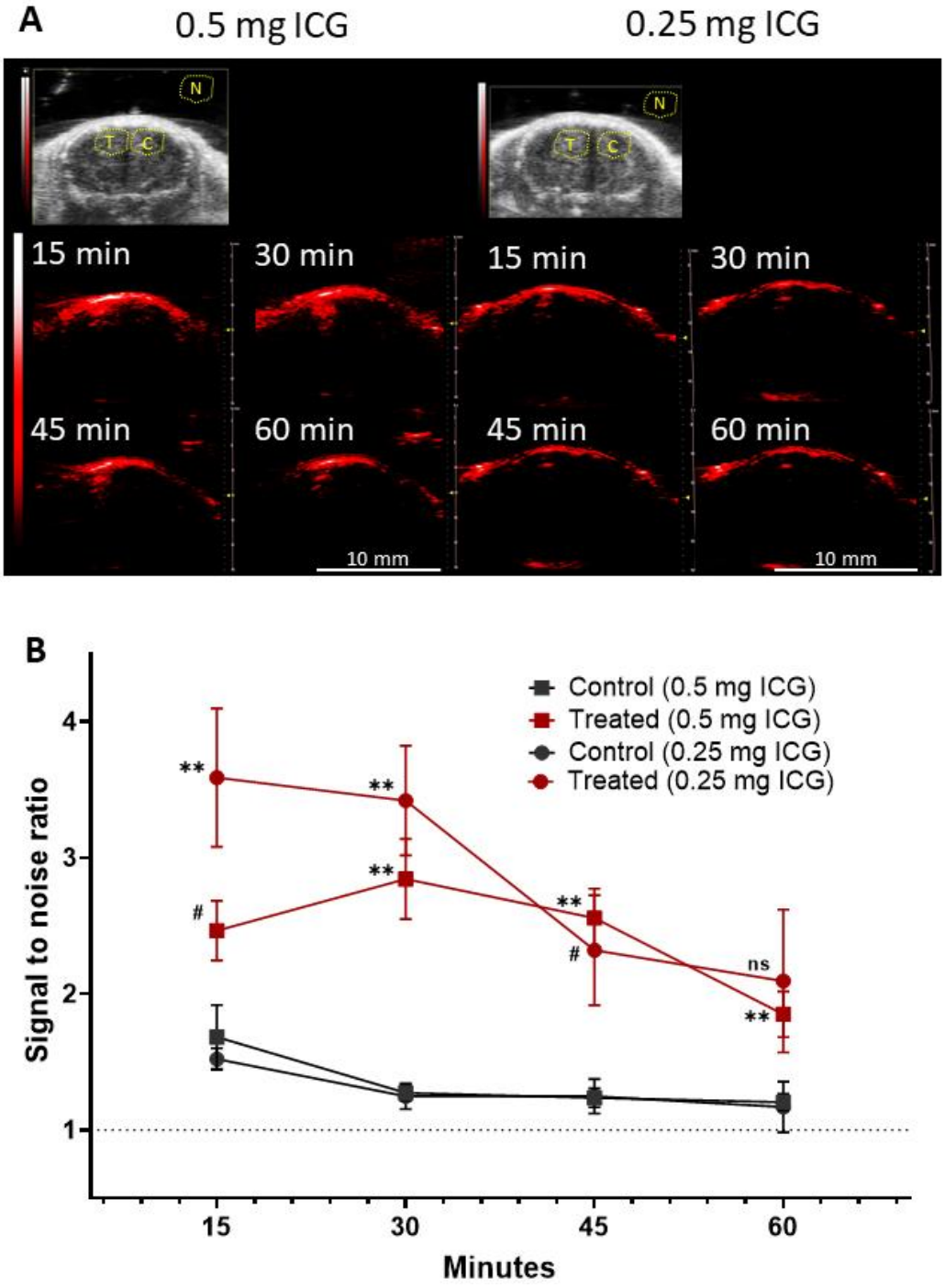

Figure 5. *In vivo* photoacoustic kinetics from 15 to 60 minutes after FUS treatment. (**A**) *In vivo* B-mode ultrasound imaging (grey) and representative photoacoustic images (red) at 800 nm in the BBB-opened region T compared to the contralateral region C. **Left:** 0.5 mg ICG. **Right:** 0.25 mg ICG. (**B**) Graphical representation of the signal-to-noise ratio calculation made by dividing the signal in the T or C region

by the noise N. (n = 4 to 6). Data expressed as mean +/- SEM. #: p-value < 0.1; *: p-value < 0.05; **: *p*-value < 0.01; Wilcoxon bilateral test Treated *vs* Control.

3.3 ICG extravasation allows detection of the BBB opening using fluorescence imaging

Fluorescence imaging is another method to detect *in vivo* BBB opening after ICG injection. Fluorescence imaging was performed 1 h, 4 h, and 24 h after the FUS treatment (Figure 6). At 1 h, no significant difference was observed between control (C) and treated (T) regions with both doses. With 0.5 mg, a 1.19-fold increase of fluorescence intensities (F.I) of T over C is observed, and a 1.34-fold increase with 0.25 mg. The same observation can be made at 4 h, with a 1.51-fold increase in T with 0.5 mg and a 1.37-fold increase for 0.25 mg. The similar responses observed at 1 to 4 h after FUS may be ascribed to the emission of ICG in the skin. Despite these high intensities in the control region, it is still possible to visually decipher the BBB-opened region in all cases using 0.5 mg and 0.25 mg ICG, but with some difficulties. At 24 h, a significant difference was observed between the control and treated regions both at 0.5 mg ICG (3.89-fold increase) and at 0.25 mg (3.52-fold increase). One can notice that the F.I obtained in T at 24 h with a 0.5 mg dose that became significantly lower than at 4 h, getting down from 6.63×10^9 to 2.59×10^9 F.I, while for 0.25 mg ICG, the difference is only significant between the 1 h and 24 h timepoints (from 4.91×10^9 to 1.58×10^9 F.I). In addition, there is a significant difference of F.I in the control region between the two doses at 4 h after FUS but not at 1 h or 24 h after FUS. These observations suggest a slightly faster clearance of ICG when used at 0.25 mg. Moreover, doubling the amount of ICG did not significantly modify the fluorescence at 24 h, which can be due to a saturation effect in the region. While the most optimal time to assess the BBB opening using photoacoustic imaging is within the first hour after sonoporation, the optimal time to assess the BBB opening using fluorescence imaging appears to be after 24 h.

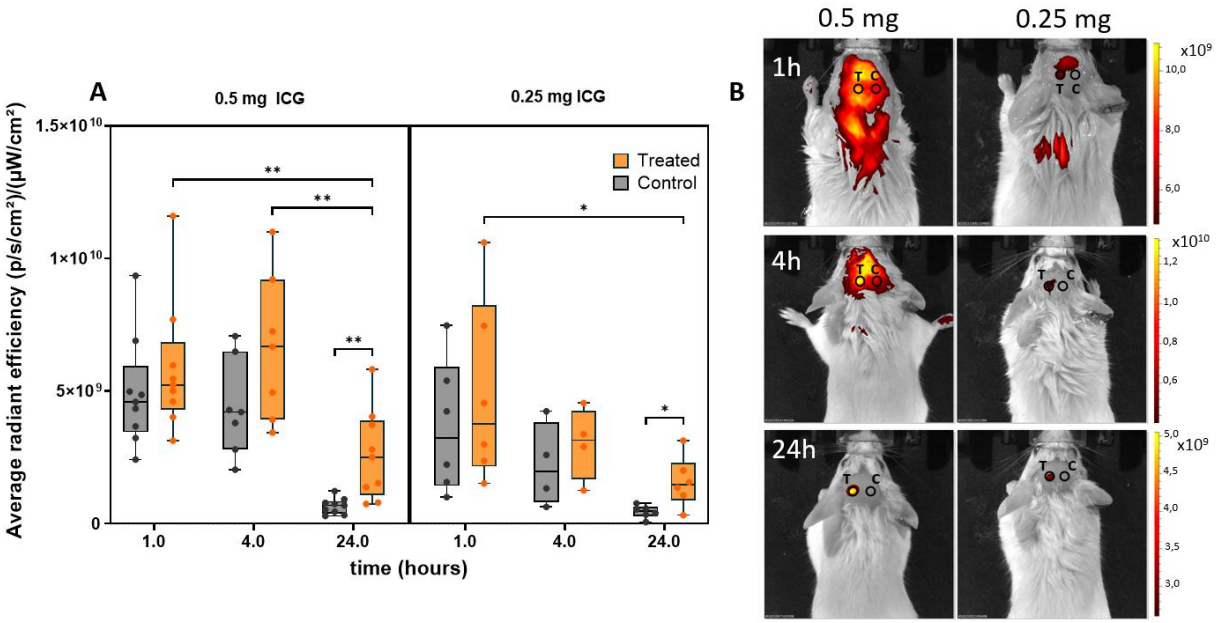

Figure 6. *In vivo* fluorescence imaging kinetics 1 h, 4 h, and 24 h after FUS treatment. (**A**) Graphical representation of the fluorescence intensity measured in the BBB-opened zone (orange) *vs* the contralateral zone (grey). **Left:** 0.5 mg of ICG (n = 7 to 9). **Right:** 0.25 mg of ICG (n = 4 to 6). (**B**) *In vivo* fluorescence images of representative mice for each point (1 h, 4 h and 24 h) with treated T and control C regions. **Left:** 0.5 mg of ICG. **Right:** 0.25 mg of ICG. *: p-value < 0.05; **: p-value < 0.01; Wilcoxon bilateral test Treated *vs* Control or Mann-Whitney test.

3.4 BBB closure kinetics can be assessed with fluorescence imaging

To evaluate the kinetics of the BBB closure, 0.5 mg ICG was injected straight away (< 2 min) or delayed by 30 or 120 min after the FUS treatment. Then, the fluorescent signal in the T and C regions was measured 24 h after FUS treatment (Figure 7). For *ex vivo* measurements with direct ICG injection, mice were treated with 1.5×10^8 MB to match the experiments shown in Figure 8 avoiding an excessive use of animals. BBB-opened region can be deciphered with up to 120 min delay both *in vivo* and *ex vivo.* For *in vivo* experiments, the difference between fluorescence intensities (F.I) of C and T regions was almost significant with a 120-min delay (5-fold increase in region T, *p*-value = 0.093) while for *ex vivo* experiments, it was significantly different with a 16.6-fold increase (Figure 7A). One can observe a slight decrease, albeit not significant, of the fluorescence signal in region T with the 30 min delay both *in vivo* and *ex vivo* (from 3.13×10^9 to 2.71×10^9 F.I *in vivo*, and from 7.44×10^9 to 5.32×10^9 F.I *ex vivo*). Then, there was a significant drop of F.I in the T region with the 2 h delay compared to the 5- or 30-min delay in both conditions. A mono-exponential decay function was adjusted to the data obtained *ex*

vivo and, thereby a half closure time of 81.41 minutes was calculated (Figure S5) (R^2 = 0.5678; $Y = 1.2637 \times e^{-0.0085x} - 0.2637$). Note that half closure time could not be accurately calculated with data obtained *in vivo*.

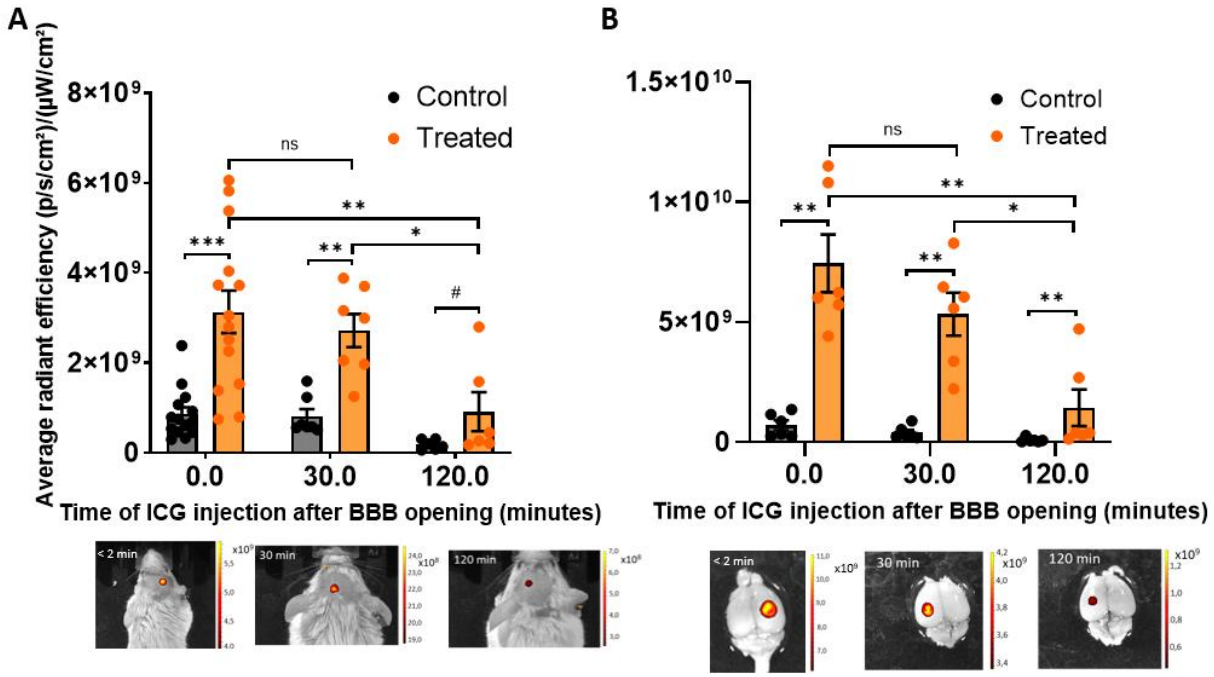

Figure 7. Assessment of BBB closure kinetics. 0.5 mg of ICG was injected either directly, 30 min or 2 h after FUS treatment. Fluorescence intensity was measured at 24 h to evaluate the amount of ICG taken at each time point. (**A**) *in vivo* (n = 6 to 14). (**B**) *ex vivo* (n = 6). Representative fluorescence images are presented below the *in vivo* and *ex vivo* graphs. Data are expressed as mean +/- SEM. #: *p*-value < 0.10; *: *p*-value < 0.05; **: *p*-value < 0.01; ***: *p*-value < 0.001. Wilcoxon bilateral test Treated *vs* Control or Mann-Whitney bilateral test.

3.5 ICG fluorescence intensity can be correlated with the number of MB injected

It is well known that BBB opening is correlated with the number of MB injected into the animal [19,57]. With our MB formulation, we have also been able to demonstrate this effect both *in vivo* and *ex vivo*, using fluorescence imaging at 24 h with 0.5 mg of ICG injected immediately after ultrasound treatment (Figure 8). *In vivo*, we observed a significant difference between the T and C ROIs with 1.5×10^8 MB injected and a close significance with 1.5×10^7 MB injected (*p*-value = 0.093). We measured a 3.4-fold increase in the T region when 1.5×10^8 MB were injected and a 2.2-fold increase with 1.5×10^7 MB. There was an ~2-fold significant decrease in fluorescence by decreasing the MB amount by a factor of 10, from 1.5×10^8 to 1.5×10^7 MB doses. For lower MB doses (3×10^6 and 1.5×10^6 MB), the reduction of signal in the T region was

moderate and not significant compared to 1.5×10^7 MB. Moreover, the difference in fluorescence between the C and the T ROIs was not significant at lower MB doses, with a 1.89- and 0.97-fold increase in the T region for 3×10^6 and 1.5×10^6 MB, respectively, injected *in vivo*. A similar observation can be made *ex vivo* with more than a 2-fold significant decrease in fluorescence signal of the region T between 1.5×10^8 and 1.5×10^7 MB injected, with 7.44×10^9 and 2.71×10^9 F.I respectively. A slight and non-significant decrease was observed with a 3×10^6 MB dose for the region T. *Ex vivo*, the reduction of MB dose by another factor of 10 (1.5×10^7 to 1.5×10^6 MB injected) induced an over 4-fold significant decrease of signal in the treated region with 2.71×10^9 and 5.92×10^8 F.I respectively. Note that the difference of fluorescence *ex vivo* is significant between T and C regions with all MB amounts tested, except with 3×10^6 MB (*p*-value = 0.095) with a 21.4-fold increase in T region F.I respectively. While the difference between the T and the C regions is not always significant, the BBB-opened region was clearly visible on all mice *ex vivo* and with all doses of MB used and up to the 3×10^6 MB dose *in vivo* (Figure 8).

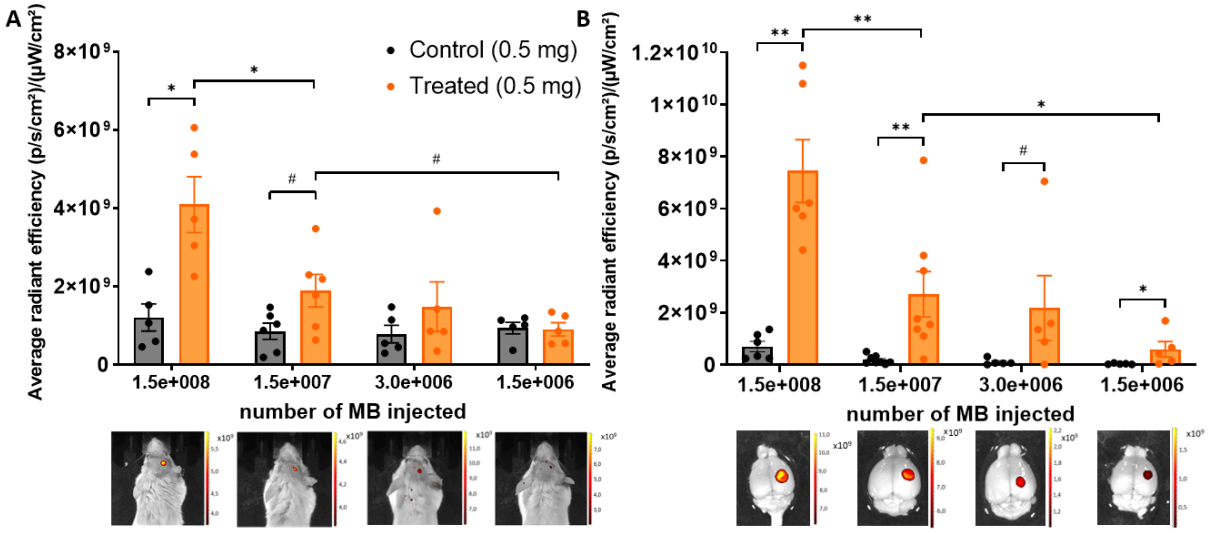

Figure 8. Assessment of the fluorescence intensity as a function of the number of MB injected. 1.5×10^6 to 1.5×10^8 MB were injected for BBB opening followed by an injection of 0.5 mg ICG. Fluorescence intensity was measured 24 h after FUS treatment (n = 5 to 8). (**A**) *In vivo*. (**B**) *Ex vivo*. Representative fluorescence images are presented below graphs *in vivo* and *ex vivo*. Data expressed as mean +/- SEM. #: p-value < 0.10; *: p-value < 0.05; **: p-value < 0.01; Wilcoxon bilateral test Treated *vs* Control or Mann-Whitney bilateral test.

3.6 BBB closure dynamics are similar using MRI or fluorescence imaging

MRI with Gadolinium (DOTAREM®, Gd-DOTA) as a contrast agent is the standard technique to evaluate the BBB opening. Comparisons between MRI and fluorescence imaging were made on the same animals. BBB was successfully opened in the left hemisphere of 14 mice (see paragraph methods 2.5.3). Gd-DOTA and ICG extravasations were evaluated *in vivo* with MRI and *ex vivo* by fluorescence (Figure 9). Like previous experiments, Gd-DOTA and ICG were injected in the same mice either immediately (<2 min) or delayed by 30 to 120 min after FUS. We observed that both the contrast enhancement of Gd-DOTA and the fluorescence of ICG follow an exponential decay, and we were able to perform a one-phase decay exponential fit on both datasets. For Gd-DOTA, the decay follows the equation $y = 0.7995 \times e^{-0.02110x} + 0.2007$ ($R^2 = 0.3980$) while for ICG, it follows the equation $y = 0.9716 \times e^{-0.02120x} + 0.02859$ ($R^2 = 0.5070$). Compared to undelayed control, we found that after 2 h, only 25% of Gd-DOTA and 10% of ICG could be detected. The calculated half closure time ($T_{1/2}$) was 32.85 for Gd-DOTA and 32.70 minutes for ICG. We also show that data from Gd-DOTA and ICG significantly follow the same distribution (F-test, *p*-value = 0.9357).

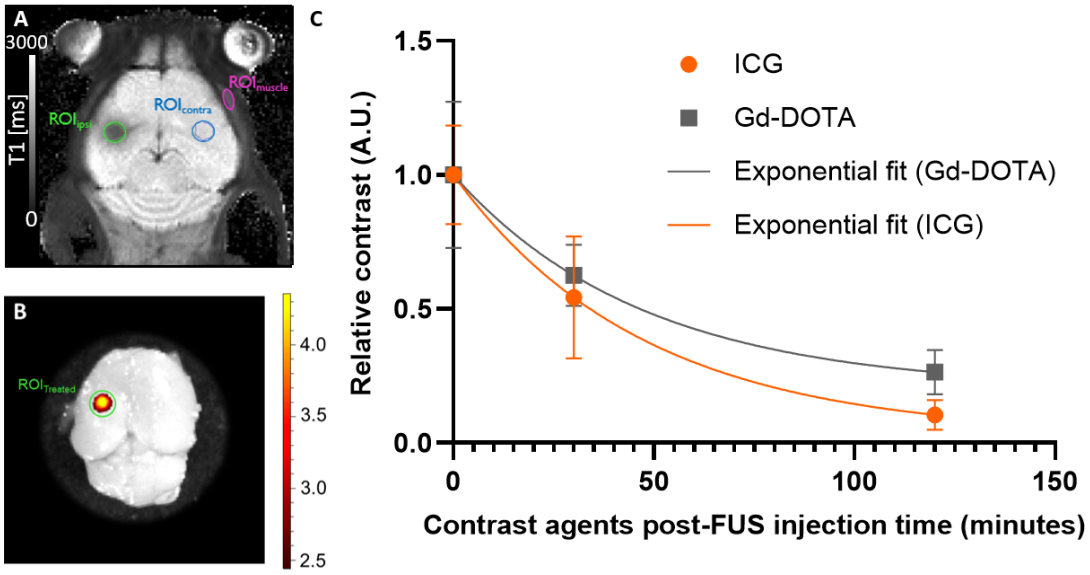

Figure 9: MRI confirmation of BBB closure dynamics (**A**, **B**) T1 map and *ex vivo* ICG fluorescence of mice following FUS treatment and co-injection, at different delays, of Gd-DOTA and 0.5 mg of ICG, with ROI used for measurement. (**C**) Kinetics of ICG and Gd-DOTA extravasation decrease normalized with mean contrast signal at t_0, measured with *in vivo* MRI and fluorescence imaging *ex vivo* respectively (n

= 4 to 5). Contrast agents were co-injected directly after the FUS procedure or with a delay of 30 to 120 minutes. *Ex vivo* fluorescence was performed on frozen brains collected 24 h after FUS. Data are expressed as mean +/- SEM. One-phase decay exponential fit and half closure time calculation ($t_{1/2}$).

4. Discussion

Opening the BBB is mandatory to treat numerous brain diseases, and focused ultrasound associated with MB is a well-known tool for this purpose [26]. Two main techniques are currently used to evaluate the BBB opening: MRI, mostly used *in vivo*, and Evans blue extravasation which requires euthanasia to evaluate the opening. Other techniques are being developed to monitor BBB opening to overcome these disadvantages, such as photoacoustic imaging [38], cavitation monitoring [24], and passive acoustic mapping [58]. The great advantage of photoacoustic imaging is to give, in addition to ICG extravasation, *in vivo* anatomic imaging and mapping of the oxygen blood saturation [38,41,43]. Fluorescence imaging also allows monitoring of the BBB opening *in vivo,* with the advantage of being cheaper and more accessible than MRI [36]. ICG has the advantage of being a contrast agent for both photoacoustic and fluorescence imaging, making it a bimodal agent. In this study, we demonstrated its effectiveness in monitoring BBB opening with both techniques, photoacoustic and fluorescence imaging, and compared it to the MRI gold standard.

We show in this study that ICG is an efficient tool to detect the BBB-opened region as the signal was improved at 800 nm after FUS treatment and ICG injection. We successfully monitored BBB opening using this wavelength in photoacoustic imaging from 15 to 60 minutes at both ICG doses (0.25 and 0.5 mg). Measured signal-to-noise ratios and BBB opening volumes were similar using both ICG doses (Figure 4 and S2). Taken together, these results suggest that the 0.25 mg dose was sufficient for the photoacoustic effect. Although, according to the manufacturer, laser penetration depth is limited to 1 cm, this penetration is decreased by the head's skull and skin as we were able to detect opened volumes only in dorsal structures of the brain. This limitation could be eliminated by removing the scalp or the skull but would make it much more invasive. As shown in Figure 5, the 0.25 mg dose seems more efficient to detect the BBB opening in the first minutes. The difference with the control area is significant for up to 30 minutes before the signal starts decreasing strongly. However, the opened area is still clearly visible for up to 60 minutes even though there is no longer a significant difference

with the control region. The same observation can be made for the 0.5 mg dose at 15 minutes, although the signal in the blood flow makes it harder to decipher the BBB-opened region. These results reveal that we were able to measure BBB opening *in vivo* with ICG for up to 60 minutes, without interference from the signal in the skin, which is about 10-fold higher than in the brain. Floc'h *et al*. previously used ICG or fluorescent nanoparticles as a contrast agent for BBB opening monitoring in photoacoustic imaging after FUS treatment [38]. They monitored BBB opening 2 h after FUS following ICG injection at 50 mg/kg (approximately over 2 times our highest dose) and managed to detect BBB opening but with difficulty for outlining the BBB-opened region. However, they had no difficulty after skin and skull removal or *ex vivo*. They did not manage to monitor BBB opening *in vivo* with their lowest dose at 10 mg/kg, similar to our lowest dose, which might be due to their 2 h delay before ICG injection and monitoring, most likely allowing partial closure of the BBB. Their results are consistent with ours, as we also show limits to outline the BBB-opened region *in vivo*, though we were able to detect BBB opening with lower concentration due to the absence of delay. It has to be noted that comparisons with previous studies are difficult due to ultrasound setup, BBB opening protocol, and imaging setup discrepancies.

The use of Evans blue allowed us to observe similar photoacoustic imaging monitoring of the BBB opening (Figure S3), with a significantly increased photoacoustic signal in the treated region over control from 15 to 45 minutes after FUS treatment and a similar measured BBB-opened region (Figure S2). Even though Evans blue was successfully detected, we measured a high background signal making BBB opening evaluation difficult. We also observed significant toxicity following Evans blue injection with 3 mice out of 4 mice dying within hours after the procedure. Evans blue toxicity is known at higher doses, as a 25 mg/kg and higher injection can cause mice death in months following injection [59–61]. Even lower doses can provoke toxic effects on cerebral endothelial or ependymal cells [62]. However, the observed toxicity was not expected with our dose, approximately 15 mg/mL, as it has been used in previous studies without reported toxicity. This could be explained by the BBB opening, which might increase Evans blue toxicity with its extravasation. Such adverse effects could be limited by reducing the injected dose, which has been shown to be possible without losing *ex vivo* fluorescence labeling of the BBB-opened region [63]. But it might reduce photoacoustic properties, with the risk of losing its ability to monitor BBB opening *in vivo*.

The ICG signal in the skin showed an important interference with *in vivo* fluorescence measurement, as seen in Figure 6. Like in photoacoustic imaging, this interference from the skin could be avoided with scalp removal, but this would not match the objectives of this article to develop a non-invasive live monitoring technique. Furthermore, no normalization was made with control or noise due to a halo effect from the treated region, distorting control or noise measurement. The BBB-opened region signal can be significantly deciphered from the control region one only 24 hours after FUS treatment and ICG injection regardless of the doses. The strong reduction of ICG signal over the first 24 h in the skin is probably due to the clearance of the ICG probe in the skin faster than in the brain once the BBB is closed. Even though the difference between control and treated regions is not significant before 24 hours, we can still see that the opened region has a slightly higher signal at 1 and 4 hours and can be visually deciphered in most cases, but with more difficulty using 0.5 mg of ICG. A previous study by Liang *et al*., using ICG as a fluorescent probe for *in vivo* BBB opening monitoring also manifests difficulty in seeing the BBB-opened region in the first 2 hours post-FUS when using a similar imaging system [36]. However, they also show that this issue can be overcome using a detection method with long-pass infrared filters (>1000 nm), even though they seem to observe a faster clearance of the fluorescence signal than us, which can be explained by their much lower ICG quantity injected (approximately 10-fold lower).

Moreover, our results indicate that compared to Evans blue, ICG is a better fluorescent marker. Indeed, even though Evans blue has fluorescent properties and BBB opening was observable *ex vivo*, this could not be detected *in vivo* by fluorescent imaging (Figure S4). This could be explained by the fact that the whole skin of the animal is colored making the opened region challenging to decipher unlike with ICG. Indeed, it might be due to a lower clearance of Evans Blue compared to ICG [63]. Unfortunately, mouse death in the hours following Evans blue injection prevented us from measuring fluorescence intensity at 24 h.

The impact of MB amount on BBB opening was previously demonstrated using SonoVue® MB [64]. The authors showed an increase of Evans Blue uptake *ex vivo* by increasing the MB dose injected. We observed the same correlation using ICG both *in vivo* and *ex vivo* with our homemade MB at a higher dose but similar gas volume range (2-200 nL gas volume injected).

We noticed that our results exhibit high variability which might be due to MB concentration fluctuations. Indeed, we observed in some vials inconsistencies in the decline in MB concentration over time after vial activation (data not shown) which can lead to differences in the BBB opening, as discussed before. Few variations in MB average size were observed, suggesting that MBs were not modified over time but simply burst over time. Therefore, freshly activated MB were used in most cases (≈60%) in this study. Efforts are currently underway to standardize and scale up the MB production process to mitigate variability. An alternative approach would be to characterize MB concentration before each injection. It is important to note that while optical microscopy is a commonly used technique to measure MB concentration, it primarily detects only micron-sized bubbles larger than 400 nm.

The MB dose-response experiment also reveals the limits of ICG fluorescence monitoring of BBB opening. At higher MB amounts, 1.5×10^{8} and 1.5×10^{7} MB, a similar 2-fold reduction of fluorescence *in vivo* and *ex vivo* of the treated area versus the control area is obtained. However, at low concentrations, fluorescence reduction is becoming complex to measure *in vivo,* which is not the case *ex vivo* with significant differences between the two regions. Those observations indicate that *ex vivo* monitoring of BBB opening using ICG's fluorescence is sensitive enough to measure the intensity of opening and material extravasation. Furthermore, although fluorescence monitoring *in vivo* of BBB opening is capable of precisely monitoring BBB opening, it lacks precision with small amounts of extravasated ICG, probably due to circulating ICG and tissues auto-fluorescence.

Regarding BBB closure kinetics, our results, both *in vivo* and *ex vivo*, show that the BBB was still open 30 minutes after FUS treatment. A partial closure was observed 120 minutes after FUS, but with 80 to 90% signal loss for ICG compared to t0 control with an 81.41 minutes half-closure time. Also, it was impossible to process *in vivo* measures with a one-phase decay, indicating the lack of sensibility of *in vivo* measurement with weak fluorescence as seen before. Nevertheless, we were able to decipher the reduction of fluorescence with delayed injections. Using MRI with an MRI-compatible FUS probe and an adapted protocol (protocol presented in Figure S1), our results reveal a colocalization of the opened region with *ex vivo* fluorescence. However, it is difficult to measure precisely the opened area with fluorescence imaging, as the light is dispersed in all possible directions, making the limits of the treated region difficult to

decipher. This indicates that MRI has a better spatial resolution. We also revealed in this experiment that the contrast decay acquired with MRI and *ex vivo* fluorescence imaging significantly follows the same exponential model with the same half closure time. It means that monitoring ICG fluorescence *ex vivo* for BBB closure kinetics is as precise as MRI. This also indicates that the differences in size between these two compounds are sufficiently close (560 Da for Gd-DOTA *versus* 775 Da for ICG) to avoid a difference in extravasation as their size greatly influences their extravasation and the measured closure kinetics [55]. A different closure kinetics was measured using our two different FUS set-ups (81.41 minutes for the set-up 1, 32.8 minutes for the MRI compatible set-up 2). This difference can be explained by the lower number of MB used and the higher FUS probe frequency with setup 2 (Figure S1). For example, Samiotaki *et al*. showed that increasing the MI from 0.245 to 0.49 also increased BBB closure time [65]. Compared to other studies, our kinetics are short, as the half closure time has been calculated in previous studies to be between 2 and 6 h [55,66], and BBB closure has been shown to vary from 2 to 72 h depending on acoustic parameters used [67–70]. Our kinetics can be explained by the lower acoustic pressure applied and the use of our homemade MB, which likely might be oscillating differently compared to Definity™ or SonoVue®.

A low-field MRI costs about $500 000 USD alone, which does not include mandatory additional costs such as shielding or maintenance. It requires highly trained operators and a significant space and is restricted to a specific animal size, making it difficult to access. Photoacoustic imaging systems have a comparable cost and still require highly trained operators but require lower maintenance and less space and can be used in both small and larger animals [71]. Fluorescence imaging allows fewer additional applications compared to MRI and photoacoustic imaging but has about a 5-fold lower cost, with little maintenance required, and can be operated with minimal training but is restricted to a specific animal size.

5. Conclusion

Overall, our data show that ICG is an efficient bimodal near-infrared probe for evaluating BBB opening and closure using photoacoustic and fluorescence imaging as an alternative to MRI. Our procedure proved to be efficient for BBB opening with a short closure kinetic, limiting potential side effects. Monitoring the BBB opening and closing is crucial for safely

controlling drug delivery to the brain. Achieving effective brain drug delivery would significantly improve treatments for brain tumors and neurodegenerative diseases.

The data that support the findings presented in this study are available from the corresponding author upon request.

6. References:

1. Zhang, S.; Gan, L.; Cao, F.; Wang, H.; Gong, P.; Ma, C.; Ren, L.; Lin, Y.; Lin, X. The Barrier and Interface Mechanisms of the Brain Barrier, and Brain Drug Delivery. Brain Res Bull 2022, 190, 69–83, doi:10.1016/j.brainresbull.2022.09.017.
2. Eng, M.E.; Imperio, G.E.; Bloise, E.; Matthews, S.G. ATP-Binding Cassette (ABC) Drug Transporters in the Developing Blood–Brain Barrier: Role in Fetal Brain Protection. Cellular and Molecular Life Sciences 2022, 79.
3. Sakakibara, Y.; Katoh, M.; Imai, K.; Kondo, Y.; Asai, Y.; Ikushiro, S.I.; Nadai, M. Expression of UGT1A Subfamily in Rat Brain. Biopharm Drug Dispos 2016, 314–319, doi:10.1002/bdd.2012.
4. Declèves, X.; Jacob, A.; Yousif, S.; Shawahna, R.; Potin, S.; Scherrmann, J.-M. Interplay of Drug Metabolizing CYP450 Enzymes and ABC Transporters in the Blood-Brain Barrier; 2011; Vol. 12;.
5. Farquhar, M.G.; Palade, G.E. Junctional Complexes in Various Epithelia. J Cell Biol 1963, 375–412.
6. Heinemann, U.; Schuetz, A. Structural Features of Tight-Junction Proteins. Int J Mol Sci 2019, 20.
7. Sugiyama, S.; Sasaki, T.; Tanaka, H.; Yan, H.; Ikegami, T.; Kanki, H.; Nishiyama, K.; Beck, G.; Gon, Y.; Okazaki, S.; et al. The Tight Junction Protein Occludin Modulates Blood–Brain Barrier Integrity and Neurological Function after Ischemic Stroke in Mice. Sci Rep 2023, 13, doi:10.1038/s41598-023-29894-1.
8. Pardridge, W.M. The Blood-Brain Barrier: Bottleneck in Brain Drug Development. The American Society for Experimental NeuroTherapeutics 2005, 2, 3–14.
9. Fischer, H.; Gottschlich, R.; Seelig, A. Blood-Brain Barrier Permeation: Molecular Parameters Governing Passive Diffusion. J. Membrane Biol. 1998, 165, 201–211.
10. Pardridge, W.M. Drug Transport across the Blood-Brain Barrier. Journal of Cerebral Blood Flow and Metabolism 2012, 32, 1959–1972.
11. Ghose, A.K.; Viswanadhan, V.N.; Wendoloski, J.J. A Knowledge-Based Approach in Designing Combinatorial or Medicinal Chemistry Libraries for Drug Discovery. 1. A Qualitative and Quantitative Characterization of Known Drug Databases. J Comb Chem 1999, 1, 55–68, doi:10.1021/cc9800071.
12. Hynynen, K.; McDannold, N.; Vykhodtseva, N.; Jolesz, F.A. Noninvasive MR Imaging-Guided Focal Opening of the Blood-Brain Barrier in Rabbits. Radiology 2001, 220, 640–646, doi:10.1148/radiol.2202001804.

13. Dauba, A.; Delalande, A.; Kamimura, H.A.S.; Conti, A.; Larrat, B.; Tsapis, N.; Novell, A. Recent Advances on Ultrasound Contrast Agents for Blood-Brain Barrier Opening with Focused Ultrasound. Pharmaceutics 2020, 12, 1125, doi:10.3390/pharmaceutics12111125.
14. Meng, Y.; Hynynen, K.; Lipsman, N. Applications of Focused Ultrasound in the Brain: From Thermoablation to Drug Delivery. Nat Rev Neurol 2021, 17, 7–22.
15. Meng, Y.; Goubran, M.; Rabin, J.S.; Mcsweeney, M.; Ottoy, J.; Pople, C.B.; Huang, Y.; Storace, A.; Ozzoude, M.; Bethune, A.; et al. Blood-Brain Barrier Opening of the Default Mode Network in Alzheimer's Disease with Magnetic Resonance-Guided Focused Ultrasound. Brain 2023, 146, 865–872, doi:10.1093/brain/awac459.
16. Wiedemair, W.; Tukovic, Z.; Jasak, H.; Poulikakos, D.; Kurtcuoglu, V. The Breakup of Intravascular Microbubbles and Its Impact on the Endothelium. Biomech Model Mechanobiol 2017, 16, 611–624, doi:10.1007/s10237-016-0840-z.
17. Khodabakhshi, Z.; Hosseinkhah, N.; Ghadiri, H. Pulsating Microbubble in a Micro-Vessel and Mechanical Effect on Vessel Wall: A Simulation Study. J Biomed Phys Eng 2021, 11, 629–640, doi:10.31661/jbpe.v0i0.1131.
18. Collis, J.; Manasseh, R.; Liovic, P.; Tho, P.; Ooi, A.; Petkovic-Duran, K.; Zhu, Y. Cavitation Microstreaming and Stress Fields Created by Microbubbles. Ultrasonics 2010, 50, 273–279, doi:10.1016/j.ultras.2009.10.002.
19. Pascal, A.; Li, N.; Lechtenberg, K.J.; Rosenberg, J.; Airan, R.D.; James, M.L.; Bouley, D.M.; Pauly, K.B. Histologic Evaluation of Activation of Acute Inflammatory Response in a Mouse Model Following Ultrasound-Mediated Blood-Brain Barrier Using Different Acoustic Pressures and Microbubble Doses. Nanotheranostics 2020, 4, 210–213, doi:10.7150/ntno.49898.
20. Mondou, P.; Mériaux, S.; Nageotte, F.; Vappou, J.; Novell, A.; Larrat, B. State of the Art on Microbubble Cavitation Monitoring and Feedback Control for Blood-Brain-Barrier Opening Using Focused Ultrasound. Phys Med Biol 2023, 68, doi:10.1088/1361-6560/ace23e.
21. Gasca-Salas, C.; Fernández-Rodríguez, B.; Pineda-Pardo, J.A.; Rodríguez-Rojas, R.; Obeso, I.; Hernández-Fernández, F.; del Álamo, M.; Mata, D.; Guida, P.; Ordás-Bandera, C.; et al. Blood-Brain Barrier Opening with Focused Ultrasound in Parkinson's Disease Dementia. Nat Commun 2021, 12, doi:10.1038/s41467-021-21022-9.
22. Gasca-Salas, C.; Pineda-Pardo, J.A.; Del Álamo, M.; Jiménez, T.; Trompeta, C.; Toltsis, G.; Garcia-Cañamaque, L.; Fernández-Rodríguez, B.; Matarazzo, M.; Plaza de las Heras, I.; et al. Nigrostriatal Blood-Brain Barrier Opening in Parkinson's Disease. J Neurol Neurosurg Psychiatry 2024, 95, 1089–1092, doi:10.1136/jnnp-2023-332967.

23. Tsai, C.H.; Zhang, J.W.; Liao, Y.Y.; Liu, H.L. Real-Time Monitoring of Focused Ultrasound Blood-Brain Barrier Opening via Subharmonic Acoustic Emission Detection: Implementation of Confocal Dual-Frequency Piezoelectric Transducers. Phys Med Biol 2016, 61, 2926–2946, doi:10.1088/0031-9155/61/7/2926.
24. Novell, A.; Kamimura, H.A.S.; Cafarelli, A.; Gerstenmayer, M.; Flament, J.; Valette, J.; Agou, P.; Conti, A.; Selingue, E.; Aron Badin, R.; et al. A New Safety Index Based on Intrapulse Monitoring of Ultra-Harmonic Cavitation during Ultrasound-Induced Blood-Brain Barrier Opening Procedures. Sci Rep 2020, 10, doi:10.1038/s41598-020-66994-8.
25. Wang, J.; Li, Z.; Pan, M.; Fiaz, M.; Hao, Y.; Yan, Y.; Sun, L.; Yan, F. Ultrasound-Mediated Blood–Brain Barrier Opening: An Effective Drug Delivery System for Theranostics of Brain Diseases. Adv Drug Deliv Rev 2022, 190, 114539, doi:10.1016/J.ADDR.2022.114539.
26. Gandhi, K.; Barzegar-Fallah, A.; Banstola, A.; Rizwan, S.B.; Reynolds, J.N.J. Ultrasound-Mediated Blood–Brain Barrier Disruption for Drug Delivery: A Systematic Review of Protocols, Efficacy, and Safety Outcomes from Preclinical and Clinical Studies. Pharmaceutics 2022, 14, doi:10.3390/pharmaceutics14040833.
27. Aryal, M.; Papademetriou, I.; Zhang, Y.Z.; Power, C.; McDannold, N.; Porter, T. MRI Monitoring and Quantification of Ultrasound-Mediated Delivery of Liposomes Dually Labeled with Gadolinium and Fluorophore through the Blood-Brain Barrier. Ultrasound Med Biol 2019, 45, 1733–1742, doi:10.1016/j.ultrasmedbio.2019.02.024.
28. Rigollet, S.; Rome, C.; Ador, T.; Dumont, E.; Pichon, C.; Delalande, A.; Barbier, E.L.; Stupar, V. FUS-Mediated BBB Opening Leads to Transient Perfusion Decrease and Inflammation without Acute or Chronic Brain Lesion. Theranostics 2024, 14, 4147–4160, doi:10.7150/thno.96721.
29. Magnin, R.; Rabusseau, F.; Salabartan, F.; Mériaux, S.; Aubry, J.F.; Le Bihan, D.; Dumont, E.; Larrat, B. Magnetic Resonance-Guided Motorized Transcranial Ultrasound System for Blood-Brain Barrier Permeabilization along Arbitrary Trajectories in Rodents. J Ther Ultrasound 2015, 3, doi:10.1186/s40349-015-0044-5.
30. Feng, W.; Zhang, C.; Yu, T.; Semyachkina-Glushkovskaya, O.; Zhu, D. In Vivo Monitoring Blood-Brain Barrier Permeability Using Spectral Imaging through Optical Clearing Skull Window. J Biophotonics 2019, 12, doi:10.1002/jbio.201800330.
31. Rich, M.; Whitsitt, Q.; Lubin, F.; Bolding, M. A Benchtop Approach to the Location Specific Blood Brain Barrier Opening Using Focused Ultrasound in a Rat Model. Journal of Visualized Experiments 2020, 2020, 1–13, doi:10.3791/61113.

32. Pansare, V.J.; Hejazi, S.; Faenza, W.J.; Prud'Homme, R.K. Review of Long-Wavelength Optical and NIR Imaging Materials: Contrast Agents, Fluorophores, and Multifunctional Nano Carriers. Chemistry of Materials 2012, 24, 812–827.
33. Reinhart, M.B.; Huntington, C.R.; Blair, L.J.; Heniford, B.T.; Augenstein, V.A. Indocyanine Green :Historical Context, Current Applications, and Future Considerations. Surg Innov 2016, 23, 166–175, doi:10.1177/1553350615604053.
34. Van Keulen, S.; Hom, M.; White, H.; Rosenthal, E.L.; Baik, F.M. The Evolution of Fluorescence-Guided Surgery. Mol Imaging Biol 2023, 25, 36–45.
35. Zhou, J.; Yang, F.; Jiang, G.; Wang, J. Applications of Indocyanine Green Based Near-Infrared Fluorescence Imaging in Thoracic Surgery. J Thorac Dis 2016, 8, S738–S743.
36. Liang, S.; Hu, D.; Li, G.; Gao, D.; Li, F.; Zheng, H.; Pan, M.; Sheng, Z. NIR-II Fluorescence Visualization of Ultrasound-Induced Blood–Brain Barrier Opening for Enhanced Photothermal Therapy against Glioblastoma Using Indocyanine Green Microbubbles. Sci Bull (Beijing) 2022, 67, 2316–2326, doi:10.1016/j.scib.2022.10.025.
37. Ku, G.; Wang, L. V Deeply Penetrating Photoacoustic Tomography in Biological Tissues Enhanced with an Optical Contrast Agent; 2005; Vol. 30;.
38. Le Floc'h, J.; Lu, H.D.; Lim, T.L.; Démoré, C.; Prud'homme, R.K.; Hynynen, K.; Foster, F.S. Transcranial Photoacoustic Detection of Blood-Brain Barrier Disruption Following Focused Ultrasound-Mediated Nanoparticle Delivery. Mol Imaging Biol 2020, 22, 324–334, doi:10.1007/s11307-019-01397-4.
39. Jo, J.; Yang, X. Functional Photoacoustic Imaging to Observe Regional Brain Activation Induced by Cocaine Hydrochloride. J Biomed Opt 2011, 16, 090506, doi:10.1117/1.3626576.
40. Sciortino, V.M.; Tran, A.; Sun, N.; Cao, R.; Sun, T.; Sun, Y.Y.; Yan, P.; Zhong, F.; Zhou, Y.; Kuan, C.Y.; et al. Longitudinal Cortex-Wide Monitoring of Cerebral Hemodynamics and Oxygen Metabolism in Awake Mice Using Multi-Parametric Photoacoustic Microscopy. Journal of Cerebral Blood Flow and Metabolism 2021, 41, 3187–3199, doi:10.1177/0271678X211034096.
41. Meombe Mbolle, A.; Yang, H.; Jiang, H. Photoacoustic Imaging for in Vivo Quantification of Alcohol-Induced Structural and Functional Changes in Cerebral Vasculature in High Alcohol-Preferring Mice (HAP). Alcohol 2022, 100, 23–30, doi:10.1016/j.alcohol.2022.01.001.
42. Tang, J.; Coleman, J.E.; Dai, X.; Jiang, H. Wearable 3-D Photoacoustic Tomography for Functional Brain Imaging in Behaving Rats. Sci Rep 2016, 6, doi:10.1038/srep25470.
43. Godefroy, G.; Arnal, B.; Bossy, E. Full-Visibility 3D Imaging of Oxygenation and Blood Flow by Simultaneous Multispectral Photoacoustic Fluctuation Imaging (MS-PAFI) and Ultrasound Doppler. Sci Rep 2023, 13, doi:10.1038/s41598-023-29177-9.

44. Yao, J.; Maslov, K.I.; Wang, L. V In Vivo Photoacoustic Tomography of Total Blood Flow and Potential Imaging of Cancer Angiogenesis and Hypermetabolism. National institutes of health 2012, 301–307.
45. Cao, R.; Li, J.; Kharel, Y.; Zhang, C.; Morris, E.; Santos, W.L.; Lynch, K.R.; Zuo, Z.; Hu, S. Photoacoustic Microscopy Reveals the Hemodynamic Basis of Sphingosine 1-Phosphate-Induced Neuroprotection against Ischemic Stroke. Theranostics 2018, 8, 6111–6120, doi:10.7150/thno.29435.
46. Da Mesquita, S.; Louveau, A.; Vaccari, A.; Smirnov, I.; Cornelison, R.C.; Kingsmore, K.M.; Contarino, C.; Onengut-Gumuscu, S.; Farber, E.; Raper, D.; et al. Functional Aspects of Meningeal Lymphatics in Ageing and Alzheimer's Disease. Nature 2018, 560, 185–191, doi:10.1038/s41586-018-0368-8.
47. Yang, F.Y.; Horng, S.C.; Lin, Y.S.; Kao, Y.H. Association between Contrast-Enhanced MR Images and Blood-Brain Barrier Disruption Following Transcranial Focused Ultrasound. Journal of Magnetic Resonance Imaging 2010, 32, 593–599, doi:10.1002/jmri.22297.
48. Chai, W.Y.; Chu, P.C.; Tsai, M.Y.; Lin, Y.C.; Wang, J.J.; Wei, K.C.; Wai, Y.Y.; Liu, H.L. Magnetic-Resonance Imaging for Kinetic Analysis of Permeability Changes during Focused Ultrasound-Induced Blood-Brain Barrier Opening and Brain Drug Delivery. Journal of Controlled Release 2014, 192, 1–9, doi:10.1016/j.jconrel.2014.06.023.
49. Drzał, A.; Delalande, A.; Dziurman, G.; Fournié, M.; Pichon, C.; Elas, M. Increasing Oxygen Tension in Tumor Tissue Using Ultrasound Sensitive O2 Microbubbles. Free Radic Biol Med 2022, 193, 567–578, doi:10.1016/j.freeradbiomed.2022.11.005.
50. Treeby, B.E.; Budisky, J.; Wise, E.S.; Jaros, J.; Cox, B.T. Rapid Calculation of Acoustic Fields from Arbitrary Continuous-Wave Sources. J Acoust Soc Am 2018, 143, 529–537, doi:10.1121/1.5021245.
51. Gerstenmayer, M.; Fellah, B.; Magnin, R.; Selingue, E.; Larrat, B.; Acoustic, B.L. Acoustic Transmission Factor through the Rat Skull as a Function of Body Mass, Frequency and Position. Ultrasound Med Biol 2018, 44, doi:10.1016/j.ultrasmedbio.2018.06.005ï.
52. Brossard, C.; Montigon, O.; Boux, F.; Delphin, A.; Christen, T.; Barbier, E.L.; Lemasson, B. MP3: Medical Software for Processing Multi-Parametric Images Pipelines. Front Neuroinform 2020, 14, doi:10.3389/fninf.2020.594799.
53. Swift, T.J.; Connick, R.E. NMR-Relaxation Mechanisms of O17 in Aqueous Solutions of Paramagnetic Cations and the Lifetime of Water Molecules in the First Coordination Sphere. J Chem Phys 1962, 37, 307–320, doi:10.1063/1.1701321.
54. Fries, P.; Runge, V.M.; Bücker, A.; Schürholz, H.; Reith, W.; Robert, P.; Jackson, C.; Lanz, T.; Schneider, G. Brain Tumor Enhancement in Magnetic Resonance Imaging at 3 Tesla

Intraindividual Comparison of Two High Relaxivity Macromolecular Contrast Media With a Standard Extracellular Gd-Chelate in a Rat Brain Tumor Model; 2009; Vol. 44;.

55. Marty, B.; Larrat, B.; Van Landeghem, M.; Robic, C.; Robert, P.; Port, M.; Le Bihan, D.; Pernot, M.; Tanter, M.; Lethimonnier, F.; et al. Dynamic Study of Blood-Brain Barrier Closure after Its Disruption Using Ultrasound: A Quantitative Analysis. Journal of Cerebral Blood Flow and Metabolism 2012, 32, 1948–1958, doi:10.1038/jcbfm.2012.100.
56. Li, Y.; Wen, T.; Zhao, R.; Liu, X.; Ji, T.; Wang, H.; Shi, X.; Shi, J.; Wei, J.; Zhao, Y.; et al. Localized Electric Field of Plasmonic Nanoplatform Enhanced Photodynamic Tumor Therapy. ACS Nano 2014, 8, 11529–11542, doi:10.1021/nn5047647.
57. McMahon, D.; Oakden, W.; Hynynen, K. Investigating the Effects of Dexamethasone on Blood-Brain Barrier Permeability and Inflammatory Response Following Focused Ultrasound and Microbubble Exposure. Theranostics 2020, 10, 1604–1618, doi:10.7150/thno.40908.
58. Singh, A.; Kusunose, J.; Phipps, M.A.; Wang, F.; Chen, L.M.; Caskey, C.F. Guiding and Monitoring Focused Ultrasound Mediated Blood–Brain Barrier Opening in Rats Using Power Doppler Imaging and Passive Acoustic Mapping. Sci Rep 2022, 12, doi:10.1038/s41598-022-18328-z.
59. Saunders, N.R.; Dziegielewska, K.M.; Møllgård, K.; Habgood, M.D. Markers for Blood-Brain Barrier Integrity: How Appropriate Is Evans Blue in the Twenty-First Century and What Are the Alternatives? Front Neurosci 2015, 9.
60. Malaowalla, A.M.; Pang, C.; E M Da, C.C. TOXICITY OF EVANS BLUE DYE IN THE MONKEY AND TRACING OF IT IN THE TOOTH PULP. 1962.
61. Taylort, S.H.; Thorp, J.M. PROPERTIES AND BIOLOGICAL BEHAVIOUR OF COOMASSIE BLUE*. 1958.
62. Moos, T.; Meillgird, K. Cerebrovascular Permeability to Azo Dyes and Plasma Proteins in Rodents of Different Ages; 1993; Vol. 19;.
63. Lee, S.; Lim, W.; Ryu, H.W.; Jo, D.; Min, J.J.; Kim, H.S.; Hyun, H. ZW800-1 for Assessment of Blood-Brain Barrier Disruption in a Photothrombotic Stroke Model. Int J Med Sci 2017, 14, 1430–1435, doi:10.7150/ijms.22294.
64. Hsu, Y.H.; Lee, W.C.; Chu, S.S.; Chao, M.E.; Wu, K.S.; Liu, R.S.; Wong, T.T. Influence of Acoustic Parameters and Sonication Schemes on Transcranial Blood–Brain Barrier Disruption Induced by Pulsed Weakly Focused Ultrasound. Pharmaceutics 2022, 14, doi:10.3390/pharmaceutics14061207.
65. Samiotaki, G.; Vlachos, F.; Tung, Y.S.; Konofagou, E.E. A Quantitative Pressure and Microbubble-Size Dependence Study of Focused Ultrasound-Induced Blood-Brain Barrier

Opening Reversibility in Vivo Using MRI. Magn Reson Med 2012, 67, 769–777, doi:10.1002/mrm.23063.

66. Park, J.; Zhang, Y.; Vykhodtseva, N.; Jolesz, F.A.; McDannold, N.J. The Kinetics of Blood Brain Barrier Permeability and Targeted Doxorubicin Delivery into Brain Induced by Focused Ultrasound. Journal of Controlled Release 2012, 162, 134–142, doi:10.1016/j.jconrel.2012.06.012.
67. Batts, A.J.; Ji, R.; Noel, R.L.; Kline-Schoder, A.R.; Bae, S.; Kwon, N.; Konofagou, E.E. Using a Novel Rapid Alternating Steering Angles Pulse Sequence to Evaluate the Impact of Theranostic Ultrasound-Mediated Ultra-Short Pulse Length on Blood-Brain Barrier Opening Volume and Closure, Cavitation Mapping, Drug Delivery Feasibility, and Safety. Theranostics 2023, 13, 1180–1197, doi:10.7150/thno.76199.
68. O'reilly, M.A.; Hough, O.; Hynynen, K. Blood-Brain Barrier Closure Time After Controlled Ultrasound-Induced Opening Is Independent of Opening Volume. Journal of Ultrasound in Medicine 2017, 36, 475–483, doi:10.7863/ULTRA.16.02005.
69. Samiotaki, G.; Konofagou, E.E. Dependence of the Reversibility of Focused-Ultrasound-Induced Blood-Brain Barrier Opening on Pressure and Pulse Length in Vivo. IEEE Trans Ultrason Ferroelectr Freq Control 2013, 60, 2257–2265, doi:10.1109/TUFFC.2013.6644731.
70. Lynch, M.; Heinen, S.; Markham-Coultes, K.; O'reilly, M.; Van Slyke, P.; Dumont, D.J.; Hynynen, K.; Aubert, I. Vasculotide Restores the Blood-Brain Barrier after Focused Ultrasound-Induced Permeability in a Mouse Model of Alzheimer's Disease. Int J Med Sci 2021, 18, 482–493, doi:10.7150/ijms.36775.
71. Fatima, A.; Kratkiewicz, K.; Manwar, R.; Zafar, M.; Zhang, R.; Huang, B.; Dadashzadeh, N.; Xia, J.; Avanaki, K. (Mohammad) Review of Cost Reduction Methods in Photoacoustic Computed Tomography. Photoacoustics 2019, 15.

Funding:

This research was funded by ANR FUSBRAIN (Grant ANR-21-CE18-0019), technological maturation project funded by C-Valo (PIA FNV Grant ANR-17-SATE-0003). Acquisition of VEVOLAZR equipment was funded by FEDER and CPER Region Centre Val de Loire. IRMaGe is partly funded by the French program "Investissement d'avenir" run by the Agence Nationale de la Recherche (grant ANR-11-INBS-0006). Part of the FUS equipment was sponsored by the Fédération pour la Recherche sur le Cerveau (FRC) and the Autun Rotary.

Acknowledgments:

The authors are grateful to Rudy Clémençon and Cyril Guimpied for their assistance in the animal care and housing at Orleans animal facility. The authors are also grateful to Nora Collomb for technical help for *in vivo* experiments at Grenoble animal facility.

Conflicts of Interest:

AD is co-founder of the company Harmonix. AD and CP are coinventors of the patent "lipid microbubbles for the targeted delivery of active agents" WO2023237842 (A1). SR is hired by Image Guided Therapy company. The other authors declare no conflict of interest.

Supplemental information:

Document S1: supplementary methods and Figures S1 to S5: supplementary figures.

Supplementary Method

1. Photoacoustic acquisition parameters

Experiments were performed with VEVOLAZR device (VisualSonics, Fujifilm, Canada), a photoacoustic imaging (PA) and ultrasound imaging system with the LZ400 probe.

- Operating frequency range: 13 to 24 MHz
- Broadband frequency range: 18 to 38 MHz
- Transmitted transducer frequency: 30 MHz
- 2D power: 100 %
- PA power: 100 %
- Wavelength range: 680-970 nm; Used 800 nm (ICG) and 684 nm (Evans Blue)
- PA gain: 39 to 44 dB
- 2D gain: 20 dB
- Image width: 15.36 mm, depth: 20 mm
- Axial resolution: 50 μm
- Sensitivity: high
- Persistence: OFF
- Correct energy: ON
- Display map: PA1
- PA brightness: 55
- PA contrast: 80
- Threshold: 20 %

3D scan parameters:

- 3D range: 8.03 mm
- Step size: 0.102 mm

2. Evans Blue imaging

Experiments have been done as described previously, the only difference being the timing of the Evans Blue injection and its concentration and the wavelengths of acquisition for both photoacoustic and fluorescence imaging. Briefly, 50 μL of a 2% solution of Evans Blue was injected (corresponding to about 30 mg/kg) directly after the catheter was placed (before MB injection and FUS treatment). Photoacoustic imaging was performed at 684 nm while fluorescence imaging was measured with λ_{em} = 625-655 nm and λ_{em} = 695-770 nm.

3. Acoustic field modelling

The modeling of the focal spot was realized with the k-wave toolbox on GraphPad (according to Treeby *et al*). Parameters used are the same as those used for BBB opening. With set-up 1: 1 MHz frequency, 45 mm probe diameter, and 35 mm radius. With set-up2: 1.5 MHz frequency, 25 mm probe diameter, and 20 mm radius.

References:

B. E. Treeby, J. Budisky, E. S. Wise, J. Jaros, and B. T. Cox, "Rapid calculation of acoustic fields from arbitrary continuous-wave sources," J. Acoust. Soc. Am., vol. 143, no. 1, pp. 529-537, 2018

Supplementary Results

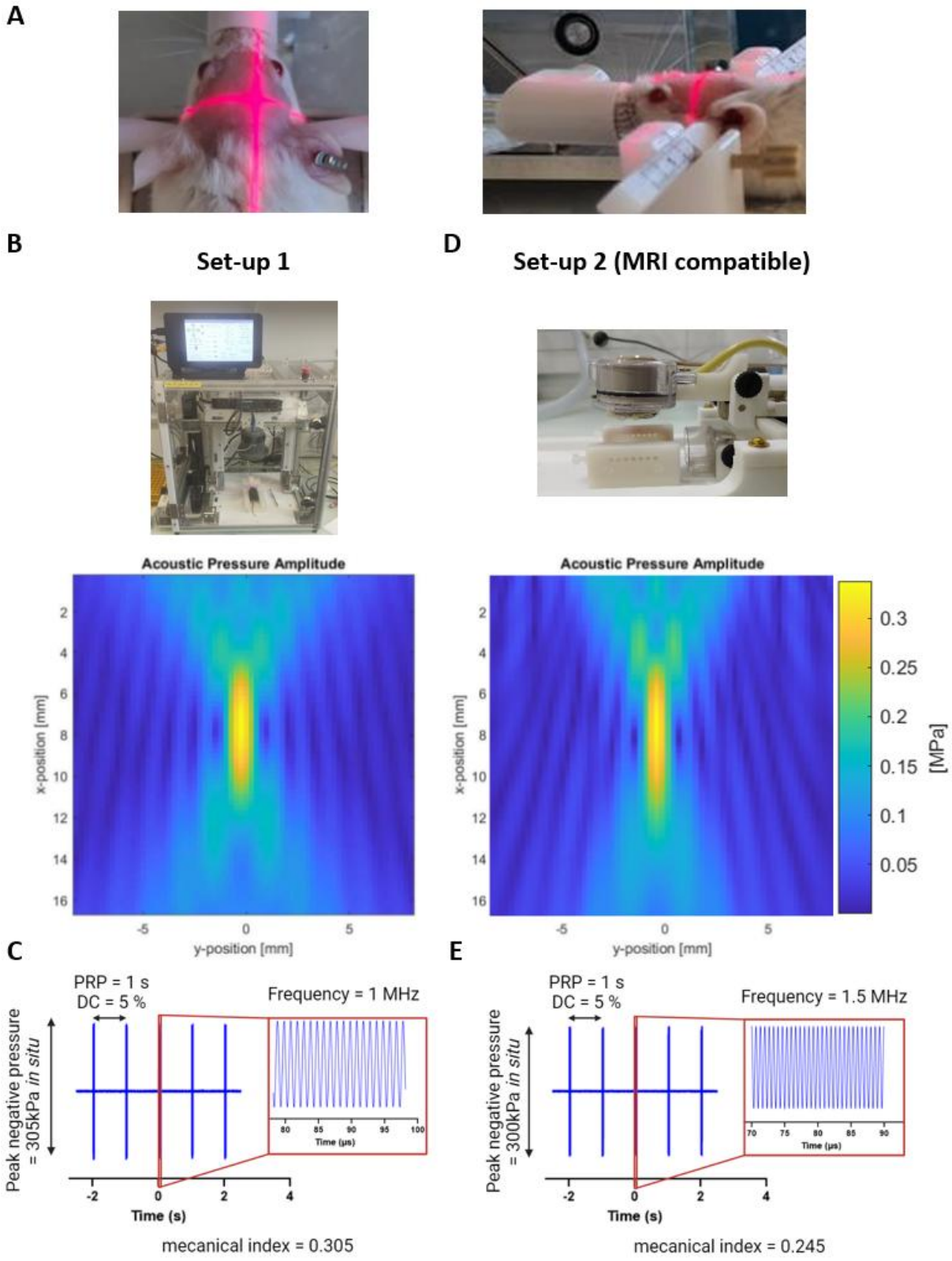

Figure S1. Focused ultrasound set-ups. (**A**) Focal spot guiding of the setup 1 (left: top view, right: side view). (**B**) Picture of set-up 1 and acoustic pressure modeling with k-Wave (1 MHz, 315 kPa PNP). (**C**)

Oscilloscope measure of the parameters used with the set-up 1, indicating pulse repetition frequency (PRP) and duty cycle (DC). (**D**) Picture of MRI compatible set-up 2 and acoustic pressure modeling with k-Wave (1.5 MHz, 380 kPa PNP). (**E**) Oscilloscope scheme of the parameters used with the MRI compatible set-up, indicating pulse repetition frequency (PRP) and duty cycle (DC).

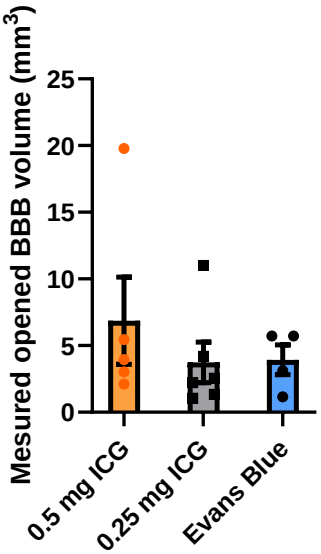

Figure S2. BBB opened volume detected *in vivo* with photoacoustic 30 minutes after FUS procedure and injection of 0.5 to 0.25 mg of ICG or 1 mg of Evans blue (n = 4 to 6). Data expressed as mean +/- SEM. #: p-value < 0.1; *: p-value < 0.05. Mann-Whitney bilateral test.

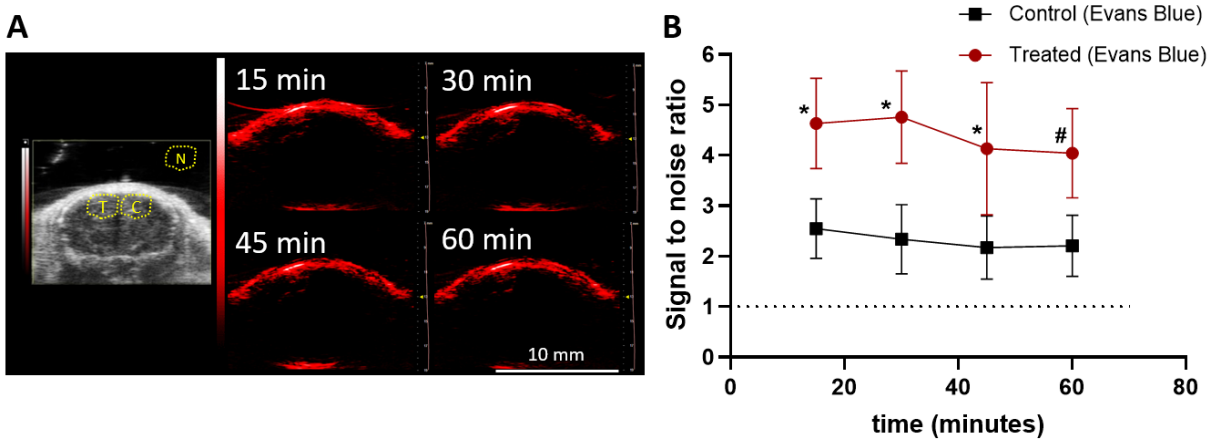

Figure S3. *In vivo* photoacoustic kinetics from 15 to 60 minutes after FUS treatment and a 50 µL injection of 2% Evans blue. (**A**) *In vivo* B-mode ultrasound imaging (grey) and representative photoacoustic images (red) at 684 nm in the ipsilateral BBB opened, treated region T compared to the contralateral control region C. (**B**) Graphical representation of the signal-to-noise ratio calculation made by dividing the signal in the T or C region by the noise N. (n = 4). Data expressed as mean +/- SEM. #: *p*-value < 0.1; *: *p*-value < 0.05; **: *p*-value < 0.01; Wilcoxon bilateral test region T *vs* region C.

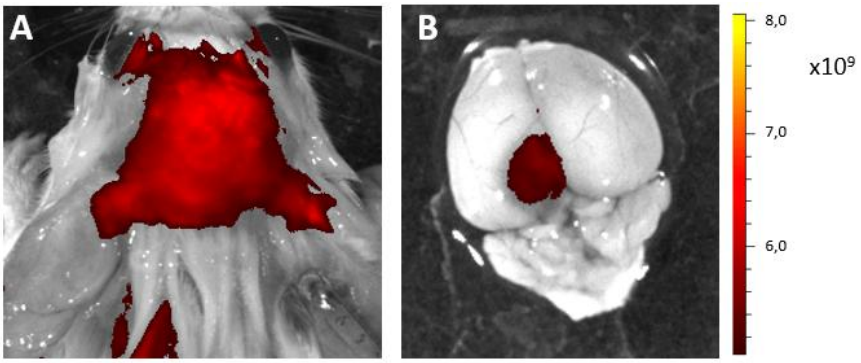

Figure S4. Fluorescence imaging of mice treated with FUS and MB after Evans Blue injection, λ_{em} = 625-655 nm and λ_{em} = 695-770 nm. (**A**) *in vivo* and (**B**) *ex vivo*. Images were taken 1 h after FUS treatment.

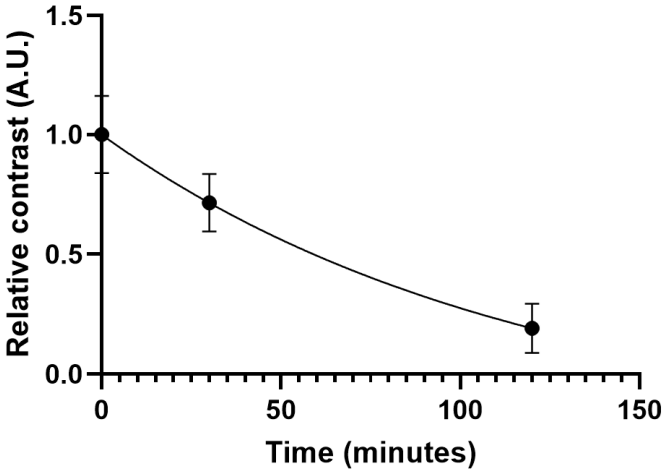

Figure S5. Kinetics of ICG extravasation decrease normalized with mean contrast signal at t_0, measured with *ex vivo* fluorescence measures as generated for Figure 7 (n = 6). Contrast agents were co-injected directly after the FUS procedure or with a delay of 30 to 120 minutes. *Ex vivo* fluorescence was performed on brains collected 24 h after FUS. Data are expressed as mean +/- SEM. One-phase decay exponential fit.

Partie 3 : Délivrance de gènes dans le cerveau assistée par ultrason et microbulles cationiques pour la thérapie du syndrome de l'X fragile

Résumé en français :

Introduction :

La thérapie génique est une technique prometteuse pour traiter de nombreuses maladies, en induisant l'expression d'un transgène ou en modulant l'expression d'un gène. Cependant, son utilisation dans le cerveau est difficile à cause de la barrière hémato-encéphalique (BHE) qui bloque le passage de plus de 98 % des molécules, y compris les vecteurs de thérapies géniques. L'utilisation de microbulles de gaz couplées à des ultrasons est une méthode efficace pour ouvrir la BHE. Cette ouverture permet la délivrance de molécules thérapeutiques telles que des acides nucléiques. Cela permet l'utilisation dans le cerveau d'une méthode non invasive de thérapie génique, ouvrant des possibilités thérapeutiques pour de nombreuses maladies du système nerveux central, telles que le syndrome de l'X fragile, qui manquent de traitements efficaces. Les microbulles utilisées pour cette application peuvent être fonctionnalisées, permettant d'améliorer la délivrance de gènes. L'utilisation de microbulles cationiques permet de fixer les acides nucléiques à leur surface, améliorant la délivrance ciblée du transgène.

L'objectif de cette partie est d'optimiser un protocole de délivrance non virale d'ADN plasmidique dans le cerveau utilisant des ultrasons focalisés couplés aux microbulles et de démontrer la preuve de concept de l'utilisation de ce protocole pour traiter le syndrome de l'X fragile.

Méthodes :

Pour cela, les microbulles cationiques de première génération précédemment présentées seront utilisées (Résultats partie 1). L'interaction de ces microbulles cationiques avec l'ADN plasmidique a été d'abord caractérisée en cytométrie en flux et en microscopie confocale. Puis, l'effet de cette interaction sur la stabilité et la cavitation sous ultrasons des microbulles a été étudié. Nous avons ensuite optimisé un protocole de transfert de gène utilisant un gène rapporteur codant pour la luciférase dans le cerveau de souris wild-type (WT) et de souris modèles du syndrome de l'X fragile (*Fmr1*-KO) en fonction de la pression acoustique utilisée et du temps de sonication. L'analyse de l'expression a été réalisée par imagerie de bioluminescence de l'expression de luciférase. Par la suite, l'efficacité de ce protocole pour

exprimer le transgène *Fmr1* dans les souris *Fmr1*-KO a été étudiée. Pour finir, un protocole de transfert de gènes dans le cerveau entier a été mis en place avec le déplacement de la sonde.

Cette étude est présentée sous la forme d'un article qui sera prochainement publié après révision des co-auteurs. Dans des expériences additionnelles à la suite de cet article, l'effet du protocole de transfert de gène sur des biomarqueurs de l'inflammation a été étudié par RT-qPCR. Des nanoparticules lipidiques ont ensuite été développées et ont été utilisées comme méthode alternative de transfert de gène non virale, en les associant avec nos microbulles non fonctionnalisées, biotinylé pour les lier aux nanoparticules, ou cationiques. Ces protocoles ont été utilisés avec la détection de cavitation passive.

Résultats :

Nous démontrons dans cette partie que la totalité de nos microbulles cationiques sont capables de complexer l'ADN plasmidique. Un ratio de complexation de 3 μg d'ADN pour 1 μL de microbulles pendant une minute a été optimisé, permettant d'éviter l'éclatement des microbulles. À ce ratio, nous montrons que l'ADN plasmidique réduit la stabilité des microbulles et délaye leur seuil de cavitation, mais garde des propriétés acoustiques satisfaisantes pour l'ouverture de la BHE. L'optimisation du protocole de délivrance dans le cerveau a révélé une corrélation entre l'ouverture de la BHE et le transfert de gène. Cela a révélé que la meilleure condition pour le transfert de gène s'opère à 410 kPa pour 5 minutes sur les souris WT et à 460 kPa pour une minute sur les *Fmr1*-KO, révélant la nécessité d'adapter le protocole en fonction du modèle utilisé. Malgré une forte expression, nos résultats montrent une cinétique d'expression relativement courte, durant sept jours. Ce protocole a également permis de restaurer l'expression de *Fmr1* dans le cerveau de souris *Fmr1*-KO, montrant le potentiel de cette stratégie. Nous avons montré que ce protocole induit des micro-saignements dans le cerveau et une inflammation transitoire, plus forte à des pressions plus élevées. L'utilisation de nanoparticules lipidiques a montré une efficacité de transfert de gène comparable aux microbulles cationiques, mais sans amélioration avec l'utilisation de microbulles fonctionnalisées. Cela a également révélé une forte corrélation entre la cavitation stable induite par les microbulles et le transfert de gène.

Pour conclure, nous avons développé dans cette partie un protocole de transfert de gène non viral dans le cerveau de souris, utilisant des microbulles cationiques complexant l'ADN ou des nanoparticules lipidiques associées à des microbulles. Ce protocole peut être utilisé pour restaurer l'expression de *Fmr1*, démontrant la preuve de principe de l'utilisation de cette méthode pour la thérapie génique du syndrome de l'X fragile.

Title:

Ultrasound and Cationic Microbubble-Assisted Gene Delivery in the Brain for Fragile X Syndrome Therapy

Authors:

Thomas Ador[1,2,3], Mylène Fournié[1], Julie Schlederer[1,2], Sebastien Rigollet[4,5], Vasile Stupar[4,6], Emmanuel Barbier[4,6], Chantal Pichon[1,2,7], Arnaud Menuet[3], Anthony Delalande[1,2,8]

Affiliation:

[1] ART mRNA INSERM US55, Orléans, France,

[2] LI²RSO, Université d'Orléans, France,

[3] Laboratory of Experimental and Molecular Immunology and Neuromodulation (INEM), UMR 7355 CNRS-University of Orleans, Orleans, France,

[4] Univ. Grenoble Alpes, Inserm, Grenoble Institut Neurosciences, U1216, Grenoble, France,

[5] Image Guided Therapy, Pessac, France,

[6] Univ. Grenoble Alpes, Inserm, CNRS, CHU Grenoble Alpes, IRMaGe, Grenoble, France, [7] Institut Universitaire de France, Paris, France, [8] Lead contact.

ABSTRACT

Fragile X syndrome (FXS) is the most common cause of hereditary intellectual disability (ID) and is caused by a mutation in the *Fmr*1 gene leading to the absence of its coded protein FMRP. Gene therapy is a promising method; however, its use in the brain is very challenging due to the inability of gene therapy vectors to cross the blood-brain barrier (BBB). In this study we produced and characterized novel cationic microbubbles (MB) capable of binding to DNA and oscillating under focused ultrasound. We showed that complexation with pDNA impacted MB cavitation, with delayed stable and inertial cavitation related to acoustic pressure. They were used to deliver a luciferase-coding plasmid in mice, and we demonstrated a correlation between BBB opening and gene expression. We optimized the transfection condition as a 410 kPa 5-minute sonication in Balb/c mice and a 460 kPa 1-minute sonication in *Fmr1*-KO mice after injection of 10^8 MB complexed with 30 μg of DNA. We demonstrated the ability of our protocol to restore *Fmr1* expression in *Fmr1*-KO mice as a proof of concept for FXS gene

therapy. Finally, we managed to use these cationic MBs with a whole-brain FUS protocol that successfully induced wide blood-brain barrier opening and gene expression.

Keywords: Ultrasound; Microbubble; Blood-brain barrier; Gene delivery; *Fmr1* gene

1. INTRODUCTION

Gene therapy shows growing interest for the treatment of monogenic disorders. Its ability to restore a specific gene expression proved to be particularly efficient with successful clinical trials and an FDA approval for onasemnogene abeparvovec (Zolgensma®) in 2019. This treatment for spinal muscular atrophy consists of a single intravenous injection of an AAV9 for children under 2 years old, reaching over 95 % survival after 12 months [1]. Despite its efficiency to transduce even motor neurons, this treatment is an exception as AAV are generally not capable to transduce efficiently the brain tissue. This is due to the blood-brain barrier (BBB) that blocks the passage of any large molecules and over 98% of molecules larger than 400 Da into the brain, including AAV or nucleic acid. This poses a significant challenge for CNS gene therapy [2–5]. The BBB is a specialized protective structure for the brain. Its impermeability arises from several properties such as active transporter or tight junction proteins expressed by endothelial cells [6–10]. Few techniques allow crossing of the BBB for gene therapy. The use of a specific serotype such as the AAV.PHP.B is an efficient method to transduce the CNS, but such serotypes are species-dependent and therefore impossible to use in clinical trials [11–14]. Intracerebral and intrathecal injection of AAV are widely used gene therapy methods in preclinical studies; however, these procedures are highly invasive and therefore challenging to implement in clinical trials. To address this limitation, the use of microbubble (MB) oscillation with focused ultrasound (FUS) for BBB opening (BBBo) shows increasing interest. This approach opens transiently the BBB in a non-invasive manner enabling the delivery of molecules or genes to the brain. This technique has been used for gene therapy and shows promising efficiency for the treatment of monogenic CNS disorders such as Alzheimer's disease or neurodevelopmental disorders such as Rett syndrome or fragile X syndrome.

Fragile X syndrome (FXS) is a monogenic X-linked pathology and the leading hereditary cause of intellectual deficiency and autism spectrum disorder [15]. It's caused by a repetition of a CGG codon in 5'UTR of the *Fmr1* gene, leading to its hypermethylation and the silencing of its expression [16–18]. This leads to the absence of the coded protein, FMRP, mostly expressed in the neuronal and glial cells of the CNS. FMRP has a paramount role in mRNA

regulation, from transport to translation, but also in the regulation of several protein functions [19,20]. Therefore, its absence results in a cascade of dysregulation leading to neuronal and glial impairments [21,22]. Clinical trials and commonly employed pharmacological strategies attempting to attend to these dysregulations mostly fail to induce significant improvement or manage to improve only partially FXS symptoms [23–27]. CNS gene therapy could be a promising treatment as shown by preclinical studies by restoring FMRP expression [11,28–30]. However, these previous studies are using viral vectors that have certain limitations in their applications.

In most cases, gene therapy using FUS-associated BBB opening (FUS-BBBo) would use standard lipidic microbubbles, generally commercially available, and co-inject a viral vector for cell transduction, allowing the expression of a transgene [31–33]. While effectively achieving high transduction and transgene expression, viral vector strategies are limited in clinical trials due to safety issues, as their injection, especially intravenous, can cause strong immune reactions. Another main limitation to viral vector gene therapy is the natural immunity to some serotypes within the population. Similarly, after one viral vector therapy, there is a risk that the patient may develop antibodies targeted to the serotype used, preventing additional treatment with the same viral vector. Viral strategies are also limited by their genome packaging capacity (about 4.7 kbp) limiting their application possibilities. In addition, AAV production is expensive, making gene therapy difficult to extend widely its use.

In order to improve gene delivery efficiency, custom MBs have been developed with functionalization improving gene delivery. Cationic MB (cMB) is a promising strategy as it is capable of complexing with nucleic acids, which can protect it from enzymes in the blood, and has been shown to enhance its ultrasound-targeted delivery to cells [34,35]. Fan *et al.* were the first to use cMB in the brain, composed of the cationic lipid DSTAP, for GDNF gene delivery in a Parkinson's mouse model. This technique allowed sufficient gene expression to restore mice behavior after a single treatment [36]. Studies using cationic microbubbles in the brain still show relatively low transgene expression and stability. Improving cMB formulation could be a way to improve these limitations. As with all MBs, stability and cavitation properties are paramount to optimize the BBBo, but in the case of cMB, their composition also needs to optimize complexation and delivery of the nucleic acid. The complexation strongly depends

on the cationic lipid used. Some cationic lipids showed strong gene transfer efficiency when used in liposomes, such as KLN25 (Figure S1.A), a lipophosphoramidate previously used in our team [37]. Ionizable lipids can also play an important role in transgene expression as they can provide intracellular endosomal escape. This is due to the hydrophilic group that gets protonated at low pH, a condition found in late endosomes leading to osmotic swelling and liposome membrane rupture. This proton-sponge effect leads to increased nucleic acid delivery and routing to the nucleus [38,39]. The ionizable lipid MM27 (Figure S1.B) used in our team previously, it showed its effectiveness for gene transfer using liposomes, suggesting that this is a suitable candidate to be used in cMB [37,40].

In this study we developed custom cationic MB using cationic and ionizable lipids based on lipophosphoramidates lipids (KLN25 and MM27) with modified fatty carbon chains allowing their use for MB formulations. We show their ability to open the BBB and efficiently deliver plasmid DNA to the mice brain, both in a targeted manner and to the whole brain, making it a potential strategy for FXS gene therapy.

2. MATERIAL AND METHODS

2.1 Animals

For the initial gene expression analysis, 57 adult female balb/c mice aged above 8 weeks (Charles River, France) were used. Then, to test the proof of concept of *Fmr1* brain gene delivery, 47 adult male *Fmr1*-KO mice under the C57BL/6JR strain [41] aged from 8 to 12 weeks (TAAM, France) and 6 adult male C57BL/6JRj mice aged from 8 to 12 weeks (Janvier Labs, France) were also used. All experiments were conducted in accordance with European ethical rules; the protocol was approved by the local ethical committees (protocols registered under numbers APAFIS#13749, APAFIS#41896, and APAFIS#43771). Mice were housed under 12/12 light conditions in a controlled atmosphere (22 °C) and fed *ad libitum*.

2.2 Chemicals

1,2-dimyristoyl-sn-glycero-3-phosphocholine (DMPC) and 1,2-dimyristoyl-sn-glycero-3-phosphoethanolamine-N-[methoxy(polyethylene glycol)-2000] (ammonium salt) (DMPE-PEG2000) were purchased from Avanti Polar Lipids (Alabaster, Alabama, USA). The cationic lipid KLN27 and the ionizable lipid MM30 were synthesized by WuxiAppTec (China). Perfluorobutane was obtained from F2 Chemicals (Preston, United Kingdom). Indocyanine Green was obtained from TCI (Portland, USA). Gadolinium contrast agent Gd-DOTA (DOTAREM®) was obtained from Guerbet (Villepinte, France).

All chemicals, unless otherwise stated, were supplied by Sigma Merck.

2.3 Microbubble formulation and characterization

Custom cationic MB were prepared by mixing DMPC, DMPE-PEG2000, KLN27 and MM30 in ethanol at a final concentration of 5.6 mM and at a molar ratio of 44.76 : 2.9 : 43.67 : 8.67 respectively. This was followed by the formation of liposomes and freeze-drying in 1.5 mL vials. Vials were sealed, and the headspace was filled with perfluorobutane. MBs were activated after solubilization of the liposomes in 500 µL of HEPES buffer (10 mM, pH = 7.4) by mechanical agitation at 4500 rpm for 45 s using a Vialmix (BMS, Princeton, New Jersey, USA). Activated MB were appropriately diluted and deposited on a 0.2 mm Thoma slide before being characterized with optical microscopy for size and concentration under an inverted microscope (Leitz, objective ×25). 8 images minimum were done in order to analyze at least 1000 events using the particle analysis plugin of ImageJ software. MB concentrations were determined 5 minutes, 6 hours, or 24 hours after activation but they were used in the first hours after activation for all other experiments.

2.4 Characterization of MB cationic properties

For all *in vitro* characterization of cMB we used the luciferase-coding plasmid. MB cationic properties were first assessed with a gel shift assay. A 0.6% agarose gel was prepared with 1/10 000th SYBR Safe (Invitrogen) and was allowed to cool down and polymerize. 1 µg of

luciferase-coding plasmid DNA (pDNA) was complexed with an increasing amount of MB solution (from 0.5 to 5 μL) for 2 minutes before the addition of the loading dye and deposition in the gel. Migration was performed with a 120 mV electric current for 20 minutes. Images were recorded under a UV light using a gel imaging system. Zeta potential was calculated with Malvern Zetasizer Ultra Red using either the liposomes before the freeze-drying step, diluted 100-fold in 10 mM NaCl, or using activated MB, diluted 50-fold in 10 mM NaCl. Confocal microscopy was performed using Confocal LSM980 AiryScan2 (Carl ZEISS SAS) with 1 μL of MB complexed with 1 μg of Cy5-labeled pDNA for 1 minute before being deposited on the slide. Luciferase coding pDNA was labeled using the Label IT® Nucleic Acid Labeling Kit Cy5 (Mirus, Madison, USA) following their protocol. The same DNA were used for flow cytometry where 2.5 μL of cMB were diluted in 250 μL of HEPES buffer (10mM, pH = 7.4) and were complexed with increasing Cy5-labeled pDNA, from 0.5 to 7.5 μg. cMB and Cy5-labeled pDNA were allowed to complex directly in the cytometer tube and fluorescence of cMB were assessed after 1, 2, 5, and 10 minutes of complexation. SSC was performed with the violet laser (λ = 450 nm) to improve sensibility with small objects, and fluorescence intensity was assessed with the red laser (λ = 633 nm) with a filter band-pass of 660/10 nm. Cytometer gating was calibrated using non-cationic MB, with the ratio 1 μL of MB for 1 μg of pDNA.

In order to assess the effect of pDNA loading on cMB stability and acoustic properties, 1×10^8 MB with or without 1-minute complexation of 30 μg of pDNA were first dispersed in 50 mL of PBS with 7.5% of BSA to mimic blood homeostasis and total protein concentration. The solution was deposited in a beaker with acoustic absorbents at the bottom, and echogenic properties over time were determined using an ultrasound imaging system (VEVOLAZR, VisualSonics, Fujifilm, Canada), with the MS250 probe (22 MHz, VisualSonics, Fujifilm, Canada) immersed in the solution. Echographic contrast power was measured for 10 minutes at a 1 Hz framerate under 150 rpm magnetic steering. Then, cavitation was assessed using a 1 MHz focused bowl transducer with a 45 mm diameter active element (DL-47 piezo material, radius of curvature 45 mm, Precision Acoustics, UK) pierced in the middle to insert a passive cavitation detector. It has an ellipsoid-shaped focal spot of 6×1.5 mm and was controlled with a custom 3-axis motorized stage (IndustryLab, Orléans, France) with a laser beam used to guide the focal spot to the targeted region. The transducer was connected to a linear amplifier

(E&I, 210L) connected to a waveform generator (Agilent 33210A) to deliver the ultrasound treatment. All systems were calibrated using a hydrophone (Onda HGL200, USA) in a separate tank in degassed water. A 1.5 % agarose phantom was prepared with a linear canal formed by an 18G needle (OD: 1.27 mm), removed once the gel was fully polymerized. Ultrasound coupling between the gel and the transducer was done with water. A 1×10^8 MB/mL solution with or without 30 μg/mL pDNA complexation (for 1 minute before measurement) was pushed into the canal at 0.5 mL/min using a syringe pump (Harvard material…) and 1 MHz pulsed ultrasound (1 Hz PRF, 5 % DC) was applied. Reflected non-linear signal from MB cavitation was detected by a 10 MHz PCD placed at the center of the bowl transducer. Signal was amplified by a 20 dB preamplifier (Precision Acoustics) and recorded by a picoscope 5244 MSO and the picoscope 7 software (Pico Technology, UK). Stable and inertial cavitation doses (SCD and ICD) were then calculated using Matlab software.

2.5 FUS-BBBo gene transfer procedure

Mice were first anesthetized with 2% isoflurane in air, and a catheter (26G) was then inserted in the tail vein. The skull was shaved using depilatory cream. Mice were placed on a contention system composed of ear bars and an isoflurane anesthesia mask (Minerve, France). A transducer was placed in a probe holder with degassed water within a silicone membrane (0.2 mm) for optimal ultrasound conduction. It was then placed on top of the mouse skull with gel for ultrasound coupling. The transducer used is a 1 MHz focused bowl transducer with a 45 mm diameter active element (DL-47 piezo material, radius of curvature 45 mm, Precision Acoustics, UK) with an ellipsoid-shaped focal spot of 6×1.5 mm. The transducer was controlled with a custom 3-axis motorized stage (IndustryLab, Orléans, France) with a laser beam used to guide the focal spot to the targeted region. The transducer was connected to a linear amplifier (E&I, 210L or 2100, USA) connected to a waveform generator (Agilent 33210A or Rigol DG1032Z) to deliver the ultrasound treatment. All systems were calibrated using a hydrophone (Onda HGL200, USA) in a separate tank in degassed water. 30 μg of pDNA diluted in 100 μL of 5% sucrose HEPES (10 mM, pH = 7.4) were complexed with 1×10^8 MBs also diluted in 100 μL of 5% sucrose HEPES for 1 minute before being injected as a bolus in the mice through the catheter. 10 seconds later, pulsed FUS treatment was applied for 1 to 5

minutes at 310 to 460 kPa, with a pulse repetition frequency of 1 Hz and a duty cycle of 5 %. After the FUS treatment, 50 µL of freshly prepared Indocyanine Green (ICG) solution (2.5 mg/mL in 5% sucrose) was injected through the catheter to analyze BBB opening. Mice were awakened in a dedicated cage and were scored once fully vigilant regarding its weight, aspect, or mobility. We used in-house plasmids coding for either luciferase or FRM1-eGFP, derived from p-EGFP-C1-Flag-mFmr1 (Addgene plasmid #87929), under a CMV promoter and modified with a 3NF enhancer sequence.

For whole-brain experiments, BBB was permeabilized with an MR-guided FUS device described in a previous study [42] (Image Guided Therapy, Pessac, France). Briefly, a 7-concentric-element transducer (Imasonic, Voray-sur-l'Ognon, France) is embedded on a 2-axis motorized system enabling planar displacement, all controlled by the Thermoguide® software (Image Guided Therapy, Pessac, France). Injection of MB complexed with luciferase-coding pDNA was performed as described above. The probe followed a pathway at 10 mm/s, allowing a treatment of the entire brain. It delivered continuous FUS treatment at 1 MHz, 500 kPa PNP during 348 seconds in raster scan (corresponding to 30 scans of the brain).

2.6 In vivo imaging

In order to monitor BBB opening, fluorescence imaging of extravasated ICG was performed on anesthetized mice with 2% isoflurane using the IVIS Lumina LT Series III (Perkin Elmer, Massachusetts, USA). The parameters used were λ_{ex} = 730-760 nm and λ_{em} = 810-875 nm, with an exposure time of 0.5 to 2 s, a binning of 2 to 4, and an f/stop of 2 to 4. Fluorescence imaging *in vivo* was performed on animals 24 hours after the FUS procedure as previously optimized. Fluorescence measurements are expressed as the total fluorescence intensity in a circular region of interest (ROI) of 5.76 mm^2.

Gene expression was determined *in vivo* whenever the luciferase pDNA was used with its bioluminescence. For this, 200 µL of luciferin solution (30 mg/mL) in PBS was injected intraperitoneally. Mice were then anesthetized with 2% isoflurane in air and then were placed in the IVIS Lumina LT Series III (Perkin Elmer, Massachusetts, USA). Images were acquired 10 minutes after luciferin injection. The parameters used were an emission filter open, an

excitation filter blocked, an exposure time of 60 to 300 seconds, and a binning of 8. Fluorescence imaging was performed at the same time as bioluminescence imaging. Bioluminescence imaging *in vivo* was performed on animals 24 hours to 7 days after the FUS procedure. Bioluminescence measurements are expressed as the total radiance in a circular ROI of 5.76 mm^2, consistent with the ROI used for fluorescence imaging.

2.7 RT-qPCR

24 hours after the procedure, brains were harvested and sliced using a brain slicer to isolate the region with BBBo (2 to 3 mm thick). Brain parts were then frozen immediately in liquid nitrogen and stored at −80 °C. Frozen brain parts were crushed using a Precellys Evolution Touch at 5500 rpm, 4 °C for 15 seconds. Sample RNA extractions were performed using an RNA II NucleoSpin® mini kit (Machery-Nagel EURL, Hoerdt, France) which includes a DNAse treatment. RNA quantification was performed using a NanoDrop spectrophotometer (Thermo Fischer). The RNA integrity was checked using a BioAnalyzer 2100 (Agilent Technologies UK Limited, Wokingham, Berkshire, UK) and was acceptable when the RNA integrity number exceeded 7. For all experiments, 500 ng to 1 μg of RNA was used for reverse transcription using 200 units of M-MuLV Reverse Transcriptase (New England Biolabs) for 1 h at 37 °C. The *Fmr1* gene expression was evaluated from 100 ng of cDNA by qPCR using a Light Cycler II 480 (Roche Applied Science, Meylan, France) with 0.1 μM of *Fmr1*-specific primers (forward: 5′-AGAAAAGTGTCCCACAAGAA-3′, reverse: 5′-AAGTGCATGTCAATCAACAT-3′) and compared to GAPDH housekeeping gene expression.

2.8 Immunological staining

Twenty-four hours after FUS, mice were anesthetized by an intraperitoneal injection of 500 μL of ketamine-xylazine. This was followed by surgery for an intracardiac injection of 25 mL of ice-cold PBS using a peristaltic pump at 2.5 mL/min followed by 25 mL injection of ice-cold 4% PFA solution at 2.5 mL/min. The brains were extracted, and a post-fixation was done in 4% PFA at 4 °C for 48 h, followed by 7 days in 30% sucrose. Brains were then embedded in

tissue-freezing medium and frozen with isopentane on dry ice. Brain slices of 14 μm thickness were done using a cryotome (Cryostar NX50, Epredia) and stored at -20 °C until hematoxylin and eosin (H&E) staining. For H&E staining, slides were incubated for 1 minute in absolute ethanol, followed by 1 minute in hematoxylin solution. Slides were rinsed with water for 15 seconds, then chloride for 15 seconds, followed by 1 minute in eosin. Slides were then dehydrated rapidly through a series of ethanol baths of increasing concentration, from 70 to 100%, and finally in 3 baths of xylene. Finally, slides were covered with a protective film, images were performed with a slide scanner (DP200, Roche).

2.9 MRI

MRI was performed at 4.7T (BioSpec 47/40, Avance III, Bruker, Ettlingen, Germany) at the IRMaGe facility (Grenoble, France). The scanner was equipped with a volume transmit coil and a single-element surface receive coil. The MRI protocol performed after the FUS treatment was as described before: T2-weighted TurboRARE sequence (TR/TE = 2200/36 ms; 13 axial slices; FOV = 20×20 mm^2; matrix 256×256; voxel size, 78×78×1000 μm3, RARE-factor, 8; Tacq = 3 min 31s), T1 map RARE VTR sequence (TR, 3000 to 18 ms; TE =6.6 ms; FOV = 20×20 mm^2; matrix 128×128; voxel size, 156×156×1000 μm3, RARE-factor, 4; 2 slices, Tacq = 12 min 39s) performed before and after the intravascular injection of a gadolinium chelate (Gd-DOTA; DOTAREM®, Guerbet, Villepinte, France), T1-weighted RARE sequence (TR/TE = 800/7 ms; 13 slices; FOV = 20×20 mm^2; matrix 256×256; voxel size, 78×78×1000 μm3, RARE-factor, 4; axial and coronal orientations; Tacq = 1 min 16 s) to evaluate the BBB opening. Then, MRI data were processed and analyzed using MP3 software [43]. Gadolinium contrast agent Gd-DOTA was obtained from Guerbet (Villepinte, France).

2.10 Statistics

Nonparametric Mann-Whitney bilateral tests were performed using the R language (version 4.4.0, used with R Studio software). Non-linear fit and F-test were performed using GraphPad Prism v10. A *p*-value below 0.05 was considered significant.

3. RESULTS

3.1 Development of cationic MB

First, optical microscopy characterization of cMB showed that we reached a concentration of 9.9×10^9 +/- 5.0×10^8 MB/mL in the vials, with a median size of 1.19 +/- 0.02 µm. The size distribution of cMB in figure 1 shows a polydisperse but relatively narrow size distribution. We then confirmed with the Zetasizer the cationic properties of these MB, with a 19.1 +/- 0.5 mV zeta potential.

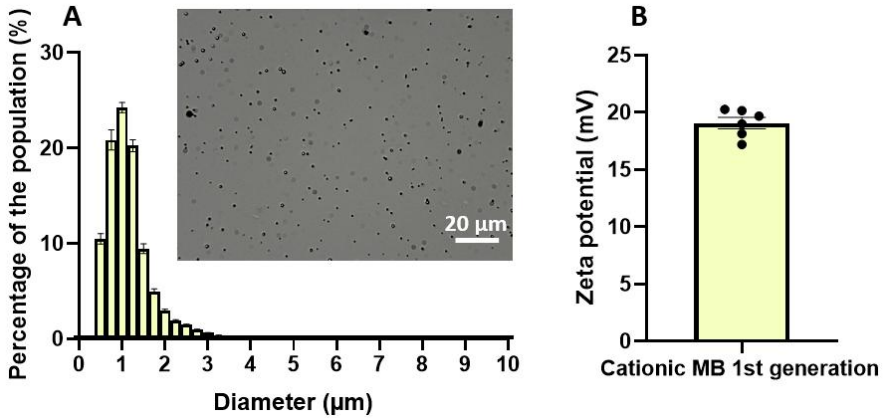

Figure 1: Cationic MB characterization. (**A**) Size distribution of the custom cationic microbubbles (mean with SEM, n = 53), with an optical image used for size and concentration determination, optical microscope, magnification ×25. (**B**) Zeta potential of cationic MB. Data expressed as mean +/- SEM.

Then the cationic properties of cMB and their ability to complex pDNA were assessed *in vitro*. Gel shift assay with increasing cMB amount showed increasing pDNA retained in the wells and lowering pDNA shifting in the gel, confirming its complexation. It also indicated that 2 µL of cMB were needed to complex 1 µg of pDNA, a ratio at which no shifted DNA remained (Figure 2.A). Increasing further the amount of MB reduced the amount of pDNA retained in the well due to the buoyancy of cMB, extracting the complexed pDNA from the well. This result was confirmed with flow cytometry of cMB complexed for 1 minute with Cy5-labeled pDNA, where the amount of fluorescent cMB increased significantly with DNA, ranging from 69.9 +/- 3.0 % to 97.6 +/- 0.6 % of fluorescent cMB using from 0.2 to 0.5 µg of Cy5-labeled pDNA, respectively, for 1 µL of cMB, where it reached its maximum (Figure 2.B). As

expected, this amount of nucleic acid corresponds to the ratio at which total complexation of pDNA was obtained in the gel shift assay. No significant difference in fluorescent cMB was observed by increasing pDNA amount further. In addition, flow cytometry following 10-minute complexation with Cy5-labeled pDNA did not show any significant difference from results obtained after a 1-minute complexation. Confocal microscopy also confirmed that pDNA complexed on the MB surface, where most MB were positively complexed with Cy5-labeled pDNA (Figure 2.D). It also showed several fluorescent events too small to be observed with the brightfield image, probably due to NB and liposomes complexing with Cy5-labeled pDNA. These data demonstrate that all cMB formed were able to complex with nucleic acid on their surface and that 1 minute of complexation was enough to load pDNA on the cMB surface.

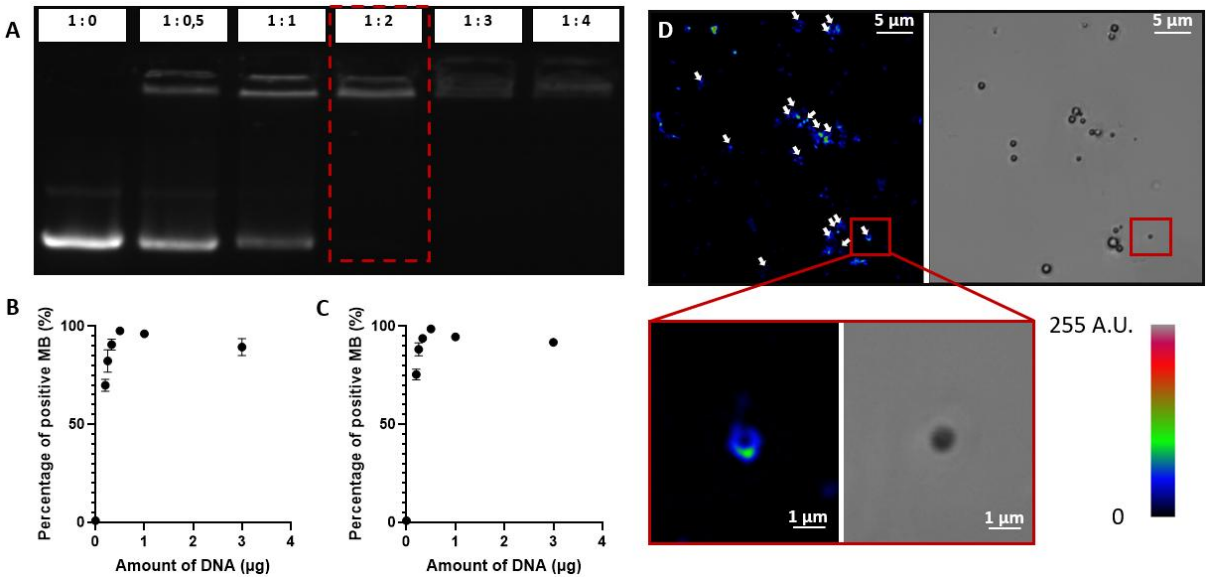

Figure 2: MB cationic properties. (**A**) Gel shift assay of 1 µg of pDNA complexed with an increasing amount of MB solution, represented as a ratio of pDNA (µg) : MB (µL). (**B**) Flow cytometry of 1 µL of cationic MB complexed for 1 minute with increasing Cy5-labeled pDNA (**C**) Flow cytometry of 1 µL of cationic MB complexed for 10 minutes with increasing Cy5-labeled pDNA (**D**) Confocal microscopy of cationic MB complexed with Cy5-labeled pDNA at a ratio of 1 µg for 1×10^7 MB with zoomed images below. White arrows indicate Cy5-labeled cMB. **Left**: fluorescence image; **right**: brightfield. Data expressed as mean +/- SEM.

3.2 pDNA loading lead to flocculation and cMB loss

Characterization of cMB complexation also demonstrated that cMB flocculates when complexed with pDNA, characterized by MB aggregation leading to their collapse. In optical microscopy, MB loss due to flocculation reaches a maximum of 70.1 +/- 0.4 % with 0.5 µg of pDNA for 1 µL of MB after over 10 minutes of complexation. This MB loss can be mitigated by either lowering or increasing pDNA amount. We observed in flow cytometry an over-complexed cMB population that evolved with the same dynamic as MB loss from flocculation (Figure 3). This population was therefore associated with the apparition of flocculated events. We assessed its evolution after one minute of complexation, time sufficient for cMB loading. It demonstrated a maximum of flocculation with 0.5 µg of pDNA for 1 µL of cMB reaching 62.2 +/- 9.1 %, and a significant decrease with higher or lower pDNA amounts, getting as low as 3.2 +/- 1.8 % and 2.5 +/- 1.3 % with 0.2 and 3 µg of pDNA, respectively (Figure 2.C). Such flocculation was important to address since it can produce MB aggregates larger than 10 µm that can be harmful for mice in intravenous injection and can lead to MB collapse. For further experiments, the use of 3 µg of pDNA for 1 µL of cMB was favored to avoid excessive MB injection in mice.

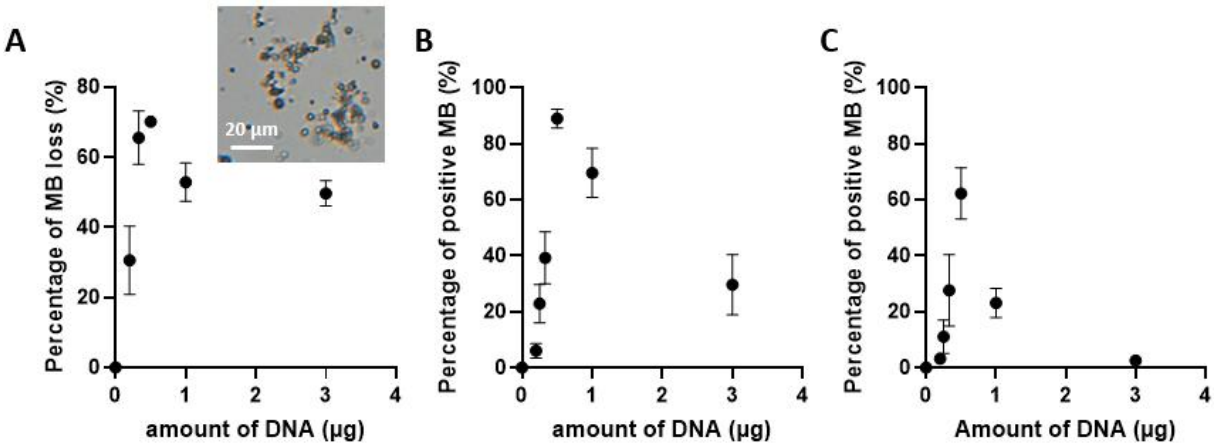

Figure 3: MB flocculation. (**A**) Percentage of loss of MB from flocculation assessed in optical microscopy after over 10 minutes of complexation with pDNA, using an increasing amount of pDNA, with an image of a typical MB flocculation. (**B**) Flow cytometry of cMB complexed with an increasing amount of pDNA (µg) using 1 µL of cMB for 10 minutes. Events were considered positive with a fluorescence superior to the first population of fluorescent events, as detailed in figure S2. (**C**) Flow cytometry of cMB complexed

with an increasing amount of pDNA (μg) using 1 μL of cMB for 1 minute. Events were considered positive with a fluorescence superior to the first population of fluorescent events, as detailed in figure S2. Data expressed as mean +/- SEM.

3.3 Loading of pDNA on cMB surface changes their acoustic properties

Plasmid DNA loading on MB surfaces can lead to the destabilization of the MB and the modification of their acoustic properties. We first assessed its effects with ultrasound contrast imaging *in vitro*, in a PBS buffer with blood-like BSA concentration to mimic *in vivo* homeostasis. Contrast enhancement was successfully detected with or without pDNA, with a calculated half-life longer than the usual FUS pulse, of 166.7 or 206.9 seconds with or without pDNA complexed. However, it showed significantly lower contrast enhancement over time with pDNA complexation.

Then cavitation of cMB showed a clear pressure-related increase of stable and inertial cavitation dose both with and without pDNA. SCD was successfully detected from 100 kPa, which shows a significant 0.95- to 0.91-fold lower SCD from 100 to 300 kPa with pDNA. Bare cMB shows a significant 1.19-fold SCD increase from 100 to 300 kPa, where a plateau is reached, followed by a significant 0.94-fold decrease from 450 to 600 kPa. Complexed cMB on the other hand, shows a significant 1.29-fold SCD increase from 100 to 600 kPa and reaches an SCD significantly higher than bare cMB at 600 kPa. This result indicates a delayed SCD with pDNA loading compared to bare cMB. Which is sustained by the fact that no significant difference in SCD is found between bare cMB and pDNA-loaded cMB at their respective maximums of 450 and 600 kPa. Similar observations can be made with ICD and precursor ICD, where precursor ICD is detected starting from 200 and 400 kPa for bare and loaded cMB, and ICD from 150 and 300 kPa respectively. Both ICD and precursor ICD with bare cMB display a significant increase, reaching their maximum at 450 kPa. Like with SCD, they also show a significant decrease from 450 to 600 kPa. Loaded cMB also showed significant ICD and precursor ICD increases up to 600 kPa. Significantly lower precursor ICD from 200 to 400 kPa was observed compared to bare cMB, and significantly lower ICD was detected from 200 to 300 kPa. Like SCD, we observe a significantly higher ICD and precursor ICD at 600 kPa with

pDNA loading, though there is no significant difference between ICD and precursor ICD using their respective maximums.

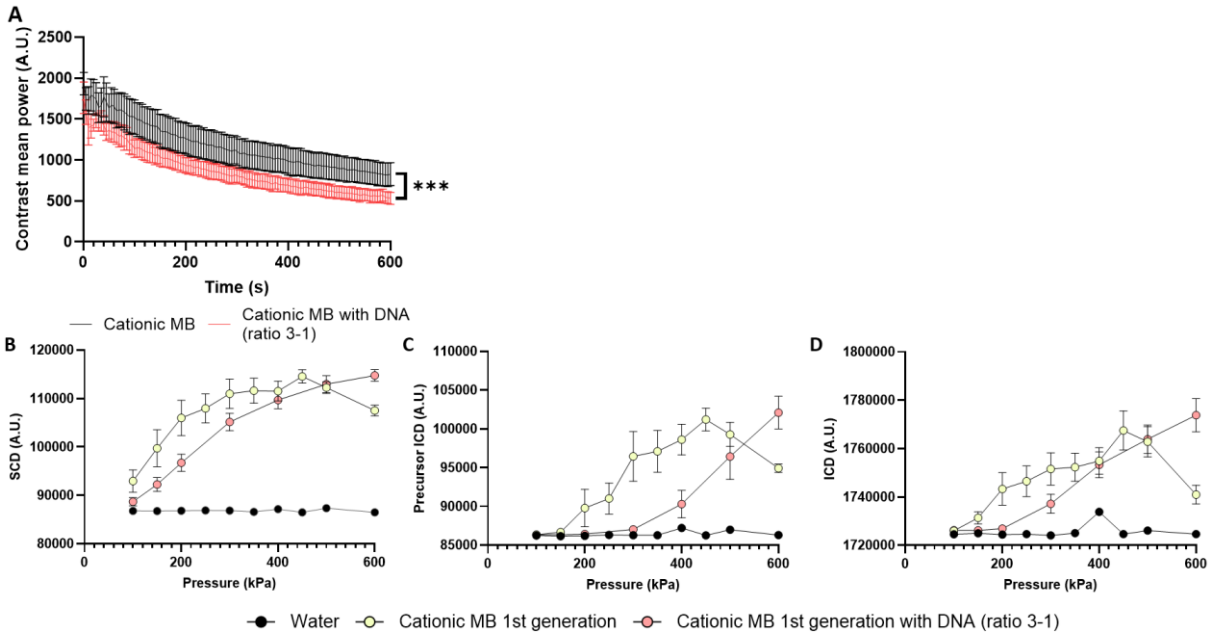

Figure 4: Cavitation analysis from the first generation of cationic microbubbles with or without pDNA. (**A**) MB ultrasound imaging contrast power over time in PBS with 7.5 % BSA of 1×10^8 MB with or without 30 µg of pDNA, non-linear regression, and F-test performed with GraphPad Prism v10. (**B**) Stable cavitation dose (**C**) Precursor inertial cavitation dose, and (**D**) inertial cavitation dose, calculated with the 50 µs pulse signal and as a function of pressure. Data expressed as mean +/- SEM. * = *p*-value < 0.05; ** = *p*-value < 0.01; *** = *p*-value < 0.001; F-test.

3.4 FUS-BBBo with Cationic MB allows targeted gene transfer to the brain

Used for BBBo and luciferase brain gene delivery, we first show that bioluminescence was detected *in vivo* by using an acoustic pressure superior to 310 kPa for 1 minute, with a radiance of 1.06×10^3 p/s at 310 kPa, identical to background level, and 6.5×10^4 p/s at 360 kPa. This bioluminescence was not significantly increased at 410 kPa, reaching 7.8×10^4 p/s, but was significantly increased at 460 kPa, compared to both 360 and 410 kPa, reaching 1.6×10^5 p/s. Increasing the sonication time from 1 to 5 minutes at 410 kPa also increased bioluminescence,

reaching 1.4×10^5 p/s. Although this increase was not significant, it reached a bioluminescence significantly higher than with 360 kPa for 1 minute and not significantly different from 460 kPa for 1 minute (Figure 5.A). This 5-minute sonication at 460 kPa induces a bioluminescence with a fast decline, with a significant decrease of bioluminescence at 3 days after the procedure, reaching 1.1×10^4 p/s. This decline continued with another significant decrease of bioluminescence at 7 days after treatment compared to 3 days, reaching 2.3×10^3 p/s on average, close to background value (Figure 5.B). The fluorescence of ICG assessed at 24 h shows a correlation with the bioluminescence 24 h after treatment (non-linear regression, $R^2 = 0.52$) with 1-minute sonication at 360, 410, and 460 kPa, with no significant difference between the curves, showing that they follow the same regression fit (Figure 5.C).

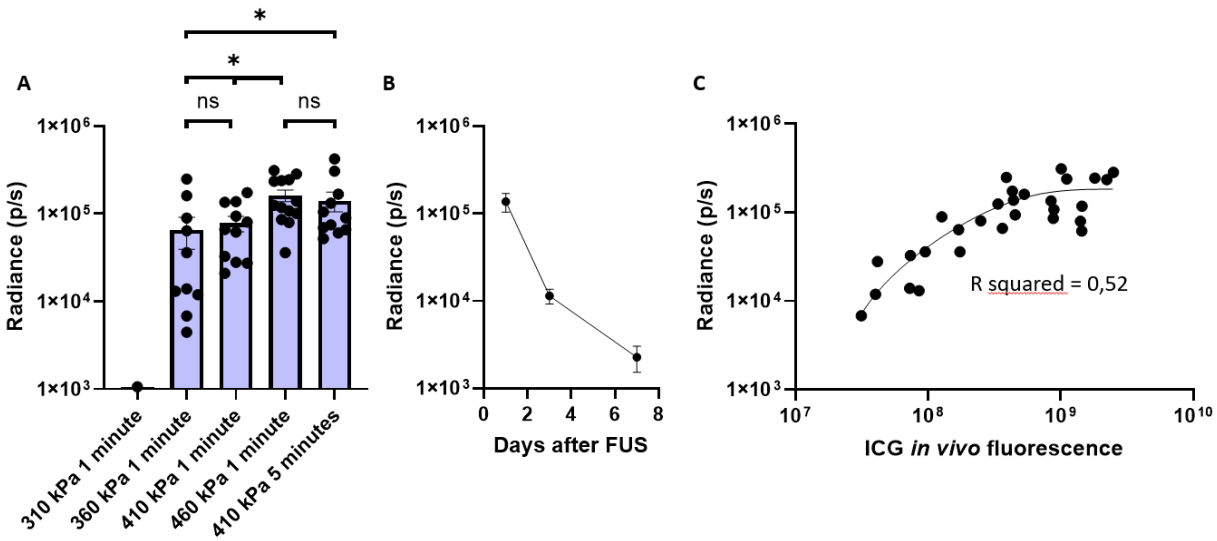

Figure 5: Brain gene transfer in balb/c mice assessed with luciferase bioluminescence. (**A**) *In vivo* bioluminescence intensity 24 h after FUS depending on acoustic pressure with a 1-minute sonication and effect of a 5-minute sonication at 410 kPa. (**B**) Bioluminescence *in vivo* as a function of time after a 5-minute sonication at 410 kPa. (**C**) Non-linear regression of *in vivo* bioluminescence as a function of *in vivo* ICG fluorescence intensity 24 h after FUS with a 1-minute sonication at different acoustic pressures (n = 29). Data expressed as mean +/- SEM. * = *p*-value < 0.05; Mann-Whitney bilateral test.

3.5 *In vivo* gene transfer procedure restores *Fmr1* expression in *Fmr1*-KO mice

The FUS-BBBo gene transfer protocol showed a significantly lower bioluminescence in *Fmr1*-KO mice compared to Balb/c mice using either a 5-minute sonication at 410 kPa or a 1-minute sonication at 460 kPa, reaching 1.7×10^4 +/- 5.5×10^3 p/s and 7.4×10^4 +/- 1.6×10^4 p/s, respectively. In *Fmr1*-KO mice, unlike with Balb/c, a significantly higher bioluminescence was induced by the 1-minute sonication at 460 kPa. Increasing the sonication time to 5 minutes at 460 kPa induced a small and non-significant increase of bioluminescence to 9.0×10^4 +/- 1.7×10^4 p/s. The sonications at 460 kPa for 1 or 5 minutes were considered the best conditions in *Fmr1*-KO mice as they are not significantly different from the 5-minute sonication at 410 kPa in balb/c mice. These sonications were used for *Fmr1* gene delivery with the *Fmr1*-coding pDNA; it induced a significant expression detected in RT-qPCR. Similarly to bioluminescence, the *Fmr1* expression induced by the 1- or 5-minute sonication at 460 kPa was not significantly different, reaching 2.9 % or 3.7 % compared to WT expression. Residual expression of *Fmr1* mRNA was detected in *Fmr1*-KO mice, of 0.4 % compared to WT expression on average. The procedure safety was assessed in *Fmr1*-KO mice with the lower 1-minute FUS length in H&E staining. In all 4 mice observed with H&E staining, microhemorrhages on the FUS path were detected. These microhemorrhages can be observed on the entirety of the brain's depth, with no visible effect of tissue thickness on the FUS effect.

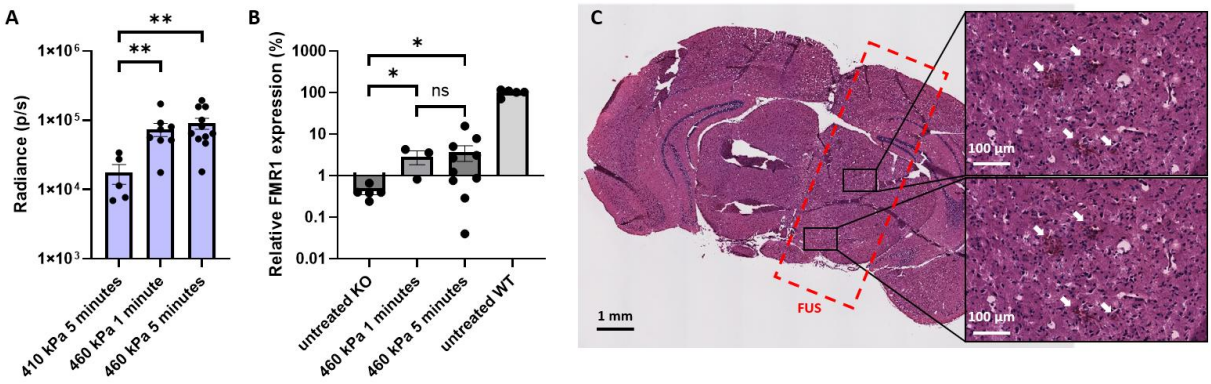

Figure 6: Brain gene transfer in *Fmr1*-KO mice. (**A**) *In vivo* bioluminescence intensity 24h after FUS with different acoustic pressure or sonication time. (**B**) *Ex vivo Fmr1* expression quantified in RT-qPCR 24 h after FUS using an *Fmr1*-eGFP pDNA, normalized with average WT expression. (**C**) H&E staining of *Fmr1*-KO mice treated with cMB and *Fmr1*-coding pDNA, with a 460 kPa 1-minute FUS; white arrows indicate microhemorrhages. Data expressed as mean +/- SEM. * = *p*-value < 0.05; ** = *p*-value < 0.01; Mann-Whitney bilateral test.

3.6 Cationic MB can be used for *in vivo* whole brain gene delivery

Finally, we used our gene transfer FUS-BBBo protocol in C57/BL6JRj WT mice with an MRI-compatible FUS probe mounted on a motor for the treatment of the whole brain. We show efficient BBB opening in all mice with 60.6 +/- 4.9 % of the brain opened on average with a 1.18 +/- 0.03 T1 contrast enhancement ratio after injection of Gd-DOTA, assessed in MRI. MRI T2 images following the procedure showed no sign of edema or microhemorrhages in all mice. Bioluminescence one day after the procedure shows 1.6×10^4 +/- 7.9×10^3 p/s/cm²/sr average radiance in the whole brain, with a homogeneous signal on the head suggesting gene expression in the whole brain. It also shows significantly lower expression with the whole brain protocol than the targeted 1-minute sonication at 460 kPa in *Fmr1*-KO mice.

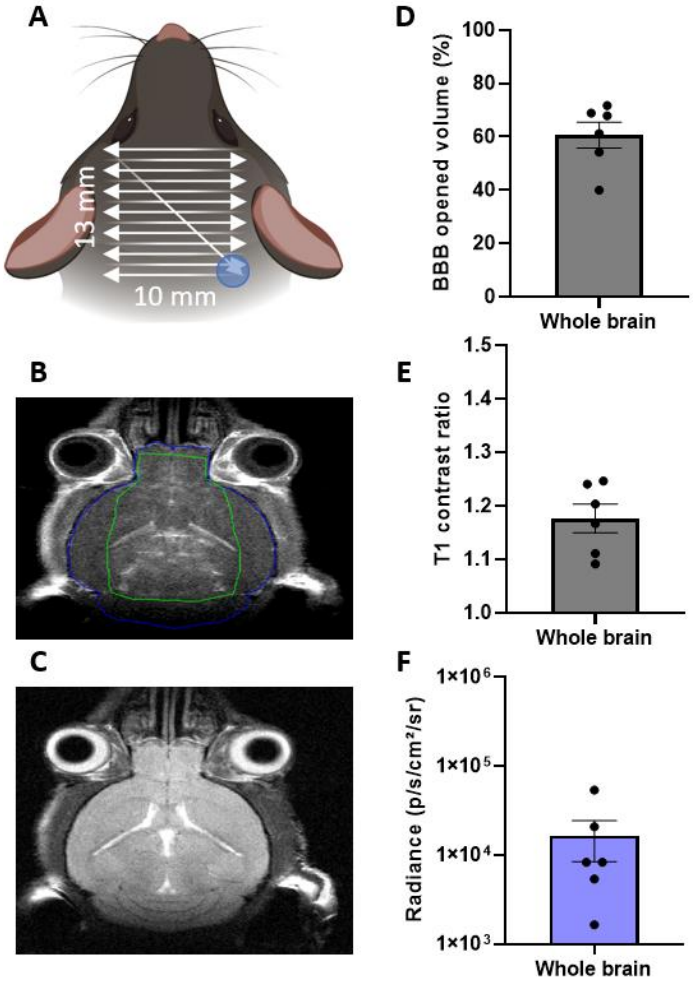

Figure 7: Whole-brain FUS-BBBo gene delivery in C57BL/6 WT mice. (**A**) Schematic representation of the FUS probe pathway; the blue circle indicates the starting point. (**B**) T1 enhanced contrast image after FUS and gadolinium injection, **green ROI**: BBB opened region, **blue ROI**: total brain region (**C**) T2 pondered images of mice brain after FUS. (**D**) Graphical representation of BBB opened volume calculated with MRI T1 enhanced contrast images. (**E**) Graphical representation of T1 contrast ratio calculated with MRI T1 enhanced contrast images. (**F**) Average bioluminescence *in vivo* 24h after FUS in the whole brain. Data expressed as mean +/- SEM.

4. DISCUSSION

Our study details the successful development of MB with cationic properties using custom cationic and ionizable lipids. These cMB show a size and concentration similar to our previously published homemade MB, though slightly lower [42]. The rapid decay of these cMB, with a 50% loss of MB within 6 hours, required their immediate use after activation (Figure S2). Cationic properties of cMB were confirmed by both gel shift assay, fluorescence microscopy, and flow cytometry with Cy5-labeled pDNA. Although the gel shift assay did not allow us to specify which object complexed with DNA, fluorescence microscopy indicates that pDNA was complexed on both cMB and a smaller object, smaller than the limitation size of optical microscopy (> 400 nm). These objects could be either remaining liposomes or nanobubbles that can be formed during the mechanical activation.

Our flow cytometry method, limited by its 500 nm detection threshold, could only assess MB and larger NB. This analysis revealed no significant differences in cMB labeling (amount or intensity) across different sized populations, suggesting uniform cationic lipid distribution and pDNA complexation, regardless of size. This method also showed that close to 100 % of cMB were labeled using over 0.5 μg of pDNA for 1 μL of cMB, further confirming that all MB formed contain cationic lipid. In addition, it demonstrated that a 1-minute complexation was sufficient, as no significant difference was observed between 1- and 10-minute complexation with all pDNA amount used. However, we showed that flocculation occurred when cMB was complexed to pDNA. Almost total flocculation occurs at the ratio with 1 μg of pDNA and 2 μL of cMB, as assessed in optical microscopy, showing that almost no MB remains formed and

outside of flocculation clusters. This makes the use of cMB impossible at such a ratio, as the loss of cMB will prevail BBBo, and the MB in clusters should not be injected, as they can reach a size too high for safe intravenous injection (> 10 μm), inducing the risk of blood clots [44]. Flocculation can be reduced by increasing or decreasing the amount of cMB per μg of pDNA, making it potentially usable. With optical microscopy it was difficult to assess flocculation over time, and it was only assessed after over 10 minutes of complexation and showed at least 30 % of MB loss. However, flow cytometry showed a population with excessive pDNA complexation that shows, after 10 minutes of complexation, similar evolution with pDNA amount than MB loss in optical microscopy. This allowed us to assess MB flocculation over time and showed that we can reach negligible flocculation with a 1-minute complexation, using either 0.2 or 3 μg for 1 μL of pDNA. As BBBo is directly influenced by MB dose, it must be reduced as much as possible to avoid severe BBBo and damages from occurring [45]. In addition, we need a sufficient pDNA amount to induce clinically relevant gene expression, which was set to 30 μg in this study. Therefore, we prioritized the use of a lower MB amount for *in vivo* experiments, where flocculation is negligible, of 1 μL of cMB for 3 μg of pDNA. As the pDNA complexed on cMB is the most biologically efficient, we normalized the amount of cMB injected in mice to 1×10^8 cMB, corresponding to around 10 μL of cMB solution, complexed with 30 μg of pDNA.

We then assessed the effect of pDNA complexation on cMB acoustic properties with this cMB: pDNA ratio to ensure their ability to open the BBBo through MB cavitation. Ultrasound imaging in PBS 7.5 % BSA was used to mimic blood osmolarity and protein concentration. It indicated that cMB remains formed and echogenic even with pDNA. Their stability was significantly lower, with a slightly reduced half-time, but that remained sufficiently long for the classical FUS procedure. However, we show the use of long FUS duration; their efficiency will most likely be lower at the end of the FUS procedure due to MB loss. The cavitation properties of complexed cMB, on the other hand, show interesting features for BBBo. Indeed, we demonstrated a delayed stable and inertial cavitation compared to bare MB, with no collapse of MB detected with the pressure studied. This suggests a higher stability during cavitation of complexed cMB compared to bare cMB probably due to a stiffer shell from pDNA [46,47]. Cavitation analyses highlight that the only acoustic pressure where only stable cavitation occurs with no inertial cavitation is at 200 kPa, a pressure much lower than any

pressure used in BBBo studies [36,45,48,49]. This suggests that at least some inertial cavitation will be required for BBBo and gene delivery. Although MB cavitation is influenced by its concentration, which was higher in our *in vitro* experiments than it will be in brain capillaries *in vivo*, preventing us from drawing direct conclusions between these measures and BBBo experiments [50]. However, 300 kPa appears as another interesting pressure, where mostly stable cavitation was detected, with no precursor ICD and few ICD. Starting from 400 kPa, inertial cavitation is clearly detected, though still significantly lower than with bare cMB considering the precursor ICD. In addition, at this pressure, no significant difference is found in SCD compared to bare cMB. It shows that this can be an interesting pressure to use *in vivo* to assess the efficiency of gene delivery and BBBo from stable cavitation associated with limited inertial cavitation. As previously stated, MB cavitation *in vivo* will probably be lower due to a lower MB concentration and skull FUS reflection; therefore, increasing the acoustic pressure higher could be needed to induce sufficient MB cavitation.

In vivo, we first used these cationic MBs with a previously used pulsed sonication of 1 minute, with a PRF of 1 Hz, 5% DC, and 310 kPa (about 300 kPa *in situ* according to Gerstenmayer *et al.* [51]), which matches a pressure where few inertial cavitation was detected, as previously stated. We were unable to detect *in vivo* the BBB opening with ICG fluorescence or bioluminescence from luciferase expression while this pulse allowed detectable BBB opening in our previous study with neutral MB. Increasing the acoustic pressure to 360 kPa allowed BBB opening detectable *in vivo* in all mice, associated with bioluminescence of luciferase strong enough to be also detected *in vivo*. In itself, this indicates that we already reached potentially stronger gene expression than the study from Fan *et al.* that needed to assess bioluminescence of luciferase *ex vivo*, as gene expression was not strong enough [36]. Increasing further the acoustic pressure increased bioluminescence, with a maximum reached at 460 kPa, where the scoring of mice started to show signs of damage in some mice, with mild impaired mobility associated with weight loss (< 20 %) one day post-treatment. This observation confirmed the previous statement, reinforcing the idea that inertial cavitation occurs at this pressure. Due to this effect, acoustic pressure was not increased further. We then assessed the effect of sonication time with 410 kPa, the strongest acoustic pressure where scoring did not show impaired mobility, and few inertial cavitations were measured. Increasing this sonication time to 5 minutes also increased the bioluminescence, although not

significantly compared to 1 minute at the same pressure. However, it reached a bioluminescence with no significant difference from the 1-minute sonication at 460 kPa. Mice scoring also showed signs of damage with this 5-minute sonication, but with fewer occurrences than with the 1-minute sonication at 460 kPa (36 % *versus* 46 % respectively). The damage observed one day post-treatment resolved within seven days in all scored mice, indicating rapid resorption.

As the 5-minute sonication at 410 kPa showed one of the highest bioluminescence with less damage it was used to study the kinetics of luciferase expression with the bioluminescence over time, although all sonication shows similar kinetics (data not shown). We observed peak gene expression one day post-treatment, followed by a rapid decline, unlike Fan *et al.*, who showed maximum bioluminescence at 54 h after treatment [36]. Bioluminescence *in vivo* reached values close to background at 7 days after treatment but was undetectable in some mice. Our protocol supports gene expression for at least 7 days post-treatment, albeit with a rapid decline. While the absence of an *in vivo* signal does not necessarily indicate the absence of gene expression, it may reflect levels below the detection limit.

BBBo was assessed *in vivo* with ICG fluorescence at 24 h after treatment. As already demonstrated with viral vectors, we show for the first time with a non-viral strategy that *in* vivo gene expression following non-viral gene delivery is correlated with BBBo [33]. This was demonstrated by the correlation between extravasated ICG fluorescence and bioluminescence from transgene expression, both assessed at 24h. Although the fit was relatively poor (R^2 = 0.52) with several unstable parameters calculated by GraphPad Prism software. In addition, all 1-minute sonications significantly follow the same fit, confirming this correlation. The 5-minute sonication also significantly follows the same distribution as the rest of the conditions (p-value = 0.95), but the resulting fit has a lower quality (R^2 = 0.37). This suggests that increasing sonication time increased gene delivery mostly by increasing BBBo.

The sonication of 5 minutes at 410 kPa was estimated as the best option to induce strong gene transfer with lower damage and was used in *Fmr1*-KO mice. We must note that bioluminescence was significantly lower in *Fmr1*-KO mice compared to Balb/c (Figure S5). The second-best condition (1 minute at 460 kPa) yielded significantly lower bioluminescence than in Balb/c mice but significantly higher bioluminescence than the 5-minute sonication at 410

kPa. This suggests that acoustic pressure in male *Fmr1*-KO mice needs to be increased compared to the female Balb/c mice. This difference likely relates to ultrasound transmission, which is affected by skull and tissue thickness which can vary across mouse strains. We still decided to avoid increasing the acoustic pressure further as scoring of mice as described above started to show signs of damage in some mice (22 %). To enhance gene transfer, we increased the sonication time to 5 minutes at 460 kPa, which showed a slight and non-significant increase of bioluminescence. As it did not increase the occurrence of signs of damage from the mice's scoring (10%), both conditions were used to restore *Fmr1* expression in mice. qPCR analysis demonstrated partial *Fmr1* restoration in the brain of treated mice, validating our gene therapy. However, expression remained significantly lower than wild-type levels. Both sonications showed similar effects. This confirmed the result assessed in bioluminescence that increasing the sonication time at this pressure and had few effects on gene delivery. This may be due to the rapid MB decline observed in ultrasound imaging, preventing full utilization of longer sonication times. The assessment of the procedure's safety with H&E staining demonstrated the presence of microhemorrhages using the 1-minute 460 kPa FUS treatment. This further indicates that inertial cavitation at this pressure is too frequent, leading to transient brain damage. We will therefore need to use lower acoustic pressures that still demonstrated strong gene expression *in vivo* and increase gene expression another way. Compared to other studies using cMB in the brain like Fan *et al.*, they induced sufficient gene expression for efficient protein restoration and behavioral effect, despite a low gene expression assessed in bioluminescence as previously stated [36]. Further experiments must be performed to increase *Fmr1* transgene expression for an efficient therapy.

For future gene therapy treatment of FXS, wide gene expression through the CNS will be required to ensure the best therapeutic effect. As a proof of concept, we used our cMB with an adapted FUS protocol associated with the probe displacement, as shown by Felix *et al.*, that allows BBBo in the whole brain. We confirmed using MRI the ability of our whole-brain FUS protocol to open the BBB in 60 % of the brain while remaining safe. We also demonstrated for the first time using a non-viral strategy wide gene expression in the brain, as assessed with bioluminescence imaging. Although gene expression was found to be lower than when using a focused FUS protocol at similar pressure. This is due to the long sonication time needed for this procedure, as with probe displacement and this focal spot of 1 mm in diameter, 348

seconds are needed to treat the whole brain with the equivalent FUS time of a focused 1-minute sonication. This duration is 2-fold longer than the half-time of MB stability previously assessed *in vitro*, indicating that a much larger part of cMB is lost over the FUS procedure compared to the focused procedure.

Overall, our study demonstrated the development of novel cationic MB partially composed of ionizable lipids and their ability to complex pDNA, cavitate under FUS, opening the BBB and delivering pDNA, allowing restoration of *Fmr1* gene expression. This is the first proof-of-concept to use of FUS-mediated non-viral gene delivery for FXS gene therapy. Recently, using mice-specific AAV.PHP.B in adult *Fmr1*-KO mice, Chadman *et al.* showed a whole-brain restoration of *Fmr1* gene expression leads to a therapeutic effect on several behavioral phenotypes [11]. This effect was obtained with a restoration of *Fmr1* expression close to WT, suggesting the need to improve gene expression with our protocol. However, unlike with AAV.PHP.B strategy, the use of FUS-mediated non-viral gene delivery can be easily translated to clinical trials, as several clinical trials already demonstrated the safety of FUS and BBBo in the brain [52–54]. Several strategies should be considered to further enhance gene delivery. One such strategy involves extending the sonication time at low acoustic pressure to improve BBB opening and subsequent gene delivery while simultaneously enhancing the safety of the procedure by mitigating the risk of inertial cavitation. Even though this would be limited by the cMB stability, a perfusion of cMB could be used to avoid this limitation. The same perfusion can also be used during the whole-brain FUS protocol, probably increasing BBBo and gene delivery. Another strategy with delocalization of the cationic charge from the MB surface could be attempted, as it can induce lower destabilization. This can be achieved by incorporating a cationic polymer into the MB shell or by complexing pDNA in liposomes or polymers that can be later attached to the MB surface [55–58].

In conclusion, our study successfully developed novel cationic microbubbles (cMB) incorporating custom cationic and ionizable lipids, demonstrating their ability to complex pDNA, cavitate under focused ultrasound (FUS), and facilitate blood-brain barrier (BBB) opening for non-viral gene delivery. While cMB characterization revealed promising acoustic properties, *in vivo* experiments highlighted the challenges of achieving robust gene expression, particularly in *Fmr1*-KO mice. Despite these challenges, the study provides the first proof-of-

concept for FUS-mediated non-viral gene delivery for FXS gene therapy. Future work should focus on strategies to enhance gene delivery and expression stability to achieve clinically relevant levels of gene expression for effective FXS treatment.

5. Bibliography

1. Fernandes, B.D.; Krug, B.C.; Rodrigues, F.D.A.; Cirilo, H.N.C.; Borges, S.S.; Schwartz, I.V.D.; Probst, L.F.; Zimmermann, I. Efficacy and Safety of Onasemnogene Abeparvovec for the Treatment of Patients with Spinal Muscular Atrophy Type 1: A Systematic Review with Meta-Analysis. PLoS One 2024, 19, doi:10.1371/journal.pone.0302860.
2. Pardridge, W.M. Drug Transport across the Blood-Brain Barrier. Journal of Cerebral Blood Flow and Metabolism 2012, 32, 1959–1972.
3. Pardridge, W.M. The Blood-Brain Barrier: Bottleneck in Brain Drug Development. The American Society for Experimental NeuroTherapeutics 2005, 2, 3–14.
4. Fischer, H.; Gottschlich, R.; Seelig, A. Blood-Brain Barrier Permeation: Molecular Parameters Governing Passive Diffusion. J. Membrane Biol. 1998, 165, 201–211.
5. Ghose, A.K.; Viswanadhan, V.N.; Wendoloski, J.J. A Knowledge-Based Approach in Designing Combinatorial or Medicinal Chemistry Libraries for Drug Discovery. 1. A Qualitative and Quantitative Characterization of Known Drug Databases. J Comb Chem 1999, 1, 55–68, doi:10.1021/cc9800071.
6. Zhang, S.; Gan, L.; Cao, F.; Wang, H.; Gong, P.; Ma, C.; Ren, L.; Lin, Y.; Lin, X. The Barrier and Interface Mechanisms of the Brain Barrier, and Brain Drug Delivery. Brain Res Bull 2022, 190, 69–83, doi:10.1016/j.brainresbull.2022.09.017.
7. Eng, M.E.; Imperio, G.E.; Bloise, E.; Matthews, S.G. ATP-Binding Cassette (ABC) Drug Transporters in the Developing Blood–Brain Barrier: Role in Fetal Brain Protection. Cellular and Molecular Life Sciences 2022, 79.
8. Farquhar, M.G.; Palade, G.E. Junctional Complexes in Various Epithelia. J Cell Biol 1963, 375–412.

9. Heinemann, U.; Schuetz, A. Structural Features of Tight-Junction Proteins. Int J Mol Sci 2019, 20.

10. Sugiyama, S.; Sasaki, T.; Tanaka, H.; Yan, H.; Ikegami, T.; Kanki, H.; Nishiyama, K.; Beck, G.; Gon, Y.; Okazaki, S.; et al. The Tight Junction Protein Occludin Modulates Blood–Brain Barrier Integrity and Neurological Function after Ischemic Stroke in Mice. Sci Rep 2023, 13, doi:10.1038/s41598-023-29894-1.

11. Chadman, K.K.; Adayev, T.; Udayan, A.; Ahmed, R.; Dai, C.L.; Goodman, J.H.; Meeker, H.; Dolzhanskaya, N.; Velinov, M. Efficient Delivery of FMR1 across the Blood Brain Barrier Using AAVphp Construct in Adult FMR1 KO Mice Suggests the Feasibility of Gene Therapy for Fragile X Syndrome. Genes (Basel) 2023, 14, doi:10.3390/genes14020505.

12. Chan, K.Y.; Jang, M.J.; Yoo, B.B.; Greenbaum, A.; Ravi, N.; Wu, W.L.; Sánchez-Guardado, L.; Lois, C.; Mazmanian, S.K.; Deverman, B.E.; et al. Engineered AAVs for Efficient Noninvasive Gene Delivery to the Central and Peripheral Nervous Systems. Nat Neurosci 2017, 20, 1172–1179, doi:10.1038/nn.4593.

13. Deverman, B.E.; Pravdo, P.L.; Simpson, B.P.; Kumar, S.R.; Chan, K.Y.; Banerjee, A.; Wu, W.L.; Yang, B.; Huber, N.; Pasca, S.P.; et al. Cre-Dependent Selection Yields AAV Variants for Widespread Gene Transfer to the Adult Brain. Nat Biotechnol 2016, 34, 204–209, doi:10.1038/nbt.3440.

14. Hordeaux, J.; Wang, Q.; Katz, N.; Buza, E.L.; Bell, P.; Wilson, J.M. The Neurotropic Properties of AAV-PHP.B Are Limited to C57BL/6J Mice. Molecular Therapy 2018, 26, 664–668.

15. Crawford, D.C.; Acuña, J.M.; Sherman, S.L. FMR1 and the Fragile X Syndrome: Human Genome Epidemiology Review. Genetics in Medicine 2001, 3, 359–371.

16. Brasa, S.; Mueller, A.; Jacquemont, S.; Hahne, F.; Rozenberg, I.; Peters, T.; He, Y.; McCormack, C.; Gasparini, F.; Chibout, S.D.; et al. Reciprocal Changes in DNA Methylation and Hydroxymethylation and a Broad Repressive Epigenetic Switch Characterize FMR1 Transcriptional Silencing in Fragile X Syndrome. Clin Epigenetics 2016, 8, doi:10.1186/s13148-016-0181-x.

17. Tassone, F.; Hagerman, P.J. Expression of the FMR1 Gene. Cytogenet Genome Res 2003, 100, 124–128, doi:10.1159/000072846.

18. Ludwig, A.L.; Espinal, G.M.; Pretto, D.I.; Jamal, A.L.; Arque, G.; Tassone, F.; Berman, R.F.; Hagerman, P.J. CNS Expression of Murine Fragile X Protein (FMRP) as a Function of CGG-Repeat Size. Hum Mol Genet 2014, 23, 3228–3238, doi:10.1093/hmg/ddu032.

19. Bülow, P.; Zlatic, S.A.; Wenner, P.A.; Bassell, G.J.; Faundez, V. FMRP Attenuates Activity Dependent Modifications in the Mitochondrial Proteome. Mol Brain 2021, 14, doi:10.1186/s13041-021-00783-w.

20. Ascano, M.; Mukherjee, N.; Bandaru, P.; Miller, J.B.; Nusbaum, J.D.; Corcoran, D.L.; Langlois, C.; Munschauer, M.; Dewell, S.; Hafner, M.; et al. FMRP Targets Distinct MRNA Sequence Elements to Regulate Protein Expression. Nature 2012, 492, 382–386, doi:10.1038/nature11737.

21. Doll, C.A.; Scott, K.; Appel, B. Fmrp Regulates Oligodendrocyte Lineage Cell Specification and Differentiation. Glia 2021, 69, 2349–2361, doi:10.1002/glia.24041.

22. Wang, X.; Zorio, D.A.R.; Schecterson, L.; Lu, Y.; Wang, Y. Postsynaptic FMRP Regulates Synaptogenesis in Vivo in the Developing Cochlear Nucleus. Journal of Neuroscience 2018, 38, 6445–6460, doi:10.1523/JNEUROSCI.0665-18.2018.

23. Berry-Kravis, E.; Hagerman, R.; Visootsak, J.; Budimirovic, D.; Kaufmann, W.E.; Cherubini, M.; Zarevics, P.; Walton-Bowen, K.; Wang, P.; Bear, M.F.; et al. Arbaclofen in Fragile X Syndrome: Results of Phase 3 Trials. J Neurodev Disord 2017, 9, doi:10.1186/s11689-016-9181-6.

24. Potter, L.A.; Scholze, D.A.; Biag, H.M.B.; Schneider, A.; Chen, Y.; Nguyen, D. V.; Rajaratnam, A.; Rivera, S.M.; Dwyer, P.S.; Tassone, F.; et al. A Randomized Controlled Trial of Sertraline in Young Children With Autism Spectrum Disorder. Front Psychiatry 2019, 10, doi:10.3389/fpsyt.2019.00810.

25. Watkins, L. V.; Moon, S.; Burrows, L.; Tromans, S.; Barwell, J.; Shankar, R. Pharmacological Management of Fragile X Syndrome: A Systematic Review and Narrative Summary of the Current Evidence. Expert Opin Pharmacother 2024, 25, 301–313.

26. Berry-Kravis, E.M.; Harnett, M.D.; Reines, S.A.; Reese, M.A.; Ethridge, L.E.; Outterson, A.H.; Michalak, C.; Furman, J.; Gurney, M.E. Inhibition of Phosphodiesterase-4D in Adults with Fragile X Syndrome: A Randomized, Placebo-Controlled, Phase 2 Clinical Trial. Nat Med 2021, 27, 862–870, doi:10.1038/s41591-021-01321-w.

27. Berry-Kravis, E.; Horrigan, J.P.; Tartaglia, N.; Hagerman, R.; Kolevzon, A.; Erickson, C.A.; Hatti, S.; Snape, M.; Yaroshinsky, A.; Stoms, G.; et al. A Double-Blind, Randomized, Placebo-

Controlled Clinical Study of Trofinetide in the Treatment of Fragile X Syndrome. Pediatr Neurol 2020, 110, 30–41, doi:10.1016/j.pediatrneurol.2020.04.019.

28. Jiang, Y.; Han, L.; Meng, J.; Wang, Z.; Zhou, Y.; Yuan, H.; Xu, H.; Zhang, X.; Zhao, Y.; Lu, J.; et al. Gene Therapy Using Human FMRP Isoforms Driven by the Human FMR1 Promoter Rescues Fragile X Syndrome Mouse Deficits. Mol Ther Methods Clin Dev 2022, 27, 246–258, doi:10.1016/j.omtm.2022.10.002.

29. Hooper, A.W.M.; Wong, H.; Niibori, Y.; Abdoli, R.; Karumuthil-Melethil, S.; Qiao, C.; Danos, O.; Bruder, J.T.; Hampson, D.R. Gene Therapy Using an Ortholog of Human Fragile X Mental Retardation Protein Partially Rescues Behavioral Abnormalities and EEG Activity. Mol Ther Methods Clin Dev 2021, 22, 196–209, doi:10.1016/j.omtm.2021.06.013.

30. Wong, H.; Hooper, A.W.M.; Kang, H.R.; Lee, S.J.; Zhao, J.; Sadhu, C.; Rawat, S.; Gray, S.J.; Hampson, D.R. CNS-Dominant Human FMRP Isoform Rescues Seizures, Fear, and Sleep Abnormalities in Fmr1-KO Mice. 2023, doi:10.1172/jci.

31. Thévenot, E.; Jordão, J.F.; O'Reilly, M.A.; Markham, K.; Weng, Y.Q.; Foust, K.D.; Kaspar, B.K.; Hynynen, K.; Aubert, I. Targeted Delivery of Self-Complementary Adeno-Associated Virus Serotype 9 to the Brain, Using Magnetic Resonance Imaging-Guided Focused Ultrasound. Hum Gene Ther 2012, 23, 1144–1155, doi:10.1089/hum.2012.013.

32. Weber-Adrian, D.; Kofoed, R.H.; Silburt, J.; Noroozian, Z.; Shah, K.; Burgess, A.; Rideout, S.; Kügler, S.; Hynynen, K.; Aubert, I. Systemic AAV6-Synapsin-GFP Administration Results in Lower Liver Biodistribution, Compared to AAV1&2 and AAV9, with Neuronal Expression Following Ultrasound-Mediated Brain Delivery. Sci Rep 2021, 11, doi:10.1038/s41598-021-81046-5.

33. Ajenjo, J.; Seo, J.W.; Foiret, J.; Wu, B.; Raie, M.N.; Wang, J.; Fite, B.Z.; Zhang, N.; Malek, R.; Beinat, C.; et al. PET Imaging of Focused-Ultrasound Enhanced Delivery of AAVs into the Murine Brain. Theranostics 2023, 13, 5151–5169, doi:10.7150/thno.85549.

34. Wu, M.X.; Zhou, Y.; Zhou, X.Y.; Xu, Y. Ultrasound-Targeted Cationic Microbubble-Mediated Gene Transfection and Inhibition of Retinal Neovascularization. Int J Ophthalmol 2022, 15, 876–885, doi:10.18240/ijo.2022.06.04.

35. Vannan, M.; McCreery, T.; Li, P.; Han, Z.; Unger, E.; Kuersten, B.; Nabel, E.; Rajagopalan, S. Ultrasound-Mediated Transfection of Canine Myocardium by Intravenous Administration of

Cationic Microbubble-Linked Plasmid DNA. Journal of the American Society of Echocardiography 2002, 15, 214–218, doi:10.1067/mje.2002.119913.

36. Fan, C.H.; Ting, C.Y.; Lin, C.Y.; Chan, H.L.; Chang, Y.C.; Chen, Y.Y.; Liu, H.L.; Yeh, C.K. Noninvasive, Targeted, and Non-Viral Ultrasound-Mediated GDNF-Plasmid Delivery for Treatment of Parkinson's Disease. Sci Rep 2016, 6, doi:10.1038/srep19579.

37. Gonçalves, C.; Akhter, S.; Pichon, C.; Midoux, P. Intracellular Availability of PDNA and MRNA after Transfection: A Comparative Study among Polyplexes, Lipoplexes, and Lipopolyplexes. Mol Pharm 2016, 13, 3153–3163, doi:10.1021/acs.molpharmaceut.6b00376.

38. Van De Wetering, P.; Moret, E.E.; Schuurmans-Nieuwenbroek, N.M.E.; Van Steenbergen, M.J.; Hennink, W.E. Structure-Activity Relationships of Water-Soluble Cationic Methacrylate/Methacrylamide Polymers for Nonviral Gene Delivery. Bioconjug Chem 1999, 10, 589–597, doi:10.1021/bc980148w.

39. Yang, S.; May, S. Release of Cationic Polymer-DNA Complexes from the Endosome: A Theoretical Investigation of the Proton Sponge Hypothesis. Journal of Chemical Physics 2008, 129, doi:10.1063/1.3009263.

40. Chatin, B.; Mével, M.; Devallière, J.; Dallet, L.; Haudebourg, T.; Peuziat, P.; Colombani, T.; Berchel, M.; Lambert, O.; Edelman, A.; et al. Liposome-Based Formulation for Intracellular Delivery of Functional Proteins. Mol Ther Nucleic Acids 2015, 4, e244, doi:10.1038/mtna.2015.17.

41. Cathy E. Bakker; Coleta Verheij; Rob Willemsen; Robert van der Heim; Frank Oerlemans; Marcel Vermey; Anne Bygrave; André T. Hoogeveen; Ben A. Oostra Fmrl Knockout Mice: A Model to Study Fragile X Mental Retardation. Cell 1994, 78, 23–33.

42. Rigollet, S.; Rome, C.; Ador, T.; Dumont, E.; Pichon, C.; Delalande, A.; Barbier, E.L.; Stupar, V. FUS-Mediated BBB Opening Leads to Transient Perfusion Decrease and Inflammation without Acute or Chronic Brain Lesion. Theranostics 2024, 14, 4147–4160, doi:10.7150/thno.96721.

43. Brossard, C.; Montigon, O.; Boux, F.; Delphin, A.; Christen, T.; Barbier, E.L.; Lemasson, B. MP3: Medical Software for Processing Multi-Parametric Images Pipelines. Front Neuroinform 2020, 14, doi:10.3389/fninf.2020.594799.

44. Steinman, J.; Koletar, M.M.; Stefanovic, B.; Sled, J.G. 3D Morphological Analysis of the Mouse Cerebral Vasculature: Comparison of in Vivo and Ex Vivo Methods. PLoS One 2017, 12, doi:10.1371/journal.pone.0186676.

45. Hsu, Y.H.; Lee, W.C.; Chu, S.S.; Chao, M.E.; Wu, K.S.; Liu, R.S.; Wong, T.T. Influence of Acoustic Parameters and Sonication Schemes on Transcranial Blood–Brain Barrier Disruption Induced by Pulsed Weakly Focused Ultrasound. Pharmaceutics 2022, 14, doi:10.3390/pharmaceutics14061207.

46. Marmottant, P.; van der Meer, S.; Emmer, M.; Versluis, M.; de Jong, N.; Hilgenfeldt, S.; Lohse, D. A Model for Large Amplitude Oscillations of Coated Bubbles Accounting for Buckling and Rupture. J Acoust Soc Am 2005, 118, 3499–3505, doi:10.1121/1.2109427.

47. van der Meer, S.M.; Dollet, B.; Voormolen, M.M.; Chin, C.T.; Bouakaz, A.; de Jong, N.; Versluis, M.; Lohse, D. Microbubble Spectroscopy of Ultrasound Contrast Agents. J Acoust Soc Am 2007, 121, 648–656, doi:10.1121/1.2390673.

48. Chen, H.; Konofagou, E.E. The Size of Blood-Brain Barrier Opening Induced by Focused Ultrasound Is Dictated by the Acoustic Pressure. Journal of Cerebral Blood Flow and Metabolism 2014, 34, 1197–1204, doi:10.1038/jcbfm.2014.71.

49. Samiotaki, G.; Konofagou, E.E. Dependence of the Reversibility of Focused-Ultrasound-Induced Blood-Brain Barrier Opening on Pressure and Pulse Length in Vivo. IEEE Trans Ultrason Ferroelectr Freq Control 2013, 60, 2257–2265, doi:10.1109/TUFFC.2013.6644731.

50. Haghi, H.; Yaali, M.; Exner, A.A.; Kolios, M.C. Experimental Investigation on the Effect of Concentration on the Resonance Frequency of Lipid Coated Ultrasonically Excited Microbubbles. Ultrason Sonochem 2025, 112, doi:10.1016/j.ultsonch.2024.107170.

51. Gerstenmayer, M.; Fellah, B.; Magnin, R.; Selingue, E.; Larrat, B.; Acoustic, B.L. Acoustic Transmission Factor through the Rat Skull as a Function of Body Mass, Frequency and Position. Ultrasound Med Biol 2018, 44, doi:10.1016/j.ultrasmedbio.2018.06.005ï.

52. Mehta, R.I.; Carpenter, J.S.; Mehta, R.I.; Haut, M.W.; Wang, P.; Ranjan, M.; Najib, U.; D'Haese, P.F.; Rezai, A.R. Ultrasound-Mediated Blood–Brain Barrier Opening Uncovers an Intracerebral Perivenous Fluid Network in Persons with Alzheimer's Disease. Fluids Barriers CNS 2023, 20, doi:10.1186/s12987-023-00447-y.

53. Rezai, A.R.; Ranjan, M.; Haut, M.W.; Carpenter, J.; D'Haese, P.F.; Mehta, R.I.; Najib, U.; Wang, P.; Claassen, D.O.; Chazen, J.L.; et al. Focused Ultrasound–Mediated Blood-Brain Barrier Opening in Alzheimer's Disease: Long-Term Safety, Imaging, and Cognitive Outcomes. J Neurosurg 2023, 139, 275–283, doi:10.3171/2022.9.JNS221565.

54. Gandhi, K.; Barzegar-Fallah, A.; Banstola, A.; Rizwan, S.B.; Reynolds, J.N.J. Ultrasound-Mediated Blood–Brain Barrier Disruption for Drug Delivery: A Systematic Review of Protocols, Efficacy, and Safety Outcomes from Preclinical and Clinical Studies. Pharmaceutics 2022, 14, doi:10.3390/pharmaceutics14040833.

55. Jin, Q.; Wang, Z.; Yan, F.; Deng, Z.; Ni, F.; Wu, J.; Shandas, R.; Liu, X.; Zheng, H. A Novel Cationic Microbubble Coated with Stearic Acid-Modified Polyethylenimine to Enhance DNA Loading and Gene Delivery by Ultrasound. PLoS One 2013, 8, doi:10.1371/journal.pone.0076544.

56. Ji, J.; Ji, J.; He Xia Preparation of Ultrasound Microbubbles Crosslinked to Albumin Nanoparticles Packaged with Tissue-Type Plasminogen Activator Gene Plasmid and Method of in Vivo Transfection. J Exp Pharmacol 2011, 35, doi:10.2147/jep.s17178.

57. Lentacker, I.; De Geest, B.G.; Vandenbroucke, R.E.; Peeters, L.; Demeester, J.; De Smedt, S.C.; Sanders, N.N. Ultrasound-Responsive Polymer-Coated Microbubbles That Bind and Protect DNA. Langmuir 2006, 22, 7273–7278, doi:10.1021/la0603828.

58. Kwak, G.; Grewal, A.; Slika, H.; Mess, G.; Li, H.; Kwatra, M.; Poulopoulos, A.; Woodworth, G.F.; Eberhart, C.G.; Ko, H.S.; et al. Brain Nucleic Acid Delivery and Genome Editing via Focused Ultrasound-Mediated Blood-Brain Barrier Opening and Long-Circulating Nanoparticles. ACS Nano 2024, 18, 24139–24153, doi:10.1021/acsnano.4c05270.

59. Di, J.; Du, Z.; Wu, K.; Jin, S.; Wang, X.; Li, T.; Xu, Y. Biodistribution and Non-Linear Gene Expression of MRNA LNPs Affected by Delivery Route and Particle Size. Pharm Res 2021, doi:10.1007/s11095-022-03166-5/Published.

60. Liu, B.; Sajiki, Y.; Sridharan, A.; Stuart, W.; Cui, X.; Siefert, M.; Araki, K.; Ziady, A.; Shi, D.; Whitsett, J.A.; et al. PBAE-PEG Based Lipid Nanoparticles for Lung Cell-Specific Gene Delivery 2024.

61. Tuma, J.; Chen, Y.J.; Collins, M.G.; Paul, A.; Li, J.; Han, H.; Sharma, R.; Murthy, N.; Lee, H.Y. Lipid Nanoparticles Deliver MRNA to the Brain after an Intracerebral Injection. Biochemistry 2023, 62, 3533–3547, doi:10.1021/acs.biochem.3c00371.

62. Khare, P.; Edgecomb, S.X.; Hamadani, C.M.; Tanner, E.E.L.; S Manickam, D. Lipid Nanoparticle-Mediated Drug Delivery to the Brain. Adv Drug Deliv Rev 2023, 197.

63. Ogawa, K.; Kato, N.; Yoshida, M.; Hiu, T.; Matsuo, T.; Mizukami, S.; Omata, D.; Suzuki, R.; Maruyama, K.; Mukai, H.; et al. Focused Ultrasound/Microbubbles-Assisted BBB Opening

Enhances LNP-Mediated MRNA Delivery to Brain. Journal of Controlled Release 2022, 348, 34–41, doi:10.1016/J.JCONREL.2022.05.042.

64. Oda, Y.; Kumagai, Y.; Kanai, M.; Iwama, Y.; Okura, I.; Minamida, T.; Yagi, Y.; Kurosawa, T.; Greener, B.; Zhang, Y.; et al. Immunogenicity and Safety of a Booster Dose of a Self-Amplifying RNA COVID-19 Vaccine (ARCT-154) versus BNT162b2 MRNA COVID-19 Vaccine: A Double-Blind, Multicentre, Randomised, Controlled, Phase 3, Non-Inferiority Trial. Lancet Infect Dis 2024, 24, 351–360, doi:10.1016/S1473-3099(23)00650-3.

65. Baden, L.R.; El Sahly, H.M.; Essink, B.; Kotloff, K.; Frey, S.; Novak, R.; Diemert, D.; Spector, S.A.; Rouphael, N.; Creech, C.B.; et al. Efficacy and Safety of the MRNA-1273 SARS-CoV-2 Vaccine. New England Journal of Medicine 2021, 384, 403–416, doi:10.1056/nejmoa2035389.

66. Polack, F.P.; Thomas, S.J.; Kitchin, N.; Absalon, J.; Gurtman, A.; Lockhart, S.; Perez, J.L.; Pérez Marc, G.; Moreira, E.D.; Zerbini, C.; et al. Safety and Efficacy of the BNT162b2 MRNA Covid-19 Vaccine. New England Journal of Medicine 2020, 383, 2603–2615, doi:10.1056/nejmoa2034577.

67. Leung, A.K.K.; Tam, Y.Y.C.; Chen, S.; Hafez, I.M.; Cullis, P.R. Microfluidic Mixing: A General Method for Encapsulating Macromolecules in Lipid Nanoparticle Systems. Journal of Physical Chemistry B 2015, 119, 8698–8706, doi:10.1021/acs.jpcb.5b02891.

68. Ji, R.; Karakatsani, M.E.; Burgess, M.; Smith, M.; Murillo, M.F.; Konofagou, E.E. Cavitation-Modulated Inflammatory Response Following Focused Ultrasound Blood-Brain Barrier Opening. Journal of Controlled Release 2021, 337, 458–471, doi:10.1016/j.jconrel.2021.07.042.

69. Marty, B.; Larrat, B.; Van Landeghem, M.; Robic, C.; Robert, P.; Port, M.; Le Bihan, D.; Pernot, M.; Tanter, M.; Lethimonnier, F.; et al. Dynamic Study of Blood-Brain Barrier Closure after Its Disruption Using Ultrasound: A Quantitative Analysis. Journal of Cerebral Blood Flow and Metabolism 2012, 32, 1948–1958, doi:10.1038/jcbfm.2012.100.

70. Hoffmann, M.; Hersch, N.; Gerlach, S.; Dreissen, G.; Springer, R.; Merkel, R.; Csiszár, A.; Hoffmann, B. Complex Size and Surface Charge Determine Nucleic Acid Transfer by Fusogenic Liposomes. Int J Mol Sci 2020, 21, doi:10.3390/ijms21062244.

71. Kheirolomoom, A.; Dayton, P.A.; Lum, A.F.H.; Little, E.; Paoli, E.E.; Zheng, H.; Ferrara, K.W. Acoustically-Active Microbubbles Conjugated to Liposomes: Characterization of a Proposed Drug Delivery Vehicle. Journal of Controlled Release 2007, 118, 275–284, doi:10.1016/j.jconrel.2006.12.015.

72. De Cock, I.; Lajoinie, G.; Versluis, M.; De Smedt, S.C.; Lentacker, I. Sonoprinting and the Importance of Microbubble Loading for the Ultrasound Mediated Cellular Delivery of Nanoparticles. Biomaterials 2016, 83, 294–307, doi:10.1016/j.biomaterials.2016.01.022.

Funding: This research was funded by ANR FUSBRAIN (Grant ANR -21-CE18-0019), C-Valo funding. FEDER and CPER funding for VEVOLAZR.

Acknowledgments

The authors are thankful to David GOSSET from the platform MO2VING and to Sebastien RIGOLLET and Vasile STUPAR from the platform IRMaGe for their precious help.

6. Supplementary results

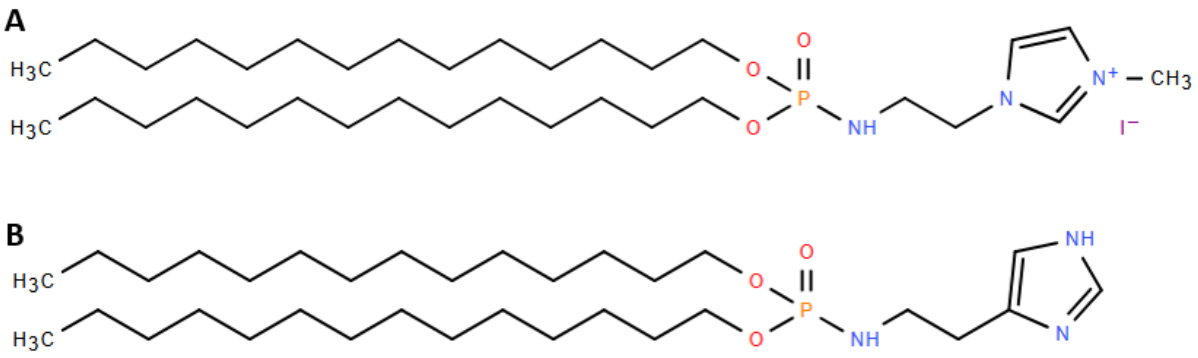

Figure S1: Lipid chemical structures (**A**) KLN27 chemical structure. (**B**) MM30 chemical structure.

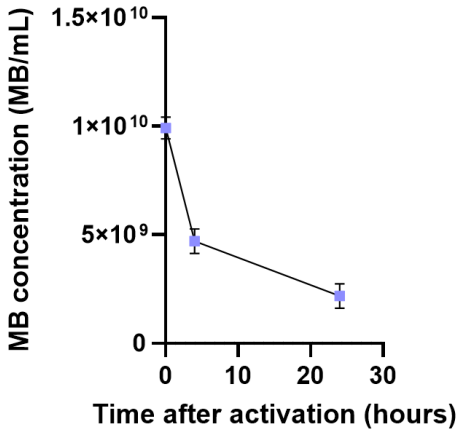

Figure S2: MB concentration decay in the vial over time after activation. Data expressed as mean +/- SEM.

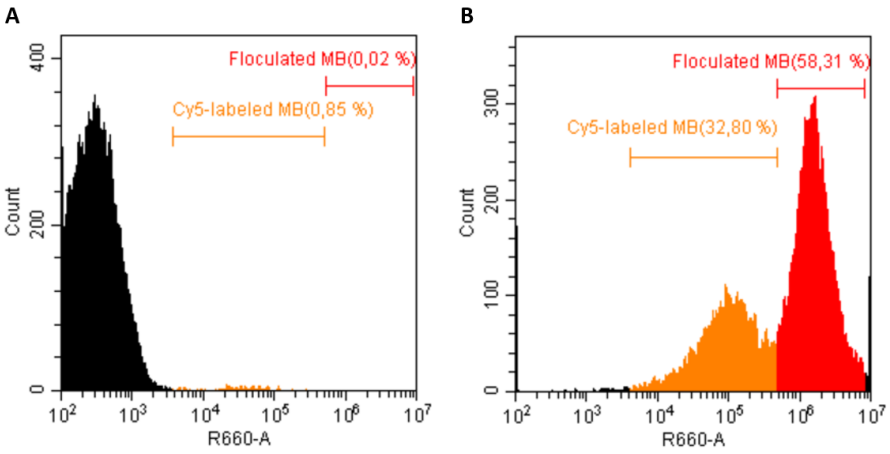

Figure S3: Cytometry fluorescence gating. (**A**) Cationic MB before addition of Cy5-labeled pDNA. (**B**) Cationic MB 10 minutes after complexation with 1 µg of Cy5-labeled pDNA, displaying the complexed and flocculated population.

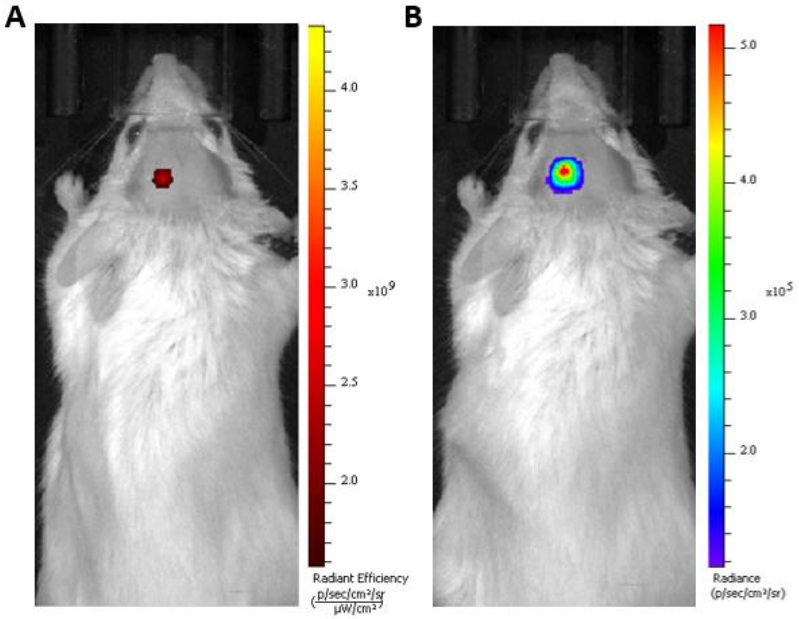

Figure S4: *In vivo* imaging. (**A**) *In vivo* fluorescence image of ICG 24 h after FUS procedure. (**B**) *In vivo* bioluminescence image of ICG 24 h after FUS procedure. Both images are done on the same animal who underwent the procedure with a 5-minute sonication at 410 kPa.

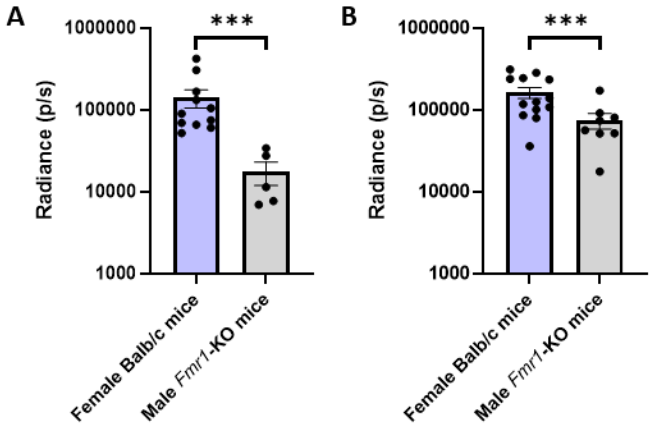

Figure S5: Gene expression in balb/c mice *versus* *Fmr1*-KO mice. (**A**) Bioluminescence of mice 24 hours after the 410 kPa for 5 minutes FUS procedure. (**B**) Bioluminescence of mice 24 hours after the 1-minute 460 kPa FUS procedure. Data expressed as mean +/- SEM. * = *p*-value < 0.05; ** = *p*-value < 0.01; *** = *p*-value < 0.001; Mann-Whitney bilateral test.

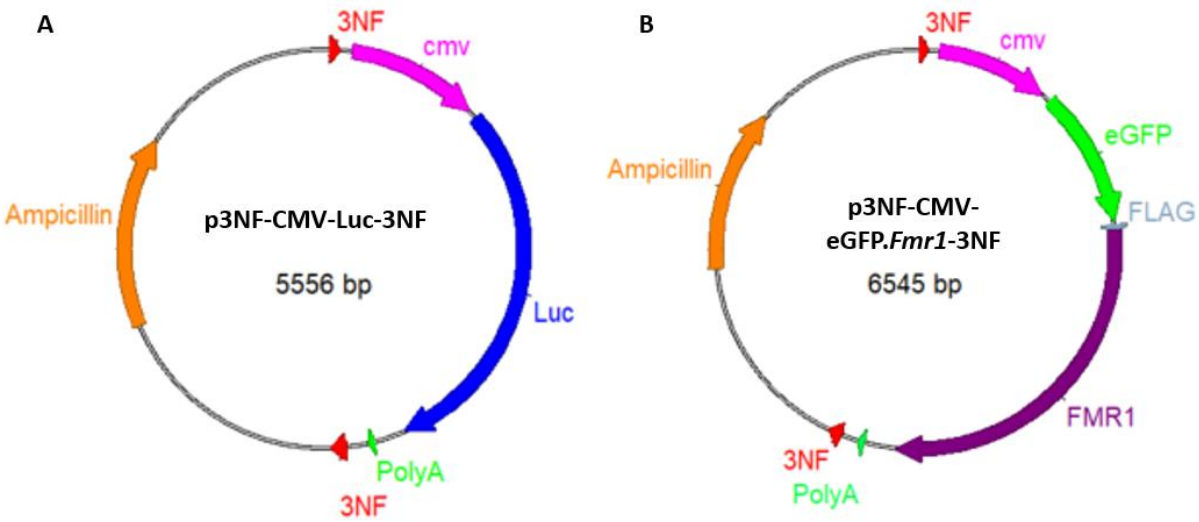

Figure S6: Plasmid DNA maps made on Ape software of the (A) luciferase-coding plasmid and of the (B) eGFP-*Fmr1*-coding plasmid

ADDITIONAL EXPERIMENTS

The previous chapter indicated the need to improve gene delivery and expression stability in order to achieve the best therapeutic effect. Lipid nanoparticles (LNPs) are non-viral vectors for gene delivery with growing interest in gene therapy. They are commonly used to deliver nucleic acids to the muscle, liver, or lungs, displaying high transfection efficiency [59,60]. They have also shown their efficiency for gene delivery to the brain using intracerebral injection [61,62]. However, such an injection route is invasive and challenging to use in clinical trials, highlighting the potential of FUS-mediated BBBo to deliver LNP. This has been previously demonstrated by Ogawa *et al*., validating such a strategy [63]. In addition, several LNPs delivering mRNA for COVID-19 vaccines have been recently FDA- and EMA-approved [64–66]. Compared to cationic MB complexing pDNA, LNPs have the advantage of allowing close to total nucleic acid complexation without the risk of injecting a large amount of MB [67].

In this additional section, we first further analyzed the effect of cationic MB-mediated gene delivery on inflammation markers. Then, we aimed to optimize gene delivery to the brain with homemade LNP in association with MB and FUS. This was performed with unfunctionalized MB (uMB), or by binding LNP to biotinylated MB (bMB), or with co-injection of cationic MB (cMB).

1. ADDITIONAL METHODS

1.1 Animals

Adult female balb/c mice aged above 8 weeks (Charles River, France) were used in this study. All experiments were conducted in accordance with European ethical rules; the protocol was approved by the local ethical committees (protocols registered under numbers APAFIS#13749). Mice were housed under 12/12 light conditions in a controlled atmosphere (22 °C) and fed *ad libitum*.

1.2 Chemicals

1,2-distearoyl-sn-glycero-3-phosphocholine (DSPC), 1,2-distearoyl-sn-glycero-3-phosphoethanolamine-N-[methoxy(polyethylene glycol)-2000] (DSPE-PEG2000), 1,2-distearoyl-sn-glycero-3-phosphoethanolamine-N-[biotinyl(polyethylene glycol)-2000] (DSPE-PEG2000-Biot), 1,2-distearoyl-sn-glycero-3-phosphoethanolamine-N-[dibenzocyclooctyl(polyethylene glycol)-2000] (DSPE-PEG2000-DBCO), 1,2-dimyristoyl-sn-glycero-3-phosphocholine (DMPC), and 1,2-dimyristoyl-sn-glycero-3-phosphoethanolamine-N-[methoxy(polyethylene glycol)-2000] (DMPE-PEG2000), 1,2-dioleoyl-sn-glycero-3-phosphoethanolamine (DOPE), and cholesterol were purchased from Avanti Polar lipids (Alabaster, Alabama, USA). MM30 was synthesized by the Synanovect platform (Brest, France).

1.3 RT-qPCR

Brains were harvested and treated as previously explained until RNA recovery and the subsequent cDNA transcription. Gene expression was evaluated from 100 ng of cDNA by qPCR using a Light Cycler II 480 (Roche Applied Science, Meylan, France) with 0.1 μM of specific primers.

1.4 Lipid nanoparticles formulation

For the custom lipid nanoparticle (LNP) formulation, lipids were first solubilized in absolute ethanol at a final concentration of 4 mg/mL. Previously described in-house luciferase-coding plasmid DNA or mRNA (OZ Biosciences, Marseille, France) was dispersed in citrate buffer (50 mM, pH 4) at a final concentration of 62 μg/mL. Liposomes were formed using the Nanoassemblr Ignite (Cytiva, Marlborough, Massachusetts, USA) by mixing both solutions in a microfluidic chip at 4 mL/min, with a mixing ratio of 3:1 (organic : aqueous), to achieve LNPs with a final N/P ratio of 6/1. The liposomes were then rapidly diluted with 1.44 times their volume of PBS, and the ethanol solvent was removed by purification using Amicon® centrifugal filter units (Millipore, Burlington, Massachusetts, USA), with a 40-minute 4000 g centrifugation. Two types of LNPs were prepared, with lipid molar ratios listed in Table 1. One formulation was modified to introduce a biotin function on the LNP surface for

subsequent streptavidin-biotin binding with bMBs. Following formation and purification, LNPs were characterized with dynamic light scattering. Briefly, 1 μL of LNP suspension was dispersed in 600 μL of PBS in a suitable tank. DLS measurements were then performed on an SZ-100 nanoparticle analyzer (Horiba Scientific); each data is the average of 3 measures. Both LNP formulations showed a similar size of 74.7 +/- 1.5 nm on average.

	DOPE	Cholesterol	DMG-PEG2000	MM27	DSPE-PEG2000-biot
LNP	10 %	39 %	1 %	50 %	0 %
Biotinylated-LNP	10 %	39 %	0.95 %	50 %	0.05 %

Table 1: Lipid molar ratio used for LNP and biotinylated-LNP formulation.

1.5 FUS-BBBo gene transfer procedure

The focused ultrasound-mediated BBB opening (FUS-BBBo) procedure was performed as previously described. Briefly, mice were anesthetized with 2% isoflurane in air, and a 26G catheter was inserted into the tail vein. The skull was then shaved and depilated. A 1 MHz focused bowl transducer with a 45 mm diameter active element (DL-47 piezo material, 45 mm radius of curvature, Precision Acoustics, UK) was used, with a passive cavitation detector (PCD) positioned in the center. The transducer was mounted in a probe holder with degassed water contained in a silicone membrane (0.2 mm), which was placed on top of the mouse skull with gel for ultrasound coupling. This transducer has an ellipsoid-shaped focal spot (6×1.5 mm), similar to the previous transducer used. The transducer was controlled by a custom 3-axis motorized stage (IndustryLab, Orléans, France), with a laser beam to guide the focal spot to the targeted region. It was connected to a linear amplifier (E&I, 210L, USA), which in turn was linked to a waveform generator (Agilent 33210A) to deliver the ultrasound treatment. The 10 MHz PCD placed at the center of the bowl transducer was connected to a 20 dB preamplifier (Precision Acoustics) for signal amplification. Signal was then recorded by a picoscope 5244 MSO and the picoscope 7 software (Pico Technology, UK), and the resulting data was processed with Matlab software to calculate the spectrum from the Fourier transform. All

systems were calibrated using a hydrophone (Onda HGL200, USA) in a separate tank filled with degassed water.

Stable cavitation dose (SCD) was calculated by averaging the values of all 60 pulses, using the area of the $3f_0$, $4f_0$, and $5f_0$ harmonics. Precursor inertial cavitation dose (ICD) was calculated using the area of the $2.5f_0$, $3.5f_0$, and $4.5f_0$ ultra-harmonics. Inertial cavitation dose was calculated using the broadband area between harmonics and ultra-harmonics. To assess the probability of inertial events, FUS sequences were performed in each animal before MB injection to measure the baseline signal. A limit for inertial cavitation was set at four times the standard deviation calculated from the baseline signal. Any pulse during the FUS-BBBo procedure that indicated an ICD or precursor ICD greater than this limit was considered to be within the inertial cavitation regime.

Using unfunctionalized MB (uMB), 0.5 µL of uMB was diluted in 50 µL of 5% sucrose HEPES (10 mM, pH = 7.4) and mixed with 100 µL of PBS solution containing either 10 µg of pDNA, or LNP containing 10 to 20 µg of pDNA, or 10 µg of mRNA.

For biotinylated MB (bMB), 0.5 µg of streptavidin was first bound to 0.5 µL of bMB for 10 minutes in 50 µL of HEPES buffer, followed by the addition of biotinylated LNP containing 10 µg of pDNA. In the control group without binding, bMB and LNP were used in the same proportions and incubated for the same duration, but without the addition of streptavidin.

For cationic MB (cMB), 10 µL of cMB were diluted in 50 µL of 5% sucrose HEPES (10 mM, pH = 7.4) and then complexed for 1 minute with 10 µg of pDNA in 100 µL of HEPES buffer or with LNP containing 10 µg of pDNA diluted in 100 µL of PBS.

The resulting mixtures were injected through the catheter, and 1 minute of pulsed FUS treatment was applied at 310 kPa, with a pulse repetition frequency of 1 Hz and a duty cycle of 5%. Following this, 50 µL of freshly prepared Indocyanine Green (ICG) solution (2.5 mg/mL in 5% sucrose) was injected through the catheter. Mice were then allowed to recover in a dedicated cage and were scored once fully alert, based on weight, appearance, and mobility. Subsequent *in vivo* imaging was performed as previously described, at 6, 24, and 48 hours after the procedure for mRNA and at 24 and 72 hours after the procedure for pDNA.

1.6 Statistics

Nonparametric Mann-Whitney bilateral tests were performed using the R language (version 4.4.0, used with R Studio software). Non-linear fit and F-test were performed using GraphPad Prism v10. A *p*-value below 0.05 was considered significant.

2. ADDITIONAL RESULTS AND DISCUSSION

2.1 Cationic microbubble-associated gene delivery induces transitory brain inflammation

Following cMB-mediated gene delivery in WT balb/c mice, we characterized the procedure's pro-inflammatory effect. We assessed it using endothelial- and leukocyte-associated inflammation markers (*ICAM-1*) and pro-inflammatory cytokine expression linked to monocytes (*CCL2*) and macrophages (*IL-1α*). We can observe a strong expression increase starting at 360 kPa of 265-fold on *CCL2*, 16-fold on *ICAM-1*, and 3-fold on *IL-1α* (Figure 1.A-C). This expression further increased with acoustic pressure and sonication time, reaching a maximum at the condition of 5-minute 410 kPa sonication, with a non-significant 3-fold increase in *CCL2* and 7-fold increase in *ICAM-1*, compared to 360 kPa. *IL-1α*, on the other hand, reached a maximum of expression with the 1-minute 410 kPa sonication, with a 4-fold increase, and did not further increase with pressure or sonication time used. This inflammation proved to be transitory as a strong decrease in *CCL2* and *ICAM-1* expression was observed at 7 days post-treatment, with 34-fold and 8-fold decreases respectively (Figure 1.D-E). However, some inflammation appears to be remaining, since this expression did not reach untreated levels, and *IL-1α* showed only a slight 1.4-fold decrease of expression (Figure 1-F). In this experiment, no significant changes were observed due to the low number of replicates and the high variability. This highlights the need to confirm our results with more thorough analyses including additional biomarkers such as Iba-1 and GFAP, to assess the inflammation of microglia and astrocytes. However, we still observe transitory pressure-related inflammation, as previously described by Ji *et al.*, which demonstrated overexpression of several markers of inflammation, including *CCL2* [68].

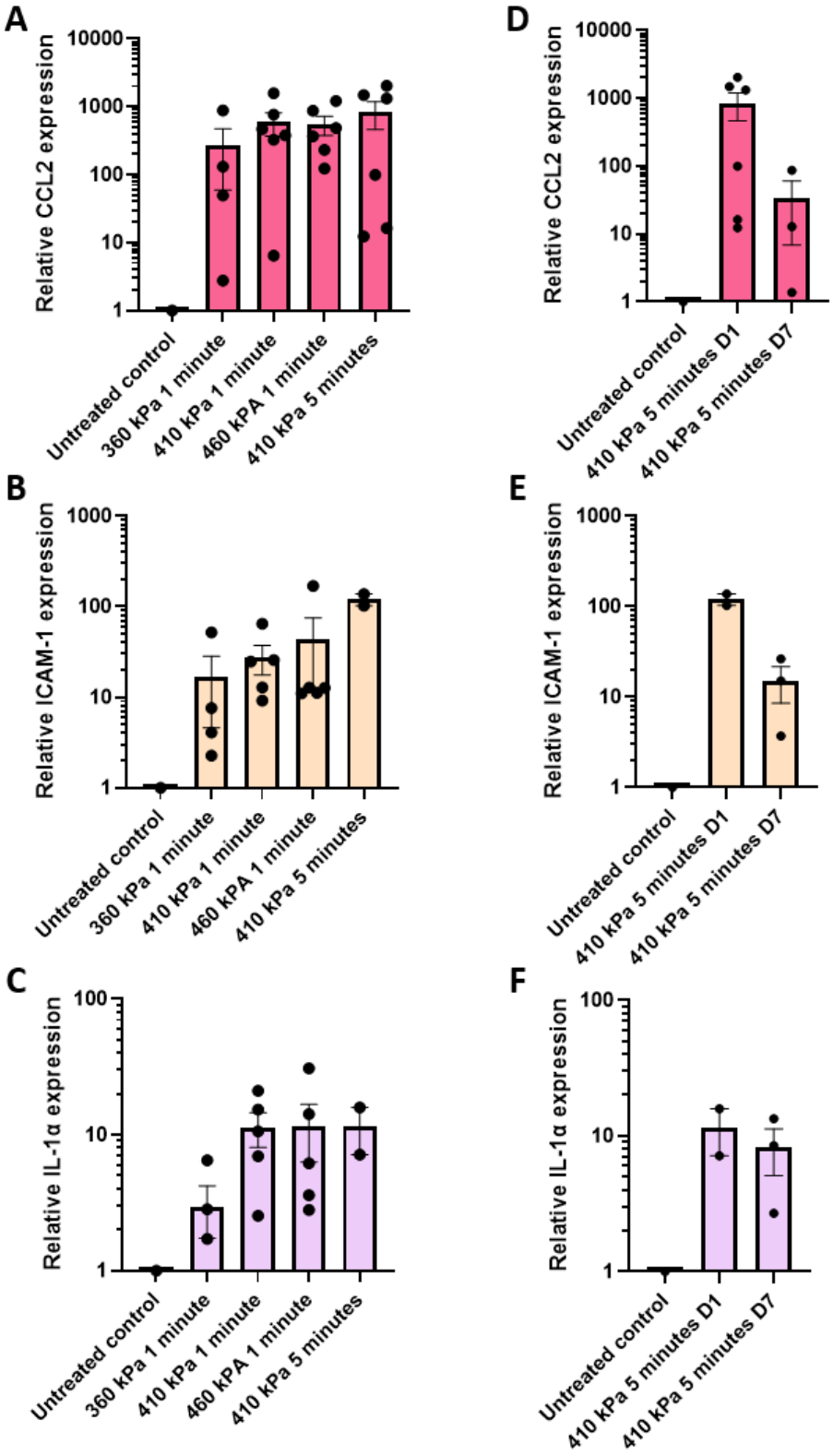

Figure 1: Short-term inflammation assessment following FUS-BBBo with pDNA-loaded cMB. (**A-C**) Relative expression of CCL2 (**A**), ICAM-1 (**B**), or IL-1α (**C**) 24 hours following FUS-BBBo with the different FUS sequences. (**D-E**) Relative expression of CCL2 (**A**), ICAM-1 (**B**), or IL-1α (**C**) 1 to 7 days following the 5-minute 410 kPa FUS.

2.2 FUS-BBBo allows LNP-mediated brain gene delivery

We first used unfunctionalized MB to deliver nucleic acid, using a BBBo protocol optimized previously, where we showed that 1.5×10^7 MB (corresponding to approximately 0.5 μL) was the lowest MB dose allowing significant BBBo assessed *in vivo* (Results part II). It showed successful gene delivery with all conditions tested, except when LNPs were injected after BBBo, where almost no bioluminescence was detected (data not shown). This led us to always co-inject LNP with MB. Using a 2-fold higher LNP dose encapsulating pDNA did not show any increase of bioluminescence, suggesting a saturation effect (Figure 2.A). The use of mRNA-loaded LNP showed similar gene expression, but with an expectedly lower expression kinetics, with a maximum reached 6 hours after treatment and a significant decrease at 24 and 48 hours (3.9×10^4 +/- 9.3×10^3, 1.2×10^4 +/- 2.8×10^3, and 3.5×10^3 +/- 1.4×10^3 p/s respectively, figure 2.E)

Surprisingly, we observed no significant differences between free pDNA and LNP, though a higher signal was detected with LNP, reaching 1.9×10^4 +/- 9.4×10^3 and 4.5×10^4 +/- 1.0×10^4 p/s, respectively (Figure 2.A). It suggests that pDNA encapsulation in LNP had few effects on gene delivery. Considering that our LNP size was relatively large compared to habitual nanoparticles delivered [48,69] and that it did not induce gene expression when injected after BBBo, they might be too large to cross the opened BBB. Gene delivery occurring with LNP co-injected might therefore be the result of LNP destruction during MB cavitation. This hypothesis is reinforced by the fact that the use of LNP bound to bMB surface through streptavidin-biotin did not enhance bioluminescence compared to co-injection of bMB and LNP (2.1×10^4 +/- 7.1×10^3 and 1.6×10^4 +/- 5.9×10^3 p/s respectively, figure 2.B). In addition, the same observation is made using cMB complexed to pDNA or with co-injection of LNP (4.8×10^4 +/- 2.5×10^3 and 5.4×10^4 +/- 9.9×10^3 p/s respectively, figure 2.C). Furthermore, using LNP-bound bMB or cMB with LNP did not enhance gene delivery compared to unfunctionalized MB (Figure 2.D). This is contradictory to the literature, which suggests that size optimization of LNP might enhance gene delivery [70–72].

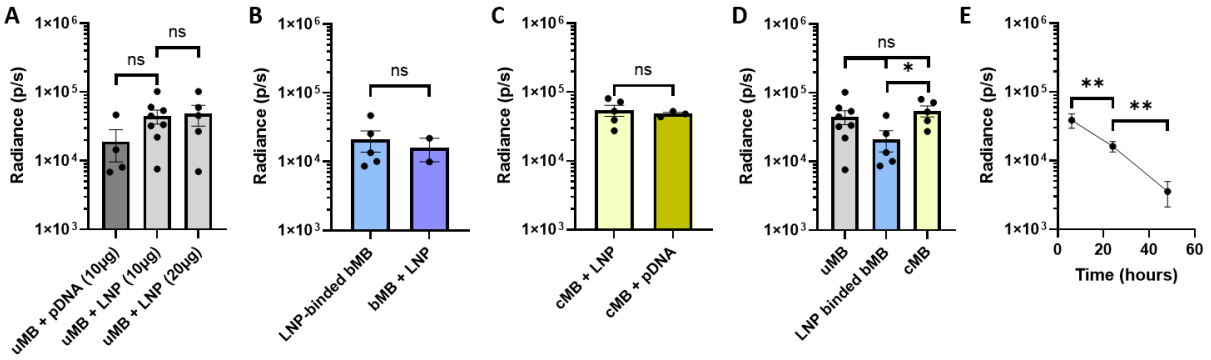

Figure 2: Brain gene transfer in balb/c mice assessed with luciferase bioluminescence. (**A**) *In vivo* bioluminescence of mice 24 hours after FUS associated with unfunctionalized MB (uMB) and injection of free pDNA of LNP and effect of pDNA amount. (**B**) *In vivo* bioluminescence of mice 24 hours after FUS associated with biotinylated MB (bMB) bound to LNP or with free LNP. (**C**) *In vivo* bioluminescence of mice 24 hours after FUS associated with cationic MB (cMB) and LNP or complexed pDNA. (**D**) Comparison of *in vivo* bioluminescence of mice 24 hours after FUS associated with uMB, bMB, or cMB and LNP injection. (**E**) *In vivo* bioluminescence of mice from 6 to 48 hours after FUS associated with uMB and injection of mRNA-LNP.

Finally, the analysis of SCD during FUS-BBBo demonstrated a strong correlation with the bioluminescence induced after treatment with uMB and LNP ($R^2 = 0.84$, figure 3.A). This was expected since BBBo is correlated with SCD, and we previously demonstrated that BBBo was also correlated with gene expression assessed in bioluminescence. Comparing this non-linear regression using an F test with uMB injected with bare pDNA demonstrated a significant difference (Figure 3.B). Thus, this indicates that LNP actually induced higher bioluminescence than bare pDNA when relativized according to the SCD generated. Comparing the different groups with LNP injection also showed significant differences, suggesting that the type of MB used slightly influenced gene delivery. Comparing the use of cMB with LNP or pDNA showed a strong difference in SCD induced, despite similar bioluminescence induced. This is further observed with the inertial cavitation, where we observe more occurrences of precursor inertial cavitation events (16.7 +/- 4.2 % and 37.2 +/- 8.4 %, respectively, $p = 0.09$) and inertial cavitation events (6.3 +/- 3.0 % and 25.0 +/- 6.3 %, respectively, $p = 0.07$). This effect of pDNA complexation on MB cavitation was previously described but is opposite to the effect observed here, where higher cavitation dose occurs with pDNA complexation, whereas *in vitro*, pDNA induced lower cavitation at the same pressure. This might be due to the difference in complexation ratio used here, of 1 µg of pDNA for 1 µL of cMB, which was used to keep the amount of cMB

previously used to ensure efficient BBBo, while using the same pDNA amount as encapsulated in LNP. Thus, this highlights the importance of the complexation ratio used in the previous article, as a higher inertial cavitation would have probably resulted in higher damage occurrences. No significant differences were observed between in all other conditions on both precursor inertial cavitation events (ranging from 1.7 to 16.7 % on average) and inertial cavitation events occurrences (ranging from 0 to 6.3 % on average). This shows that gene delivery using LNP under these conditions allowed safe BBBo, as few inertial cavitation events were observed.

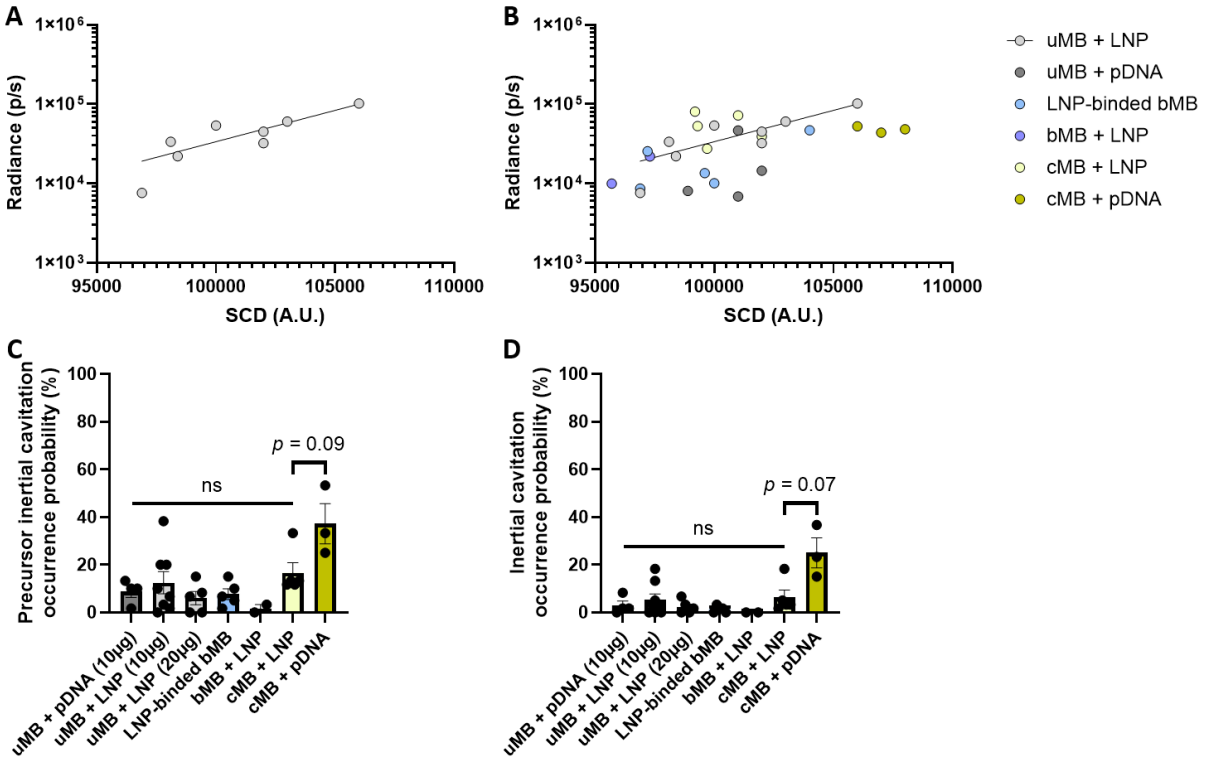

Figure 3: *In vivo* analysis of MB cavitation during FUS-BBBo. (**A**) *In vivo* bioluminescence of mice 24 hours after FUS associated with unfunctionalized MB (uMB) as a function of stable cavitation dose (SCD). (**B**) *In vivo* bioluminescence of mice 24 hours after FUS-BBBo as a function of SCD. (**C**) Occurrence probability of precursor inertial cavitation dose *in vivo* during FUS-BBBo. (**D**) Occurrence probability of inertial cavitation dose *in vivo* during FUS-BBBo.

Partie 4 : Évaluation des effets comportementaux d'une thérapie génique du syndrome de l'X fragile par ultrasons focalisés et ouverture de la BHE

Résumé en français :

Introduction :

Le syndrome de l'X fragile est une maladie neurodéveloppementale causée par l'absence d'expression du gène *Fmr1*. Cette maladie est la première cause héréditaire de déficience intellectuelle et de trouble du spectre de l'autisme. Il n'existe actuellement aucun traitement efficace et seuls des traitements symptomatiques sont actuellement disponibles. La thérapie génique montre des résultats prometteurs dans des études précliniques, mais les méthodes utilisées sont difficiles à transférer en essai clinique. La délivrance de gènes par ouverture de la barrière hémato-encéphalique (BHE) assistée par microbulles est une méthode prometteuse, non invasive et sûre qui pourrait permettre un transfert plus facile en essai clinique.

L'objectif de cette partie est d'évaluer l'efficacité d'un protocole viral de transfert de gène par ultrasons associé à des microbulles pour la thérapie du syndrome de l'X fragile, et d'étudier les effets thérapeutiques sur le comportement de souris modèles.

Méthode :

Pour cela, nos microbulles non fonctionnalisées ont été utilisées et co-injecté avec un AAV2/9 codant pour la luciférase pour l'analyse de l'expression ou codant pour *Fmr1*-eGFP pour évaluer la thérapie génique. Les ultrasons focalisés ont été délivrés dans le cerveau entier grâce au déplacement de la sonde et le suivi de l'ouverture a été réalisé en imagerie par résonance magnétique avec injection d'un agent de contraste de gadolinium. L'effet de la procédure sur les souris *Fmr1*-KO traitées a été évalué en étude comportementale et comparé à des souris wild-type (WT) et *Fmr1*-KO non traitées ainsi qu'à des souris *Fmr1*-KO ayant reçu la procédure ultrasonore associée à des microbulles sans injection d'AAV. Les phénotypes d'hyperactivité, de troubles sociaux et de l'anxiété ont été évalués. À la fin des études comportementales, l'expression du transgène et les effets à long terme de la procédure ont été évalués en RT-qPCR et en histologie.

Les résultats de cette partie sont présentés sous forme d'article qui sera publié prochainement après relecture des co-auteurs. Une analyse comportementale supplémentaire est présentée en tant qu'expériences additionnelles après cet article.

Principaux résultats :

Notre étude montre tout d'abord une large ouverture du cerveau des souris, couvrant plus de 60 % du cerveau. Aucun dommage n'a été observé en imagerie par résonance magnétique immédiatement après la procédure, et aucun dommage ni marqueurs d'inflammation ne sont observés trois semaines après la procédure. L'expression du transgène a atteint en moyenne 15 % de l'expression des souris WT et a été détecté principalement dans les neurones du cortex préfrontal, de l'hypothalamus et dans une moindre mesure de l'hippocampe. Cette expression de *Fmr1* a démontré un effet thérapeutique sur les phénotypes d'hyperactivité et de trouble de l'anxiété. Curieusement, l'ouverture de la BHE seule a également montré un effet thérapeutique sur le phénotype de troubles sociaux et a participé aux effets de l'expression de *Fmr1* sur les phénotypes d'hyperactivité et de trouble de l'anxiété.

Cette étude démontre l'intérêt et la preuve de concept de l'utilisation de notre méthode de thérapie génique pour le syndrome de l'X fragile. Elle apporte aussi un nouvel axe de recherche pour la thérapie du syndrome de l'X fragile, combinant des effets thérapeutiques de la thérapie génique et de l'ouverture de la BHE.

Title:

Evaluating Behavioral Outcomes of Whole-Brain Viral Gene Therapy for Fragile X Syndrome via Focused Ultrasound and BBB Opening

Authors:

Thomas Ador[1,2,3], Sebastien Rigollet[4,5], Anthony Laugeray[6], Mylène Fournié[1], Vasile Stupar[4,7], Emmanuel Barbier[4,7], Chantal Pichon[1,2,8], Arnaud Menuet[3], Anthony Delalande[1,2,9]

Affiliations:

[1] ART mRNA INSERM US55, Orléans, France

[2] Université d'Orléans, LI²RSO, France

[3] Laboratory of Experimental and Molecular Immunology and Neuromodulation (INEM), UMR 7355 CNRS-University of Orleans, Orleans, France

[4] Univ. Grenoble Alpes, Inserm, Grenoble Institut Neurosciences, U1216, Grenoble, France

[5] Image Guided Therapy, Pessac, France

[6] NBPHARMATOX, Orléans, France

[7] Univ. Grenoble Alpes, Inserm, CNRS, CHU Grenoble Alpes, IRMaGe, Grenoble, France

[8] Institut Universitaire de France, Paris, France

[9] Lead contact.

ABSTRACT

Fragile X syndrome is the leading inherited cause of intellectual disability and currently lacks effective treatments. This neurodevelopmental disorder is caused by a CGG repeat across the 5'-non-coding region of the fragile X messenger ribonucleoprotein 1 (*Fmr1*) gene, silencing its expression. Gene therapy designed for monogenic neurodisorders is a promising strategy but requires an efficient method to bypass the blood-brain barrier (BBB). In this study, using *Fmr1*-KO mice, a whole-brain BBB opening protocol was performed using focused ultrasound associated with microbubbles (FUS-BBBo) to deliver an AAV vector. At first, using the AAV-luciferase vector, we showed over 60 % successful BBB opening on average and widespread expression of the luciferase transgene, assessed with bioluminescence. Using the AAV-*Fmr1*

vector, our data showed a more variable and efficient rescue of *Fmr1* expression. Thus, our analysis by RT-qPCR demonstrated an *Fmr1* expression level of approximately 15% in the brains of treated *Fmr1* KO mice, relative to those of WT. Furthermore, immunohistochemical analysis indicated that FMRP expression coded by the transgene was also limited and was predominantly localized to neuronal populations in treated *Fmr1* KO mice. In order to assess the therapeutic effectiveness of our approach, we conducted a behavioral analysis 3 weeks after treatment. Re-expression of *Fmr1,* although limited, appeared to rescue hyperactivity and anxiety-like behaviors. Interestingly, in this experimental condition, whole-brain BBB opening itself appeared to rescue social impairment and contributed to behavioral rescue promoted by transgene expression. These data provide proof-of-concept for the efficacy of FUS-BBBo combined with AAV as a potential therapy for FXS-related behaviors, though further research is warranted.

Keywords: Gene therapy; Ultrasound; Microbubble; Adeno-associated Virus; Blood-brain barrier; *Fmr1* gene

1. INTRODUCTION

Fragile X syndrome (FXS) is a neurodevelopmental disorder and the leading cause of hereditary intellectual disability and autism spectrum disorder, with a prevalence of about 1 in 4000 males and 1 in 8000 females [1]. FXS results from a genetic alteration in the promoter region of the fragile X messenger ribonucleoprotein 1 (*Fmr1*) gene, where the CGG codon gets over-repeated beyond the typical 5 to 55 units, reaching over 200 iterations in the full mutation. This repetition leads to the hypermethylation of this locus, resulting in the silencing of *Fmr1* expression and, consequently, the absence of the encoded FMRP (fragile X messenger ribonucleoprotein) [2–5].

The *Fmr1* knockout (KO) mouse model recapitulates the behavioral symptoms observed in FXS patients including hyperactivity (one of the most commonly reported), anxiety, and social and cognitive impairments [6]. Currently, despite numerous clinical trials exploring various pharmacological agents, this neurodevelopmental disorder remains without an effective treatment [7–13]. Thus, although various treatment strategies effective for other central nervous system (CNS) disorders such as Alzheimer's disease have been explored in FXS, including acetylcholinesterase inhibitors (Donepezil), neuroprotective agents (Minocycline), or metabotropic glutamate receptor (Mavoglurant), these efforts have not yielded significant results [14–17]. Accordingly, available treatments for FXS are only symptomatic, and even the ongoing most promising clinical trials have only shown partial improvement [18,19]. Effective treatments currently in clinical trials include methylphenidate with effects on attention deficit and social skills (FDA-approved as Ritalin), melatonin for improving sleep time and quality, and cannabidiol for communication improvement [20–22].

Innovative approaches, particularly gene therapy, offer promising potential by aiming to restore FMRP expression. Like other neuropathologies, gene therapy dedicated to the brain remains very challenging due to the highly selective blood-brain barrier (BBB), which restricts the passage of all molecules larger than 400 Da and of 98% of smaller molecules [23–26]. This barrier impermeability is caused by several properties [27], such as active transporters and tight junction proteins sealing the endothelial cells together to prevent passive passage of molecules [28–31]. Previous attempts at gene therapy for FXS have demonstrated the

therapeutic efficiency of an *Fmr1* re-expression strategy. However, the methods used to bypass the BBB were invasive, such as intracerebral or intrathecal injections, or specific to mouse strains such as using AAV.PHP.B serotype. All these strategies are currently challenging to use in clinical trials [32–35].

While few safe methods exist to open the BBB and enable molecule passage, focused ultrasound (FUS) combined with microbubbles has emerged as a leading non-invasive technique for this purpose currently explored in clinical trials [36–39]. Microbubbles, initially developed as ultrasound contrast agents, are composed of a gas core stabilized by a lipid, protein, or polymer shell [40–42]. When subjected to an ultrasound field, microbubbles oscillate, generating mechanical forces that transiently disrupt tight junctions through push-pull actions or microstreaming and shear forces [43–45]. The FUS-mediated BBB transient opening (FUS-BBBo) method has recently gained significant interest with ongoing clinical trials for the treatment of Alzheimer's or Parkinson's disease [46–48]. Several preclinical studies have also shown the potential of FUS-BBBo for gene therapy with a co-injection of nucleic acids or an AAV9, allowing transgene expression either locally [49] or across the entire brain [50]. Such preclinical studies report promising transgene expression and transduction rates in rodents and larger animals including primates [51]. Localized FUS-BBBo gene delivery has already demonstrated its efficiency to induce behavioral rescue in Parkinson's disease [52]. This method holds promise for treating monogenic neurodisorders and is relatively scalable for clinical trials, as demonstrated by existing clinical studies.

The current study investigates the efficacy of a viral gene therapy approach, using an FUS-BBBo method, to restore *Fmr1* gene expression and to rescue the behavioral phenotypes of *Fmr1* KO mice. Bioluminescence imaging, RT-qPCR, and immunohistochemistry were performed to evaluate the spatiotemporal success of transgene delivery. Subsequently, the therapeutic effects were evaluated on behavioral deficits of *Fmr1* KO mice, including hyperactivity, anxiety, and social impairments.

2. MATERIAL AND METHODS

2.1 Animals

This study was conducted in two steps. The first step was intended for the kinetic analysis of gene delivery efficiency based on luciferase expression, and the second step for *Fmr1* re-expression and behavior analysis. Firstly, for luciferase expression analysis with bioluminescence imaging, wild-type males (C57BL/6J strain) aged between 8 and 12 weeks were used (Janvier Labs, France). Secondly, for *Fmr1* re-expression and behavioral analysis, male *Fmr1*-KO2 mice (*Fmr1*$^{-/y}$) and *Fmr1*$^{+/y}$ control mice (*Fmr1*$^{+/y}$) aged over 8 weeks. These mice were kindly gifted from the Netherlands Institute for Neuroscience (Ben Oostra) [6] and bred in the TAAM laboratory (UAR44 - CNRS, Orléans, France). Mice *Fmr1* genotypes were assessed as previously described by PCR on tail biopsy [6]. All experiments were conducted in accordance with European ethical rules; the protocol was approved by the local ethical committees (protocols registered under numbers APAFIS#47771, APAFIS#47394, and APAFIS#43777). Mice were housed under a reverse 12h/12h light/dark cycle in a controlled atmosphere (22 °C) and fed ad libitum.

2.2 Chemicals

1,2-distearistoyl-sn-glycero-3-phosphocholine (DSPC) and 1,2-distearistoyl-sn-glycero-3-phosphoethanolamine-N-[methoxy(polyethylene glycol)-2000] (ammonium salt) (DSPE-PEG2000) were purchased from Avanti Polar Lipids (Alabaster, Alabama, USA). Perfluorobutane was obtained from F2 Chemicals (Preston, United Kingdom).

2.3 Microbubble formulation

Homemade lipidic microbubbles composed of DSPC and DSPE-PEG2000 (22:3 molar ratio) were prepared as previously described [53]. Briefly, lipids were mixed in ethanol at a final concentration of 5 mg/mL in 1.5 mL glass vials, followed by the formation of liposomes and freeze-drying of the sample. The headspace of the vial was filled with perfluorobutane. Microbubbles were activated by mechanical agitation at 4500 rpm for 45 s using a Vialmix (BMS, Princeton, New Jersey, USA). MB concentration and size distribution were measured by optical imaging on a 0.2 mm Thoma slide using an upright trinocular microscope (Leitz Laborlux D, obj ×25) connected to a camera (The Imaging Source, Germany). Images were analyzed using the particle analysis plugin of ImageJ software. Our custom microbubble

formulations were concentrated at $2.35\times10^{10} \pm 1.93\times10^{9}$ MB/mL, with a median diameter of 1.37 ± 0.2 μm.

2.4 Whole-brain FUS-BBBo procedure

Mice were initially anesthetized with 2% isoflurane in an air/O_2 mix (80/20). A catheter was placed on the tail vein, and the mice's skulls were shaved using depilatory cream. A dose of 50 μL containing 1×10^{11} viral genomes (vg) of AAV was injected through the catheter under a laminar flow hood. Subsequently, mice were then placed in a custom contention system under the FUS probe, as previously described [53]. Two types of AAV were used: AAV2/9.CMV.Luciferase (AAV-Luc) to monitor gene expression over time and AAV2/9.CMV.Fmr1-eGFP (AAV-*Fmr1*) to induce FMRP re-expression. AAV2.9 viral vectors were obtained from the CAPACITES platform (Nantes, France). The *Fmr1* gene was cloned from the plasmid p-EGFP-C1-Flag-mFmr1(wt) [54]. p-EGFP-C1-Flag-mFmr1(wt) was a gift from Stephanie Ceman (Addgene plasmid # 87929).

The experimental setup consisted of a 7-concentric-element transducer (Imasonic, Voray-sur-l'Ognon, France) embedded on a 2-axis motorized system enabling planar displacement. The system was controlled by the Thermoguide® software (Image Guided Therapy, Pessac, France). MB were then injected through the catheter, directly followed by a continuous 1.5 MHz FUS treatment at 456 kPa (PNP in water) for 92 s. The displacement speed of the probe during the treatment was set at 10 mm/s, following a raster scan allowing the treatment of the whole brain as described previously by Felix *et al* [50]. Mice were then placed in the MRI for evaluation of the BBB opening.

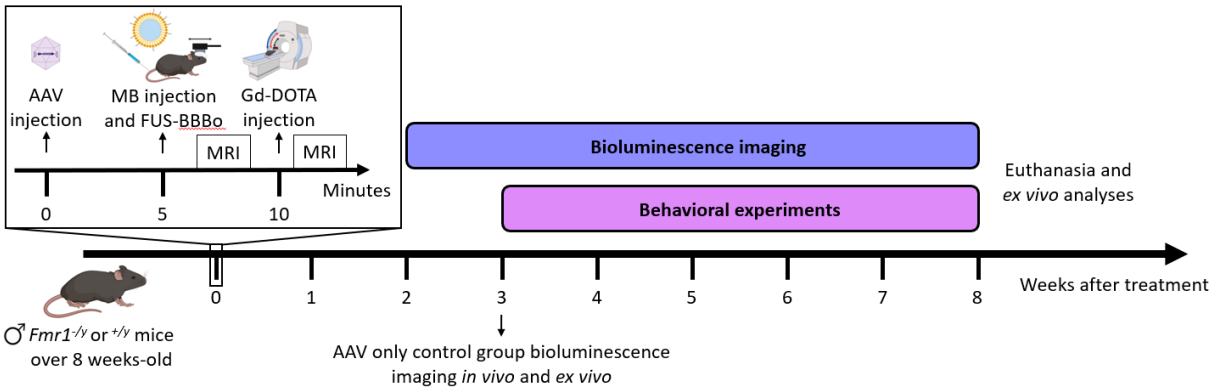

Figure 1: Timeline of FUS-BBBo procedure and following experiments.

2.5 MRI

MRI was performed at 4.7T (BioSpec 47/40, Avance III, Bruker, Ettlingen, Germany) at the IRMaGe facility (Grenoble, France). The scanner was equipped with a volume transmit coil and a single-element surface receive coil. The MRI protocol performed after the FUS treatment was as described before: T2-weighted TurboRARE sequence (TR/TE = 2200/36 ms; 13 axial slices; FOV = 20×20 mm²; matrix 256×256; voxel size, 78×78×1000 µm3, RARE-factor, 8; Tacq = 3 min 31s), T1 map RARE VTR sequence (TR, 3000 to 18 ms; TE =6.6 ms; FOV = 20×20 mm²; matrix 128×128; voxel size, 156×156×1000 µm3, RARE-factor, 4; 2 slices, Tacq = 12 min 39s) performed before and after the intravascular injection of a gadolinium chelate (Gd-DOTA; DOTAREM®, Guerbet, Villepinte, France), T1-weighted RARE sequence (TR/TE = 800/7 ms; 13 slices; FOV = 20×20 mm²; matrix 256×256; voxel size, 78×78×1000 µm3, RARE-factor, 4; axial and coronal orientations; Tacq = 1 min 16 s) to evaluate the BBB opening. Gadolinium contrast agent Gd-DOTA was obtained from Guerbet (Villepinte, France) MRI data were processed and analyzed using MP3 software [55].

2.6 Bioluminescence imaging

Bioluminescence imaging of mice was performed at the small animal imaging platform OPTIMAL (Grenoble, France). Briefly, mice were injected intraperitoneally with 200 µl of a solution of luciferin (30 mg/mL, Promega) in PBS. Mice were then anesthetized with 2%

isoflurane in air and imaged using an IVIS Lumina LT series III (Perkin Elmer, Massachusetts, USA) 10 minutes after injection. Two groups of mice underwent bioluminescence imaging. The first group was treated with FUS-BBBo and injection of AAV2/9-CMV-Luciferase as described in section 2.4 and underwent bioluminescence imaging once a week from day 14 to 53 post-treatment. In order to control AAV expression in tissues without BBB opening, a second group was treated only with 1×10^{11} vg AAV2/9-CMV-Luciferase injection in the tail vein and underwent bioluminescence imaging once 21 days after treatment.

For *ex vivo* bioluminescence, tissues of interest were rapidly excised, placed into 24-well tissue culture plates with 300 μg/mL D-luciferin in DPBS, and imaged in IVIS Lumina LT series III. *Ex vivo* bioluminescence was performed at the end of *in vivo* kinetic experiment 53 days after treatment for the first group and 21 days after treatment for the second group.

2.7 RT-qPCR

Treated mice that underwent behavioral experiments were harvested 7 to 8 weeks after treatment. An additional *Fmr1*$^{+/y}$ mice group treated with the AAV-*Fmr1* injection and FUS-BBBo was harvested at 3 weeks post-treatment to further analyze treatment effects at the beginning of AAV expression. Brains were harvested and sliced using a brain slicer to separate the optic bulbs and cerebellum from the rest of the brain. Brain hemispheres were separated and sliced axially (2 to 3 mm thick). All brain parts were then frozen immediately in liquid nitrogen and stored at −80 °C. Frozen brain parts were crushed using a Precellys Evolution Touch (Bertin Technologies, France) at 5500 rpm, 4 °C for 15 seconds. Sample RNA extractions were performed using an RNA II NucleoSpin® mini kit (Machery-Nagel EURL, Hoerdt, France) which includes a DNAse treatment. RNA quantification was performed using a NanoDropOne spectrophotometer (Thermo Fischer). The RNA integrity was checked using a BioAnalyzer 2100 (Agilent Technologies UK Limited, Wokingham, Berkshire, UK) and was acceptable when the RNA integrity number exceeded 7. For all experiments, 500 ng to 1 μg of RNA was used for reverse transcription using 200 units of M-MuLV Reverse Transcriptase (New England Biolabs) for 1 h at 37 °C. The gene expression was evaluated from 100 ng of cDNA by qPCR using a Light Cycler II 480 (Roche Applied Science, Meylan, France) with 0.1 μM of specific primers (*Frm1*: forward: 5′-AGAAAAGTGTCCCACAAGAA-3′, reverse: 5′-

AAGTGCATGTCAATCAACAT-3′) and compared to GAPDH housekeeping gene expression (using Mm_Gapdh_3_SG QuantiTect Primer Assay, Qiagen).

2.8 Immunological staining

At the end of behavioral experiments, 3 mice of each group that underwent behavioral experiments were euthanized. Briefly, after a subcutaneous carprofen injection (5 mg/kg), mice were anesthetized with a lethal intraperitoneal injection of pentobarbital (150 mg/kg). Once the mice were totally unconscious, they underwent an intracardiac injection of 25 mL of cold PBS-EDTA (5 mL/min) followed by an injection of 25 mL of 4% PFA (5 mL/min). Brains were then harvested and were post-fixated in 4% PFA for 48 to 72 hours at 4 °C; they were then put in a 30% sucrose solution for 2 to 3 weeks at 4 °C. Brains were then rapidly frozen in tissue-freezing medium in an isopentane bath kept at -80 °C with dry ice. Brains were stored at -80 °C until slicing with a cryostat (CryoStar NX50, Epredia). Brains were sliced in the sagittal axis with a 7 µm thickness and deposited on adhesive slides (TOMO, Matsunami Glass, Osaka, JAPAN), and then kept at -20 °C.

For Hematoxylin and Eosin (H&E) staining, slides underwent an absolute ethanol bath followed by a 1-minute bath in Hematoxylin solution, were rinsed for 15 seconds in water, then incubated 15 seconds in chloride, 15 seconds in a 1 % Phloxine bath, and rinsed 15 seconds in water. Then, slides were sequentially dehydrated in increasing concentrations of ethanol (70% to 100%) and finally rinsed in 3 baths of xylene. Slides were then covered with a protective film, and images were taken with a slide scanner (DP200, Roche).

For immunological staining, slides were first deprotected in a citrate buffer at 90 °C and rinsed in 3× 5-minute TBS baths. Brains slices were incubated for 2 hours in a saturation solution (1 % BSA, 10 % FBS, 0.2 % Triton in TBS buffer) and then co-incubated with a primary antibody in the same solution for 40 hours. Antibodies used were FMRP-phosphorylated-ser (Invitrogen, reference PA5-35385, dilution 1: 200) and NeuN (Millipore, reference MAB377, dilution 1: 500). The slides were washed in 3x 5-minutes TBS baths and incubated with the appropriate secondary antibody in a saturation solution (1% BSA, 10% FBS in TBS buffer). Secondary antibodies used were Alexa 488 anti-mouse (reference A-11029, dilution 1: 1000)

and Alexa 594 anti-rabbit (reference A-11029, dilution 1: 1000). After 3 washings in TBS baths (5 minutes each) and a quick bath in deionized water, slides were mounted in paramount medium under a glass coverslip. Mosaic images were performed with a fluorescence inverted microscope (Video Observer Z7 Apotome2, Zeiss), and close-up images were taken using a confocal microscope (LSM 980 Airyscan2, Zeiss).

2.9 Behavioral experiments

Behavioral experiments were conducted concurrently for all groups within a 4-hour window to minimize the influence of circadian rhythms. Mice were acclimated to the red-light conditions in the experimental room for 30 minutes before testing.

First, a direct interaction test was performed 3 weeks after treatment. Mice were first put in the experimental cage with fresh litter and were given 30 minutes of habituation, and the mice's movements were tracked. A stimulus mouse was then added, and the active social interaction of the test mice was manually assessed for 10 minutes. For the analysis, the parameters estimated relevant for the locomotion Z-score were the total distance travelled by the mice and time immobile during the first 5 minutes of the habituation. For the social interaction assessment, all sniffing of the stimulus mice by the tested mice was timed and was decomposed depending on the sniffed body area (head, body, and urogenital). The parameters estimated relevant for social Z-score were time sniffing the whole body, the head, and the urogenital areas during the first 10 minutes and the time sniffing the whole body, the head, and the urogenital areas during the last 5 minutes.

The next day, open field tests were performed, and mice movement was tracked and analyzed for 5 minutes. For the locomotion Z-score, total distance traveled and time spent immobile were analyzed. For the anxiety Z-score, the following parameters were included: time spent in the center and periphery, the ratio of time spent in the periphery to the center, distance traveled in the center and periphery, and the ratio of distance traveled in the periphery to the center.

In the same week, the elevated plus maze (EPM) test was performed, where mice were put in a closed arm of the EPM and their movement was tracked for 5 minutes.

Finally, from 7 to 8 weeks after treatment, marble-burying tests were performed. Mice were placed in a clean cage with fresh bedding (4-5 cm deep) and allowed to acclimate for 30 minutes. Then the mice were removed, the litter level was evened, and 20 glass marbles were dispersed in a grid pattern. The mice were put back in the experimental cages and were allowed to bury the marbles for 30 minutes. Mice were then removed, and the number of marbles buried by over 75% were manually assessed. The number of marbles buried was manually counted every 5 minutes from video recordings of the test.

At the end of each test and before the first test of the day, the apparatus was thoroughly cleaned using a detergent.

2.10 Statistics

Nonparametric Mann-Whitney bilateral tests were performed using the R language (version 4.4.0, used with R Studio software). Z-scores were calculated as described by Guilloux *et al.*, where several relevant parameters of the same test were averaged by first dividing each value by the average value of control untreated *Fmr1*$^{+/y}$ [56]. A p-value below 0.05 was considered significant.

3. RESULTS

3.1 FUS-BBBo induced strong and stable transgene expression

MRI scans conducted after the FUS-BBBo procedure demonstrated a significant uptake of Gd-DOTA in all treated mice (n = 41). The T1 contrast ratio following Gd/DOTA injection increased to an average of 1.342 +/- 0.029. Image analysis quantified that approximately 64.4 +/- 1.2% of total brain volume showed enhanced T1 signal, indicating a broad and successful opening of the blood-brain barrier (Figure 2). No significant differences in contrast ratio or BBBo volume were observed between groups treated with FUS-BBBo.

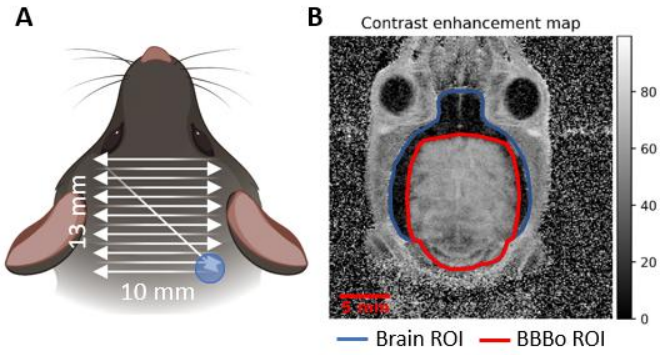

Figure 2: Whole brain BBBo (**A**) FUS probe pathway for whole brain FUS-BBBo procedure, blue circle: starting point. (**B**) T1 contrast enhancement map of FUS-BBBo mouse recorded with MRI and Gd-DOTA uptake, with ROI used for BBBo volume assessment and contrast enhancement measure.

In vivo bioluminescence of *Fmr1*$^{+/y}$ mice treated with FUS-BBBo and AAV-Luc injection revealed a significantly stronger signal in the brain 21 days after the procedure than mice with AAV-Luc injection only, with an over 20-fold increase (4.2×10^6 +/- 5.2×10^5 *vs*. 3.6×10^5 +/- 7.3×10^4 p/s/cm²/sr). Over time, bioluminescence following FUS-BBBo exhibited a significant signal increase between days 14 and 21 and reached its peak at 28 days post-treatment, rising from 1.9×10^6 +/- 4.2×10^5 to 6.2×10^6 +/- 2.1×10^5 p/s/cm²/sr. No significant difference was observed between the peak and the final timepoint at 53 days, where the signal stabilized at 5.8×10^6 +/- 1.3×10^5 p/s/cm²/sr, indicating sustained bioluminescence over time.

At the end of this expression kinetics (day 53), organs were harvested for *ex vivo* bioluminescence measurements. Organs from control mice (no FUS-BBBo treatment) were harvested at 21 days. No expression kinetics were assessed for this group. Similarly to *in vivo* measures, significantly stronger bioluminescence was observed in the FUS-BBBo group, showing over a 200-fold increase (Figure 3C). In other organs, bioluminescence was similar or lower with FUS-BBBo compared to AAV-Luc injection alone, indicating that total viral load was comparable. A near-significant reduction was observed in the liver (p = 0.052), with bioluminescence levels of 7.8×10^6 +/- 1.9×10^6 *vs*. 1.9×10^7 +/- 3.4×10^6 p/s/cm²/sr for treated and untreated mice respectively. Similar trends were seen in the heart, and significant reductions were detected in the pancreas, kidney, and spleen. Comparable bioluminescence levels between the two groups were observed only in the lungs and intestines (Figure S1).

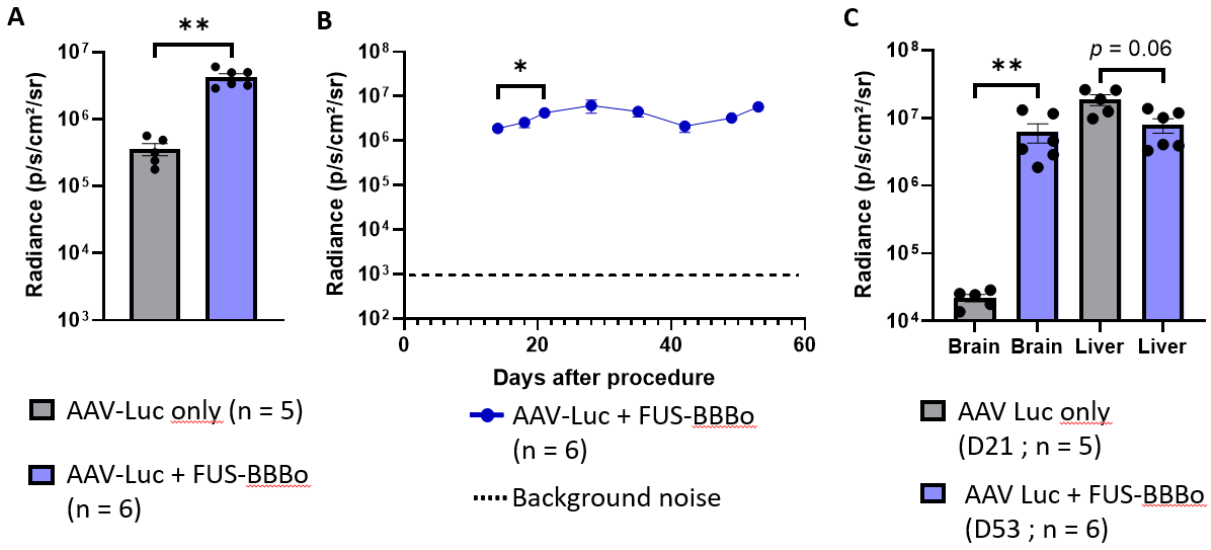

Figure 3: Transgene expression analysis of C57BL/6 *Fmr1*$^{+/y}$ mice following AAV2/9.CMV.Luciferase injection. (**A**) *In vivo* bioluminescence of mice 21 days after AAV-Luc injection with or without FUS-BBBo. (**B**) *In vivo* bioluminescence from 14 to 53 days after AAV-Luc injection and FUS-BBBo. (**C**) *Ex vivo* bioluminescence of mice's brains and livers at the end of respective expression kinetics, 21 days after AAV-Luc injection only or 53 days after AAV-Luc injection and FUS-BBBo. Data expressed as mean +/- SEM. * = *p*-value < 0.05; ** = *p*-value < 0.01; Mann-Whitney bilateral test.

3.2 FUS-BBBo induces FMRP expression without long-term damage

Mice brains treated with FUS-BBBo and AAV-*Fmr1* injection were further analyzed at the end of behavioral experiments. Additional treated *Fmr1*$^{+/y}$ mice were analyzed 21 days after treatment to investigate the biological effects of the procedure at the beginning of the behavioral experiments. H&E staining showed no visible hemorrhages or local immune cell recruitments in treated *Fmr1*$^{-/y}$ mice or *Fmr1*$^{+/y}$ mice (Figure 4 A). T2-weighted images confirmed the absence of edema or hemorrhages in all FUS-BBBo-treated mice (Figure 4.B). In addition, RT-qPCR analysis showed no significant difference in the expression of CCL2, GFAP, or Iba1 biomarkers between treated and control groups (Figure 4 C-E) suggesting an absence of a neuroinflammatory effect of the FUS-BBBo method.

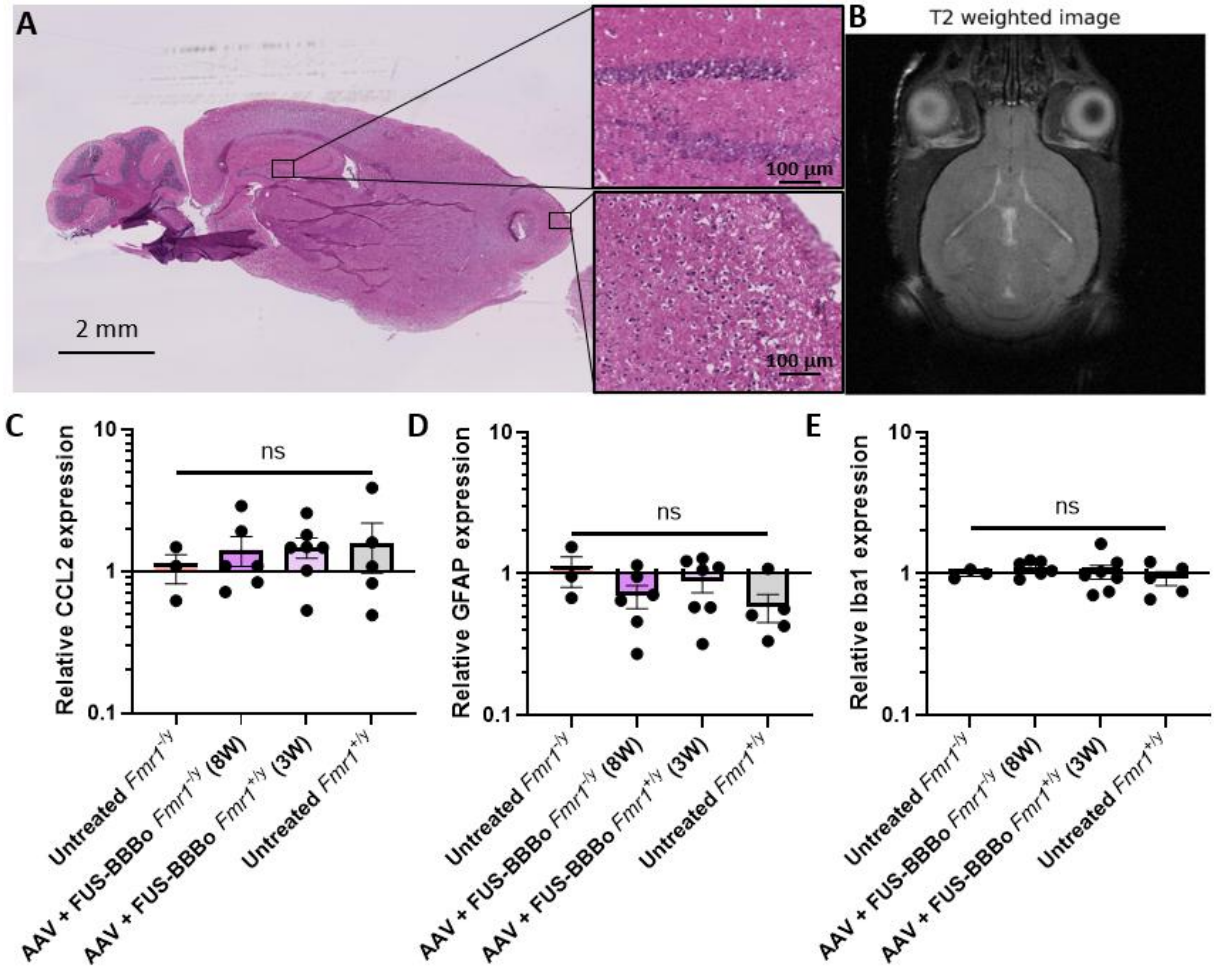

Figure 4: Long-term safety assessment of FUS-BBBo procedure. (**A**) H&E staining of *Fmr1*$^{-/y}$ mice 8 weeks after the FUS-BBBo procedure and zoom in on the hippocampus and prefrontal cortex area. (**B**) T2-weighted image of the same FUS-BBBo mouse showing no edema or hemorrhages. (**C**) Relative expression of CCL2 in control untreated mice and mice treated with FUS-BBBo and AAV-*Fmr1* injection, assessed in RT-qPCR 3 or 8 weeks after treatment. (**D**) Relative expression of GFAP in control untreated mice and mice treated with FUS-BBBo and AAV-*Fmr1* injection, assessed in RT-qPCR 3 or 8 weeks after treatment (**E**) Relative expression of Iba1 in control untreated mice and mice treated with FUS-BBBo and AAV-*Fmr1* injection, assessed in RT-qPCR 3 or 8 weeks after treatment. Data expressed as mean +/- SEM. ns = p-value > 0.05; Mann-Whitney bilateral test.

Immunohistochemistry analysis in *Fmr1*$^{-/y}$ mice revealed widespread restoration of FMRP expression throughout the brain, with variations observed depending on region and on treated mouse. FMRP-expressing cells can be observed in several brain regions, including the cortex and hypothalamus in all examined mice, and more episodically in the hippocampus

(one out of three mice). FMRP-expressing cells appeared in clusters across brain slices but were not uniformly distributed (Figure 5). Most of these cells colocalized with NeuN, indicating predominant restored expression in neurons. High-magnification analysis revealed a predominantly perinuclear, punctate staining pattern, except in the hypothalamus, where cytoplasmic localization predominated. Additionally, some endothelial-like cells expressing FMRP were observed, as suggested by their shape, distributed more homogeneously throughout the brain (data not shown).

RT-qPCR analysis showed *Fmr1* expression in *Fmr1*$^{-/y}$ treated mice of 15.2 +/- 7.6 % compared to *Fmr1*$^{+/y}$ expression (Figure 5.C). These data also revealed substantial inter-individual variability in rescued *Fmr1* expression, ranging from 2.8 to 50.5% of *Fmr1*$^{+/y}$ levels. In addition, due to the low efficiency of the FUS-BBBo method, the treatment did not allow the detection of an Fmr1 overexpression linked to transgene expression in the *Fmr1*$^{+/y}$ group.

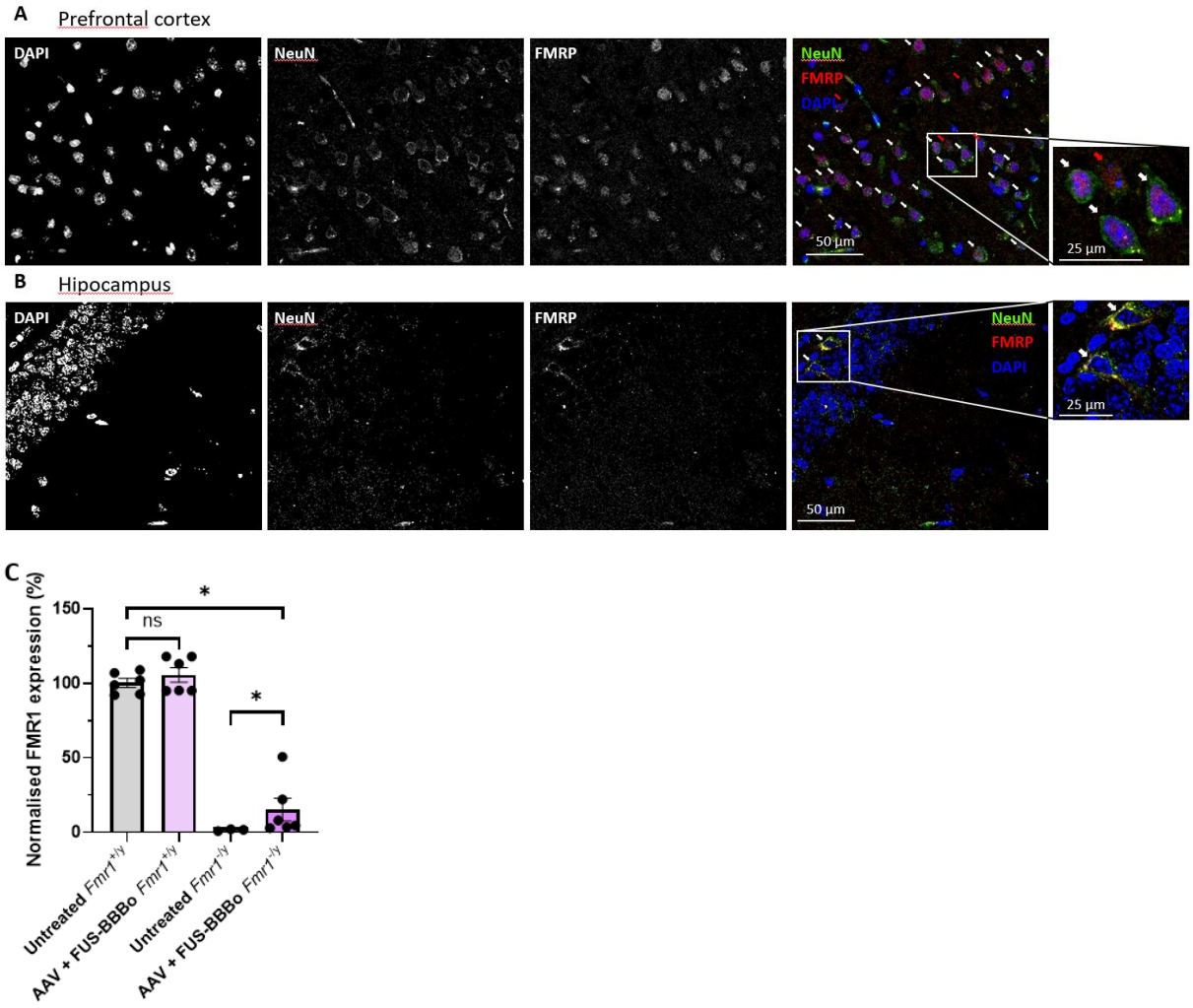

Figure 5: *Fmr1* transgene expression analyses. (**A**) Immunohistochemistry of FMRP protein on a sagittal cut of treated *Fmr1*$^{-/y}$ mice. (**green**: NeuN; **red**: FMRP; **blue**: DAPI; white arrow: FMRP+ and NeuN+ cell; red arrow: FRMP+ and NeuN- cell) (**B**) Immunohistochemistry of FMRP protein on a sagittal cut of treated *Fmr1*$^{-/y}$ mice 8 weeks after FUS-BBBo and AAV injection. (**green**: NeuN; **red**: FMRP; **blue**: DAPI) (**C**) *Fmr1* mRNA expression normalized on control untreated *Fmr1*$^{+/y}$ mice of mice treated with FUS-BBBo and AAV-*Fmr1* injection. Data expressed as mean +/- SEM. * = p-value < 0.05; Mann-Whitney bilateral test.

3.3 FUS-BBBo and FMRP expression rescues several phenotypes in *Fmr1*-KO mice

Mice behavior following FUS-BBBo and AAV-*Fmr1* injection was evaluated and compared to untreated *Fmr1*$^{-/y}$ mice, *Fmr1*$^{-/y}$ mice treated with FUS-BBBo only, and untreated *Fmr1*$^{+/y}$ mice as controls. At first, the locomotion was assessed using the distance travelled in an open field for 5 minutes. Untreated *Fmr1*$^{-/y}$ mice travelled significantly greater distances than untreated *Fmr1*$^{+/y}$ mice, reaching 27.1 +/- 1.4 and 22.1 +/- 1.29 m, respectively. Both treatment groups exhibited a significant decrease in distance travelled to levels comparable to *Fmr1*$^{+/y}$ mice, with values of 22.7 +/- 1.9 for the FUS-BBBo-only group and 21.0 +/- 1.1 m for FUS-BBBo combined with AAV injection (Figure 6.A). Using the Z-score of this locomotion parameter, a significant reduction to *Fmr1*$^{+/y}$ values in both treated groups in the open field was observed, but it was not significant with the FUS-BBBo treatment alone (Figure 6.B).

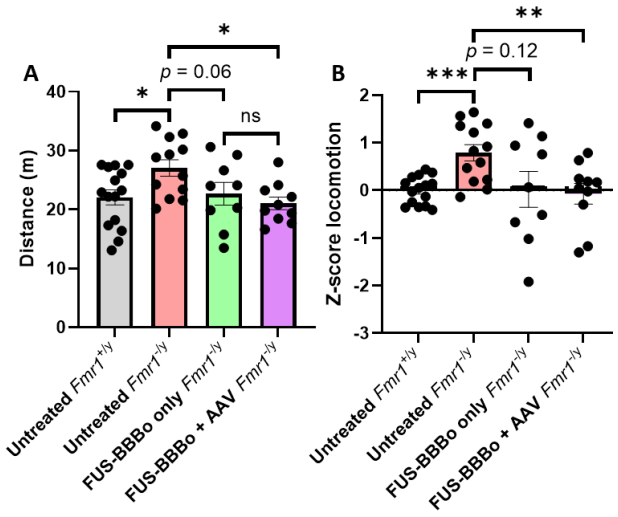

Figure 6: *Fmr1*$^{-/y}$ mice hyperactivity phenotype over *Fmr1*$^{+/y}$ mice and partial rescue of FUS-BBBo and FMRP expression. (**A**) Total distance travelled in the open field in 5 minutes. (**B**) Z-scores of locomotion parameters in the open field. Data expressed as mean +/- SEM. * = p-value < 0.05; ** = p-value < 0.01; *** = p-value < 0.001; Mann-Whitney bilateral test.

Then, the marble-burying test was used to analyze the anxiety state of mice. First, data showed a significantly lower number of marbles buried over time in untreated *Fmr1*$^{-/y}$ mice compared to untreated *Fmr1*$^{+/y}$ mice, with a calculated area under the curve of 302.7 +/- 24.93 and 373.5 +/- 16.29 A.U., respectively. FUS-BBBo treatment increased the number of marbles buried, though not significantly, with an area under the curve of 341.1 +/- 25.64 A.U. Only the treatment with AAV injection demonstrated a significant increase in marbles buried over time,

reaching *Fmr1*$^{+/y}$ value with an area under the curve of 374.8 +/- 21.24 A.U. (Figure 7A). Similarly, in the elevated plus maze, we can observe an almost significant increase in the percentage of time spent in open arms of untreated *Fmr1*$^{-/y}$ mice compared to untreated *Fmr1*$^{+/y}$ mice, reaching 23.5 +/- 3.3 and 15.7 +/- 2.4 % respectively. Both treated groups show an almost significant decrease to *Fmr1*$^{+/y}$ values, getting down to 15.6 +/- 2.8 and 15.8 +/- 2.4 % without or with AAV (Figure 7B).

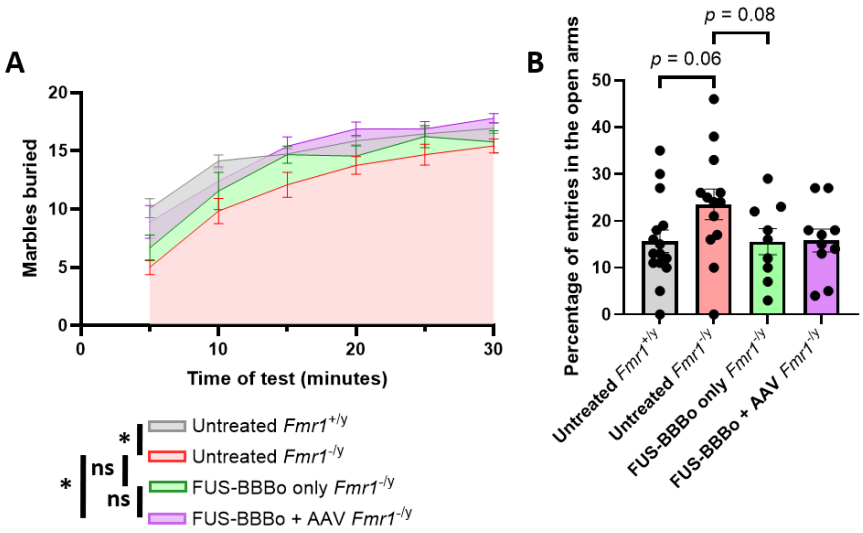

Figure 7: *Fmr1*$^{-/y}$ anxiolysis phenotype over *Fmr1*$^{+/y}$ mice and partial rescue of FUS-BBBo and FMRP expression. (**A**) Number of marbles buried every 5 minutes in the marbles burying test. (**B**) Percentage of entries in the novel arm over 5 minutes in the elevated plus maze. Data expressed as mean +/- SEM. * = p-value < 0.05; ** = p-value < 0.01; Mann-Whitney bilateral test.

The social behavior of mice was assessed using the direct interaction test. Compared to untreated *Fmr1*$^{+/y}$, untreated *Fmr1*$^{-/y}$ mice showed a significantly higher time spent in social interaction, reaching 69.7 +/- 12.09 and 116.8 +/- 14.12 seconds, respectively. This time is decreased, with a close significance, with both treatments, getting down to 74.9 +/- 13.8 and 81.0 +/- 14.7 seconds without or with AAV (Figure 8A). The Z score including additional social parameters, confirmed these results, with a significant difference in the Z-score values from untreated *Fmr1*$^{-/y}$ mice compared to untreated *Fmr1*$^{+/y}$ mice. Both treatments resulted in Z-scores approaching significance compared to *Fmr1*$^{+/y}$ values.

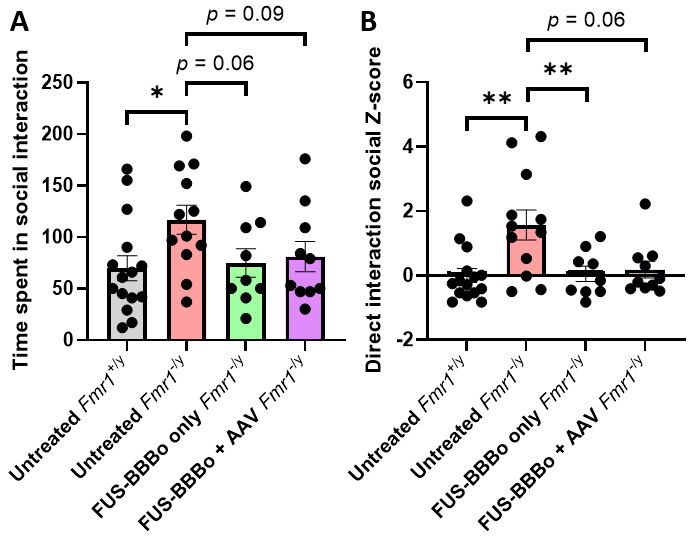

Figure 8: *Fmr1*$^{-/y}$ social impairment phenotype and partial rescue after FUS-BBBo treatment and FMRP expression. (**A**) Total time spent in active social interaction of mice with a stimulus mouse during the direct interaction test. (**B**) Z-score of social parameters in the direst interaction test. Data expressed as mean +/- SEM. * = p-value < 0.05; ** = p-value < 0.01; Mann-Whitney bilateral test.

4. DISCUSSION

Focused ultrasound drug delivery in the brain is gaining increasing interest due to its ability to precisely target specific tissue without damaging the surrounding area. Its application in gene therapy represents a promising approach for treating monogenic CNS disorders such as FXS by enabling their restoration of the missing gene expression. Such disease needs to be treated in the whole CNS to ensure optimal therapeutic effect, but developing an effective delivery method remains a major challenge. As a proof of concept, we performed whole-brain BBBo with FUS and MB combined with the injection of *Fmr1*-coding AAV. We then analyzed the transgene expression and the procedure's effect on behavior in the FXS mouse model.

For this purpose, we applied a displacement of the FUS probe during a FUS-BBBo protocol, as previously described by Felix *et al.*, achieving BBBo in approximately 60 % of the brain in our experimental process [50]. This protocol resulted in a strong luciferase transgene

expression, significantly higher than the expression with AAV-Luc injection alone, both *in vivo* and *ex vivo*. Surprisingly, while the expression *in vivo* from AAV-Luc alone seemed much stronger than background values, the expression *ex vivo* was extremely low and close to background values. This suggests a detection *in vivo* of other organs with high expression, like the liver or the heart in the AAV-Luc only group (Figure S1). Conversely, the *in vivo* bioluminescence signal detected following FUS-BBBo and AAV-Luc injection was confirmed with a strong signal *ex vivo*, significantly as strong as the signal in the liver, an organ that naturally gets highly transduced by AAV due to its clearance role. The bioluminescence signal over time was relatively stable, but *in vivo* measurement was challenging at some timepoints due to fur regrowth and melanin pigmentation leading to slight variations of signal [57]. However, we show no significant variations of bioluminescence from 21 to 53 days after the procedure, confirming the stable transgene expression. On another part, for the AAV-only group, organs were harvested at 21 days due to the lack of expression and to avoid unnecessary intervention on mice. Therefore, *ex vivo* bioluminescence comparisons between the two groups are challenging, as organs from the FUS-BBBo group were harvested at the end of the expression kinetic study, 53 days post-procedure. Although bioluminescence appears lower in most untargeted organs in the FUS-BBBo group, which is unexpected since brain expression remains stable from 21 to 53 days *in vivo*. There are two possible explanations for this: either untargeted organs follow a different expression kinetic than the brain after FUS-BBBo, or fewer viral vectors reached untargeted organs due to viral vectors entering the brain. This would mean that in addition to allowing gene expression in the brain, FUS-BBBo also reduces off-target transgene expression.

In order to be able to transfer our therapeutic strategy to clinical applications, we first need to control its safety. Short-term safety was addressed with T2 MRI and daily clinical scoring. Even though no damage was observed in MRI on any mice, 16% of mice showed signs of slight discomfort at 24 h post-treatment, and we observed unexpected mortality in the hours following the FUS-BBBo procedure in 19 % of mice. This mortality is equally distributed between groups treated with FUS-BBBo, suggesting that this was not an effect of the genotype nor the AAV injection. This was not expected as it is not observed in other studies even when damages are visible with MRI. Knowing that no edema nor hemorrhages were detectable with T2-weighted images is it unlikely that this mortality occurred due to brain damage. It is more

likely that severe brain inflammation following BBB opening or seizure induction contributed to this mortality, as BBB opening can promote seizures in some conditions [58–60]. However, Mathon *et al*. showed that FUS-BBBo does not promote seizures with their parameters [61]. We hypothesized that changing our FUS-BBBo parameters could mitigate this reaction. On another part, a slight weight loss was observed 24 h post-treatment in *Fmr1*$^{-/y}$ mice treated with FUS-BBBo/AAV-*Fmr1* compared to those treated with FUS-BBBo alone. This weight loss was recovered at 48 h post-treatment, suggesting a transient neuroinflammation response potentially induced by AAV injection (Figure S2).

Due to the need to allow time for the transgene to be expressed, the long-term safety was assessed at two distinct time points, at 3 weeks post-procedure and at the end of behavioral experiments (8 weeks post-procedure). Thus, it allows us to assess the effect of FUS-BBBo with AAV-*Fmr1* injection on neuroinflammation and brain damage in the same range of days post-procedure as behavioral experiments. H&E staining confirmed the absence of microhemorrhages observed with T2-weighted MRI images in all mice studied, both 3 weeks and 8 weeks post-procedure. This shows that transitory brain damage (if it occurred) that could have been generated during the initial procedure was limited enough and transitory enough to not be detected in MRI and was resorbed in less than 3 weeks. Similarly, RT-qPCR assays demonstrated an absence of a permanent neuroinflammatory state based on the expression of our studied biomarkers. In fact, CCL2 expression was not disrupted 3 or 8 weeks after the procedure, whereas it was described as overexpressed in a manner dependent on the FUS-BBBo procedure's intensity [62]. Furthermore, no evidence of persistent glial reactivity was demonstrated, as indicated by the absence of significant changes in GFAP expression, a marker for astrocytes, and Iba-1 expression, a marker for microglia. Long-term safety was further supported by the monitoring of the mice's well-being. Daily scoring from 24 hours to 3 weeks post-procedure revealed no signs of discomfort, with no adverse effects observed at 7 weeks.

Immunohistology and RT-qPCR further confirmed transgene expression with the AAV-*Fmr1* vector, therefore validating the proof of concept of our method to re-express FMRP in the CNS. Expression levels of the transgene may require further optimization to achieve optimal therapeutic efficacy, as initially indicated by RT-qPCR showing a significantly lower rescued expression compared to *Fmr1*$^{+/y}$, with a substantial variability, ranging from 4 to 50 %

of *Fmr1*$^{+/y}$ expression. Similarly, immunohistochemistry shows scarce expression through the brain, with clusters in some brain regions. In these areas, FMRP expression was primarily observed in neurons, as indicated by co-localization with NeuN. The other FMRP-positive cells likely represent glial cell populations. FMRP expression appears to be mostly perinuclear, except in the hippocampus, where FMRP+ cells show cytoplasmic FMRP expression. The localization patterns of FMRP suggest that its subcellular distribution is influenced by the cell type transduced. This finding indicates that the transgene-encoded FMRP may exhibit differential biological activities. FMRP expression was also observed in endothelial-like cells throughout the brain, suggesting efficient AAV transduction of these cells following FUS-BBBo stimulation, as expected given the sonoporative effects of FUS-BBBo. Although immunohistochemistry revealed a relatively low transgene expression rate, it is likely that a significant number of FMRP-positive cells with low levels of transgene expression were undetected due to the limitations of the method's sensitivity. This hypothesis is supported by the observed variability in transgene *Fmr1* expression levels measured by RT-qPCR, which was 50- to 2-fold lower than that in *Fmr1* +/y mice. This suggests that FMRP re-expression should be in a larger population of cells potentially varying across individual mice and brain regions. Further experiments employing in situ hybridization, a more sensitive technique, are warranted to refine these hypotheses.

Finally, we studied the effect of the FUS-BBBo procedure associated with the AAV vector on *Fmr1*-KO mice behavior in order to assess the therapeutic potential of our procedure. Firstly, we focused on the robust hyperactivity phenotype of *Fmr1*$^{-/y}$ mice usually assessed by exposition to a novel environment such as an open field [34,63,64]. This phenotype was minimally affected by the FUS-BBBo procedure alone. However, significant behavioral rescue was observed following AAV-*Fmr1* administration using the FUS-BBBo method. These findings suggest that even modest levels of transgene *Fmr1* expression in the brain can exert beneficial effects. This is particularly promising given the significant impact of this phenotype on a range of other deficits, including emotional and cognitive impairments [65].

The anxiety-related behaviors were also successfully observed using the marble-burying test and elevated plus maze. *Fmr1*$^{-/y}$ mice exhibited reduced anxiety, illustrated by a lower anxiety-driven marble burying over time and higher exploration of open arms [33,66]. The marble-burying test also shows a significant effect of AAV-*Fmr1* expression on anxiety as only

the treatment with AAV-*Fmr1* shows a significant rescue to *Fmr1*$^{+/y}$ values. However, we must note that the FUS-BBBo itself showed a slight rescue with no significant difference with AAV-*Fmr1* treatment. These observations suggest that the impact of FMRP re-expression on the emotional part of the *Fmr1* phenotype may be limited. The beneficial effects observed could be primarily attributed to the FUS-BBBo procedure itself. This hypothesis was supported by elevated plus maze tests, which also demonstrated a partial rescue of the phenotype following FUS-BBBo treatment alone. Thereafter, the direct social interaction test was performed. Even though the social impairment phenotype of *Fmr1*$^{-/y}$ mice is generally described as a reduction of social affiliation of *Fmr1*$^{-/y}$ mice [33,67], we show here instead a significant increase of social interaction. A similar observation has been previously reported [63]. Indeed, the investigation of social behaviors is known to often be complicated by their inherent complexity and their dependence on the environmental context, such as housing conditions. Nevertheless, a clear disturbance in social behavior was observed in *Fmr1*$^{-/y}$ mice, and this impairment was rescued to *Fmr1*$^{+/y}$ levels in both treated groups. We observed that FUS-BBBo treatment was sufficient to significantly improve the social defects related to emotional behavior. This rescue, partially observed in all studied behavior after FUS-BBBo treatment, may be related to its demonstrated beneficial effects in Alzheimer's disease [68–70]. Indeed, when used as a treatment for this disease, FUS-BBBo induces a clearance of amyloid beta in the brains of rodent models [71–74]. This therapeutic strategy is currently used in clinical trials for Alzheimer’s disease showing promising effects [75–77]. Importantly, amyloid-beta and phosphorylated tau are also overexpressed in FXS, and silencing APP, the amyloid-beta precursor, has demonstrated therapeutic effects on anxiety behavior [78]. Based on these findings, we hypothesized that the observed anxiety-reducing effects of the FUS-BBBo procedure might be mediated, at least in part, by enhanced amyloid clearance. However, it is important to note that effective Alzheimer's disease therapies often require repeated treatments [71–73], unlike our single FUS-BBBo application. Remarkably, we observed a rescue of anxiety and social behavior after a single FUS-BBBo exposure, with therapeutic effects persisting for at least 8 weeks. Further investigation is warranted to assess amyloid-beta clearance and other relevant biomarkers following our protocol to elucidate the precise mechanisms underlying FUS-BBBo's beneficial effects.

Compared to other FXS gene therapy strategies, we show a lower transduction rate and transgene expression [32,34,35]. A recent study by Chadman *et al.* showed a similar strategy of whole-brain gene therapy in the adult mouse brain, but using a mouse-specific AAV.PHP.B vector able to efficiently transfect brains without BBB opening [34]. They induced a much stronger expression of FMRP compared to our study, reaching *Fmr1*$^{+/y}$ level or higher, and showed a significant effect of transgene *Fmr1* expression on motor learning and fear conditioning. Our data suggest that achieving a substantial increase in FMRP expression within our experimental model could lead to significant therapeutic effects across a range of behavioral deficits, encompassing social, cognitive, and emotional domains.

Our limited FMRP expression could be assessed by improving BBBo, with a higher acoustic pressure, MB dose, or with further optimized acoustic pulses [79,80]. In addition, the AAV dose should be higher to increase transduction rate and transgene expression. As compared to other FUS-BBBo studies, we used a relatively low amount of AAV, which has been used in the range of 1×10^{11} to 5.5×10^{11} vg [50,81–86]. Indeed, Nouraein *et al.* showed their ability to reach up to 60 % widespread transduction rate through the brain with a lower mechanical index (0.21) and over twice as much AAV as in this study [85]. We can also use a different capsid, like an AAV specific to BBBo, as developed by Li *et al.*, that can also greatly improve transduction rate and transgene expression [84,87,88]. Another possible improvement would be the use of non-viral strategies, like cationic microbubbles, that could be used several times to improve transgene expression [52,89,90]. Furthermore, while our procedure was performed on adult mice, earlier intervention in juveniles might yield even greater therapeutic benefits, as suggested by previous studies [32,35,91]. In addition, to improve safety, we could also use cavitation-feedback monitoring, allowing us to avoid excessive inertial cavitation and severe BBBo [92,93]. All of these parameters clearly impact therapeutic efficacy, and further experiments are necessary to improve the effectiveness, stability, and reproducibility of our therapeutic strategy.

Compared to other studies employing gene therapy in rodent models of FXS, which often utilized more invasive methods such as intracranial injections, only partial behavioral rescue was also obtained despite higher FMRP expression [32–35]. Our study marks a significant breakthrough by demonstrating the positive impact of the FUS-BBBo method itself on the behavior of *Fmr1*-KO mice. This innovative approach, combined with AAV gene therapy,

offers a promising avenue for future therapeutic development, although further technological refinements are necessary.

ACKNOLEDGEMENT

The authors are thankful to David GOSSET from the platform MO2VING and to Sebastien RIGOLLET and Vasile STUPAR from the platform IRMaGe for their precious help and insight.

5. BIBLIOGRAPHY

1. Crawford, D.C.; Acuña, J.M.; Sherman, S.L. FMR1 and the Fragile X Syndrome: Human Genome Epidemiology Review. Genetics in Medicine 2001, 3, 359–371.

2. Brasa, S.; Mueller, A.; Jacquemont, S.; Hahne, F.; Rozenberg, I.; Peters, T.; He, Y.; McCormack, C.; Gasparini, F.; Chibout, S.D.; et al. Reciprocal Changes in DNA Methylation and Hydroxymethylation and a Broad Repressive Epigenetic Switch Characterize FMR1 Transcriptional Silencing in Fragile X Syndrome. Clin Epigenetics 2016, 8, doi:10.1186/s13148-016-0181-x.

3. Tassone, F.; Hagerman, P.J. Expression of the FMR1 Gene. Cytogenet Genome Res 2003, 100, 124–128, doi:10.1159/000072846.

4. Ludwig, A.L.; Espinal, G.M.; Pretto, D.I.; Jamal, A.L.; Arque, G.; Tassone, F.; Berman, R.F.; Hagerman, P.J. CNS Expression of Murine Fragile X Protein (FMRP) as a Function of CGG-Repeat Size. Hum Mol Genet 2014, 23, 3228–3238, doi:10.1093/hmg/ddu032.

5. Nolin, S.L.; Brown, W.T.; Glicksman, A.; Houck, G.E.; Gargano, A.D.; Sullivan, A.; Biancalana, V.; Bröndum-Nielsen, K.; Hjalgrim, H.; Holinski-Feder, E.; et al. Expansion of the Fragile X CGG Repeat in Females with Premutation or Intermediate Alleles; 2003; Vol. 72;.

6. Mientjes, E.J.; Nieuwenhuizen, I.; Kirkpatrick, L.; Zu, T.; Hoogeveen-Westerveld, M.; Severijnen, L.; Rifé, M.; Willemsen, R.; Nelson, D.L.; Oostra, B.A. The Generation of a Conditional Fmr1 Knock out Mouse Model to Study Fmrp Function in Vivo. Neurobiol Dis 2006, 21, 549–555, doi:10.1016/j.nbd.2005.08.019.

7. Doll, C.A.; Scott, K.; Appel, B. Fmrp Regulates Oligodendrocyte Lineage Cell Specification and Differentiation. Glia 2021, 69, 2349–2361, doi:10.1002/glia.24041.

8. Bülow, P.; Zlatic, S.A.; Wenner, P.A.; Bassell, G.J.; Faundez, V. FMRP Attenuates Activity Dependent Modifications in the Mitochondrial Proteome. Mol Brain 2021, 14, doi:10.1186/s13041-021-00783-w.

9. Ascano, M.; Mukherjee, N.; Bandaru, P.; Miller, J.B.; Nusbaum, J.D.; Corcoran, D.L.; Langlois, C.; Munschauer, M.; Dewell, S.; Hafner, M.; et al. FMRP Targets Distinct MRNA Sequence Elements to Regulate Protein Expression. Nature 2012, 492, 382–386, doi:10.1038/nature11737.

10. Wang, X.; Zorio, D.A.R.; Schecterson, L.; Lu, Y.; Wang, Y. Postsynaptic FMRP Regulates Synaptogenesis in Vivo in the Developing Cochlear Nucleus. Journal of Neuroscience 2018, 38, 6445–6460, doi:10.1523/JNEUROSCI.0665-18.2018.

11. Watkins, L. V.; Moon, S.; Burrows, L.; Tromans, S.; Barwell, J.; Shankar, R. Pharmacological Management of Fragile X Syndrome: A Systematic Review and Narrative Summary of the Current Evidence. Expert Opin Pharmacother 2024, 25, 301–313.

12. Berry-Kravis, E.; Hagerman, R.; Visootsak, J.; Budimirovic, D.; Kaufmann, W.E.; Cherubini, M.; Zarevics, P.; Walton-Bowen, K.; Wang, P.; Bear, M.F.; et al. Arbaclofen in Fragile X Syndrome: Results of Phase 3 Trials. J Neurodev Disord 2017, 9, doi:10.1186/s11689-016-9181-6.

13. Potter, L.A.; Scholze, D.A.; Biag, H.M.B.; Schneider, A.; Chen, Y.; Nguyen, D. V.; Rajaratnam, A.; Rivera, S.M.; Dwyer, P.S.; Tassone, F.; et al. A Randomized Controlled Trial of Sertraline in Young Children With Autism Spectrum Disorder. Front Psychiatry 2019, 10, doi:10.3389/fpsyt.2019.00810.

14. Sahu, J.K.; Gulati, S.; Sapra, S.; Arya, R.; Chauhan, S.; Chowdhury, M.R.; Gupta, N.; Kabra, M.; Gupta, Y.K.; Dwivedi, S.N.; et al. Effectiveness and Safety of Donepezil in Boys with Fragile x Syndrome: A Double-Blind, Randomized, Controlled Pilot Study. J Child Neurol 2013, 28, 570–575, doi:10.1177/0883073812449381.

15. Leigh, M.J.S.; Nguyen, D. V.; Mu, Y.; Winarni, T.I.; Schneider, A.; Chechi, T.; Polussa, J.; Doucet, P.; Tassone, F.; Rivera, S.M.; et al. A Randomized Double-Blind, Placebo-Controlled Trial of Minocycline in Children and Adolescents with Fragile x Syndrome. Journal of Developmental and Behavioral Pediatrics 2013, 34, 147–155, doi:10.1097/DBP.0b013e318287cd17.

16. Berry-Kravis, E.; Des Portes, V.; Hagerman, R.; Jacquemont, S.; Charles, P.; Visootsak, J.; Brinkman, M.; Rerat, K.; Koumaras, B.; Zhu, L.; et al. Mavoglurant in Fragile X Syndrome: Results of Two Randomized, Double-Blind, Placebo-Controlled Trials. Sci Transl Med 2016, 13.

17. Youssef, E.A.; Berry-Kravis, E.; Czech, C.; Hagerman, R.J.; Hessl, D.; Wong, C.Y.; Rabbia, M.; Deptula, D.; John, A.; Kinch, R.; et al. Effect of the MGluR5-NAM Basimglurant on Behavior in Adolescents and Adults with Fragile X Syndrome in a Randomized, Double-Blind, Placebo-Controlled Trial: FragXis Phase 2 Results. Neuropsychopharmacology 2018, 43, 503–512, doi:10.1038/npp.2017.177.

18. Berry-Kravis, E.M.; Harnett, M.D.; Reines, S.A.; Reese, M.A.; Ethridge, L.E.; Outterson, A.H.; Michalak, C.; Furman, J.; Gurney, M.E. Inhibition of Phosphodiesterase-4D in Adults with Fragile X Syndrome: A Randomized, Placebo-Controlled, Phase 2 Clinical Trial. Nat Med 2021, 27, 862–870, doi:10.1038/s41591-021-01321-w.

19. Berry-Kravis, E.; Horrigan, J.P.; Tartaglia, N.; Hagerman, R.; Kolevzon, A.; Erickson, C.A.; Hatti, S.; Snape, M.; Yaroshinsky, A.; Stoms, G.; et al. A Double-Blind, Randomized, Placebo-Controlled Clinical Study of Trofinetide in the Treatment of Fragile X Syndrome. Pediatr Neurol 2020, 110, 30–41, doi:10.1016/j.pediatrneurol.2020.04.019.

20. Berry-Kravis, E.; Hagerman, R.; Budimirovic, D.; Erickson, C.; Heussler, H.; Tartaglia, N.; Cohen, J.; Tassone, F.; Dobbins, T.; Merikle, E.; et al. A Randomized, Controlled Trial of ZYN002 Cannabidiol Transdermal Gel in Children and Adolescents with Fragile X Syndrome (CONNECT-FX). J Neurodev Disord 2022, 14, doi:10.1186/s11689-022-09466-6.

21. Wirojanan, J.; Jacquemont, S.; Goodlin-Jones, B.L. The Efficacy of Melatonin for Sleep Problems in Children with Autism, Fragile X Syndrome, or Autism and Fragile X Syndrome. Journal of clinical sleep medicine 2009, 5.

22. Hagerman, R.J.; Murphy, M.A.; Wittenberger, M.D. A CONTROLLED TRIAL OF STIMULANT MEDICATION IN CHILDREN WITH THE. Am J Med Genet 1988, 377–392.

23. Pardridge, W.M. The Blood-Brain Barrier: Bottleneck in Brain Drug Development. The American Society for Experimental NeuroTherapeutics 2005, 2, 3–14.

24. Fischer, H.; Gottschlich, R.; Seelig, A. Blood-Brain Barrier Permeation: Molecular Parameters Governing Passive Diffusion. J. Membrane Biol. 1998, 165, 201–211.

25. Pardridge, W.M. Drug Transport across the Blood-Brain Barrier. Journal of Cerebral Blood Flow and Metabolism 2012, 32, 1959–1972.

26. Ghose, A.K.; Viswanadhan, V.N.; Wendoloski, J.J. A Knowledge-Based Approach in Designing Combinatorial or Medicinal Chemistry Libraries for Drug Discovery. 1. A Qualitative and Quantitative Characterization of Known Drug Databases. J Comb Chem 1999, 1, 55–68, doi:10.1021/cc9800071.

27. Zhang, S.; Gan, L.; Cao, F.; Wang, H.; Gong, P.; Ma, C.; Ren, L.; Lin, Y.; Lin, X. The Barrier and Interface Mechanisms of the Brain Barrier, and Brain Drug Delivery. Brain Res Bull 2022, 190, 69–83, doi:10.1016/j.brainresbull.2022.09.017.

28. Eng, M.E.; Imperio, G.E.; Bloise, E.; Matthews, S.G. ATP-Binding Cassette (ABC) Drug Transporters in the Developing Blood–Brain Barrier: Role in Fetal Brain Protection. Cellular and Molecular Life Sciences 2022, 79.

29. Farquhar, M.G.; Palade, G.E. Junctional Complexes in Various Epithelia. J Cell Biol 1963, 375–412.

30. Heinemann, U.; Schuetz, A. Structural Features of Tight-Junction Proteins. Int J Mol Sci 2019, 20.

31. Sugiyama, S.; Sasaki, T.; Tanaka, H.; Yan, H.; Ikegami, T.; Kanki, H.; Nishiyama, K.; Beck, G.; Gon, Y.; Okazaki, S.; et al. The Tight Junction Protein Occludin Modulates Blood–Brain Barrier Integrity and Neurological Function after Ischemic Stroke in Mice. Sci Rep 2023, 13, doi:10.1038/s41598-023-29894-1.

32. Hooper, A.W.M.; Wong, H.; Niibori, Y.; Abdoli, R.; Karumuthil-Melethil, S.; Qiao, C.; Danos, O.; Bruder, J.T.; Hampson, D.R. Gene Therapy Using an Ortholog of Human Fragile X Mental Retardation Protein Partially Rescues Behavioral Abnormalities and EEG Activity. Mol Ther Methods Clin Dev 2021, 22, 196–209, doi:10.1016/j.omtm.2021.06.013.

33. Jiang, Y.; Han, L.; Meng, J.; Wang, Z.; Zhou, Y.; Yuan, H.; Xu, H.; Zhang, X.; Zhao, Y.; Lu, J.; et al. Gene Therapy Using Human FMRP Isoforms Driven by the Human FMR1 Promoter Rescues Fragile X Syndrome Mouse Deficits. Mol Ther Methods Clin Dev 2022, 27, 246–258, doi:10.1016/j.omtm.2022.10.002.

34. Chadman, K.K.; Adayev, T.; Udayan, A.; Ahmed, R.; Dai, C.L.; Goodman, J.H.; Meeker, H.; Dolzhanskaya, N.; Velinov, M. Efficient Delivery of FMR1 across the Blood Brain Barrier Using AAVphp Construct in Adult FMR1 KO Mice Suggests the Feasibility of Gene Therapy for Fragile X Syndrome. Genes (Basel) 2023, 14, doi:10.3390/genes14020505.

35. Wong, H.; Hooper, A.W.M.; Kang, H.R.; Lee, S.J.; Zhao, J.; Sadhu, C.; Rawat, S.; Gray, S.J.; Hampson, D.R. CNS-Dominant Human FMRP Isoform Rescues Seizures, Fear, and Sleep Abnormalities in Fmr1-KO Mice. 2023, doi:10.1172/jci.

36. Hynynen, K.; McDannold, N.; Vykhodtseva, N.; Jolesz, F.A. Noninvasive MR Imaging-Guided Focal Opening of the Blood-Brain Barrier in Rabbits. Radiology 2001, 220, 640–646, doi:10.1148/radiol.2202001804.

37. Dauba, A.; Delalande, A.; Kamimura, H.A.S.; Conti, A.; Larrat, B.; Tsapis, N.; Novell, A. Recent Advances on Ultrasound Contrast Agents for Blood-Brain Barrier Opening with Focused Ultrasound. Pharmaceutics 2020, 12, 1–30.

38. Meng, Y.; Hynynen, K.; Lipsman, N. Applications of Focused Ultrasound in the Brain: From Thermoablation to Drug Delivery. Nat Rev Neurol 2021, 17, 7–22.

39. Meng, Y.; Goubran, M.; Rabin, J.S.; Mcsweeney, M.; Ottoy, J.; Pople, C.B.; Huang, Y.; Storace, A.; Ozzoude, M.; Bethune, A.; et al. Blood-Brain Barrier Opening of the Default Mode Network in Alzheimer's Disease with Magnetic Resonance-Guided Focused Ultrasound. Brain 2023, 146, 865–872, doi:10.1093/brain/awac459.

40. 'Estifeeva, T.M. 'Barmin, R.A. 'Rudakovskaya, P.G. 'Gorin, D.A. Hybrid (Bovine Serum Albumin)/Poly(N-Vinyl-2-Pyrrolidone- Co-Acrylic Acid)-Shelled Microbubbles as Advanced Ultrasound Contrast Agents. ACS Appl Bio Mater 2022, 5, 3338–3348.

41. Da Ros, V.; Oddo, L.; Toumia, Y.; Guida, E.; Minosse, S.; Strigari, L.; Strolin, S.; Paolani, G.; Di Giuliano, F.; Floris, R.; et al. PVA-Microbubbles as a Radioembolization Platform: Formulation and the In Vitro Proof of Concept. Pharmaceutics 2023, 15, doi:10.3390/pharmaceutics15010217.

42. Unga, J.; Omata, D.; Kudo, N.; Ueno, S.; Munakata, L.; Shima, T.; Suzuki, R.; Maruyama, K. Development and Evaluation of Stability and Ultrasound Response of DSPC-DPSG-Based Freeze-Dried Microbubbles. J Liposome Res 2019, 29, 368–374, doi:10.1080/08982104.2018.1556294.

43. Wiedemair, W.; Tukovic, Z.; Jasak, H.; Poulikakos, D.; Kurtcuoglu, V. The Breakup of Intravascular Microbubbles and Its Impact on the Endothelium. Biomech Model Mechanobiol 2017, 16, 611–624, doi:10.1007/s10237-016-0840-z.

44. Khodabakhshi, Z.; Hosseinkhah, N.; Ghadiri, H. Pulsating Microbubble in a Micro-Vessel and Mechanical Effect on Vessel Wall: A Simulation Study. J Biomed Phys Eng 2021, 11, 629–640, doi:10.31661/jbpe.v0i0.1131.

45. Collis, J.; Manasseh, R.; Liovic, P.; Tho, P.; Ooi, A.; Petkovic-Duran, K.; Zhu, Y. Cavitation Microstreaming and Stress Fields Created by Microbubbles. Ultrasonics 2010, 50, 273–279, doi:10.1016/j.ultras.2009.10.002.

46. Mehta, R.I.; Carpenter, J.S.; Mehta, R.I.; Haut, M.W.; Wang, P.; Ranjan, M.; Najib, U.; D'Haese, P.F.; Rezai, A.R. Ultrasound-Mediated Blood–Brain Barrier Opening Uncovers an Intracerebral Perivenous Fluid Network in Persons with Alzheimer's Disease. Fluids Barriers CNS 2023, 20, doi:10.1186/s12987-023-00447-y.

47. Rezai, A.R.; Ranjan, M.; Haut, M.W.; Carpenter, J.; D'Haese, P.F.; Mehta, R.I.; Najib, U.; Wang, P.; Claassen, D.O.; Chazen, J.L.; et al. Focused Ultrasound-Mediated Blood-Brain Barrier Opening in Alzheimer's Disease: Long-Term Safety, Imaging, and Cognitive Outcomes. J Neurosurg 2023, 139, 275–283, doi:10.3171/2022.9.JNS221565.

48. Gasca-Salas, C.; Fernández-Rodríguez, B.; Pineda-Pardo, J.A.; Rodríguez-Rojas, R.; Obeso, I.; Hernández-Fernández, F.; del Álamo, M.; Mata, D.; Guida, P.; Ordás-Bandera, C.; et al. Blood-Brain Barrier Opening with Focused Ultrasound in Parkinson's Disease Dementia. Nat Commun 2021, 12, doi:10.1038/s41467-021-21022-9.

49. Thévenot, E.; Jordão, J.F.; O'Reilly, M.A.; Markham, K.; Weng, Y.Q.; Foust, K.D.; Kaspar, B.K.; Hynynen, K.; Aubert, I. Targeted Delivery of Self-Complementary Adeno-Associated Virus Serotype 9 to the Brain, Using Magnetic Resonance Imaging-Guided Focused Ultrasound. Hum Gene Ther 2012, 23, 1144–1155, doi:10.1089/hum.2012.013.

50. Felix, M.S.; Borloz, E.; Metwally, K.; Dauba, A.; Larrat, B.; Matagne, V.; Ehinger, Y.; Villard, L.; Novell, A.; Mensah, S.; et al. Ultrasound-Mediated Blood-Brain Barrier Opening Improves Whole Brain Gene Delivery in Mice. Pharmaceutics 2021, 13, doi:10.3390/pharmaceutics13081245.

51. Blesa, J.; Pineda-Pardo, J.A.; Inoue, K.-I.; Gasca-Salas, C.; Balzano, T.; López-González, N.; Rey, D.; Reinares-Sebastián, A.; Esteban-García, N.; Rodríguez-Rojas, R.; et al. BBB Opening with Focused Ultrasound in Nonhuman Primates and Parkinson's Disease Patients: Targeted AAV Vector Delivery and PET Imaging. Neuroscience 2023.

52. Fan, C.H.; Ting, C.Y.; Lin, C.Y.; Chan, H.L.; Chang, Y.C.; Chen, Y.Y.; Liu, H.L.; Yeh, C.K. Noninvasive, Targeted, and Non-Viral Ultrasound-Mediated GDNF-Plasmid Delivery for Treatment of Parkinson's Disease. Sci Rep 2016, 6, doi:10.1038/srep19579.

53. Rigollet, S.; Rome, C.; Ador, T.; Dumont, E.; Pichon, C.; Delalande, A.; Barbier, E.L.; Stupar, V. FUS-Mediated BBB Opening Leads to Transient Perfusion Decrease and Inflammation without Acute or Chronic Brain Lesion. Theranostics 2024, 14, 4147–4160, doi:10.7150/thno.96721.

54. Stetler, A.; Winograd, C.; Sayegh, J.; Cheever, A.; Patton, E.; Zhang, X.; Clarke, S.; Ceman, S. Identification and Characterization of the Methyl Arginines in the Fragile X Mental Retardation Protein Fmrp. Hum Mol Genet 2006, 15, 87–96, doi:10.1093/hmg/ddi429.

55. Brossard, C.; Montigon, O.; Boux, F.; Delphin, A.; Christen, T.; Barbier, E.L.; Lemasson, B. MP3: Medical Software for Processing Multi-Parametric Images Pipelines. Front Neuroinform 2020, 14, doi:10.3389/fninf.2020.594799.

56. Guilloux, J.P.; Seney, M.; Edgar, N.; Sibille, E. Integrated Behavioral Z-Scoring Increases the Sensitivity and Reliability of Behavioral Phenotyping in Mice: Relevance to Emotionality and Sex. J Neurosci Methods 2011, 197, 21–31, doi:10.1016/j.jneumeth.2011.01.019.

57. Curtis, A.; Calabro, K.; Galarneau, J.R.; Bigio, I.J.; Krucker, T. Temporal Variations of Skin Pigmentation in C57Bl/6 Mice Affect Optical Bioluminescence Quantitation. Mol Imaging Biol 2011, 13, 1114–1123, doi:10.1007/s11307-010-0440-8.

58. Marchi, N.; Teng, Q.; Ghosh, C.; Fan, Q.; Nguyen, M.T.; Desai, N.K.; Bawa, H.; Rasmussen, P.; Masaryk, T.K.; Janigro, D. Blood-Brain Barrier Damage, but Not Parenchymal White Blood Cells, Is a Hallmark of Seizure Activity. Brain Res 2010, 1353, 176–186, doi:10.1016/j.brainres.2010.06.051.

59. Marchi, N.; Angelov, L.; Masaryk, T.; Fazio, V.; Granata, T.; Hernandez, N.; Hallene, K.; Diglaw, T.; Franic, L.; Najm, I.; et al. Seizure-Promoting Effect of Blood-Brain Barrier Disruption. Epilepsia 2007, 48, 732–742, doi:10.1111/j.1528-1167.2007.00988.x.

60. Marchi, N.; Banjara, M.; Janigro, D. Blood-Brain Barrier, Bulk Flow, and Interstitial Clearance in Epilepsy. J Neurosci Methods 2016, 260, 118–124, doi:10.1016/j.jneumeth.2015.06.011.

61. Mathon, B.; Navarro, V.; Lecas, S.; Roussel, D.; Charpier, S.; Carpentier, A. Safety Profile of Low-Intensity Pulsed Ultrasound–Induced Blood–Brain Barrier Opening in Non-Epileptic Mice and in a Mouse Model of Mesial Temporal Lobe Epilepsy. Ultrasound Med Biol 2023, 49, 1327–1336, doi:10.1016/j.ultrasmedbio.2023.02.002.

62. Ji, R.; Karakatsani, M.E.; Burgess, M.; Smith, M.; Murillo, M.F.; Konofagou, E.E. Cavitation-Modulated Inflammatory Response Following Focused Ultrasound Blood-Brain Barrier Opening. Journal of Controlled Release 2021, 337, 458–471, doi:10.1016/j.jconrel.2021.07.042.

63. Spencer, C.M.; Graham, D.F.; Yuva-Paylor, L.A.; Nelson, D.L.; Paylor, R. Social Behavior in Fmr1 Knockout Mice Carrying a Human FMR1 Transgene. Behavioral Neuroscience 2008, 122, 710–715, doi:10.1037/0735-7044.122.3.710.

64. Qin, M.; Kang, J.; Smith, C.B. A Null Mutation for Fmr1 in Female Mice: Effects on Regional Cerebral Metabolic Rate for Glucose and Relationship to Behavior. Neuroscience 2005, 135, 999–1009, doi:10.1016/j.neuroscience.2005.06.081.

65. Kramvis, I.; Mansvelder, H.D.; Loos, M.; Meredith, R. Hyperactivity, Perseveration and Increased Responding during Attentional Rule Acquisition in the Fragile X Mouse Model. Front Behav Neurosci 2013, doi:10.3389/fnbeh.2013.00172.

66. Felgerolle, C.; Hébert, B.; Ardourel, M.; Meyer-Dilhet, G.; Menuet, A.; Pinto-Morais, K.; Bizot, J.C.; Pichon, J.; Briault, S.; Perche, O. Visual Behavior Impairments as an Aberrant Sensory Processing in the Mouse Model of Fragile X Syndrome. Front Behav Neurosci 2019, 13, doi:10.3389/fnbeh.2019.00228.

67. Martín, R.; Suárez-Pinilla, A.S.; García-Font, N.; Laguna-Luque, M.L.; López-Ramos, J.C.; Oset-Gasque, M.J.; Gruart, A.; Delgado-García, J.M.; Torres, M.; Sánchez-Prieto, J. The Activation of MGluR4 Rescues Parallel Fiber Synaptic Transmission and LTP, Motor Learning and Social Behavior in a Mouse Model of Fragile X Syndrome. Mol Autism 2023, 14, doi:10.1186/s13229-023-00547-4.

68. Hourani, S.; Pouladi, M.A. Oligodendroglia and Myelin Pathology in Fragile X Syndrome. J Neurochem 2024.

69. Cencelli, G.; Pacini, L.; De Luca, A.; Messia, I.; Gentile, A.; Kang, Y.; Nobile, V.; Tabolacci, E.; Jin, P.; Farace, M.G.; et al. Age-Dependent Dysregulation of APP in Neuronal and Skin Cells from Fragile X Individuals. Cells 2023, 12, doi:10.3390/cells12050758.

70. Zhao, S.; Jiang, X.; Han, L.; Jiang, Y.; Wang, Y.; Meng, J.; Zhu, X.; Zhang, X.; Luo, H.; Zhang, Y. wu Tau Reduction Attenuates Autism-like Features in Fmr1 Knockout Mice. Mol Autism 2023, 14, doi:10.1186/s13229-023-00574-1.

71. Shen, Y.; Hua, L.; Yeh, C.K.; Shen, L.; Ying, M.; Zhang, Z.; Liu, G.; Li, S.; Chen, S.; Chen, X.; et al. Ultrasound with Microbubbles Improves Memory, Ameliorates Pathology and Modulates Hippocampal Proteomic Changes in a Triple Transgenic Mouse Model of Alzheimer's Disease. Theranostics 2020, 10, 11794–11819, doi:10.7150/thno.44152.

72. Jordão, J.F.; Thévenot, E.; Markham-Coultes, K.; Scarcelli, T.; Weng, Y.Q.; Xhima, K.; O'Reilly, M.; Huang, Y.; McLaurin, J.A.; Hynynen, K.; et al. Amyloid-β Plaque Reduction, Endogenous Antibody Delivery and Glial Activation by Brain-Targeted, Transcranial Focused Ultrasound. Exp Neurol 2013, 248, 16–29, doi:10.1016/j.expneurol.2013.05.008.

73. Lee, Y.; Choi, Y.; Park, E.J.; Kwon, S.; Kim, H.; Lee, J.Y.; Lee, D.S. Improvement of Glymphatic–Lymphatic Drainage of Beta-Amyloid by Focused Ultrasound in Alzheimer's Disease Model. Sci Rep 2020, 10, doi:10.1038/s41598-020-73151-8.

74. Liu, X.; Maria, N.S.S.; Lin, S.W.; Jacobs, R.E. The Applications of Focused Ultrasound (FUS) in Alzheimer's Disease Treatment: A Systematic Review on Both Animal and Human Studies. Aging Dis 2021, 12, 1977–2002, doi:10.14336/AD.2021.0510.

75. Rezai, A.R.; Ranjan, M.; Haut, M.W.; Carpenter, J.; D'Haese, P.F.; Mehta, R.I.; Najib, U.; Wang, P.; Claassen, D.O.; Chazen, J.L.; et al. Focused Ultrasound–Mediated Blood-Brain Barrier Opening in Alzheimer's Disease: Long-Term Safety, Imaging, and Cognitive Outcomes. J Neurosurg 2023, 139, 275–283, doi:10.3171/2022.9.JNS221565.

76. Karakatsani, M.E.; Ji, R.; Murillo, M.F.; Kugelman, T.; Kwon, N.; Lao, Y.H.; Liu, K.; Pouliopoulos, A.N.; Honig, L.S.; Duff, K.E.; et al. Focused Ultrasound Mitigates Pathology and Improves Spatial Memory in Alzheimer's Mice and Patients. Theranostics 2023, 13, 4102–4120, doi:10.7150/thno.79898.

77. Epelbaum, S.; Burgos, N.; Canney, M.; Matthews, D.; Houot, M.; Santin, M.D.; Desseaux, C.; Bouchoux, G.; Stroer, S.; Martin, C.; et al. Pilot Study of Repeated Blood-Brain Barrier Disruption in Patients with Mild Alzheimer's Disease with an Implantable Ultrasound Device. Alzheimers Res Ther 2022, 14, doi:10.1186/s13195-022-00981-1.

78. Westmark, C.J.; Westmark, P.R.; O'Riordan, K.J.; Ray, B.C.; Hervey, C.M.; Salamat, M.S.; Abozeid, S.H.; Stein, K.M.; Stodola, L.A.; Tranfaglia, M.; et al. Reversal of Fragile X Phenotypes by Manipulation of AβPP/Aβ Levels in Fmr1 KO Mice. PLoS One 2011, 6, doi:10.1371/journal.pone.0026549.

79. Hsu, Y.H.; Lee, W.C.; Chu, S.S.; Chao, M.E.; Wu, K.S.; Liu, R.S.; Wong, T.T. Influence of Acoustic Parameters and Sonication Schemes on Transcranial Blood–Brain Barrier Disruption Induced by Pulsed Weakly Focused Ultrasound. Pharmaceutics 2022, 14, doi:10.3390/pharmaceutics14061207.

80. Chen, H.; Konofagou, E.E. The Size of Blood-Brain Barrier Opening Induced by Focused Ultrasound Is Dictated by the Acoustic Pressure. Journal of Cerebral Blood Flow and Metabolism 2014, 34, 1197–1204, doi:10.1038/jcbfm.2014.71.

81. Batts, A.J.; Ji, R.; Noel, R.L.; Kline-Schoder, A.R.; Bae, S.; Kwon, N.; Konofagou, E.E. Using a Novel Rapid Alternating Steering Angles Pulse Sequence to Evaluate the Impact of Theranostic Ultrasound-Mediated Ultra-Short Pulse Length on Blood-Brain Barrier Opening Volume and Closure, Cavitation Mapping, Drug Delivery Feasibility, and Safety. Theranostics 2023, 13, 1180–1197, doi:10.7150/thno.76199.

82. Ajenjo, J.; Seo, J.W.; Foiret, J.; Wu, B.; Raie, M.N.; Wang, J.; Fite, B.Z.; Zhang, N.; Malek, R.; Beinat, C.; et al. PET Imaging of Focused-Ultrasound Enhanced Delivery of AAVs into the Murine Brain. Theranostics 2023, 13, 5151–5169, doi:10.7150/thno.85549.

83. Kofoed, R.H.; Noseworthy, K.; Wu, K.; Sivadas, S.; Stanek, L.; Elmer, B.; Hynynen, K.; Shihabuddin, L.S.; Aubert, I. The Engineered AAV2-HBKO Promotes Non-Invasive Gene Delivery to Large Brain Regions beyond Ultrasound Targeted Sites. Mol Ther Methods Clin Dev 2022, 27, 167–184, doi:10.1016/j.omtm.2022.09.011.

84. Kofoed, R.H.; Dibia, C.L.; Noseworthy, K.; Xhima, K.; Vacaresse, N.; Hynynen, K.; Aubert, I. Efficacy of Gene Delivery to the Brain Using AAV and Ultrasound Depends on Serotypes and Brain Areas. Journal of Controlled Release 2022, 351, 667–680, doi:10.1016/j.jconrel.2022.09.048.

85. Nouraein, S.; Lee, S.; Saenz, V.A.; Del Mundo, H.C.; Yiu, J.; Szablowski, J.O. Acoustically Targeted Noninvasive Gene Therapy in Large Brain Volumes. Gene Ther 2024, 31, 85–94, doi:10.1038/s41434-023-00421-1.

86. Owusu-Yaw, B.S.; Zhang, Y.; Garrett, L.; Yao, A.; Shing, K.; Batista, A.R.; Sena-Esteves, M.; Upadhyay, J.; Kegel-Gleason, K.; Todd, N. Focused Ultrasound-Mediated Disruption of the Blood–Brain Barrier for AAV9 Delivery in a Mouse Model of Huntington's Disease. Pharmaceutics 2024, 16, doi:10.3390/pharmaceutics16060710.

87. Li, H.R.; Harb, M.; Heath, J.E.; Trippett, J.S.; Shapiro, M.G.; Szablowski, J.O. Engineering Viral Vectors for Acoustically Targeted Gene Delivery. Nat Commun 2024, 15, 4924, doi:10.1038/s41467-024-48974-y.

88. Weber-Adrian, D.; Kofoed, R.H.; Silburt, J.; Noroozian, Z.; Shah, K.; Burgess, A.; Rideout, S.; Kügler, S.; Hynynen, K.; Aubert, I. Systemic AAV6-Synapsin-GFP Administration Results in Lower Liver Biodistribution, Compared to AAV1&2 and AAV9, with Neuronal Expression

Following Ultrasound-Mediated Brain Delivery. Sci Rep 2021, 11, doi:10.1038/s41598-021-81046-5.

89. Ogawa, K.; Kato, N.; Yoshida, M.; Hiu, T.; Matsuo, T.; Mizukami, S.; Omata, D.; Suzuki, R.; Maruyama, K.; Mukai, H.; et al. Focused Ultrasound/Microbubbles-Assisted BBB Opening Enhances LNP-Mediated MRNA Delivery to Brain. Journal of Controlled Release 2022, 348, 34–41, doi:10.1016/J.JCONREL.2022.05.042.

90. Kwak, G.; Grewal, A.; Slika, H.; Mess, G.; Li, H.; Kwatra, M.; Poulopoulos, A.; Woodworth, G.F.; Eberhart, C.G.; Ko, H.S.; et al. Brain Nucleic Acid Delivery and Genome Editing via Focused Ultrasound-Mediated Blood-Brain Barrier Opening and Long-Circulating Nanoparticles. ACS Nano 2024, 18, 24139–24153, doi:10.1021/acsnano.4c05270.

91. Lee, B.; Lee, K.; Panda, S.; Gonzales-Rojas, R.; Chong, A.; Bugay, V.; Park, H.M.; Brenner, R.; Murthy, N.; Lee, H.Y. Nanoparticle Delivery of CRISPR into the Brain Rescues a Mouse Model of Fragile X Syndrome from Exaggerated Repetitive Behaviours. Nat Biomed Eng 2018, 2, 497–507, doi:10.1038/s41551-018-0252-8.

92. O'Reilly, M.A.; Hynynen, K. Blood-Brain Barrier: Real-Time Feedback-Controlled Focused Ultrasound Disruption by Using an Acoustic Emissions-Based Controller. Radiology 2012, 263, 96–106, doi:10.1148/radiol.11111417.

93. Novell, A.; Kamimura, H.A.S.; Cafarelli, A.; Gerstenmayer, M.; Flament, J.; Valette, J.; Agou, P.; Conti, A.; Selingue, E.; Aron Badin, R.; et al. A New Safety Index Based on Intrapulse Monitoring of Ultra-Harmonic Cavitation during Ultrasound-Induced Blood-Brain Barrier Opening Procedures. Sci Rep 2020, 10, doi:10.1038/s41598-020-66994-8.

6. SUPPLEMENTARY RESULTS

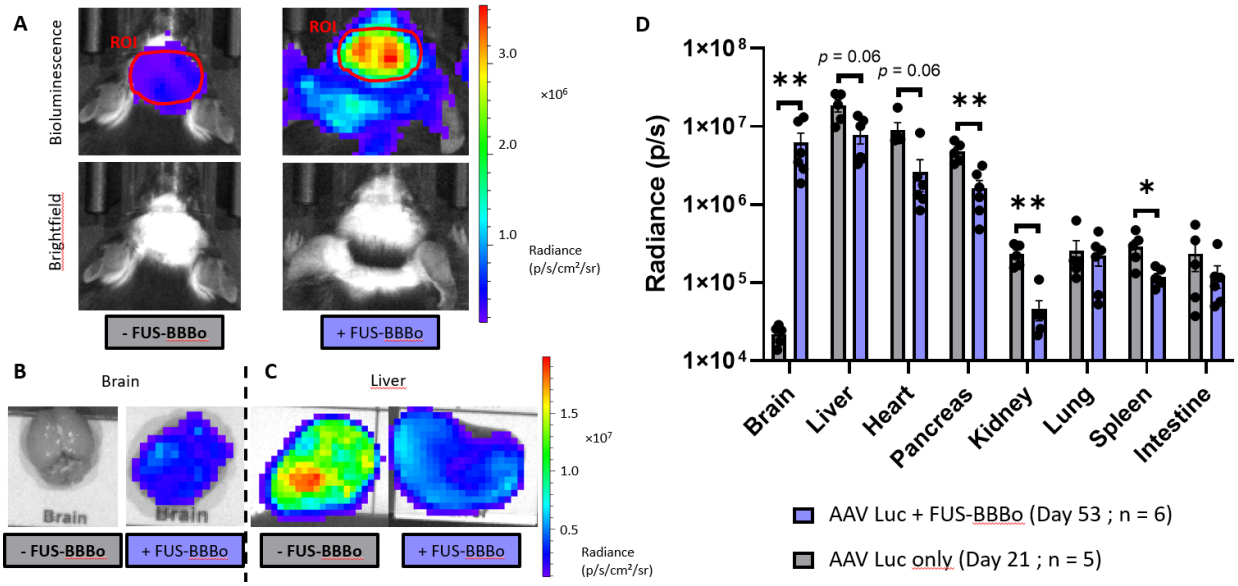

Figure 1S: Transgene expression analysis of *Fmr1*$^{+/y}$ mice following AAV2/9.CMV.Luciferase injection. (**A**) *In vivo* bioluminescence pictures of mice 21 days after AAV-Luc injection with or without FUS-BBBo; red circles: ROI used for measures (**B**) *Ex vivo* bioluminescence pictures of mice's brains 21 days after AAV-Luc injection or 53 days after AAV-Luc injection and FUS-BBBo. (**C**) *Ex vivo* bioluminescence pictures of mice's livers 21 days after AAV-Luc injection or 53 days after AAV-Luc injection and FUS-BBBo. (**D**) *Ex vivo* bioluminescence of mice's organs at the end of respective expression kinetics, 21 days after AAV-Luc injection only or 53 days after AAV-Luc injection and FUS-BBBo. Data expressed as mean +/- SEM. * = p-value < 0.05; ** = p-value < 0.01; Mann-Whitney bilateral test.

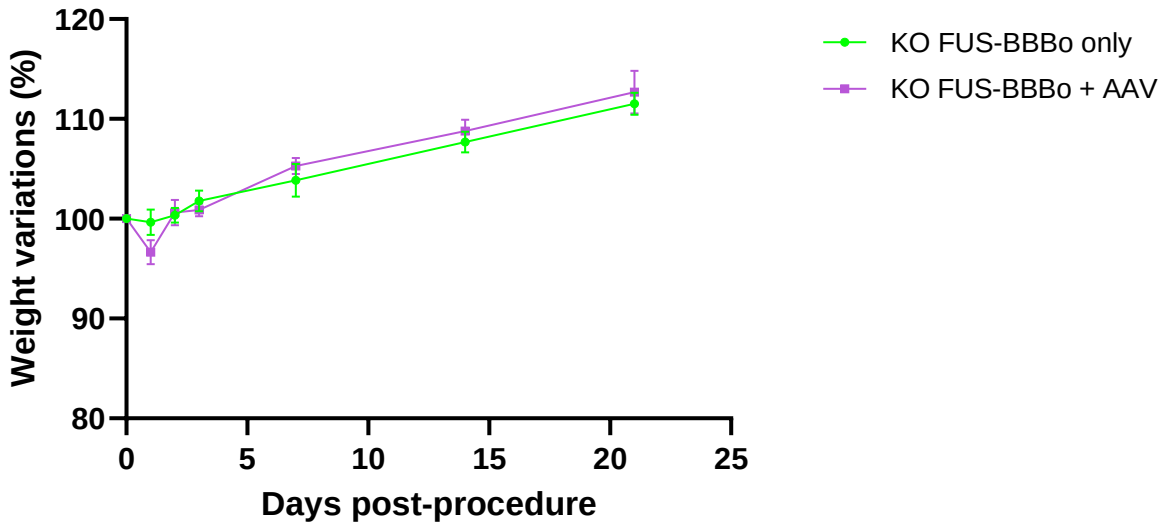

Figure 2S: Weight variations in percentage of initial weight following FUS-BBBo procedure.

ADDITIONAL EXPERIMENTS

Previous chapter only discussed behavioral experiments that successfully depicted the knock-out (KO) phenotype compared to Wild-Type (WT) mice. This analysis was also mostly limited to the main behavioral information usually studied with each test. However, each behavioral test can bring additional information on other behavior by performing a thinner analysis, and especially when using Z-scores with parameters specific to certain behaviors [56]. This analysis will be performed in this additional section along with behavioral tests that did not show a significant *Fmr1*-KO phenotype.

1. Additional methods

The following behavioral tests were conducted in the same general condition as those described in the previous section.

Social open fields were performed 3 weeks after treatment. Mice were first put in the empty open field like the previous day, and their movements were tracked for 5 minutes. Mice were then removed from the open field, and an empty cage was placed in a corner of the apparatus. Mice were put back in the open field, and their movements were tracked for 5 minutes. Mice were then removed again from the open field, and a stimulus mouse, different from the mouse used during the direct interaction test, was placed in the open field's cage. Mice were put back in the open field, and their movements were tracked again for 5 minutes. The apparatus was not cleaned between these stages but only at the end of the entire test. The parameters estimated relevant for the social Z-score were the number of entries, time spent, average duration of visit in the social target area during the stage with the stimulus mice, and the ratio of time spent in the social target zone during the stage with the stimulus mice over the stage with an empty cage. For locomotion and anxiety Z-scores, the same parameters were estimated relevant as those used in the open field.

In EPM, the parameters estimated relevant for the anxiety Z-score were the number of entries and time spent in the open arms, the percentage of entries and time spent in the open arms, and the number of entries and time spent in unprotected head dipping. The parameters estimated relevant for the locomotion Z-score were the distance travelled, the time spent immobile, the number of entries in the closed arms, and the total number of entries in the different areas.

Then, from 5 to 6 weeks after treatment, the novel object recognition test (NOR) was carried out. For this test we performed 5 habituation stages, once a day, with the novel object stage on the fifth day. For the habituation stages, the mice were placed in the open field with two identical objects, and their movements were tracked for 5 minutes. The novel object stage was performed directly after the fifth habituation stage. The mice were removed from the open field, and one object was changed with an object with a different size, shape, and color. The mice were then put back in the open field, and their movements were tracked for 5 minutes. A discrimination ratio was calculated with values of the last stage as "time with novel object - time with old object" / "time with novel object + time with old object". Parameters estimated relevant for the cognition Z-score were the discrimination ratio, the number of entries, and time spent in the novel object area during the trial with the novel object.

Finally, from 7 to 8 weeks after treatment, Y-maze were performed, where the mice were placed in a random arm of the maze, with another arm closed, and its exploration were tracked for 5 minutes. The mice were then removed, and the third arm opened. The entire apparatus was cleaned to avoid recognition from scent. Mice were then placed back in the Y-maze, in the same arm as the previous stage, and their exploration was tracked for 5 minutes. The parameters estimated relevant for the cognition Z-score were the number of entries, average duration of visit, time spent in the novel arm for 5 minutes, and a discrimination ratio calculated as "time in new arm" / "total time in the 3 arms".

2. Additional results and discussion

In addition to the open field, locomotion parameters can also be assessed across other tests, providing insight on the hyperactivity phenotype in other contexts. A locomotion Z-score was calculated in several tests and showed significantly higher values in untreated *Fmr1*$^{-/y}$ mice compared to untreated *Fmr1*$^{+/y}$ mice in all tests except with the elevated plus maze (Figure 1). This absence of phenotype can probably be explained by the high-anxiety environment created by this test. No difference was observed from the treatments in all tests apart from the open field, except with the social open field where the FUS-BBBo with AAV injection showed a significantly higher value than untreated *Fmr1*$^{-/y}$. Although the open field is the main test to characterize this phenotype, the information brought by other tests validating the phenotypes shows no effect from both treatments. This suggests that although the hyperactivity phenotype is strongly expressed by *Fmr1*$^{-/y}$ mice, both FUS-BBBo treatments, with or without AAV-*Fmr1* injection, rescue only partially the hyperactivity phenotype. This absence of rescue seems to emerge in context with lower anxiety, like in the habituation phase which takes place in a new cage with fresh litter, a context known from the mouse, or in the Y-maze, where the light intensity is lower due to the protected arms. And this absence of rescue also appears in a social context as shown by the social open field.

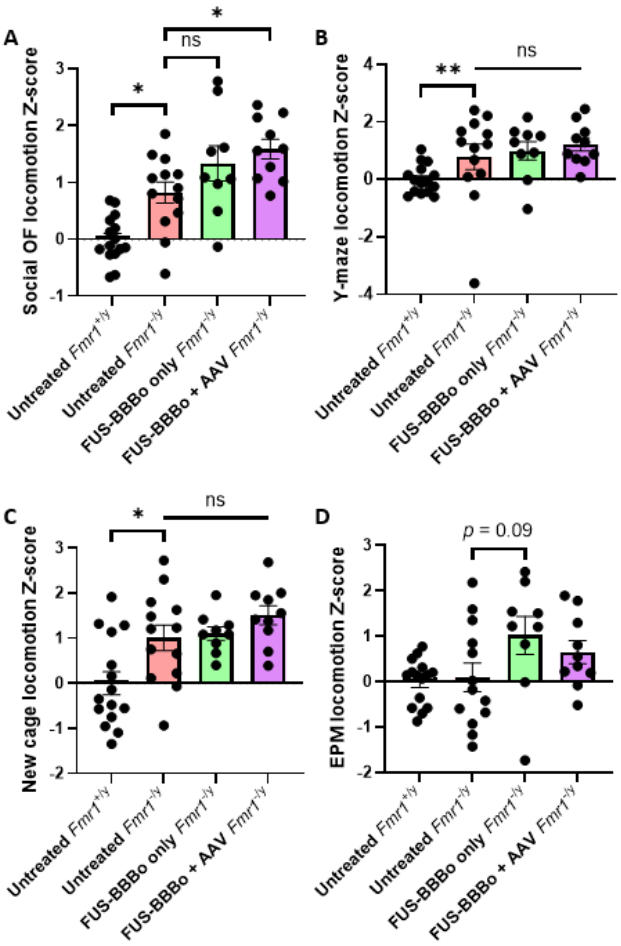

Figure 1: *Fmr1*$^{-/y}$ mice hyperactivity phenotype over *Fmr1*$^{+/y}$ mice and partial rescue of FUS-BBBo and FMRP expression. (**A**) Z-scores of locomotion parameters in the social open field. (**B**) Z-scores of locomotion parameters in the Y-maze. (**C**) Z-scores of locomotion parameters in the novel cage during the first 5 minutes of the habituation for the direct interaction test. (**D**) Z-scores of locomotion parameters in the elevated plus maze. Data expressed as mean +/- SEM. * = p-value < 0.05; ** = p-value < 0.01; *** = p-value < 0.001; Mann-Whitney bilateral test.

In conjunction with the results obtained with the marble-burying test and EPM, the Z-score of anxiety assessed in the social open field and elevated plus maze also shows significant, or close to significant, increased values from untreated *Fmr1*$^{-/y}$ mice compared to untreated *Fmr1*$^{+/y}$ mice (Figure 2). Thus, further confirming the strong anxiety phenotype of *Fmr1*-KO mice. And both Z-scores show decreased values with both treatments, but not significantly. Anxiety Z-score assessed in an open field shows a slight and non-significant increase in values from untreated *Fmr1*$^{-/y}$ mice compared to untreated *Fmr1*$^{+/y}$ and shows a significant decrease with both treatments. This suggests a strong effect of FUS-BBBo on rescuing anxiety

phenotype, as seen on all relevant tests, though it remains partial as seen with some tests that do not show a significant rescue.

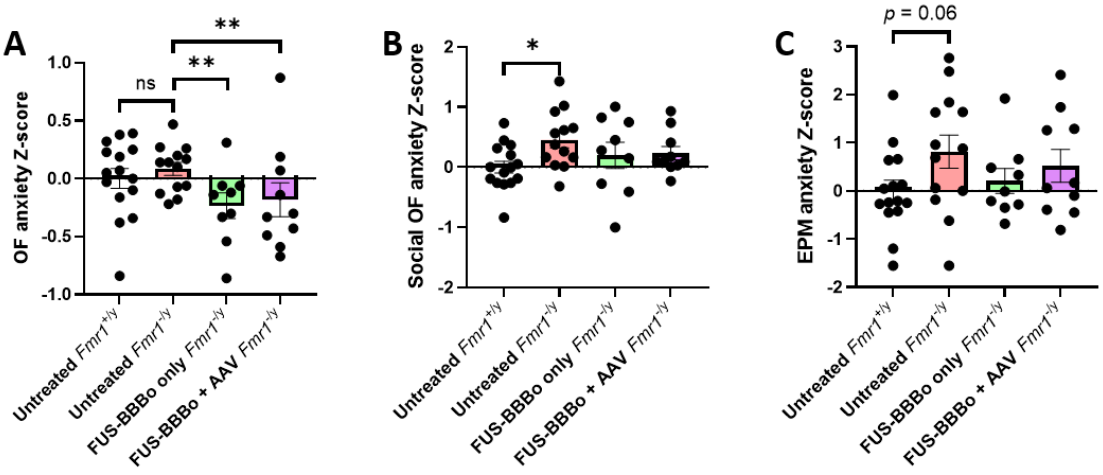

Figure 2: *Fmr1*$^{-/y}$ anxiolysis phenotype over *Fmr1*$^{+/y}$ mice and partial rescue of FUS-BBBo and FMRP expression. (**A**) Z-scores of anxiety parameters in the open field. (**B**) Z-scores of anxiety parameters in the social open field. (**C**) Z-scores of anxiety parameters in the elevated plus maze. Data expressed as mean +/- SEM. * = p-value < 0.05; ** = p-value < 0.01; Mann-Whitney bilateral test.

Besides the direct interaction test, a social open field was performed to assess social behavior that showed no difference in the preference ratio to the social target from untreated *Fmr1*$^{-/y}$ mice compared to untreated *Fmr1*$^{+/y}$ mice, reaching 2.02 and 1.87 A.U., respectively. It showed a non-significant decrease from both treatments, getting down to 1.03 and 1.26 A.U. without or with AAV, respectively (Figure 3). And in the social open field the Z-scores confirm the absence of significant differences in this test between untreated *Fmr1*$^{-/y}$ and untreated *Fmr1*$^{+/y}$ mice. It also confirms the absence of significant differences from treated groups compared to untreated *Fmr1*$^{-/y}$ mice in this test, but with no tendencies to a diminution of social behaviors. These results indicate that the social open field test did not successfully describe the social impairment of *Fmr1*$^{-/y}$ mice. Although this test generally shows similar results to a 3-chamber test that described a phenotype in previous studies, in this study we manipulated the mice a lot between the different stages; that might explain the lack of phenotype observed. This test would have provided information on social behavior in a protected context, in contrast to the unprotected context from the direct interaction test.

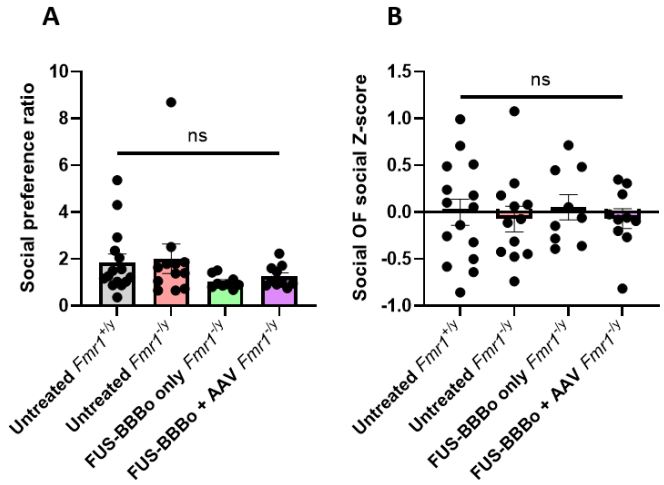

Figure 3: Social behavior of mice assessed with social open field. (**A**) Social preference ratio of time spent around social target over empty cage. (**B**) Z-score of social parameters in the social open field. Data expressed as mean +/- SEM. * = p-value < 0.05; Mann-Whitney bilateral test.

Finally, the cognitive behavior was assessed, first with the novel object recognition test. It showed a high recognition of the novel object in all groups, with a 3- to 4-fold higher time spent with the novel object during the test trial. Yet no significative difference could be observed between groups in the ability to recognize the object, with a discrimination ratio for the novel object of 0.53, 0.56, 0.57, 0.55 A.U. for the untreated *Fmr1*$^{-/y}$, *Fmr1*$^{+/y}$, FUS-BBBo only treatment, and FUS-BBBo with AAV treatment respectively (Figure 4.B.). Similarly, the Y-maze shows a recognition of the novel arm in all groups, but with no significant difference in all groups. The percentage of time spent in the novel arm reached 40.7, 40.3, 38.0, and 38.37 % for the untreated *Fmr1*$^{-/y}$, *Fmr1*$^{+/y}$, FUS-BBBo only treatment, and FUS-BBBo with AAV treatment respectively showing higher interest for the novel arm than the known arms, but with no difference between groups (Figure 4.C.). Z-scores confirm the absence of significant differences between untreated *Fmr1*$^{-/y}$ and untreated *Fmr1*$^{+/y}$ mice in cognitive-related parameters in both the NOR and Y-test. They also show no significant difference in the treated groups values compared to untreated *Fmr1*$^{-/y}$, although they show a tendency to modified behaviors from both treated groups with a close significance in the Y-maze for the group with AAV injection. The cognitive impairment is also a well-described phenotype in *Fmr1*-KO mice that was expected to be observed in the novel object recognition test and the Y-maze. But in our study, although we show a strong recognition of the novel object during the NOR, as seen

with the time spent around objects, we observe no difference between the different groups. This could be due to the objects that some mice managed to climb onto, therefore using them for a purpose different from exploring the environment and therefore invalidating the test despite the apparent recognition of the object. In the Y-maze though, no specificities were observed that could invalidate the test, and mice showed the ability to recognize the novel arm, as shown by the higher time spent in the novel arm compared to the known arms, therefore validating the test. Despite that, the different groups show no difference in recognition of the novel arm. This suggests that our mice did not express a cognitive impairment phenotype in this test. We therefore have no information on the cognitive sphere in this study to analyze the therapeutic effect of our treatment on this sphere.

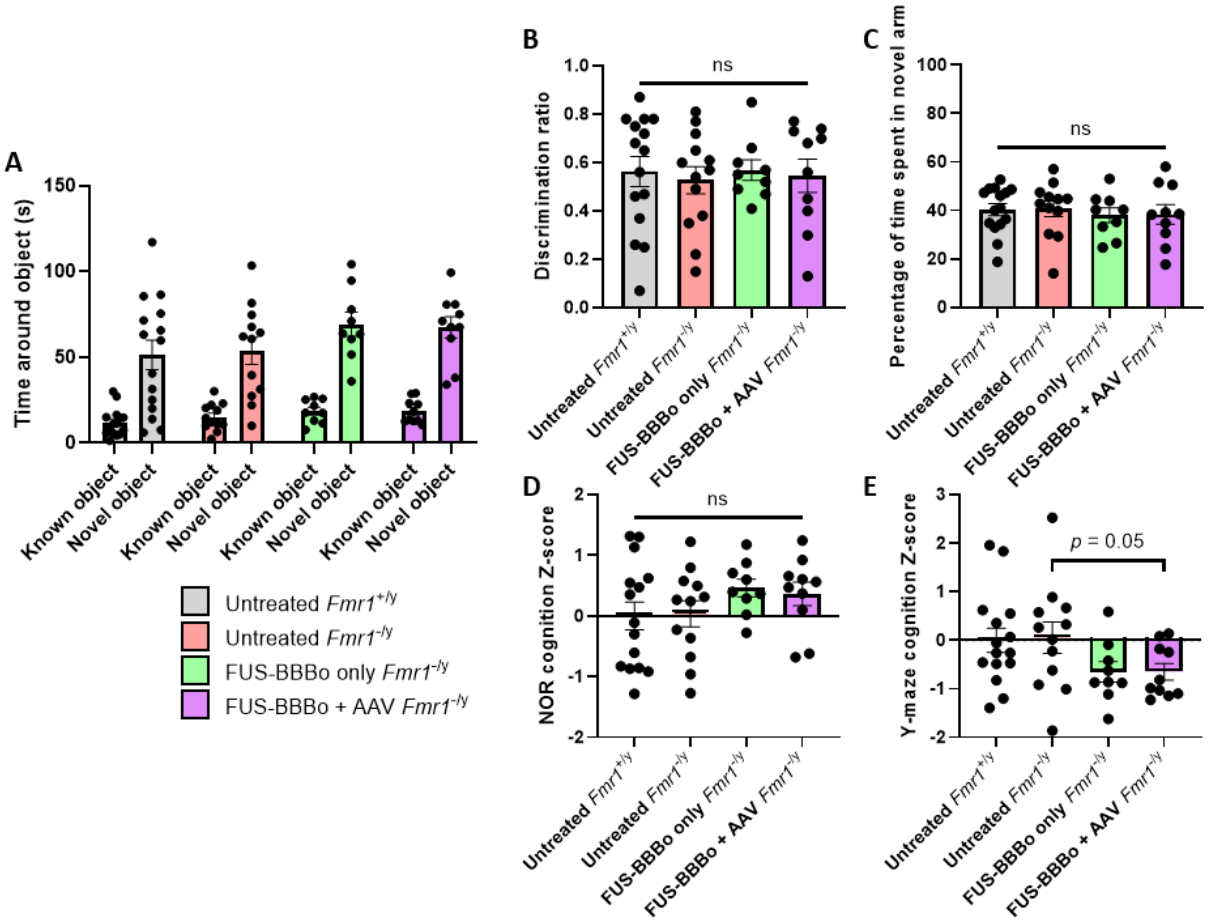

Figure 4: *Fmr1*$^{-/y}$ cognitive impairment phenotype over *Fmr1*$^{+/y}$ mice was not detected in our tests. (**A**) Total time spent around known or novel objects during the test stage of the novel object recognition test. (**B**) Time ratio spent around novel object out of the total time spent around objects during the test stage of the novel object recognition test. (**C**) Percentage of time spent in the novel arm during the first 2 minutes of the Y-maze test. (**D**) Z-score of cognition parameters in the novel object recognition test.

(**E**) Z-score of cognition parameters in the Y-maze test. Data expressed as mean +/- SEM. * = p-value < 0.05; Mann-Whitney bilateral test.

GENERAL DISCUSSION

In this PhD, I evaluated various gene delivery modalities to the brain using focused ultrasound-mediated blood-brain barrier opening (FUS-BBBo) and demonstrated their potential for gene therapy in fragile X syndrome. This was initially achieved by developing several custom microbubbles (MB) with magnetic, targeting, or cationic properties (Results part I). The cationic MBs were based on either cationic lipids, which allowed direct binding of nucleic acids to the MB surface, or cationic polymers anchored to the MB shell, which delocalized the nucleic acids from the surface. These cationic MBs were the first to incorporate ionizable components capable of enhancing endosomal escape, such as ionizable lipids or histidine groups attached to the polymer.

Before using these custom MBs, a FUS-BBBo protocol and its monitoring system were developed. I successfully opened the blood-brain barrier (BBB) and confirmed it *in vivo* using both fluorescence and photoacoustic imaging with Indocyanine Green (ICG) as a bimodal agent. We validated this monitoring approach against the gold standard, magnetic resonance imaging (MRI), demonstrating comparable precision using *ex vivo* fluorescence imaging (Results part II). I further used fluorescence imaging all along this PhD, validating its efficiency as an alternative to MRI and Evans blue for the monitoring of BBB opening (BBBo).

The first modality where brain gene delivery *in vivo* was achieved was using lipidic cationic MB, demonstrating high gene transfer into mice brains with an optimized protocol and correlated with BBBo (Results part III). It also showed the ability to enable gene expression throughout the entire brain with a specific protocol. Next, lipid nanoparticles (LNPs) were used, achieving similar gene transfer compared to the first modality with either plasmid DNA or messenger RNA. The use of LNPs also revealed a clear correlation with stable cavitation, underscoring the importance of cavitation monitoring. Finally, gene transfer was achieved throughout the entire brain using a viral vector, which resulted in significantly higher gene expression compared to the previous non-viral strategies, with stable expression observed from 21 to 53 days post-treatment (Results part IV).

The use of these strategies for fragile X syndrome gene therapy was ultimately assessed. Both non-viral and viral approaches demonstrated the ability to restore *Fmr1* expression in the

Fmr1-KO model, although still lower than wild-type (WT). The viral approach restored *Fmr1* expression in several brain regions, particularly in the prefrontal cortex and hypothalamus, with expression mainly observed in neurons. Behavioral studies on *Fmr1*-KO mice following whole-brain FUS-BBBo and viral injection showed a therapeutic effect of FUS-BBBo only on hyperactivity, anxiety, and social impairment phenotypes. This effect was enhanced with the restored FMRP expression on the hyperactivity and anxiety impairment (Results part IV).

I. Fluorescence and photoacoustic imaging interest for the monitoring of BBB opening

Throughout this PhD, in order to monitor BBBo, I used fluorescence imaging and photoacoustic imaging with ICG extravasation as a bimodal agent, but also Evans blue dye extravasation and MRI with gadolinium extravasation. As demonstrated by Gandhi *et al.* in a systematic review, Evans blue extravasation and MRI are the most frequent modalities used for the monitoring of BBBo [1].

Evans blue extravasation allows qualitative monitoring

The use of Evans blue extravasation in this PhD demonstrated its inaptitude to monitor BBBo with *in vivo* fluorescence imaging. Though it was still able to monitor it *ex vivo* either with fluorescence imaging or with direct visualization of the blue dye. In photoacoustic imaging, it allowed us to significantly decipher the opened region *in vivo*. However, the toxicity of Evans blue was also demonstrated in our study in the concentration used, with 75 % of mortality following FUS-BBBo [2]. Due to this toxicity, its use for *in vivo* and non-invasive monitoring of BBBo is challenging, but its properties allowing it to assess BBBo visually with Evans blue extravasation make it an interesting low-cost method for qualitative monitoring of the BBBo.

MRI demonstrates the best sensibility for BBB opening monitoring

On the opposite, MRI is a non-invasive method for *in vivo* monitoring of BBBo, but with a very high cost, and it requires highly trained operators. In this PhD, MRI monitoring of BBBo was used exclusively *in vivo* with gadolinium and first allowed us to calculate a half-closure time of 32.85 minutes after FUS-BBBo in the parameters used. This is a much faster closure kinetic compared to other studies that generally show half closure time ranging from 2 to 6 h [3,4]. MRI monitoring also demonstrated precise measurement of the opened region, allowing us to confirm that we were able to open over 60 % of the brain with our whole-brain FUS-BBBo protocol. Furthermore, the detected open region is displayed with a mapping of brain structures, allowing the identification of the brain regions where the procedure was efficient. This is particularly important, as the therapeutic effect of any therapeutic strategy will depend on the treated brain region. Using T2 images, MRI also allowed us to confirm that we did not produce any edema or hemorrhages in mice brains after FUS-BBBo, using both focused and whole-brain protocols. In addition to these advantages, MRI is also an efficient tool to assess physiological changes following FUS-BBBo treatment using specific sequences that measured a drop of cerebral blood flow and blood volume fraction following FUS-BBBo [5]. This can also be performed using resting-state functional MRI, as realized by Todd *et al.* showing a significant reduction of functional connectivity [6]. Furthermore, MRI can also be used to guide FUS to a precise location, using the heating generated by FUS to localize the beam [7]. Thus, it makes of MRI an efficient and precise modality to assess qualitatively or quantitatively BBBo and the biological effects it generates.

Photoacoustic and fluorescence imaging as monitoring alternatives

With photoacoustic imaging and fluorescence imaging, ICG is generally used in much higher amounts in photoacoustic imaging compared to fluorescence imaging. We therefore tested two doses ranging between approximately 10-fold higher and 3-fold lower compared to Liang *et al.* and Floc'h *et al.*, who used ICG extravasation to monitor BBBo *in vivo* in fluorescence imaging or photoacoustic imaging respectively [8,9]. Both doses tested demonstrated significant detection of the opened region using both modalities. It also indicated that the best timepoint to assess BBBo was under 1 hour after FUS-BBBo and ICG

injection using photoacoustic imaging and at 24 hours using fluorescence imaging. We therefore developed a ready-to-use protocol for BBBo monitoring for both photoacoustic imaging and fluorescence imaging.

The use of fluorescence imaging was preferred to assess BBBo going further as it is a cheaper and less time-consuming modality. It allowed us to confirm the effect of MB dose on BBBo intensity using our homemade MB [10]. It also allowed us to assess the BBB closure kinetics following FUS-BBBo at our parameters. However, these experiments also highlighted the limits of fluorescence imaging to measure BBBo *in vivo*, as it showed that minimal BBBo was not significantly deciphered *in vivo,* unlike in *ex vivo* measurements. Using *in vivo* fluorescence imaging, it indicated that a minimal amount of 1.5×10^7 MB was required for BBBo, while *ex vivo* fluorescence imaging demonstrated that we still induce BBBo with 1.5×10^6 MB. In addition, the measure of closure kinetics *in vivo* did not allow the calculation of a half-closure time due to its low sensibility using a 2-hour delayed ICG injection. On the opposite, *ex vivo* fluorescence imaging allowed calculating a half closure time of 81.41 minutes using the first FUS-BBBo protocol and of 32.70 minutes using a second FUS-BBBo protocol. This demonstrated the effect of MB dose and mechanical index reduction on the diminution of closure kinetics, which also indicates that this kinetic is correlated with BBBo intensity [11]. Furthermore, as no significant difference was found with the closure kinetics assessed with MRI, it further validates the sensitivity of *ex vivo* fluorescence for BBBo monitoring. However, fluorescence imaging was still used *in vivo* in the subsequent experiments, as high sensitivity was not required to confirm BBBo after gene delivery. It still showed enough precision to be used as a qualitative marker of BBBo but also to demonstrate the correlation between gene delivery and BBBo. Thus, we demonstrated that fluorescence imaging of ICG extravasation is a pertinent technology for the community as a non-invasive, time-efficient, and low-cost *in vivo* BBBo monitoring method, which is now used routinely in our team.

Overall, by comparing these modalities, we highlight the different usage of each technique (Figure 1). Evans blue remains the most cost-effective way to decipher BBBo *ex vivo*, while MRI is the best method for *in vivo* quantitative monitoring of BBBo and physiological changes. Fluorescence imaging with ICG extravasation is demonstrated here as a cost-effective

alternative to these techniques to qualitatively and quantitatively monitor BBBo *in vivo* or *ex vivo* for higher sensibility. Though we showed the efficiency of photoacoustic imaging to monitor BBBo *in vivo*, its use remains undervalued in this study. Moving forward, reproducing the assessment previously observed in MRI or fluorescence imaging will need to be performed to evaluate the technique's efficiency to assess BBBo intensity or precise opened volume. This should be performed with either non-invasive photoacoustic imaging, like what was performed in this study, or with removal of the skull, which should allow better precision and evaluation of BBBo in deeper tissues as demonstrated by Floc'h *et al* [8]. More importantly, as photoacoustic imaging can be used to measure physiological parameters, its potential to assess physiological changes following FUS-BBBo should be investigated. It would allow us to confirm the results shown in a collaborative study with Rigollet *et al.* on cerebral blood flow and blood volume fraction changes following FUS-BBBo [5]. In addition, photoacoustic imaging can achieve these measures with multiple hemodynamic parameters, like saturated oxygenation or vessel diameter [12]. Furthermore, it can also be used to monitor therapeutic effects in neurodegenerative disorders such as Alzheimer's disease, as demonstrated by Tang *et al.* using scanning ultrasound treatment [13]. Confirmation of these application of photoacoustic imaging in FUS-BBBo would make of it an efficient modality for BBBo monitoring and assessment of biological changes induced, making of it an alternative to MRI.

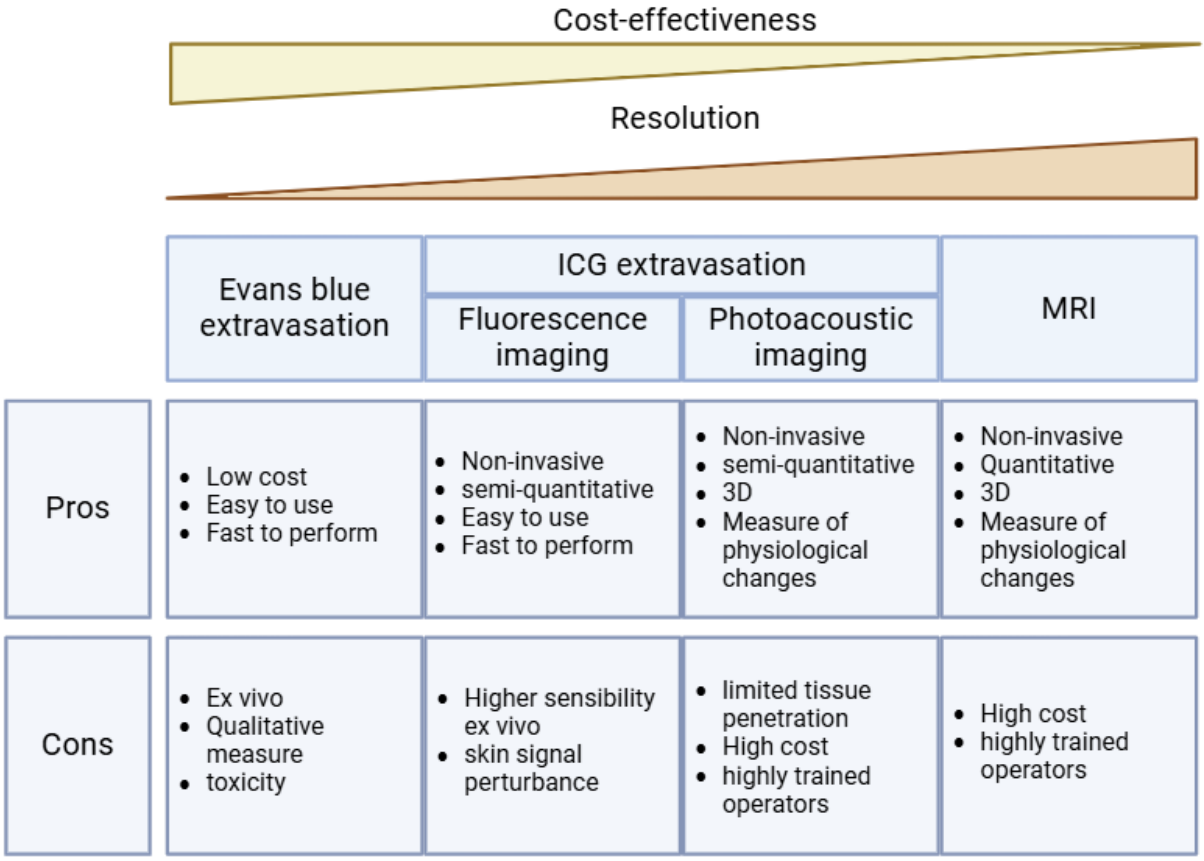

Figure 1: Comparisons of different modalities for the monitoring of BBB opening.

II. FUS-BBBo allows efficient transgene expression through both viral and non-viral modalities

Several methods for gene delivery associated with FUS-BBBo were assessed through this PhD. This included first the use of cationic MB with plasmid DNA (pDNA) complexed at its surface, then with lipid nanoparticles encapsulating pDNA, and finally using an adeno-associated vector (AAV). In addition, several custom MBs were developed as a way to improve gene delivery.

MB properties for BBBo and gene delivery

In order to use them in the different gene delivery strategies, we first needed to assess the properties of the MB used (Figure 2). The first generation of cationic MBs were used for both cationic MB-mediated and LNP-mediated gene delivery. Unfunctionalized MB was used with

co-injection of LNP or AAV, and biotinylated MB was also used for LNP-mediated gene delivery. Unfunctionalized and biotinylated MB showed similar size distribution and concentrations of both MB and nanobubbles (NB), due to their close components and formation methods. On the other hand, the first generation of cationic MB demonstrated a significantly lower concentration of both MB and NB, probably due to the different lipidic chain length used. Using *in vitro* cavitation characterization of MB, this difference was further highlighted since the first generation of cationic MB demonstrated lower stable and inertial cavitation compared to unfunctionalized MB. For unfunctionalized MB, it highlighted the efficiency of the 300 kPa pressure to induce strong stable cavitation with limited inertial cavitation. Cationic MB, on the other hand, demonstrated much lower stable cavitation at 300 kPa, highlighting the potential need to further increase acoustic pressure with this MB formulation. In addition, cationic MB demonstrated their ability to complex with pDNA, as confirmed by gel shift assay, confocal microscopy, and flow cytometry. Although, it also revealed a major inconvenience of cationic MB, as they showed flocculation depending on the amount of pDNA per μL of MB. We still managed to identify that 3 μg of pDNA complexed with 1 μL of MB induced negligible flocculation. As suggested by Lin *et al.* with doxorubicin, drug loading on MB induces a modification of their cavitation by the modification of their shell properties [14]. We confirmed this assertion with *in vitro* characterization of acoustic properties following pDNA complexation. It demonstrated slightly lower acoustic echogenicity and stability in ultrasound imaging. More importantly, it demonstrated lower MB collapse and a delayed cavitation and highlighted the potential of a 400 kPa pressure that induces strong stable cavitation and limited inertial cavitation using cationic MB.

	MB formulation	Concentration	Median diameter	Function
Unfunctionalized MB	• 88% DSPC • 12% DSPE-PEG2000	2.41×10^{10} +/- 2.11×10^{9} MB/mL	1.30 +/- 0.01 µm	Ø
Cationic MB 1st generation	• 44.76% DMPC • 2.9% DMPE-PEG2000 • 43.67% KLN27 • 8.67% MM30	9.9×10^{9} +/- 5.0×10^{8} MB/mL	1.19 +/- 0.02 µm	Cationic 19.1 +/- 0.5 mV
Polymeric cationic MB	• 87% DSPC • 12% DSPE-PEG2000 • 1% DSPE-PEI-His	1.6×10^{10} +/- 1.6×10^{9} MB/mL	1.24 +/- 0.04 µm	Cationic 19.3 +/- 0.7 mV
Biotinylated MB	• 88% DSPC • 11.5% DSPE-PEG2000 • 0.5% DSPE-PEG2000-biot	2.3×10^{10} +/- 2.3×10^{9} MB/mL	1.33 +/- 0.01 µm	Biotin-streptavidin binding
DBCO-MB	• 88% DSPC • 11.5% DSPE-PEG2000 • 0.5% DSPE-PEG2000-DBCO	1.9×10^{10} +/- 1.9×10^{9} MB/mL	1.33 +/- 0.05 µm	DBCO-N3 binding

Figure 2: Overview of homemade functionalized MB

Cationic MB for non-viral gene delivery

Based on these results, we first confirmed using cationic MB the need to increase acoustic pressure higher than 300 kPa, where no gene expression was detected with *in vivo* fluorescence. A threshold of 350 kPa was then detected, where significant bioluminescence was detected demonstrating efficient gene expression. The correlation between BBBo and viral gene delivery was previously demonstrated using PET imaging [15]. We confirmed that this correlation still exists with non-viral strategy, as increased acoustic pressure leads to increased bioluminescence, and fluorescence imaging induced by BBBo correlates with gene delivery. This led to showing that a maximum of bioluminescence was reached at 460 kPa, pressure where inertial cavitation was clearly detected *in vitro* and that induced transitory damages as assessed by mice clinical scoring at 24 hours post-treatment. In addition to gene delivery and BBBo, we also demonstrated that increased acoustic pressure induced increased inflammation, as assessed in RT-qPCR of *ICAM-1*, *CCL2*, and *IL-1α* markers. They all showed pressure-related increases and strong reductions after 7 days, demonstrating its transitory characteristic. This link between FUS-BBBo intensity and inflammation was previously described by Ji *et al.*, who demonstrated overexpression of several inflammatory markers, confirmed in our study with *CCL2* [16]. Then, we confirmed the influence of sonication duration on gene delivery with

a 5-minute sonication at 410 kPa that allowed us to increase gene delivery to a similar intensity as the 1-minute sonication at 460 kPa. This confirmed the advantage of the 400 kPa acoustic pressure, where strong stable cavitation but limited inertial cavitation was detected, and that induced strong gene delivery with limited damage. However, the limited stability of cationic MB suggests that this effect of sonication time could be enhanced with more stable MB or with perfusion of MB solution instead of a bolus injection. Indeed, assessed *in vitro* in ultrasound imaging, they demonstrated a half-life of 166.7 seconds in addition to MB collapse due to FUS treatment, demonstrating that a limited amount of MB remains at the end of a 5-minute pulse. We still concluded that the 410 kPa 5-minute pulse was demonstrated to be the most efficient gene delivery protocol in our study. It showed strong gene expression compared to previous studies like Fan *et al*. (35) that did not induce gene expression strong enough to assess bioluminescence *in vivo*. In addition, bioluminescence assessed over time demonstrated longer gene expression kinetics, lasting for 7 days compared to 72 hours in this previous study. However, this kinetic remains limited compared to viral strategies that can last for over 6 months and was further confirmed with our viral strategy [17].

LNP interest and limitation

Using unfunctionalized MB, we first confirmed their ability to induce BBBo at 310 kPa, as assessed in fluorescence microscopy, using 10 µL of MB solution. Although, in order to induce a BBBo as safe as possible for gene delivery, we preferred using the lowest MB amount allowing significant BBBo, as assessed by *in vivo* fluorescence imaging, of 1.5×10^7 MB (corresponding to approximately 0.5 µL). This protocol was used for LNP-mediated gene delivery and demonstrated strong gene expression detectable with *in vivo* bioluminescence. It also allowed us to confirm that gene delivery is strongly correlated with stable cavitation dose. We did not show any increase in gene delivery using a 2-fold higher amount of LNP, suggesting a saturation of pDNA delivered. Compared to co-injection of bare pDNA, it only showed a slight non-significant increase of bioluminescence, though a significant difference was found in contrast to the stable cavitation dose measured. This suggests, surprisingly, that LNP had a limited effect on gene transfer. However, LNP injected directly after FUS-BBBo instead of co-injected with MB did not induce gene expression sufficient to be detected *in vivo.*

This suggests LNP destruction during FUS-BBBo, liberating pDNA and allowing gene transfer. This is further suggested by Marty *et al*. and Chen et al. that demonstrated a limited drug delivery with objects of 7 nm size or higher, much lower than our LNP (74.7 nm average modal diameter), though they used a FUS-BBBo protocol inducing longer closure kinetics, suggesting a more severe opening [3,18]. This explains the limited effect of LNPs, which primarily protect nucleic acids from enzymes. It still allowed efficient mRNA delivery that would be degraded too fast without complexation, as RNase has a much faster kinetic than DNase. Cavitation analysis *in vivo* also allowed us to validate the measures made *in vitro*, as a strong stable cavitation was detected with few pulses entering the inertial cavitation regime. Increasing acoustic pressure would most likely induce more inertial cavitation and therefore more damage in the brain. Thus, further optimization of this strategy should rely on MB functionalization or LNP optimization rather than on acoustic parameters.

As cell membranes are negatively charged, the use of a cationic vector increases gene delivery by enhancing the vector fusion with the cell's membrane [19]. As nucleic acids are complexed in our LNP with ionizable lipids, it forms neutral particles at neutral pH, and their transfection into cells could be enhanced with the addition of a cationic vector. For this purpose, we used our cationic MB previously described for LNP-mediated gene delivery to assess these cationic properties effect on *in vivo* transfection. It did not allow for inducing stronger gene delivery compared to the use of unfunctionalized MB, which is not surprising considering that if LNP destruction occurs, then it might not transfect cells through the usual pathways. Compared to a similar amount of bare pDNA complexed on cationic MB, it did not show different gene expression. However, it showed much lower stable cavitation with LNP and significantly less inertial regime occurrence, further demonstrating the pDNA complexation effect on MB cavitation. Similarly, the binding of LNP on MB surface with biotin-streptavidin coupling, did not enhance gene delivery compared to unfunctionalized MB nor compared to bare pDNA. As previously stated, this is probably due to LNP destruction following FUS-BBBo [20]. However, De Cock *et al.* demonstrated that this strategy allowed enhanced mRNA delivery into cells *in vitro*, suggesting that nanoparticle destruction can be avoided or is not total [21].

Model transition challenges

Changing our rodent model from female Balb/c to male *Fmr1*-KO mice (C57BL/6J strain) highlighted the need for adjustments in the acoustic pressure used to reach similar BBBo and gene delivery. This increase, from 410 to 460 kPa, can be easily explained by the difference in the skull thickness related to the mice's weight. In addition to body weight, this skull thickness can be different regarding genotype and reduce FUS transmission, as demonstrated by Gerstenmayer *et al.* [22–24]. This was further confirmed by Felix *et al.* that showed in young C57BL/6 mice exponential transmission loss as a function of body mass, getting up to 30 % [25]. However, this effect is limited in our study by the 1 MHz frequency used, which shows less transmission loss with tissue and skull compared to 1.5 MHz. These differences of transmission between animals still induce important heterogeneity between animals and are a barrier to the transposition of the technique to different models. However, as we showed that this can be addressed with variation of acoustic pressure and that gene delivery is correlated with stable cavitation induced, the use of a cavitation monitoring protocol should be used to address these difficulties. Indeed, MB cavitation can be monitored in real time, with pressure incrementation until the desired cavitation is reached [26]. This would allow us to reduce the heterogeneity in BBBo and gene delivery protocol. In addition, it would assure the absence of inertial cavitation and the induction of damages as previously stated.

Viral gene delivery for enhanced and lasting transgene expression

Similarly to the LNP strategy, viral gene delivery was used in co-injection with unfunctionalized MB, but with a whole brain protocol with a slightly higher mechanical index and MB dose to compensate for the delay during probe displacement. It efficiently induced gene expression in the whole brain, with about 10-fold higher bioluminescence compared to our non-viral strategies, and was stable over at least 21 to 53 days after the procedure. According to Stavarache et al., gene expression can remain stable over 6 months after the FUS-BBBo procedure [17]. Although they used a different AAV, this suggests that we might have induced an expression stable over several months. In addition, they also demonstrated that they reached over 50 % of neurons transduced in the opened region, a statement confirmed by Nouraein *et al.* in a whole-brain protocol with an AAV9 vector [27]. These statements suggest

that FMRP-eGFP expression might actually be expressed more widely through the brain than what we detected due to the low sensibility of FMRP immunohistochemistry, resulting in the detection of the protein only in clusters.

Overall, we showed here that the viral gene delivery modality associated with FUS-BBBo was the most efficient in terms of gene expression and stability over time. The main possible optimizations of this method rely on the use of a higher AAV amount or on the use of FUS-BBBo-specific AAV, as developed by Li *et al.* [28]. However, the use of AAV is limited in clinical trials due to the possibility of inducing a strong immune response and the natural prevalence of immunity to AAV within the population [29–31]. In addition, this immunity will be obtained by a treated patient following the procedure, preventing additional treatments. Non-viral strategies are not concerned by these limitations, making them an important alternative to the viral strategy. In addition, as repeated treatments are possible with non-viral strategies, weekly treatments could allow persistent gene expression, since we demonstrated that it lasted for 7 days after treatment. McDannold *et al.* confirmed on macaques that repeated treatment did not show an impact on its safety, with no increase in hemorrhages or behavioral effects [32]. Both LNP- and cationic MB-mediated gene delivery displayed similar gene expression, though the MB used displayed different efficiencies. Indeed, unfunctionalized MB displayed higher stable cavitation as previously discussed, and its higher stability *in vivo* allows a more efficient whole-brain BBBo. However, we demonstrated the need to better optimize LNP to improve gene delivery efficiency. More specifically, the optimization of a smaller LNP reaching a size small enough to cross an open BBB should be investigated. Belliveau *et al.* developed LNP with a similar microfluidic to what was used in this PhD, reaching a size as low as 22.4 nm assessed in Cryo-TEM [33]. Evidence suggests that such LNP would be able to cross an opened BBB, potentially increasing gene delivery. Cationic MB-mediated gene delivery's main limitations are the lower cavitation induced by the first generation of cationic MB and the low amount of pDNA complexed at its surface in the condition preventing flocculation. Optimization of this modality therefore relies mostly on cationic MB formulation.

The functionalized MB developed in our study is a promising perspective to improve this gene delivery. Firstly, the polymeric cationic MB developed demonstrated much higher stable cavitation than the first generation of cationic MB, with better stability under ultrasound. It remains to be further studied which MB-to-pDNA ratio should be used to avoid flocculation and how it would affect MB cavitation. However, as the cationic charge is delocalized from the MB surface, it should limit the nucleic acid complexation effect on MB shell properties, therefore limiting differences in cavitation. The modification of unfunctionalized MB with biotin or DBCO function did not show an effect on concentration and size. In addition, as the lipidic constitution of polymeric cationic MB is close to unfunctionalized MB, it is likely that the addition of biotin or DBCO would not affect these cationic MB either. Moving forward, the use of these polymeric cationic MBs should therefore be investigated, with the addition of the functionalization developed in this PhD, like magnetic or targeting properties. Prior to their use, *in vitro* characterization of the effect of pDNA complexation and binding of antibody or magnetic particle needs to be assessed. This will confirm that these MBs retain sufficient stability and acoustic properties for cavitation-induced BBBo and sonoporation.

Magnetic functionalization associated with cationic MB should enhance gene delivery, both *in vitro* and *in vivo*, with magnetic accumulation of MB. This effect was demonstrated *in vitro* by Stride *et al.* that showed similar magnetic properties as we did, with homogeneous displacement of MB. They indicated that such magnetic MBs were able to get in contact with cells at the bottom of the sample thanks to the magnetic field [34]. *In vivo* drug delivery enhancement to the brain was demonstrated by Fan *et al.* using doxorubicin, with tumor-targeted accumulation of MB with the magnetic field. They also show another advantage of magnetic MB, their contrast properties in MRI from the iron oxide nanoparticles used in their formulation [35]. However, the use of magnetic MB for gene delivery to the brain remains limited to tumor treatments, as their accumulation is targeted at a precise region. This makes their use challenging for the treatment of genetic brain diseases like FXS, where whole-brain treatments ensure an optimal effect. However, we can still use such a strategy by focusing both magnetic targeting and FUS on a relevant brain region like the hippocampus, allowing enhanced gene delivery and restored expression in the area.

Similarly, targeting functionalization associated with cationic MB allows enhanced gene delivery, both *in vitro* and *in vivo*, also by MB accumulation and spatial rapprochement to cells. Beekers *et al.* demonstrated *in vitro* that targeted MB increased by approaching MB on cells and by increasing MB internalization [36]. Therefore, this shows the particular advantages targeted functionalization brings to loaded MB, like cationic MB, to deliver its cargo. However, their use in the brain *in vivo* needs to target brain vasculature to accumulate them in the brain for enhanced BBBo, as demonstrated by Li *et al*. using the binding peptide for apolipoprotein E receptor bound to the MB surface [37]. This strategy strongly enhanced ICG delivery into the brain but does not take advantage of the enhanced internalization. The streptavidin-to-antibody ratio only uses about 9 % of available streptavidin binding sites, suggesting that we could probably bind an additional antibody to the MB surface. Using a neuron-specific antibody like NCAM (neural cell adhesion molecule) in addition to the brain vasculature binding peptide it would allow enhanced BBBo followed by enhanced cationic MB internalization into neurons, improving pDNA delivery [38]. Another strategy combining magnetic targeting to a specific brain region for MB accumulation, enhancing BBBo, and neuron-specific targeting with an antibody for enhanced cell internalization for gene delivery can also be attempted. This would avoid MB internalization into endothelial cells promoted by molecular targeting of brain vasculature as previously described. Such strategies will therefore be attempted with our polymeric cationic MB further functionalized with biotin function for additional binding.

III. FUS-BBBo gene therapy for the fragile X syndrome

Proof of concept of fragile X syndrome gene therapy was demonstrated in our work using both non-viral and viral gene delivery associated with FUS-BBBo, restoring 3.7 and 15.2 % of WT expression respectively. The difference of restored expression further highlights the difference of gene delivery efficiency of both strategies. Alongside the gene expression kinetics, lasting 1 and over 5 weeks respectively, it encouraged us to focus on the viral strategy to study the therapeutic potential of this gene therapy. Thus, we still have to confirm FMRP expression

in neurons and if a similar behavioral effect would be induced by the non-viral strategy with repeated treatments to compensate for the expression kinetics. We previously established several strategies to enhance non-viral gene expression; therefore, an optimized strategy should be used to enhance potential therapeutic effect.

BBB opening therapeutic effect

The behavioral study we performed following whole-brain FUS-BBBo and viral gene delivery demonstrated a partial rescue from BBBo itself on hyperactivity, anxiety, and social impairments. This effect of BBBo was not expected and should be extensively analyzed moving forward. The most likely explanation from this effect is the know ability of FUS-BBBo to activate microglia, neuroinflammation, and protein clearance. This was first described by Jordão *et al*. in a mouse model of Alzheimer's disease. They demonstrated that astrocyte and microglia activation and endogenous antibody extravasation occurred after FUS-BBBo and that it reduced Aβ plaque number and surface area through microglia-associated clearance [39]. This finding was later corroborated and completed by several studies [40], notably with the identification of tau clearance following BBBo [41] and the demonstration by Leinenga and Götz of the efficiency of FUS-BBBo to improve memory in model mice [42]. These studies led to clinical trials for the treatment of Alzheimer's disease and demonstrate the therapeutic potential of FUS-BBBo [43].

Interestingly, the amyloid β precursor protein (APP) expression is downregulated by FMRP, leading to its upregulation in FXS and the accumulation of Aβ in the brain [44]. Westmark *et al*. demonstrated the therapeutic effect from Aβ downregulation by silencing one allele of the APP gene, thus generating *Fmr1*$^{-/y}$ mice with heterozygous APP expression (APP$^{-/+}$), and therefore reduced Aβ [45]. These mice demonstrated total rescue of anxiety phenotype, assessed in the marble burying test and open field, and a partial rescue of seizures, mGluR-mediated long-term depression, and dendritic spine abnormalities. In addition, Zhao *et al*. demonstrated in *Fmr1*$^{-/y}$ mice that the reduction of tau protein led to partial rescue of repetitive behaviors and aggressivity [46]. This highlights the therapeutic potential of Aβ and tau clearance triggered by FUS-BBBo. However, the marbles burying test was one of the last tests performed in our study, at 8 weeks after the procedure, compared to 3 weeks for the elevated

plus maze, open field, or social open field where the FUS-BBBo effect was clearly detected. This suggests that the therapeutic effect of FUS-BBBo faded over time. Considering that all studies on Alzheimer's use weekly treatments to ensure a therapeutic effect, it is likely that the same kind of protocol would be required here.

We also demonstrated that the rescue generated by FUS-BBBo was enhanced on the hyperactivity and anxiety phenotype by the *Fmr1* expression, highlighting the potential of our strategy as a combinational strategy associated with gene therapy and FUS-BBBo for the treatment of FXS.

Fmr1 transgene expression induces partial behavioral rescue

Hyperactivity and anxiety impairment phenotypes could be detected in several tests in addition to the ones usually used to describe these behaviors: the open field or marbles burying test and the elevated plus maze respectively [47,48]. It demonstrates the robust phenotype expressed by *Fmr1*-KO mice in different contexts. It also demonstrates that the rescue induced by BBBo and *Fmr1* expression remains partial as their effect could not be detected depending on context. This highlights the limited effect of restored *Fmr1* expression over behavior despite over 15 % of WT expression on average and expression in neurons of several brain regions. However, Graef et al. demonstrated *in vitro* that partial expression of FMRP allowed the restoration of neuronal activity, with a significant effect from FMRP expression in 20 % of neurons and no improvement from higher expression [49]. It suggests that our gene expression might be sufficient and that limited improvement would be achieved with stronger *Fmr1* expression. This is supported by the study from Chadman *et al.* that used a PHP.eB AAV in adult *Fmr1*-KO mice to transfect neurons without the need of opening the BBB. They reached FMRP expression similar to 2-fold higher compared to WT. However, without *Fmr1* expression analysis, comparison with our study is challenging. They still observed only partial rescue on fear conditioning and motor learning with no effect on hyperactivity [50]. This suggests that restored FMRP expression to WT levels is not sufficient to fully rescue FXS phenotypes and that other parameters need to be considered. In the Chadman *et al*. study, FMRP expression was only restored in neurons with the use of a neuron-specific promoter [50]. As astrocytes and other cell types also play an important role in the

disease, we can hypothesize that the use of a ubiquitous promoter might improve therapy's efficiency [51]. This is the reason that led us to use a CMV promoter in our study; thus, although gene expression in astrocytes and microglia still needs to be confirmed, we should not be concerned by this limitation.

Fmr1 transgene expression during development increases behavioral rescue

The age of animals, on the other hand, might be an important limitation to our study. We demonstrated that restored *Frm1* expression leads to partial phenotype rescue, but it might be enhanced with *Fmr1* expression during brain development, considering that FXS is a neurodevelopmental disorder. Several studies assessed this gene therapy strategy using an intracranial AAV injection in young mice. First, Hooper *et al*. showed that combined intracerebroventricular (ICV) and intra-cisterna magna AAV-*Fmr1* injection in rats on post-natal day (PND) 2 or 3 allowed widespread FMRP expression up to PND 70. They demonstrated a rescue of social impairment associated with partial improvement of sleep quality and partial rescue of hyperactivity from *Fmr1* expression, but showed no effect on repetitive behavior and fear conditioning [52]. Jiang *et al.* used ICV injection of AAV-*Fmr1* in mice on PND 0, allowing widespread FMRP expression close to WT level. They demonstrated a rescue over anxiety, social recognition, and repetitive behavior phenotypes associated with alleviated dendritic spine abnormality [48]. More recently, Wong *et al*. treated *Fmr1*-KO mice with intrathecal injection of AAV-*Fmr1*, also allowing widespread expression of FMRP through the brain. They demonstrated significant rescue over seizures, fear conditioning, and sleep impairment, but with limited effect on hyperactivity [53]. Overall, despite discrepancies between studies over the rescue of repetitive behavior or sleep impairment, they show that a stronger rescue is achieved from restored FRMP expression at a young age compared to adult mice, as depicted by Chadman *et al*. studies. This highlights the potential of a treatment at a young age. In addition, all these gene therapy studies still demonstrated a partial rescue of *the Fmr1-KO* behavioral phenotype, probably due to *Fmr1*$^{-/-}$ maternal care as demonstrated by Zupan and Toth [54]. More specifically, no studies showed a significant effect of treatment on hyperactivity phenotype, unlike in our study, where significant rescue to WT value was

observed. This further highlight the advantage of FUS-BBBo and *Fmr1* gene expression as a combinational therapy for the treatment of FXS.

Alternative gene therapy strategy

Previously mentioned gene therapy studies for FXS highlight that even with widespread *Fmr1* expression with levels close to WT, total behavioral rescue is never observed. This highlights the difficulty of restoring such gene expression that is very precisely regulated in cells throughout development. In addition, despite a transgene expression lower than WT, we still demonstrated a relatively strong expression as assessed in bioluminescence. Comparing it to previous studies, like Fan *et al.*, that did not induce sufficient bioluminescence to detect it *in vivo*, unlike in this PhD, suggests that we induced a stronger gene expression [55]. In their model, they still induced gene expression close to WT level, suggesting that with FXS, a much stronger gene expression is required to restore *Fmr1* expression to WT level. Their study used glial cell line-derived neurotrophic factor (GDNF) expression in a chemically-induced Parkinson's model that only reduced GDNF expression. This explains their reduced need for strong gene expression and highlights the potential of our strategy to restore gene expression less impacted than *Fmr1*. Indeed, by restoring a relevant gene expression with a lower WT-to-KO difference, we could potentially restore its expression to WT level, even with our non-viral strategy. We would not use GDNF, as it is not differently expressed in KO mice [56], but the expression of cAMP or IGF-1 would be an interesting candidate. Indeed, cAMP is downregulated in FXS, and its upregulation through phosphodiesterase-4D inhibition induced positive results in a phase 2 clinical trial [57]. IGF-1 is also downregulated in FXS, and Robert et al. demonstrated that the administration of an analog of IGF-1 (NNZ-2566) induced behavioral therapeutic effects over cognitive, hyperactivity, and social phenotypes [58]. However, its use in clinical trials showed poor effect. [59]. Restoring IGF-1 expression could therefore be an interesting alternative to this analog.

In addition, the use of an epigenetic strategy should also be looked at, as we have the possibility to reduce gene expression with siRNA or miRNA injection instead of pDNA or by expressing an shRNA with an AAV, silencing a specific gene expression. Many targets for this strategy can be studied in FXS, where several thousands of genes are dysregulated, and many are overexpressed [60]. It could be used to reduce phosphodiesterase-4D expression, whose inhibition has demonstrated efficiency in clinical trials as previously stated. It could also be

used over mGlur5 expression as an alternative to mGlur5 antagonists that are well studied in preclinical trials and showed important effects but that proved inefficient in clinical trials [61,62].

BIBLIOGRAPHY

1. Gandhi, K.; Barzegar-Fallah, A.; Banstola, A.; Rizwan, S.B.; Reynolds, J.N.J. Ultrasound-Mediated Blood–Brain Barrier Disruption for Drug Delivery: A Systematic Review of Protocols, Efficacy, and Safety Outcomes from Preclinical and Clinical Studies. Pharmaceutics 2022, 14, doi:10.3390/pharmaceutics14040833.

2. Taylort, S.H.; Thorp, J.M. PROPERTIES AND BIOLOGICAL BEHAVIOUR OF COOMASSIE BLUE*. 1958.

3. Marty, B.; Larrat, B.; Van Landeghem, M.; Robic, C.; Robert, P.; Port, M.; Le Bihan, D.; Pernot, M.; Tanter, M.; Lethimonnier, F.; et al. Dynamic Study of Blood-Brain Barrier Closure after Its Disruption Using Ultrasound: A Quantitative Analysis. Journal of Cerebral Blood Flow and Metabolism 2012, 32, 1948–1958, doi:10.1038/jcbfm.2012.100.

4. Park, J.; Zhang, Y.; Vykhodtseva, N.; Jolesz, F.A.; McDannold, N.J. The Kinetics of Blood Brain Barrier Permeability and Targeted Doxorubicin Delivery into Brain Induced by Focused Ultrasound. Journal of Controlled Release 2012, 162, 134–142, doi:10.1016/j.jconrel.2012.06.012.

5. Rigollet, S.; Rome, C.; Ador, T.; Dumont, E.; Pichon, C.; Delalande, A.; Barbier, E.L.; Stupar, V. FUS-Mediated BBB Opening Leads to Transient Perfusion Decrease and Inflammation without Acute or Chronic Brain Lesion. Theranostics 2024, 14, 4147–4160, doi:10.7150/thno.96721.

6. Todd, N.; Zhang, Y.; Arcaro, M.; Becerra, L.; Borsook, D.; Livingstone, M.; McDannold, N. Focused Ultrasound Induced Opening of the Blood-Brain Barrier Disrupts Inter-Hemispheric Resting State Functional Connectivity in the Rat Brain. Neuroimage 2018, 178, 414–422, doi:10.1016/j.neuroimage.2018.05.063.

7. Chopra, R.; Curiel, L.; Staruch, R.; Morrison, L.; Hynynen, K. An MRI-Compatible System for Focused Ultrasound Experiments in Small Animal Models. Med Phys 2009, 36, 1867–1874, doi:10.1118/1.3115680.

8. Le Floc'h, J.; Lu, H.D.; Lim, T.L.; Démoré, C.; Prud'homme, R.K.; Hynynen, K.; Foster, F.S. Transcranial Photoacoustic Detection of Blood-Brain Barrier Disruption Following Focused

Ultrasound-Mediated Nanoparticle Delivery. Mol Imaging Biol 2020, 22, 324–334, doi:10.1007/s11307-019-01397-4.

9. Liang, S.; Hu, D.; Li, G.; Gao, D.; Li, F.; Zheng, H.; Pan, M.; Sheng, Z. NIR-II Fluorescence Visualization of Ultrasound-Induced Blood–Brain Barrier Opening for Enhanced Photothermal Therapy against Glioblastoma Using Indocyanine Green Microbubbles. Sci Bull (Beijing) 2022, 67, 2316–2326, doi:10.1016/j.scib.2022.10.025.

10. Hsu, Y.H.; Lee, W.C.; Chu, S.S.; Chao, M.E.; Wu, K.S.; Liu, R.S.; Wong, T.T. Influence of Acoustic Parameters and Sonication Schemes on Transcranial Blood–Brain Barrier Disruption Induced by Pulsed Weakly Focused Ultrasound. Pharmaceutics 2022, 14, doi:10.3390/pharmaceutics14061207.

11. Samiotaki, G.; Vlachos, F.; Tung, Y.S.; Konofagou, E.E. A Quantitative Pressure and Microbubble-Size Dependence Study of Focused Ultrasound-Induced Blood-Brain Barrier Opening Reversibility in Vivo Using MRI. Magn Reson Med 2012, 67, 769–777, doi:10.1002/mrm.23063.

12. Sciortino, V.M.; Tran, A.; Sun, N.; Cao, R.; Sun, T.; Sun, Y.Y.; Yan, P.; Zhong, F.; Zhou, Y.; Kuan, C.Y.; et al. Longitudinal Cortex-Wide Monitoring of Cerebral Hemodynamics and Oxygen Metabolism in Awake Mice Using Multi-Parametric Photoacoustic Microscopy. Journal of Cerebral Blood Flow and Metabolism 2021, 41, 3187–3199, doi:10.1177/0271678X211034096.

13. Tang, Y.; Qian, X.; Lee, D.J.; Zhou, Q.; Yao, J. From Light to Sound: Photoacoustic and Ultrasound Imaging in Fundamental Research of Alzheimer's Disease. OBM Neurobiol 2020, 4.

14. Lin, C.W.; Fan, C.H.; Yeh, C.K. The Impact of Surface Drug Distribution on the Acoustic Behavior of DOX-Loaded Microbubbles. Pharmaceutics 2021, 13, doi:10.3390/pharmaceutics13122080.

15. Ajenjo, J.; Seo, J.W.; Foiret, J.; Wu, B.; Raie, M.N.; Wang, J.; Fite, B.Z.; Zhang, N.; Malek, R.; Beinat, C.; et al. PET Imaging of Focused-Ultrasound Enhanced Delivery of AAVs into the Murine Brain. Theranostics 2023, 13, 5151–5169, doi:10.7150/thno.85549.

16. Ji, R.; Karakatsani, M.E.; Burgess, M.; Smith, M.; Murillo, M.F.; Konofagou, E.E. Cavitation-Modulated Inflammatory Response Following Focused Ultrasound Blood-Brain Barrier Opening. Journal of Controlled Release 2021, 337, 458–471, doi:10.1016/j.jconrel.2021.07.042.

17. Stavarache, M.A.; Petersen, N.; Jurgens, E.M.; Milstein, E.R.; Rosenfeld, Z.B.; Ballon, D.J.; Kaplitt, M.G. Safe and Stable Noninvasive Focal Gene Delivery to the Mammalian Brain Following Focused Ultrasound. J Neurosurg 2019, 130, 989–998, doi:10.3171/2017.8.JNS17790.

18. Chen, H.; Konofagou, E.E. The Size of Blood-Brain Barrier Opening Induced by Focused Ultrasound Is Dictated by the Acoustic Pressure. Journal of Cerebral Blood Flow and Metabolism 2014, 34, 1197–1204, doi:10.1038/jcbfm.2014.71.

19. Hoffmann, M.; Hersch, N.; Gerlach, S.; Dreissen, G.; Springer, R.; Merkel, R.; Csiszár, A.; Hoffmann, B. Complex Size and Surface Charge Determine Nucleic Acid Transfer by Fusogenic Liposomes. Int J Mol Sci 2020, 21, doi:10.3390/ijms21062244.

20. Kheirolomoom, A.; Dayton, P.A.; Lum, A.F.H.; Little, E.; Paoli, E.E.; Zheng, H.; Ferrara, K.W. Acoustically-Active Microbubbles Conjugated to Liposomes: Characterization of a Proposed Drug Delivery Vehicle. Journal of Controlled Release 2007, 118, 275–284, doi:10.1016/j.jconrel.2006.12.015.

21. De Cock, I.; Lajoinie, G.; Versluis, M.; De Smedt, S.C.; Lentacker, I. Sonoprinting and the Importance of Microbubble Loading for the Ultrasound Mediated Cellular Delivery of Nanoparticles. Biomaterials 2016, 83, 294–307, doi:10.1016/j.biomaterials.2016.01.022.

22. Gerstenmayer, M.; Fellah, B.; Magnin, R.; Selingue, E.; Larrat, B.; Acoustic, B.L. Acoustic Transmission Factor through the Rat Skull as a Function of Body Mass, Frequency and Position. Ultrasound Med Biol 2018, 44, doi:10.1016/j.ultrasmedbio.2018.06.005ï.

23. Atar, M.; Yasmin, R.; Sharma, R.; Le Comber, S.C.; Verry, P.; Polly, P.D. Of Mice and Mutations: Phenotypic Effects of the Diabetic Db/Db and Ob/Ob Mutations on the Skull and Teeth of Mice. European Archives of Paediatric Dentistry 2008, 9.

24. Wang, X.; Zhang, H.; Hu, L.; He, J.; Jiang, Q.; Ren, L.; Yu, K.; Fu, M.; Li, Z.; He, Z.; et al. The High-Bone-Mass Phenotype of Novel Transgenic Mice with LRP5 A241T Mutation. Bone 2024, 187, doi:10.1016/j.bone.2024.117172.

25. Felix, M.S.; Borloz, E.; Metwally, K.; Dauba, A.; Larrat, B.; Matagne, V.; Ehinger, Y.; Villard, L.; Novell, A.; Mensah, S.; et al. Ultrasound-Mediated Blood-Brain Barrier Opening Improves Whole Brain Gene Delivery in Mice. Pharmaceutics 2021, 13, doi:10.3390/pharmaceutics13081245.

26. O'Reilly, M.A.; Hynynen, K. Blood-Brain Barrier: Real-Time Feedback-Controlled Focused Ultrasound Disruption by Using an Acoustic Emissions-Based Controller. Radiology 2012, 263, 96–106, doi:10.1148/radiol.11111417.

27. Nouraein, S.; Lee, S.; Saenz, V.A.; Del Mundo, H.C.; Yiu, J.; Szablowski, J.O. Acoustically Targeted Noninvasive Gene Therapy in Large Brain Volumes. Gene Ther 2024, 31, 85–94, doi:10.1038/s41434-023-00421-1.

28. Li, H.R.; Harb, M.; Heath, J.E.; Trippett, J.S.; Shapiro, M.G.; Szablowski, J.O. Engineering Viral Vectors for Acoustically Targeted Gene Delivery. Nat Commun 2024, 15, 4924, doi:10.1038/s41467-024-48974-y.

29. Calcedo, R.; Vandenberghe, L.H.; Gao, G.; Lin, J.; Wilson, J.M. Worldwide Epidemiology of Neutralizing Antibodies to Adeno-Associated Viruses. Journal of Infectious Diseases 2009, 199, 381–390, doi:10.1086/595830.

30. Halbert, C.L.; Miller, A.D.; McNamara, S.; Emerson, J.; Gibson, R.L.; Ramsey, B.; Aitken, M.L. Prevalence of Neutralizing Antibodies against Adeno-Associated Virus (AAV) Types 2, 5, and 6 in Cystic Fibrosis and Normal Populations: Implications for Gene Therapy Using AAV Vectors. Hum Gene Ther 2006, 17, 440–447, doi:10.1089/hum.2006.17.440.

31. Chirmule, N.; Propert, K.J.; Magosin, S.A.; Qian, Y.; Qian, R.; Wilson, J.M. Immune Responses to Adenovirus and Adeno-Associated Virus in Humans; 1999; Vol. 6;.

32. McDannold, N.; Arvanitis, C.D.; Vykhodtseva, N.; Livingstone, M.S. Temporary Disruption of the Blood-Brain Barrier by Use of Ultrasound and Microbubbles: Safety and Efficacy Evaluation in Rhesus Macaques. Cancer Res 2012, 72, 3652–3663, doi:10.1158/0008-5472.CAN-12-0128.

33. Belliveau, N.M.; Huft, J.; Lin, P.J.; Chen, S.; Leung, A.K.; Leaver, T.J.; Wild, A.W.; Lee, J.B.; Taylor, R.J.; Tam, Y.K.; et al. Microfluidic Synthesis of Highly Potent Limit-Size Lipid Nanoparticles for in Vivo Delivery of SiRNA. Mol Ther Nucleic Acids 2012, 1, e37, doi:10.1038/mtna.2012.28.

34. Stride, E.; Porter, C.; Prieto, A.G.; Pankhurst, Q. Enhancement of Microbubble Mediated Gene Delivery by Simultaneous Exposure to Ultrasonic and Magnetic Fields. Ultrasound Med Biol 2009, 35, 861–868, doi:10.1016/j.ultrasmedbio.2008.11.010.

35. Fan, C.H.; Cheng, Y.H.; Ting, C.Y.; Ho, Y.J.; Hsu, P.H.; Liu, H.L.; Yeh, C.K. Ultrasound/Magnetic Targeting with SPIO-DOX-Microbubble Complex for Image-Guided Drug Delivery in Brain Tumors. Theranostics 2016, 6, 1542–1556, doi:10.7150/thno.15297.

36. Beekers, I.; Langeveld, S.A.G.; Meijlink, B.; van der Steen, A.F.W.; de Jong, N.; Verweij, M.D.; Kooiman, K. Internalization of Targeted Microbubbles by Endothelial Cells and Drug Delivery by Pores and Tunnels. Journal of Controlled Release 2022, 347, 460–475, doi:10.1016/j.jconrel.2022.05.008.

37. Li, B.; Lin, Y.; Chen, G.; Cai, M.; Zhong, H.; Xiao, Z.; Lin, M.; Li, T.; Cai, Y.; Shuai, X.; et al. Anchoring Microbubbles on Cerebrovascular Endothelium as a New Strategy Enabling Low-Energy Ultrasound-Assisted Delivery of Varisized Agents Across Blood-Brain Barrier. Advanced Science 2023, 10, doi:10.1002/advs.202302134.

38. Berezin, V.; Walmod, P.S.; Filippov, M.; Dityatev, A. Targeting of ECM Molecules and Their Metabolizing Enzymes and Receptors for the Treatment of CNS Diseases. In Progress in Brain Research; Elsevier B.V., 2014; Vol. 214, pp. 353–388.

39. Jordão, J.F.; Thévenot, E.; Markham-Coultes, K.; Scarcelli, T.; Weng, Y.Q.; Xhima, K.; O'Reilly, M.; Huang, Y.; McLaurin, J.A.; Hynynen, K.; et al. Amyloid-β Plaque Reduction, Endogenous Antibody Delivery and Glial Activation by Brain-Targeted, Transcranial Focused Ultrasound. Exp Neurol 2013, 248, 16–29, doi:10.1016/j.expneurol.2013.05.008.

40. Liu, X.; Maria, N.S.S.; Lin, S.W.; Jacobs, R.E. The Applications of Focused Ultrasound (FUS) in Alzheimer's Disease Treatment: A Systematic Review on Both Animal and Human Studies. Aging Dis 2021, 12, 1977–2002, doi:10.14336/AD.2021.0510.

41. Pandit, R.; Leinenga, G.; Götz, J. Repeated Ultrasound Treatment of Tau Transgenic Mice Clears Neuronal Tau by Autophagy and Improves Behavioral Functions. Theranostics 2019, 9, 3754–3767, doi:10.7150/thno.34388.

42. Leinenga, G.; Götz, J. Scanning Ultrasound Removes Amyloid-b and Restores Memory in an Alzheimer's Disease Mouse Model; 2015;

43. Rezai, A.R.; Ranjan, M.; Haut, M.W.; Carpenter, J.; D'Haese, P.F.; Mehta, R.I.; Najib, U.; Wang, P.; Claassen, D.O.; Chazen, J.L.; et al. Focused Ultrasound–Mediated Blood-Brain Barrier Opening in Alzheimer's Disease: Long-Term Safety, Imaging, and Cognitive Outcomes. J Neurosurg 2023, 139, 275–283, doi:10.3171/2022.9.JNS221565.

44. Cencelli, G.; Pacini, L.; De Luca, A.; Messia, I.; Gentile, A.; Kang, Y.; Nobile, V.; Tabolacci, E.; Jin, P.; Farace, M.G.; et al. Age-Dependent Dysregulation of APP in Neuronal and Skin Cells from Fragile X Individuals. Cells 2023, 12, doi:10.3390/cells12050758.

45. Westmark, C.J.; Westmark, P.R.; O'Riordan, K.J.; Ray, B.C.; Hervey, C.M.; Salamat, M.S.; Abozeid, S.H.; Stein, K.M.; Stodola, L.A.; Tranfaglia, M.; et al. Reversal of Fragile X Phenotypes by Manipulation of AβPP/Aβ Levels in Fmr1 KO Mice. PLoS One 2011, 6, doi:10.1371/journal.pone.0026549.

46. Zhao, S.; Jiang, X.; Han, L.; Jiang, Y.; Wang, Y.; Meng, J.; Zhu, X.; Zhang, X.; Luo, H.; Zhang, Y. wu Tau Reduction Attenuates Autism-like Features in Fmr1 Knockout Mice. Mol Autism 2023, 14, doi:10.1186/s13229-023-00574-1.

47. Spencer, C.M.; Graham, D.F.; Yuva-Paylor, L.A.; Nelson, D.L.; Paylor, R. Social Behavior in Fmr1 Knockout Mice Carrying a Human FMR1 Transgene. Behavioral Neuroscience 2008, 122, 710–715, doi:10.1037/0735-7044.122.3.710.

48. Jiang, Y.; Han, L.; Meng, J.; Wang, Z.; Zhou, Y.; Yuan, H.; Xu, H.; Zhang, X.; Zhao, Y.; Lu, J.; et al. Gene Therapy Using Human FMRP Isoforms Driven by the Human FMR1 Promoter Rescues Fragile X Syndrome Mouse Deficits. Mol Ther Methods Clin Dev 2022, 27, 246–258, doi:10.1016/j.omtm.2022.10.002.

49. Graef, J.D.; Wu, H.; Ng, C.; Sun, C.; Villegas, V.; Qadir, D.; Jesseman, K.; Warren, S.T.; Jaenisch, R.; Cacace, A.; et al. Partial FMRP Expression Is Sufficient to Normalize Neuronal Hyperactivity in Fragile X Neurons. European Journal of Neuroscience 2020, 51, 2143–2157, doi:10.1111/ejn.14660.

50. Chadman, K.K.; Adayev, T.; Udayan, A.; Ahmed, R.; Dai, C.L.; Goodman, J.H.; Meeker, H.; Dolzhanskaya, N.; Velinov, M. Efficient Delivery of FMR1 across the Blood Brain Barrier Using AAVphp Construct in Adult FMR1 KO Mice Suggests the Feasibility of Gene Therapy for Fragile X Syndrome. Genes (Basel) 2023, 14, doi:10.3390/genes14020505.

51. Lucas, A.; Poleg, S.; Klug, A.; McCullagh, E.A. Myelination Deficits in the Auditory Brainstem of a Mouse Model of Fragile X Syndrome. Front Neurosci 2021, 15, doi:10.3389/fnins.2021.772943.

52. Hooper, A.W.M.; Wong, H.; Niibori, Y.; Abdoli, R.; Karumuthil-Melethil, S.; Qiao, C.; Danos, O.; Bruder, J.T.; Hampson, D.R. Gene Therapy Using an Ortholog of Human Fragile X Mental

Retardation Protein Partially Rescues Behavioral Abnormalities and EEG Activity. Mol Ther Methods Clin Dev 2021, 22, 196–209, doi:10.1016/j.omtm.2021.06.013.

53. Wong, H.; Hooper, A.W.M.; Kang, H.R.; Lee, S.J.; Zhao, J.; Sadhu, C.; Rawat, S.; Gray, S.J.; Hampson, D.R. CNS-Dominant Human FMRP Isoform Rescues Seizures, Fear, and Sleep Abnormalities in Fmr1-KO Mice. 2023, doi:10.1172/jci.

54. Zupan, B.; Toth, M. Wild-Type Male Offspring of Fmr-1+/- Mothers Exhibit Characteristics of the Fragile X Phenotype. Neuropsychopharmacology 2008, 33, 2667–2675, doi:10.1038/sj.npp.1301651.

55. Fan, C.H.; Ting, C.Y.; Lin, C.Y.; Chan, H.L.; Chang, Y.C.; Chen, Y.Y.; Liu, H.L.; Yeh, C.K. Noninvasive, Targeted, and Non-Viral Ultrasound-Mediated GDNF-Plasmid Delivery for Treatment of Parkinson's Disease. Sci Rep 2016, 6, doi:10.1038/srep19579.

56. Yang, Q.; Feng, B.; Zhang, K.; Guo, Y. yan; Liu, S. bing; Wu, Y. mei; Li, X. qiang; Zhao, M. gao Excessive Astrocyte-Derived Neurotrophin-3 Contributes to the Abnormal Neuronal Dendritic Development in a Mouse Model of Fragile X Syndrome. PLoS Genet 2012, 8, doi:10.1371/journal.pgen.1003172.

57. Berry-Kravis, E.M.; Harnett, M.D.; Reines, S.A.; Reese, M.A.; Ethridge, L.E.; Outterson, A.H.; Michalak, C.; Furman, J.; Gurney, M.E. Inhibition of Phosphodiesterase-4D in Adults with Fragile X Syndrome: A Randomized, Placebo-Controlled, Phase 2 Clinical Trial. Nat Med 2021, 27, 862–870, doi:10.1038/s41591-021-01321-w.

58. Deacon, R.M.J.; Glass, L.; Snape, M.; Hurley, M.J.; Altimiras, F.J.; Biekofsky, R.R.; Cogram, P. NNZ-2566, a Novel Analog of (1–3) IGF-1, as a Potential Therapeutic Agent for Fragile X Syndrome. Neuromolecular Med 2015, 17, 71–82, doi:10.1007/s12017-015-8341-2.

59. Berry-Kravis, E.; Horrigan, J.P.; Tartaglia, N.; Hagerman, R.; Kolevzon, A.; Erickson, C.A.; Hatti, S.; Snape, M.; Yaroshinsky, A.; Stoms, G.; et al. A Double-Blind, Randomized, Placebo-Controlled Clinical Study of Trofinetide in the Treatment of Fragile X Syndrome. Pediatr Neurol 2020, 110, 30–41, doi:10.1016/j.pediatrneurol.2020.04.019.

60. Li, M.; Shin, J.; Risgaard, R.D.; Parries, M.J.; Wang, J.; Chasman, D.; Liu, S.; Roy, S.; Bhattacharyya, A.; Zhao, X. Identification of FMR1-Regulated Molecular Networks in Human Neurodevelopment. Genome Res 2020, 30, 361–374, doi:10.1101/gr.251405.119.

61. Berry-Kravis, E.; Des Portes, V.; Hagerman, R.; Jacquemont, S.; Charles, P.; Visootsak, J.; Brinkman, M.; Rerat, K.; Koumaras, B.; Zhu, L.; et al. Mavoglurant in Fragile X Syndrome: Results of Two Randomized, Double-Blind, Placebo-Controlled Trials. Sci Transl Med 2016, 13.

62. Westmark, P.R.; Dekundy, A.; Gravius, A.; Danysz, W.; Westmark, C.J. Rescue of Fmr1KO Phenotypes with MGluR5 Inhibitors: MRZ-8456 versus AFQ-056. Neurobiol Dis 2018, 119, 190–198, doi:10.1016/j.nbd.2018.08.008.

Thomas ADOR

Délivrance de gènes par sonoporation pour la thérapie du syndrome de l'X fragile

Comme de nombreuses maladies monogéniques du système nerveux central, le syndrome de l'X fragile manque de traitement efficace. Si la thérapie génique offre un grand potentiel thérapeutique, la barrière hémato-encéphalique (BHE) reste une limite majeure à son efficacité. L'utilisation de microbulles de gaz associée à des ultrasons focalisés est une méthode prometteuse pour ouvrir cette barrière, de façon non invasive et transitoire, afin de délivrer des molécules thérapeutiques. L'objectif de cette thèse a été de développer une méthode de thérapie génique basée sur ce principe utilisant le modèle murin du syndrome de l'X fragile, les souris Fmr1-KO. Dans une première partie, des microbulles innovantes ont été développées avec succès, possédant des propriétés magnétiques, de ciblage, ou cationiques. Nous avons démontré l'efficacité de nos microbulles cationiques pour complexer et délivrer de l'ADN plasmidique, tout en gardant les propriétés acoustiques permettant l'ouverture de la BHE.
Dans une seconde partie, un protocole d'ouverture focalisé de la BHE a été mis en place avec succès. Un suivi in vivo de l'ouverture de cette barrière a été développé par imagerie photoacoustique ainsi que par imagerie de fluorescence, utilisant l'Indocyanine Green comme agent de contraste bimodal. Une comparaison avec l'IRM a été réalisée, démontrant l'efficacité de l'imagerie de fluorescence, en particulier ex vivo, pour le suivi de l'ouverture. Dans une troisième partie, un protocole de transfert de gène focalisé dans le cerveau a été optimisé, utilisant les microbulles cationiques complexées avec de l'ADN. Cette méthode a été utilisée pour la première fois sur le modèle Fmr1-KO, démontrant la capacité de cette méthode à réexprimer le gène Fmr1.
Enfin, nous avons comparé notre précédente méthode de transfert de gène non virale, avec une méthode virale utilisant un AAV2/9, co-injecté avec des microbulles non fonctionnalisées, pour l'ouverture de la BHE dans le cerveau entier des souris Fmr1-KO. Nos résultats montrent que la méthode virale permet une expression plus forte et stable sur plusieurs semaines en comparaison à la méthode non virale. Par la suite, une étude comportementale a été réalisée révélant, pour la première fois, un effet thérapeutique de l'ouverture seule de la BHE dans le cerveau entier, effet renforcé par l'expression du transgène Fmr1. Cette thèse contribue à de nouvelles perspectives pour la thérapie génique du système nerveux central en utilisant des microbulles associées à des ultrasons focalisés. Elle apporte également une nouvelle approche thérapeutique associant l'ouverture de la BHE avec une thérapie génique réexprimant Fmr1.

Mots clés : Sonoporation, Transfert de gène, Syndrome de l'X fragile, Microbulles cationiques, Déficience intellectuelle, comportement

Gene delivery by sonoporation for Fragile X syndrome therapy

Like many monogenic diseases of the central nervous system, Fragile X syndrome lacks effective treatment. While gene therapy holds great therapeutic potential, the blood-brain barrier (BBB) remains a major limitation to its effectiveness. The use of microbubbles combined with focused ultrasound is a promising method to open this barrier, in a non-invasive and transient manner, in order to deliver therapeutic molecules. The objective of this thesis was to develop a gene therapy method based on this principle using the mouse model of fragile X syndrome, Fmr1-KO mice. In a first part, innovative microbubbles have been successfully developed, with magnetic, targeting or cationic properties. We demonstrated the effectiveness of our cationic microbubbles to complex and deliver plasmid DNA, while maintaining acoustic properties allowing the opening of the BBB.
In a second part, a focused protocol for BBB opening was successfully developed. An in vivo monitoring of the BBB opening was also developed by photoacoustic and fluorescence imaging, using Indocyanine Green as a bimodal contrast agent. A comparison with MRI was performed demonstrating the efficacy of fluorescence imaging, especially ex vivo, to monitor BBB closure kinetics.
In a third part, a focused gene transfer protocol in the brain was optimized, using cationic microbubbles complexed with DNA. This method was used for the first time on the Fmr1-KO model, demonstrating the ability of this method to re-express the Fmr1 gene. Finally, we compared our previous non-viral gene transfer method with a viral method using AAV2/9 co-injected with non-functionalized microbubbles for the opening of the BBB in the whole brain of the Fmr1-KO model. Our results show that the viral method allows a stronger and more stable expression over several weeks compared to the non-viral method. Subsequently, a behavioral study was conducted, revealing for the first time a therapeutic effect of the BBB opening alone in the whole brain, effect reinforced in some aspects by the expression of the Fmr1 transgene. This thesis contributes to new perspectives for central nervous system gene therapy, using microbubbles associated with focused ultrasound. It also provides a new therapeutic approach combining the opening of the BBB with gene therapy restoring Fmr1 expression.

Keywords : Sonoporation, gene delivery, Fragile X syndrome, Cationic microbubbles, Intellectual defiency, Behavior

ART-ARNm INSERM US-55
14 Avenue de l'Hôpital
45100 Orléans